# Synthesis and fabrication of optically tuned graphene quantum dots as sensing platforms for ultrasensitive detection of environmental pollutants

Thesis Submitted to AcSIR for the Award of the Degree of
DOCTOR OF PHILOSOPHY
in CHEMICAL SCIENCES

By
Raji V. Nair

Registration No: 10CC15J39002

Under the guidance of
Dr. Saju Pillai

MATERIALS SCIENCE AND TECHNOLOGY DIVISION
CSIR-NATIONAL INSTITUTE FOR INTERDISCIPLINARY SCIENCE
AND TECHNOLOGY (CSIR-NIIST)
THIRUVANANTHAPURAM-695019, KERALA, INDIA

December, 2019

*Dedicated to My Beloved Family, Teachers &*
*God Almighty*

# DECLARATION

I hereby declare that the Ph.D. thesis entitled "**Synthesis and Fabrication of Optically Tuned Graphene Quantum Dots as Sensing Platforms for Ultrasensitive Detection of Environmental Pollutants**" is an independent work carried out by me at the **Materials Science and Technology Division (MSTD), CSIR-National Institute for Interdisciplinary Science and Technology (CSIR-NIIST), Thiruvananthapuram** under the supervision of **Dr. Saju Pillai, Senior Scientist** and it has not been submitted anywhere else for any other degree, diploma, or title.

31/12/2019

**Raji V. Nair**

Thiruvananthapuram

December, 2019

i

# CERTIFICATE

This is to certify that the work incorporated in this Ph.D. thesis entitled *"Synthesis and Fabrication of Optically Tuned Graphene Quantum Dots as Sensing Platforms for Ultrasensitive Detection of Environmental Pollutants"* submitted by *Ms. Raji V Nair* to *Academy of Scientific and Innovative Research (AcSIR)* in partial fulfilment of the requirements for the award of the *Degree of Doctor of Philosophy* in *Chemical Sciences* embodies original research work under my guidance. I further certify that this work has not been submitted to any other University or Institution in part or full for the award of any degree or diploma. Research materials obtained from other sources have been duly acknowledged in the thesis. Any text, illustrations and tables used in the thesis from other sources have also been duly cited and acknowledged.

31/12/2019
**Dr. Saju Pillai**

**(Thesis Supervisor)**

Thiruvananthapuram

December, 2019

31/12/2019
**Raji V. Nair**

**(Student)**

# ACKNOWLEDGEMENT

# CONTENTS

---

**Chapter 3        Sulphur-Doped Graphene Quantum Dots Based Fluorescent Sensors in Aqueous and Flexible Forms for Sensitive Detection of Pesticides**        **95-125**

---

---

**Chapter 4**        **Sulphur-Doped Graphene Quantum Dots Based**        **127-150**

**Fluorescent Sensors in Aqueous and Flexible Forms**

**for Sensitive Detection of Pesticides**

---

# LIST OF FIGURES

### Chapter 3

## Chapter 4

## Chapter 5

# LIST OF SCHEMES

# LIST OF TABLES

# LIST OF ABBREVATIONS

| | |
|---|---|
| **µm** | Micrometer |
| **µM** | Micromolar |
| **°C** | Degree Celsius |
| **0D** | Zero-dimensional |
| **1D** | One-dimensional |
| **2D** | Two-dimensional |
| **3D** | Three-dimensional |
| **AC** | Acetamiprid |
| **AFM** | Atomic Force Microscopy |
| **AIEE** | Aggregation induced enhancement emission |
| **Apt** | Aptamer |
| **BE** | Binding energy |
| **BF** | Breath figure |
| **cm** | Centimeter |
| **CF** | Carbofuran |
| **CIE** | Commission Internationale de l'Eclairage |
| **CNT** | Carbon nanotube |
| **CPC** | Colloidal photonic crystal |
| **DLS** | Dynamic light scattering |
| **eV** | Electron volt |
| **EPA** | Environmental Protection Agency |
| **FFT** | Fast Fourier Transform |
| **FRET** | Fluorescence Resonance Energy Transfer |
| **FT-IR** | Fourier Transform Infrared Spectroscopy |
| **GO** | Graphene oxide |
| **GQD** | Graphene quantum dot |
| **h** | Hours |
| **HOMO** | Highest Occupied Molecular Orbital |
| **HR-TEM** | High Resolution Transmission Electron Microscope |
| **IFE** | Inner Filter Effect |
| **IM** | Imidacloprid |

| | |
|---|---|
| **IR** | Infrared |
| **LOD** | Limit of detection |
| **LUMO** | Lowest Unoccupied Molecular Orbital |
| **m** | Metre |
| **mg** | Milligram |
| **min** | Minutes |
| **mL** | Milliliter |
| **M** | Molar |
| **MS** | Microwave-assisted sonochemical synthesis |
| **MPr** | Methyl parathion |
| **MT** | Metalaxyl |
| **MTT** | [3-(4,5-dimethylthiazol-2-yl)-2,5-diphenyltetrazolium bromide] |
| **nm** | Nanometer |
| **nM** | Nanomolar |
| **OM** | Omethoate |
| **PBG** | Photonic band gap |
| **PL** | Photoluminescence |
| **ppb** | Parts per billion |
| **ppm** | Parts per million |
| **PS** | Polystyrene |
| **PVA** | Poly(vinyl) alcohol |
| **SEM** | Scanning Electron Microscope |
| **SERS** | Surface-enhanced Raman spectroscopy |
| **TCSPC** | Time-correlated single-photon counting |
| **TEM** | Transmission Electron Microscope |
| **Tr** | Thiram |
| **UV-Vis** | Ultraviolet-Visible |
| **WAXS** | Wide-Angle X-ray Scattering |
| **WHO** | World Health Organization |
| **wt %** | Weight percentage |
| **XPS** | X-ray Photoelectron Spectroscopy |
| **XRD** | X-ray Diffraction |

# Abstract

Graphene quantum dots (GQDs), one of the newly emerging carbonaceous material of its zero-dimensional (0D) kind, can exhibit characteristics of both graphene and quantum dots. The biocompatibility, low cytotoxicity, tunable band gap, aqueous dispersibility, high photo stability and chemical inertness makes it an excellent alternative for organic fluorophores and other conventional semiconductor quantum dots that possess demerits like its toxic and non-biocompatible nature.

Challenges in developing efficient GQDs with excellent physical and chemical properties involves the process development that routes to a facile rapid synthesis that yields high production yield of size-tunable GQDs with better quantum yield. Unlike the other heat treatment methods, the microwave-assisted sonochemical method makes a low- temperature rapid process for the synthesis of GQDs with narrow size distribution. Herein, the GQDs were synthesized by oxidative cutting of GO using $KMnO_4$ as an oxidizing agent in an acid-free condition within a short span of time (30 min) under the combined effect of microwave energy and ultrasonication effect. Tuning of particle size is achieved by modulating the microwave reaction power. The synthesized GQDs are highly crystalline and have uniform size distribution. The method yielded higher quantum yield for GQDs up to 23.8 % with high product yield (75-81 %) and stable size-dependent photoluminescence in aqueous solutions. The GQDs synthesized were demonstrated for the detection of physiologically relevant metal ions and particularly for the sensing of $Fe^{3+}$ ions in aqueous media. Our studies reaffirm that the GQDs possess very good biocompatibility, good aqueous dispersibility, low cytotoxicity and high photostability. Further, we conducted the live-cell imaging of cancer cells (HeLa) with GQDs as the fluorescent probe.

To address the relatively low emission efficiency of GQDs, PL enhancement strategies is adopted for effective utilization in various applications. Strategies involve either the use of patterned substrates or chemical doping. The method of using patterned substrates exploits the geometrical advantage of the substrate for the PL enhancement. Herein, we have adopted two methodologies, namely breath figure technique and photonic band gap effect. PL enhancement using the breath figure method achieved a 77-fold enhancement of fluorescence emission through

aggregation-induced emission enhancement and thus the sensitivity towards $Fe^{3+}$ was also enhanced with LOD as low as 80 nM. In another method, a 102-fold enhancement of fluorescent emission of GQDs was achieved by slow photon effect using colloidal photonic crystals (CPC) having micro and nano-topographies due to closed-pack arrangement of polystyrene microspheres. CPC based GQD platform was further used for the sensitive detection of $Fe^{3+}$ ions with much lower LOD as 30 nM.

Doping carbon nanomaterials with heteroatoms can induce electronic and structural distortion, providing an efficient way to tune their band gap and optical properties. Herein, we achieved band gap tuning by sulphur doping, produced the green fluorescent sulphur-doped graphene quantum dots (S-GQDs) with improved quantum yield of 27.8 %. Strong oxidation with acidified $KMnO_4$ as oxidizing agent drastically reduced the reaction time to 5 min. Aqueous S-GQD and PVA/S-GQD composite films fabricated as a flexible solid-state fluorescent sensor were used for the ultrasensitive detection of pesticides. They showed a remarkable limit of detection at ppb level for carbofuran and Thiram and also carried out real sample analysis.

The S-GQD based sensor exhibited high sensitivity towards various pesticides, however selectivity is a matter of concern. To tackle this issue, we designed a simple and efficient fluorescent turn-on aptasensor based on S-GQD, utilizing specific recognition and binding properties of aptamer (Apt) for the selective and sensitive detection of a model pesticide, omethoate (OM). The fluorescence turn OFF-ON is based on the aggregation-disaggregation mechanism of S-GQD in the presence of aptamer and omethoate respectively. The developed 'switch-on' aptasensor has achieved a limit of detection as low as 1 ppb with high selectivity for omethoate over other control pesticides. Considering all the above advantages, we believe that the developed aptamer strategy can offer alternative approaches for other targets of interest in the field of environmental monitoring and food safety.

The approach we developed was reliable and have high selectivity, but not sensitive enough for the trace level detection with better accuracy. To address this concern, a complementary dual-mode sensing system can be designed which can provide two kinds of output signals, making the results more convincing. With the objective of achieving an enhanced sensitivity for the trace level detection of OM with better accuracy, we developed an efficient surface-enhanced Raman scattering

(SERS)/fluorescence dual-mode sensor (S-GQD/Au-Apt) based on aptamer modified gold nanoparticles (Au-Apt) and S-GQDs. Upon the addition of OM to the designed sensing probe, it induces structural switching of aptamer with the formation of Au-Apt/OM with the simultaneous release of S-GQDs from the complex. The released S-GQDs turn-on the fluorescence signal and the component Au-Apt/OM gives the SERS signal. The sensing based on the fluorescence turn-on exhibited a LOD of 1.7 ppm with high selectivity. The sensing based on the formation of Au-Apt/OM SERS probe showed enhanced sensitivity with LOD 0.05 ppb. This strategy offers a new method for designing dual-mode aptasensors combined with different specific aptamers for other targets which can be applied in the field of food analysis and environmental monitoring.

In summary, a facile and rapid synthesis strategy was developed wherein simultaneous action of microwaves and ultrasonic radiation was utilized for the synthesis of size-tunable GQDs with tunable optical properties, which shows immense potential in biomedical and sensing applications.

# Chapter 1

## Introduction

## Abstract

This chapter provides a brief introduction to graphene quantum dots (GQDs), their properties, challenges, synthesis methods and applications induced by its fluorescent properties. Discussions are structured on different synthetic approaches to produce GQDs with the emphasis on the top-down routes. The new advances in enhancing the fluorescent properties of GQDs have been focused especially the emission efficiency which is highly desirable to broaden its widespread application. Further, the chapter briefs the significance of microwave assisted-sonochemical methods over other conventional synthetic methods considering the state of art, the chapter is more focused on the sensors and analytical systems that utilises GQDs as a key component.

## 1.1. History of the development of carbon materials

Carbon, one of the amplest elements, has been widely explored since 19th century and has encountered a constant flow in its explorations. In 1859, Brodie prepared graphite oxide by means of some hazardous experiments to determine the molecular weight of graphite and was termed as 'Graphon'.[1] But the properties of graphite oxide was not studied till 1918. In 1924, Bernal discovered the structural property studies of graphite oxide via single-crystal diffraction method.[2] With the development of various characterization techniques, Wallace investigated the electronic properties of graphite and the idea of graphene was introduced in 1947.[3] Later in 1957, Hummers and Offeman developed a new strategy for the preparation of graphite oxide, which is safer and more effective than Brodie's method.[4] The concept of a single-layer graphite sheet was first defined by Boehm[5] in 1962 and by some theoretical physicists with a massless Dirac equation in 1984[6] was viewed as implausible at that time. In 1985, Smalley discovered a football-shaped fullerene which is the first allotrope of carbon making eureka moment in the scientific world, contributing to the Nobel Prize in 1996.[7] Mouras coined the word 'graphene' in 1987 to describe single sheets of graphite even though stable single-layer graphite sheet remained non-existent according to theoretical calculations.[8] Later in 1991, Sumio Iijima discovered another allotrope of carbon so-called carbon nanotubes (CNTs).[9] Ten years later in 2004, Geim and Novoslov from Manchester University conducted an amazing experiment to develop monolayer graphene using scotch tape

technique.[10] This discovery has led to a lot of exciting scientific research into the two-dimensional material that could offer a lot of new applications. Geim and Novoslov received Nobel Prize in 2010 for the work. The various graphitic forms, such as 0D fullerene, 1D carbon nanotubes, 2D graphene and 3D graphite, have been successfully identified to date.

## 1.2. Graphene quantum dots

The discovery of graphene opened an explosion of research due to its excellent thermal, electronic and mechanical properties.[11] Nevertheless, some drawbacks of graphene, such as zero bandgap, low absorption, etc. have been realized by researchers. As graphene possess zero bandgap, it is impossible to observe luminescence behaviour, restricting its applications in optoelectronics.[12] Graphene, however exhibits an infinite exciton Bohr radius, therefore quantum confinement could take effect in graphene of any finite size which results in many interesting phenomena that cannot be obtained in other semiconductors.[13] Hypothetically, the band gap of graphene can be tuned from 0 eV to that of benzene by tuning their sizes.[14] Thus, its band gap can be tuned by converting two-dimensional (2D) graphene sheets into 0D graphene quantum dots (GQDs), by quantum confinement and edge effect allowing the thought of a wide range of applications. Consequently, GQDs have emerged as a new type of quantum dots and have sparked considerable interest in materials science.

GQDs were first developed in 2008 by Ponomarenko and Geim on the basis of Xu *et al*.'s previous work on carbon dots (CDs) in 2004.[15] The major difference between GQDs and CDs is the observation of graphene lattice inside the dots, which are smaller than 100 nm in size and less than 10 layers thick.[16] Typically, CDs are quasi-sphere carbon nanoparticles of size less than 10 nm. In 2010, Pan *et al*. discovered the unique fluorescent properties of GQDs owing to its quantum confinement.[17] GQDs have many benefits as new carbon-based materials due to the additional novel structural and chemical properties due to the pronounced quantum confinement and edge effects that result from their nanoscale size.[18] When the size of the crystal is reduced to nanoscale, the crystal boundary greatly alters the distribution of electrons resulting in quantum containment and edge effect. The unique physical and chemical properties of GQDs such

as biocompatibility, solubility, inertness, low toxicity and surface grafting are resulted from this.[19, 20] A series of applications were built taking advantage of all these properties.

GQDs consist of a nano-sized graphite layer that exhibits excellent properties of graphene-like high charge transport mobility, large surface area, higher mechanical flexibility and outstanding chemical and thermal stability. GQDs have some fascinating merits compared to other widely explored conventional semiconductor quantum dots, such as good biocompatibility, low cytotoxicity, tunable band gap, aqueous dispersibility, high photostability and low cost which makes them promising candidates for photovoltaic devices, sensors, light-emitting diodes, solar cells, catalysis and bioimaging.[21-27] In addition, their excellent photo- or electro-catalytic efficiency also enables their use in energy conservation application and environmental monitoring.[28, 29] GQDs also have good optical properties such as bright excitonic fluorescence, high molar extinction coefficients and strong excitonic absorption bands extending to the visible region.[30, 31] Electrochemical energy storage-related applications such as electrochemical capacitors and Li-ion batteries have also gained a great deal of attention recently.[32, 33] Researchers are trying to develop GQD based energy-related and environmentally friendly products because of its large surface area, high transparency and strong PL intensity.[34] Due to its high solubility, devices with low cost and large area can be assembled through solution processed fabrication.[35]

## 1.3 Challenges of GQDs

Research on GQDs is still at an early stage and there are many challenges yet to be tackled. Although there are many significant benefits and potential applications of GQDs, further research is needed to enhance the properties of materials in order to satisfy the application requirements. Research on GQDs has therefore been carried out to address the five major challenges which include, low production yield, low quantum yield, lack of accuracy in controlling size and shape, confusing photoluminescence (PL) mechanism and narrow spectral coverage. Mass production is critically needed at relatively low cost to meet the industry requirement. However, the production yield of GQDs using current synthetic routes is significantly low and therefore new methods like microwave-assisted synthetic approaches that can improve the production yield need to

be exploited. Besides, the reported quantum yield (QY) of GQDs is much lower than the semiconductor QDs. Thus, low QY is also a real challenge for practical applications. Recent researches show that QY can be improved by various factors like surface functionalization, chemical doping and tuning the degree of oxidation.[36] Most of the reported GQDs have the emission colours ranging from blue to yellow. This narrow spectral range limits its application in the field of optoelectronics. Extending the spectral range of GQDs to the whole visible region and even near-infrared (NIR) is an important area of research. Some groups obtained NIR PL spectrum for GQDs by nitrogen doping.[37] PL is one of the most attractive features of GQDs but, the exact PL mechanism still remains unsettled. However, the new mechanisms were discussed mainly on the basis of optical activity that leads to contradictory results due to the different conditions of preparation. Therefore, the exact PL mechanism of GQDs is lacking and its widely accepted mechanism needs to be investigated systematically. The optical and electronic properties of GQDs such as fluorescence and band gap depend on its size and shape. Consequently, modulation of GQD's intrinsic properties depends on the accuracy of regulating their scale, shape, etc. Controlling the fabrication conditions are the keys to solve the issue. The future of GQDs is more promising once the above problems have been overcome.

## 1.4 Various synthesis methods of GQDs

Mass production is critically required for any application of GQDs in different fields. To date, a variety of methods have been developed to prepare GQDs with good properties and high yield. Generally, the approaches for the synthesis of GQDs can be classified into two types namely, top-down and bottom-up methods **(Figure 1.1).** The top-down synthetic approach involves cutting of three-dimensional bulk carbonaceous materials or two dimensional exfoliated sheets via chemical exfoliation,[38] electron beam lithography,[39] solvothermal,[40] microwave-assisted hydrothermal,[41] acidic exfoliation,[40] electrochemical cutting[42] and nanolithography.[43] By this strategy, GQDs can be synthesized from graphene-related materials like graphene[17], graphite powder,[44] graphene oxide,[22] carbon black,[45] carbon nanotubes,[37] carbon fibres,[40] coal[46] etc. The GQDs prepared by the top-down approach possess several advantages like high

production yield, abundant source and simple operation.[45] Besides, these facts, it contains oxygen-rich functional groups at the edges which help in enhancing its solubility, surface passivation and functionalization. In the bottom-up approach, GQDs can be prepared from smaller building blocks or precursors of comparable size by different methods like solution chemistry,[47] carbonization[25], 7-cyclodehydrogenation of polyphenylene precursors[36] etc. Here, GQDs can be chemically assembled from small molecules like polycyclic aromatic hydrocarbons (hexa-peri-hexabenzocoronene,[48] benzene[49]) glucose[50] and fullerenes.[51] Moreover, bottom-up preparation of GQDs requires some tedious and difficult synthetic procedures and in some cases production yield is also very poor, whereas top-down approach is simple and easy and therefore ideal for mass production. Top-down approaches will be discussed first followed by bottom-up approach.
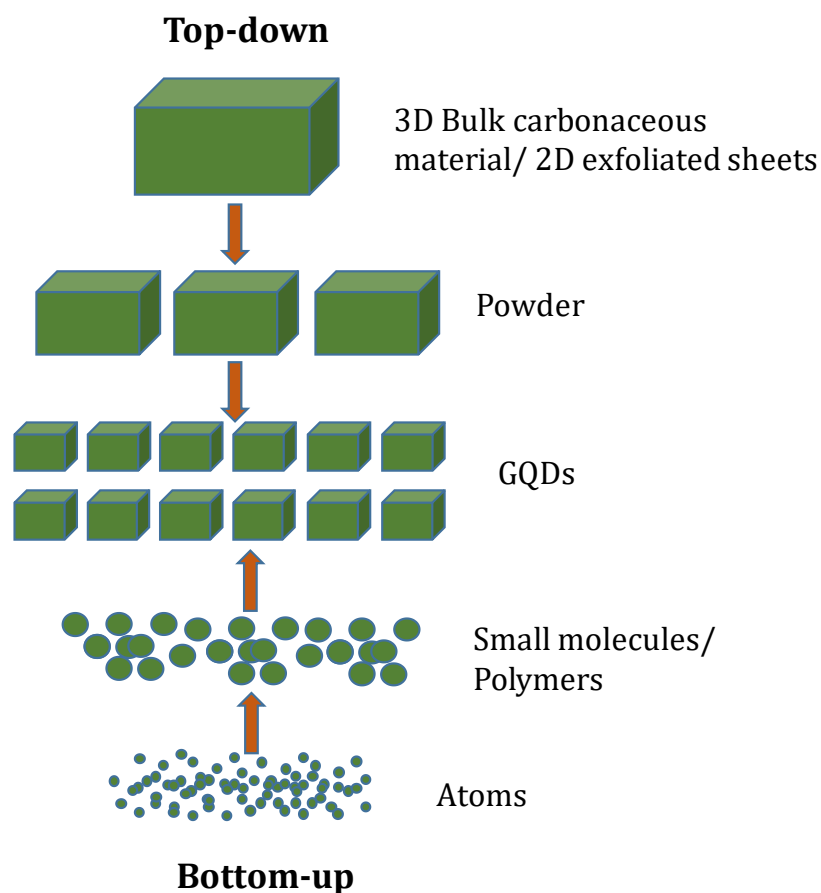


**Figure 1.1**. Schematic illustration for the preparative methods of GQDs.

**1.4.1. Top-down approach**

Great efforts have been paid for the advanced synthesis of GQDs over the past few years, and the above-mentioned shortcomings have been slowly overcome through elaborate designs by means of the top-down approach. As mentioned in the above section, GQDs can be fabricated by cutting down bulk carbonaceous material via physical or chemical techniques. The mechanism of top-down chemical routes can be defined as defect-mediated processes of fragmentation.[25, 52] Specifically, the functional groups containing oxygen such as hydroxyl and epoxy groups may produce defects on graphene oxide (GO) sheets which serve as chemical reactive sites, allowing GO to be cleaved into smaller sizes.[53, 54] The epoxy chain is energetically preferable for further oxidation into epoxy pairs and can then be converted to more stable carbonyl pairs at room temperature.[17, 40] Such linear defects make the graphitic domains fragile and readily targeted. Finally, this sub-nanometre sized aromatic $sp^2$ domains bonded by these epoxy lines or edges, may further breakdown to form GQDs. For the first time, Pan *et al.* developed GQDs through this approach by heating GO at 200-300 °C for more than 24 h.[17] So, GO and any other carbon materials containing aromatic $sp^2$ domains such as carbon nanotubes, carbon fibres, carbon black etc. could be used as the source for GQD synthesis via a top-down approach. Among top-down routes, hydro/solvothermal, electrochemical, liquid exfoliation, acid oxidation, sonication and microwave-assisted methods are more widely used.

*1.4.1.1. Hydro/solvothermal method*

It is a facile synthetic approach carried out in controlled temperature and pressure conditions for the preparation of GQDs. It usually involves the usage of strong alkali to break down the carbonaceous precursors into GQDs. The synthesis is carried out in a closed Teflon lined autoclave enclosed in a steel vessel. In hydrothermal method water is used as the solvent and the temperature rise above the boiling point of water that produces high vapor pressure which aids in the fragmentation of the particles. In the case of solvothermal synthesis, non-aqueous solvents are used. Hence, compared to hydrothermal synthesis, solvothermal synthesis can be carried out in much higher temperature by using high boiling point solvents. In 2010, Pan *et al.* first synthesized

GQDs with an average size of 9.6 nm via hydrothermal route by heating micrometre sized GO at 200-300 °C for more than 24 h.[17] Later in 2011, they modified this hydrothermal route to prepare well-crystallized GQDs with an average size of 3 nm using high temperature thermally reduced GO sheets as a precursor under strongly alkaline water.[55] Using this method Tetsuka *et al.* synthesized amino functionalized GQDs via ammonia-mediated cleavage reaction by heating oxidized graphene sheet at 70-150 °C for 5 h.[56] Zhu *et al.* synthesized green fluorescence GQDs with an average size of 5.3 nm by one-step solvothermal method.[57]

### 1.4.1.2. Electrochemical method

Carbon-based materials such as graphite and multi-walled carbon nanotubes (MWCNTs) have been widely used as the electrode for electrochemical synthesis of GQDs. [58, 59] Li *et al*, first synthesized green fluorescence GQDs with an average size of 3-5 nm by electrochemical oxidation using graphene electrode in phosphate buffer solution.[60]  This approach adopted a high redox potential to either oxidize the C – C bonds or oxidize water to produce oxygen and hydroxyl radicals in its oxidative cleavage reaction.[61] Recently, Shinde and Pillai synthesized GQDs from MWCNTs by electrochemical method.[42] This approach offered a new strategy for the preparation of size-tunable GQDs by varying oxidation time. Using this approach, they have tuned the fluorescence of GQDs through a systematic change in reaction parameters, like the electric field, the diameter of carbon nanotube, the concentration of supporting electrolyte and temperature.

### 1.4.1.3. Liquid Exfoliation method

Currently, liquid exfoliation method is often used for the synthesis of GQDs by many research groups.[62-64] Sarkar *et al.* prepared blue fluorescence GQDs with uniform size distribution via liquid exfoliation method.[65] By this approach, it is possible to use bulk carbon materials as GQD precursors. For e.g. Peng *et al.* synthesized GQDs from carbon fibres via liquid exfoliation method.[40] They have also tuned fluorescence emission colour by varying synthesis temperature. By using this method Tour *et al.* could increase the production yield of GQDs.[66] Recently, Zuo *et al.* developed a more facile route for the synthesis of GQDs using cotton as starting material. Here, cotton was first

annealed followed by liquid exfoliation to obtain high-quality GQDs. Shih *et al.* used high-purity platelet graphite nanofibers with 10-40 nm diameter as carbon source to synthesize GQDs with good crystallinity by the same method.[67]

### *1.4.1.4. Acidic oxidation method*

Acidic oxidation is an approach suitable for large-scale production of GQDs for widespread applications from carbonaceous materials like GO, carbon black, coal, carbon fibres etc. Acidic oxidation of GO is a commonly adopted procedure, usually followed by excess acid neutralization and dialysis. As discussed above GO will break down into smaller parts during oxidation process. However, it is difficult to remove the excess amount of oxidant from the solution. Dong *et al.* reported a facile method for preparation of single and multi-layer graphene quantum dots by chemical oxidation of carbon black using $HNO_3$ as the oxidizing agent.[45] Li *et al.* suggested that, compared to heat or sonic treatment, a well-controlled oxidation induced graphene cleavage could lead to GQDs with more smooth edges.[54] Peng *et al.* reported large scale synthesis of GQDs in via acidic exfoliation and etching of carbon fibres.[40] As a result, GQDs with different emission colour were synthesized by tuning the synthesis temperature.

### *1.4.1.5. Sonochemical method*

Sonochemical approach was commonly used for the synthesis of various nanocrystals including quantum dots. Sonochemical synthesis utilizes the powerful ultrasound radiation (20 kHz–10 MHz) for the preparation of nanomaterials.[68] The mechanism of the process is acoustic cavitation, i.e., formation, growth and collapse of bubble formed in the liquid release high energy for the nanomaterial synthesis.[69] The reaction starts with the formation of a bubble may be of impurity or from reactants. This bubble grown in size, on reaching its maximum size, will go for hot spot mechanism. The collapse of the bubbles generates localized hot spots. These hot spots will have a high temperature of about 5000 K and pressure of 2000 atm, this energy would allow carbon-layered materials to be sheared into GQDs.[70] **Figure 1.2** represents the acoustic cavitation in sonochemical synthesis. Zhuo and co-workers synthesized GQDs from graphene via an acid-mediated ultrasonic method.[71] Ultra-small particles with protruding edges were formed, during the cutting process. Advantageous of

sonochemical synthesis include increased reaction rates that lead to higher yield in endothermic reactions and the production of nanostructures with finer size.[72] Ultrasound can also induce the formation of unique morphologies during the synthesis of nanostructured materials in the presence of soft templates. Usually, ultrasonication methods can be combined with solvothermal and microwave treatments. Till date, several ultrasound-assisted methods are reported for the preparation of GQDs.[73]
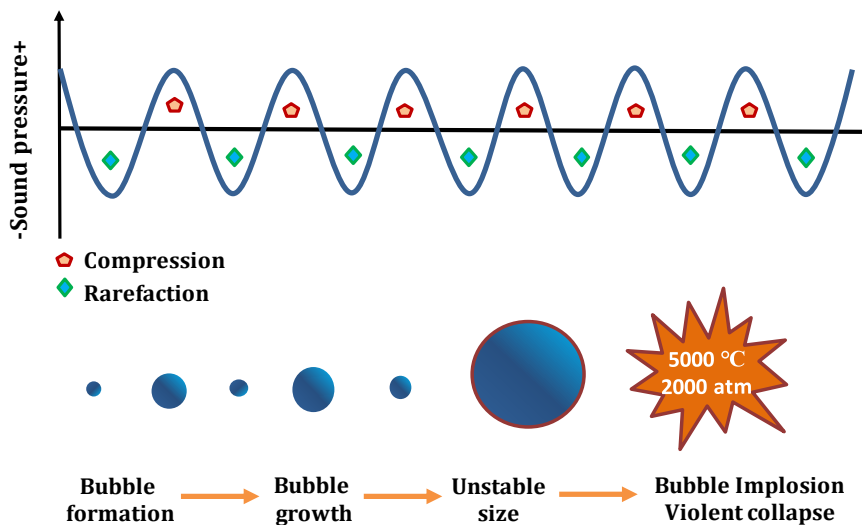


**Figure 1.2.** Principle of ultrasonication, acoustic cavitation process

### 1.4.1.6. Microwave method

To date, most reports have included hydrothermal and acid oxidation methods for GQD synthesis. However, these approaches have some limitations like longer synthesis duration. As a result, some high-energy technologies have been introduced with the goal of seeking facile synthetic approaches for GQDs. Microwave-assisted techniques have been widely used for the synthesis of nanomaterials because it could cover the advantages of microwave and the corresponding assisted techniques like sonication, hydrothermal treatment etc. Microwave methods utilize the heat that is emitted as a result of molecular rotation of polar solvent molecules with an electric dipole moment by microwave energy. This microwave method can be applied to synthesize organic and inorganic materials in a short time with a higher yield. Microwave synthesis of nanomaterials is considered to be low temperature, rapid and efficient green method of synthesis compared to conventional heating methods. In

electromagnetic spectra, microwaves have wavelength of 1mm-1m and frequency range between 300 MHz to 300GHz. The commonly used microwave frequency for the nanomaterial heating is 2.45 GHz.[74] In microwave approach, direct in-core heating takes place in the material through the molecular interaction with the electromagnetic field, resulting in volumetric heating. In dipolar mechanism, heating occurs via change in the dipole moment, i.e., material must possess a dipole characteristic to have microwave dielectric heating.[75] For example, polar solvent like water on applying microwaves will have dipole moment. These dipoles will interact with the microwaves and try to align itself with the electric field by rotation **(Figure 1.3a)**. The applied field provides energy for this rotation of dipoles and the material gets heated. In conduction mechanism, ions or clusters in solution will have collisions by the movement in the solution by the influence of applied field **(Figure 1.3b)**, this kinetic energy is converted into heat. The conduction mechanism is superior to dipolar mechanism while considering the heat generation. Major benefit of microwave heating is that it is almost instantaneous, it directly heats the substance without heating the vessel.[74] Microwave-assisted exfoliation and subsequent reduction of GO was reported as a convenient and fast heating approach. By this method, graphite oxide materials could be readily obtained in large scale within short span of reaction time and improved production yield.[41] Li *et al*. reported acid-mediated microwave-assisted reduction of GO to GQDs with shorter reaction time when compared to solvothermal process.[54]  A facile microwave-assisted approach was used by Li and co-workers for the preparation of stabilizer-free two-colour GQDs from GO nanosheets in acidic medium.[38]
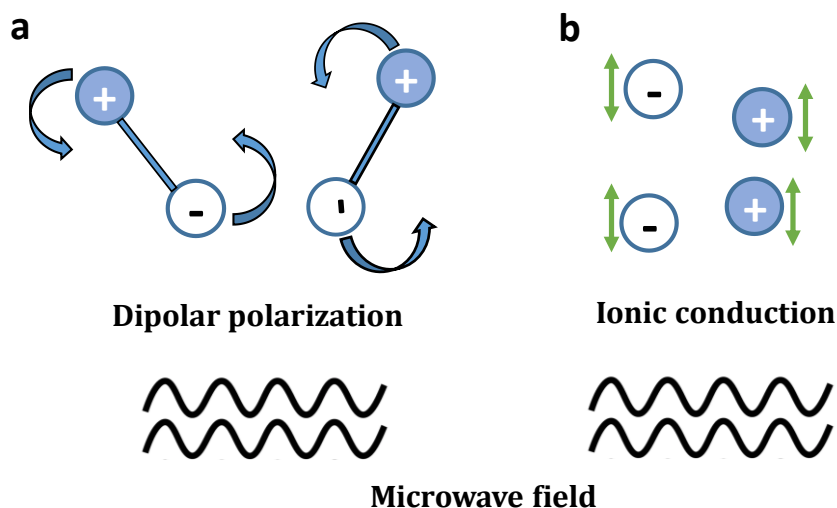
**Figure 1.3.** Two heating mechanisms under microwave irradiation: (a) dipolar mechanism: dipoles try to align with filed, (b) conduction mechanism: charged ions under collision in presence of an electric field.

### 1.4.2. Bottom-up approach

Reports on bottom-up methods were relatively rare compared to top-down approaches. This method provides us exciting opportunities to fabricate GQDs with well-defined structure and properties. However, this approach involves complex and challenging synthetic procedures and also requires some special organic precursors which may be very difficult to obtain. Some of the bottom-up routes for the preparation of GQDs includes solution chemistry, cage opening of fullerenes, carbonization of some special organic precursors.[25, 76]

### *1.4.2.1. Solution chemistry methods*

By the bottom-up approach, solution-phase chemical methods are successfully applied to generate GQDs by oxidative condensation of aryl groups. Yan *et al.* synthesized GQDs based on oxidative condensation reaction through stepwise step solution chemistry.[14] Liu *et al.* recently prepared multicolour GQDs with larger size of 60 nm using unsubstituted hexa-peri-hexabenzocoronene as the starting material.[48] The thickness of as-prepared GQDs was 2-3 nm signifying the presence of two or three graphene layers. This is the largest GQD reported so far. Although intramolecular

oxidative cyclodehydrogenation has been shown to be useful for the synthesis of large polycyclic aromatic hydrocarbons, the solubility of such GQDs was poor and they got aggregated easily due to strong inter-graphene attraction.[77, 78] Guo *et al.* used 1,5-dinitronaphthalene as the starting material for the synthesis of GQDs with tunable fluorescence emission.[79]

### 1.4.2.2. Cage opening of fullerenes

Graphitic carbon layers can be obtained via surface-catalysed decomposition of fullerene adlayers. Loh *et al.* synthesized geometrically well-defined GQDs on ruthenium surface using C60 molecules as a precursor based on a mechanistic approach.[53] They obtained triangular and hexagonal shaped GQDs at different annealing temperatures. Here, ruthenium-catalysed cage-opening of C60 resulted in the formation of nanostructures. The strong interaction between C60 and Ru caused the creation of surface vacancies in Ru single crystal where C60 molecules are embedded. At high temperature, the embedded molecules got fragmented to produce carbon clusters that further diffused and aggregated to form GQDs. **Table 1.1** summarizes different synthetic approaches and the related properties of GQDs for various applications.

**Table 1.1.** Related properties and applications of GQDs synthesized via various routes.

| Method of synthesis | Precursor | Size (nm) | Emission Color | PL QY (%) | Product yield (%) | Applications | Ref. |
|---|---|---|---|---|---|---|---|
| Acidic oxidation | GO | 5-25 | Blue | 28 | - | Photovoltaics | [80] |
| Acidic oxidation | Carbon fibres | 1-4 | Green | - | - | Bioimaging | [40] |
| Acidic oxidation | Carbon black | 15 | Green | - | 44.5 | Bioimaging | [45] |
| Hydrothermal | GO | 5-13 | Blue | - | 5 | - | [17] |
| Hydrothermal | rGO | 2-5 | Blue | - | - | Fluorescent sensing | [81] |
| Hydrothermal | Citric acid | 5-10 | Blue | 75.2 | 60-70 | - | [82] |

| Method | Precursor | Size | Color | | | Application | Ref |
|---|---|---|---|---|---|---|---|
| Hydrothermal | Pyrene | 3.5 | Green | 23 | 63 | Bioimaging | 83 |
| Solvothermal | GO | 5.3 | Green | 11.4 | 1.6 | Bioimaging | 84 |
| Microwave | GO | 2-7 | Green/ Blue | - | 8 | Fluorescent sensing | 54 |
| Microwave-Assisted hydrothermal | Glycerol | 1-5 | Green/ Blue | | 9.8 | Photovoltaics | 85 |
| Microwave-Assisted hydrothermal | Graphite | 2.5 | Yellow green | - | - | LED | 41 |
| Ultrasonication | Graphene | 3-5 | Blue | 3.4 | - | Photocatalysis | 71 |
| Liquid exfoliation | Graphite | 5.6 | Blue | 13.6 | - | Sensing, Bioimaging | 86 |
| Solvothermal liquid exfoliation | Coal | 4.7 | Blue | 47 | 25.6 | - | 87 |
| Ultrasonic-assisted liquid exfoliation | GO | 3 | Blue | 27 | - | Fluorescent Sensing | 73 |
| Electrochemical | Monolithic 3D graphene | 3 | Blue | 10 | - | Fluorescent Sensing | 88 |
| Electrochemical exfoliation | Graphene paper | 3-8 | Cyan | 46 | 28 | Bioimaging | 89 |
| Step wise solution chemistry | Organic precursor | 2.5-5 | Red | - | - | Photovoltaics | 14 |
| Precursor pyrolysis | Glucose | 1.65-21 | Blue | 7-11 | - | - | 90 |
| Pyrolysis and exfoliation | Unsubstituted HBC | 60 | Blue | 3.8 | - | - | 48 |
| Hydrothermal carbonization | Orange waste peel | 2-7 | Blue | 11.4 | 12.3 | Photocatalysis | 91 |

## 1.5. Physical and chemical properties of GQDs

### 1.5.1. Morphology and composition

The morphological analysis of GQDs can be carried out through transmission electron microscopy (TEM) and atomic force microscopy (AFM). The morphological

parameters including the size and height of GQDs depend largely on synthetic approaches, but irrespective of the starting material. For e.g., Pan *et al.* synthesized two types of GQDs with average sizes of 9.6 nm and 3 nm via two different synthetic approaches using GO as the starting material.[17, 55] The average size of GQDs is mostly below 10 nm and 60 nm, which is the largest GQDs reported to date. Similar to size, the height obtained also depends on the adopted synthetic strategy. The heights of GQDs prepared by different methods are not related to their size, but that synthesized by the same process increases with an increase in size.[36] Generally, most GQDs are made up of not more than 5 layers. There has been a limited number of monolayer GQDs reported to date.[22, 92] The chemical composition of GQDs are commonly analysed by Fourier transform infrared (FT-IR) and X-ray photoelectron spectroscopy (XPS) spectroscopy. In general, GQDs are only composed of elemental C, H and O. The presence of oxygen-containing functionalities in GQDs like hydroxyl, carbonyl, carboxyl and epoxy groups can be analysed from FT-IR and XPS spectra. The O/C atomic ratio can be calculated from XPS spectra which can be used to evaluate the extent of oxidation in GQDs.[93]

### 1.5.2. Crystalline nature

GQDs are normally crystalline in nature when compared to GO. It usually exhibits two interlayer spacing (002) and (100), but the former has been commonly studied.[94] The interlayer spacing of GQDs is strongly dependent on their degree of oxidation, i.e. the attached functionalities like hydroxyl, carbonyl and carboxyl groups can increase the interlayer spacing of GQDs. The exact interlayer spacing also depends upon the method of preparation. GQDs prepared by carbonization of citric acid and electrochemical cutting from graphene showed an interlayer spacing of around 0.34 nm.[95] However, carbon fibre-derived GQDs had a greater interlayer spacing of around 0.403 nm which could be due to the inclusion of oxygen-containing groups during oxidation and exfoliation.[40] It is observed that the oxygen-containing functionalities may be able to expand the graphene layer spacing, infact, contrary  certain highly oxidized GQDs reported smaller interlayer spacing. For example, for carbon fibre-derived GQDs, the O/C atomic ratio was 23.7% with a higher interlayer spacing of 0.403 nm., whereas, a smaller interlayer spacing of 0.34 nm was observed in electrochemically synthesized

GQDs with a higher atomic O/C ratio (27%). The oxygen-containing groups present on the basal plane can contribute to a greater spacing than that at the edges of the graphene sheets.

### 1.5.3. Optical absorption

GQDs exhibit strong absorption in the UV region and its tail ranging to visible range. Similar to GO, GQD possesses two peaks corresponds to π-π* and n–π * transitions with hypsochromic shift. Generally, GQDs show π-π* transition peak centred between 200 and 270 nm and n–π * transition peak at 260 nm whereas, GO exhibited two peaks at 230 nm and 300 nm respectively.[96] GQDs was found to exhibit size-dependent absorption due to quantum confinement effect. Peng *et al.* reported a red shift in carbon fibre-derived GQDs as its average size increased from 1-11 nm.[40] Apart from the size effect, synthetic approach also affects the optical absorption of GQD. For example, citric acid carbonized GQDs of average size15 nm showed an absorption peak at 362 nm,[25] whereas, GQDs with 60 nm size derived from the unsubstituted hexa-peri-hexabenzocoronene (HBC) showed only a weak shoulder peak at 280 nm.[48] Thus, the position of absorption maxima also depends on the synthetic strategy. The variation in the oxygen content of GQDs has also played a vital role in determining the absorption peak position.[97]

### 1.5.4. Photoluminescence

The photoluminescence (PL) can be regarded as a transition of electrons from the lowest unoccupied molecular orbital (LUMO) to the highest occupied molecular orbital (HOMO). When compared to other organic fluorophores, PL spectra of GQDs are generally broader. It also exhibited excitation dependent emission behaviour, i.e. when the excitation wavelength is increased, the PL emission maxima shifted to longer wavelength. The excitation dependent behaviour arises from optical selection of different sized GQDs or different emissive traps on GQDs. This multi-PL colours with different excitation wavelengths is significant for certain practical applications.

### 1.5.4.1. Photoluminescence mechanism

The photoluminescence of GQDs was originated as a result of quantum confinement effect, emissive traps, free zig zag sites, aromatic structures, oxygen-containing functional groups and edge defects.[52, 61, 98] The effect of quantum confinement is observed when the particle size is too small to be equivalent to the wavelength of the charge carriers.[99] Consequently, these QDs limit the movement of valence band holes, conduction band electrons, or excitons in all spatial directions. As depicted in **Figure 1.4,** the energy difference between the conduction band and valence band increases typically as the crystal size decreases. Thus, more energy is needed for the particle to reach the higher energy state and simultaneously, more energy is released when it returns to its ground state, which results in a colour shift from red to blue in the light emitted.[100] As a result, QDs of different emission colours can be made from the same material by tuning its size.
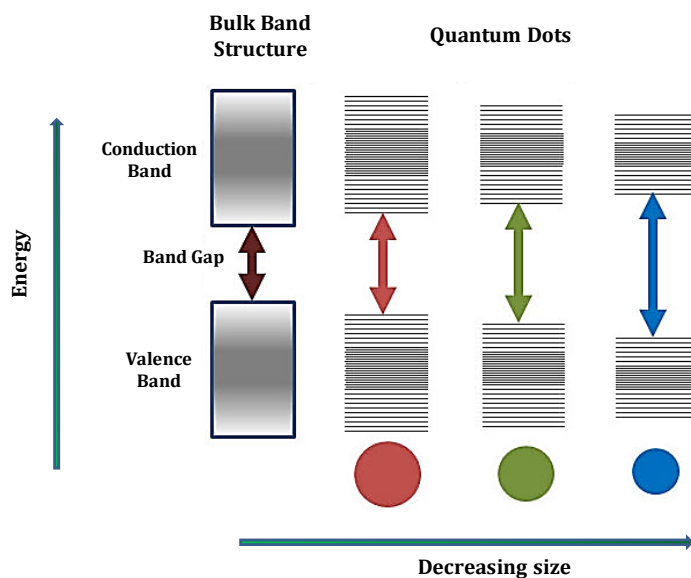


**Figure 1.4.** Schematic representation of quantum confinement effect.

The exact PL mechanism of GQDs still remains unsettled. A widely accepted fluorescence mechanism of GQD needs to be investigated systematically. The PL mechanism may typically derive from defect state and intrinsic state emission. The former is caused by the defects in the basal planes or edges, while the latter arises due to quantum confinement effect or recombination of electron-hole pair. It is reported that

the band gap of GQDs depends on the size of graphene fragments and it decreases as the size increases. **Figure 1.5** represents the band gap of π–π* transitions calculated as a function of the number of fused aromatic rings based on the density functional theory (DFT). GQDs synthesized using different synthetic approaches are likely to exhibit distinct PL mechanisms, resulting in their dependences of PL on size, solvent, pH, etc.
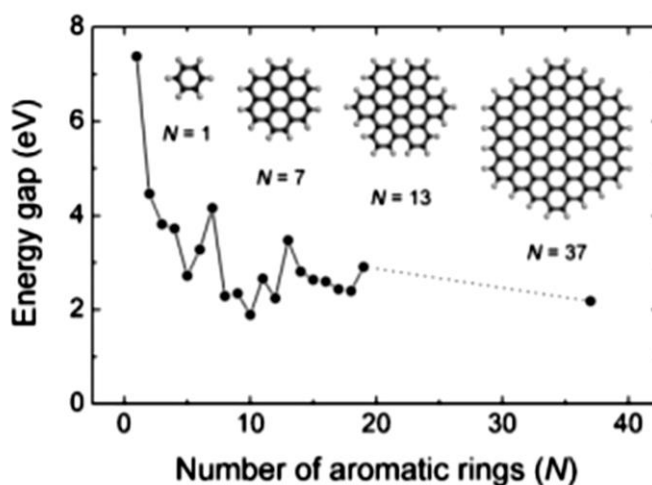


**Figure 1.5.** Energy gap of π–π* transitions on the basis of DFT as a function of the number of fused aromatic rings (N). The inset displays the structures of the graphene fragments used for calculations.[36]

### *1.5.4.2. Size dependence*

The quantity confinement effect arises when quantum dots are smaller than the Bohr radius of their exciton.[100, 101] The main consequence of this effect is its size dependency on band gap, resulting in distinct optical and spectroscopic properties.[102-104] Thus, GQDs exhibit size-dependent PL particularly due to quantum confinement effect. That is, when the particle size is reduced, the emission energy is shifted to lower wavelength **(Figure 1.6).** This size effect can result in different emission colours for different sized GQDs. GQDs prepared from carbon black by acid oxidation method showed a PL shift from green to yellow with increase in its size form 15-18 nm.[45] Size independent PL emission was also observed for GQDs synthesized via glucose carbonization which may be possibly due to surface state emission.[90]
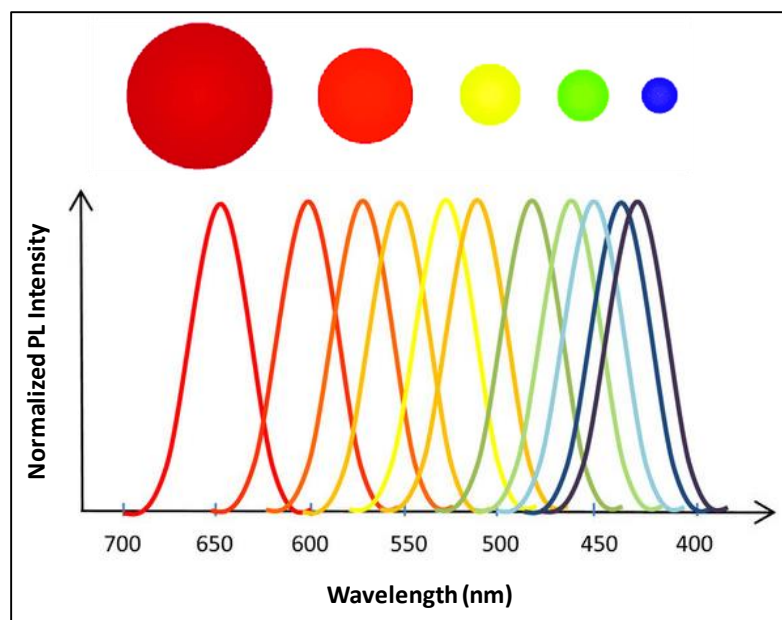
**Figure 1.6.** Size-dependent normalized PL spectra of QDs.[105]

### 1.5.4.3. Solvent dependence

GQDs show high solubility in water and other polar organic solvents as it possesses oxygen-containing functionalities like hydroxyl, carboxyl groups etc.[23] It is reported that GQDs prepared through solvothermal method exhibited a PL shift from 475 to 515 nm with a set of solvents like acetone, dimethyl sulfoxide (DMSO), tetrahydrofuran (THF), ethanol, DMF and water.[84] This shift in emission behaviour was attributed to the introduction of defects in the system. The GQDs synthesized by acidic oxidation methods also showed solvent dependent emission shift which was caused by lone pair of electrons that could modify the electron state of GQDs.[106]

### 1.5.4.4. pH dependence

The pH-dependent emission shift was also observed for some GQDs. It is reported that GQDs prepared by hydrothermal method emitted strong fluorescence under alkaline conditions, whereas its fluorescence was completely quenched under acidic conditions.[107] Here, the PL intensity varied reversibly, as the pH was changed repetitively between 12 and 1. A similar trend was also observed in GQDs with emissive zigzag sites.[108, 109] Citric acid carbonized GQDs reported by Dong *et al.* exhibited strong PL intensities in acidic medium, but a decreased PL intensity in alkaline medium

indicating a distinct mechanism from emissive free zigzag sites.[25] These pH-dependent fluorescence properties may be due to emissive traps on the surface of GQDs, except for the zigzag-derived ones.

### 1.5.4.5. Quantum Yield

Quantum yield (QY) determines the photoemissive efficiency of a material. The fluorescence QY is defined as the ratio of the number of photons emitted to the number of photons absorbed. The QY of GQDs depends on various factors such as method of synthesis, surface chemistry etc. Usually, GQDs contain carboxylic and epoxy groups that can act as non-radiative electron–hole recombination centres.[53] The removal of these oxygen-containing groups by surface passivation or reduction can increase the QY. By simple reduction with $NaBH_4$, Li *et al.* enhanced the QY to 22.9 % from 11.7 %.[54] Shen *et al.* reported PEG passivated GQDs with QY 28 % which was twice as high as its initial GQDs.[32] This enhancement probably arises due to the stabilization effect of excitons in GQDs after the surface passivation. Recently, Sangam and co-workers synthesized single crystalline sulphur-doped GQDs (S-GQDs) with a very high quantum yield of 46 % from sugarcane molasses through hydrothermal method.[110] It is reported that the doping in GQDs reduces the aromatic-rich carbon-domains which introduces additional energy levels, that effectively create new electron transition pathways in the band structures, thereby improving its QY.[111]

### 1.5.5. Upconversion luminescence

Upcoversion luminescence (UCL)is a non-linear anti-Stokes emission in which the concurrent absorption of two or more photons results in light emission at a shorter wavelength than its excitation wavelength.[112] The general principle of UCL is shown in **Figure 1.7.** In addition to the strong down conversion behaviour, some of the GQDs clearly exhibit the UCL. In UCL, the system in the ground state (1) is initially transferred to the first excited state (2) by an excitation photon ($h\nu_1$). The system is further excited into level 3 by receiving energy from another excitation photon or energy transfer process ($h\nu_2$). The radiative transition from the excited state (3) to the ground state (1), where the emitted photon has higher energy than the individual excitation photons results in UCL ($h\nu_3$).[113] For PEG passivated GQDs synthesised by acidic oxidation

approach, Shen *et al*. observed the upconverted emissions peaks got shifted from 390 to 468 nm, when the excitation wavelength is increased from 600 to 800 nm, respectively.[80] Here, the energy difference between upconverted emission light and excitation light almost remained the same, about 1.1 eV. They assumed that the UCL is the anti-stoke transition where the multiplicity of the carbine ground-state provided the energy levels of s and p orbitals. If low-energy photons excite the p electrons, they will be excited to a higher-energy state and subsequently the electrons relax back to a low state of energy, which results in UCL. Instead, the excitation of the s orbital electrons results in normal PL. The same anti-Stokes transition induced UCL has also observed in PEG passivated GQDs synthesized using a one-pot hydrothermal reaction.[80] Zhu *et al.* also reported UCL in GQDs prepared through solvothermal method.[98]
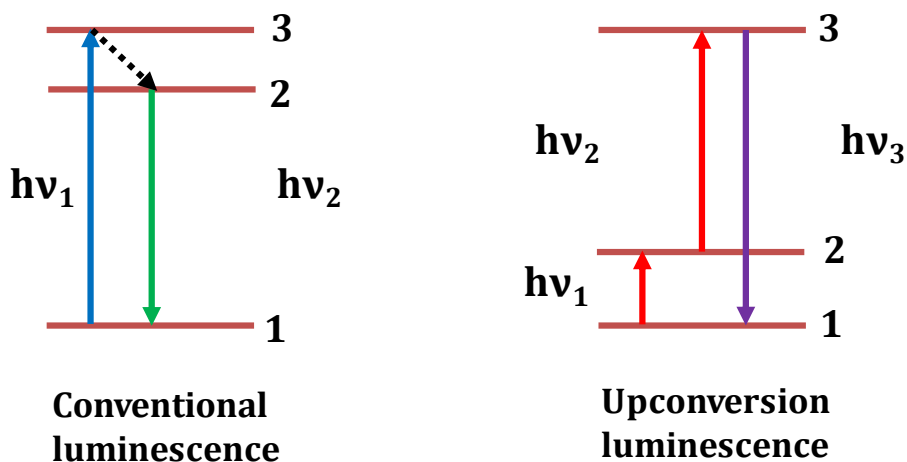


**Figure 1.7.** Schematic illustration of normal PL and UCL.

### 1.5.6. Band gap engineering

The band gap of graphene-based materials can be tuned from 0 eV to that of benzene either by tuning its size or by changing the surface chemistry which makes it an efficient fluorescent material.[56] The tunable bandgap of GQDs is due to its quantum confinement and edge effect. The optical features of GQDs, especially its PL properties can be tuned by band gap engineering which results in the formation of different emission colours of GQDs. Currently, there have been growing efforts to tune the band gaps of GQDs in order to customize its optical properties. **Figure 1.8a** shows a reduction in the band gap energy with the increase in size of GQDs, indicating a relationship

between band gap energy and material size. Chen *et al.* used DFT and time-dependent density calculations to investigate the relationship between band gap and particle size.[114] It was proposed that PL of a larger GQD which contain heterogeneously hybridized carbon system was determined by smaller $sp^2$ clusters isolated by $sp^3$ carbon **(Figure 1.8b).** A slight difference was observed in the degree of band gap tuning of GQDs on its size variation between experimental work and theoretical prediction. However, the trend was in good agreement with the studies of Ye *et al.*[115] Thus, the band gap energy of GQDs that determines its PL can be tuned by the particle size. For band gap tuning several other strategies can be adopted, which include controlling the intrinsic properties, surface functionalization, tuning the degree of oxidation and chemical doping.
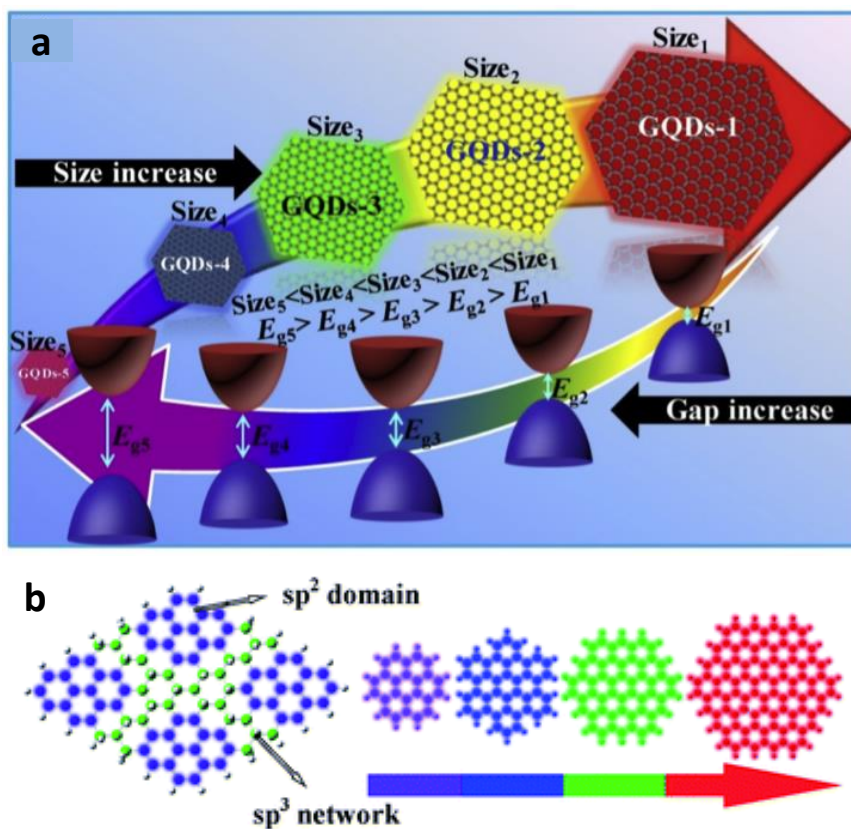


**Figure 1.8.** Schematic illustration showing (a) variation of band gap of GQDs with its size[93] (b) variation of PL emission determined by small $sp^2$ clusters isolated by $sp^3$ carbon.[114]

### 1.5.6.1. Controlling the intrinsic properties

The optical characteristics of GQDs are theoretically based on their intrinsic properties such as size, shape and layer or edge configuration, which are strictly related to their band gaps.[116] The versatility of various synthetic approaches results in great differences in the intrinsic properties of GQDs, which eventually leads to its PL diversity. Peng *et al.* reported that the size of GQDs has a great effect on band gap, which can further result in different PL emission colour.[40] Three forms of GQDs with average sizes of 1-4 nm, 4-8 and 7-11 nm were synthesized by varying the reaction temperatures. The as-prepared GQDs exhibited different PL emission maxima which corresponds to blue, green and yellow as the band gap value decreased from 3.90 to 2.89 eV. Yan *et al.* also demonstrated that the band gap of GQDs can be effectively tuned by controlling its size.[47] Recently, Zhang *et al.* used gel electrophoresis method to prepare three sets of GQDs with different size distributions of 5.5 nm, 12.5 nm and 16 nm which corresponds to blue, green and yellow emission respectively.[117] They also pointed out that the increase in the size of GQDs would cause a red shift in its PL emission, but it is rather weak due to the less prominent contribution of the quantum effect for larger sized particles.

As GQDs are fragments derived from graphene sheets, the layers of GQDs contribute significantly to the perpendicular size, which results in the shift in their PL efficiency. By a top-down synthesis route, Dong *et al.* simultaneously prepared single-layer and multi-layered GQDs with green and yellow emissions respectively from carbon black as precursor.[45] It has been shown that nano-sized GQDs have larger proportions of edge sites, namely, zigzag or armchair edges relative to graphene, but the edge states of GQDs contribute significantly to its optical properties.[118] Band gap reduction is usually associated with zigzag edge sites, but it would be extended by the armchair edges with a blue emission shift.[114] Thus, the band gap and PL emission of GQDs can also be tuned by modulating its edge amount.

### 1.5.6.2. Surface functionalization

GQDs possess large surface area and good surface grafting features because of the π-π conjugation.[30] Hence, surface functionalization can be used for tuning the band gap of GQDs in order to modify its structure and optical properties. Surface

modifications using electron donating or accepting molecules could have a significant impact on graphene's electronic characteristics. Because of their unique protonation mechanism, diamines are among the common organic molecules used for the functionalization of GQDs.[119] Tetsuka *et al.* reported amino-functionalized graphene quantum dots with tunable optical properties using oxidized graphene sheets as starting material.[56] The as-prepared GQDs exhibited multiple colour fluorescence upon the excitation of single-wavelength with a quantum yield of up to 40%. It is also reported that functionalization of GQDs with amino group results in a blue shift with enhanced PL intensity. Sun *et al.* demonstrated that GQDs with greenish-yellow emission and low quantum yield (2.5%) are changed over to blue emissive GQDs with enhanced quantum yield (16.4%) after amino-functionalization.[120] The enhanced PL emission is due to the increased $sp^2$ carbon domains after amine functionalization which provide a better ability to donate electrons compared to hydroxyl groups. The blue shift of GQDs arises due to the change in their chemical structure, as the introduced nitrogen can suppress GQD's non-radiative transition. Thus, functionalization induced protonation/deprotonation results in charge transfer between GQDs and functional groups, which provide a new pathway to tune the band gap of GQDs.

### 1.5.6.3. Tuning the degree of oxidation

It is due to the oxygen-containing functionalities on GQDs that will result in radiative recombination of localized electron-hole pairs and surface emissive traps.[121] The degree of oxidation or reduction will cause changes in localized $sp^2$ clusters and structural defects, which in turn result in PL shift.[53] A high degree of surface oxidation would result in red-shifted PL emissions of GQDs with low quantity yield, while reducing surface oxidation is a promising alternative method for achieving blue-shifted PL emissions with increased quantum yield.[122] The oxidation can increase excessive oxygen functionalities which results in non-radiative pathway that reduces the quantum yield of GQDs. The partial exclusion of oxygen-containing functional groups from the oxidized GQDs will covert carbonyl, amide and epoxy groups into –OH groups.[30] Consequently, it suppresses the non-radiative recombination and strengthens the integrity of the π conjugated mechanism. Due to the suppression of this non-radiative recombination and

the enrichment of electron density, the reduced GQDs have wider band gaps relative to oxidized GQDs, which contribute significantly to high quantum yield.[123]  Jang *et al*. investigated on the effect of oxidation on the band gap and optical properties of GQDs with different oxygen contents and they observed a shift in PL emission from sky-blue to greenish-yellow with the increase in the degree of oxidation.[124] Similarly, they demonstrated a blue shift of PL emission after sodium borohydride reduction due to the formation of small $sp^2$ domains.

### 1.5.6.4. Chemical doping

Doping is a significant process in the semiconductor industry because it can control the physical, chemical and electronic properties of materials, which makes them suitable for device applications. Certainly, doping carbon nanomaterials with heteroatoms can induce electronic and structural distortion, which provides an efficient way to tune their intrinsic properties, including surface chemistry, chemical composition, electronic properties and band gap.[125] Chemical doping is a commonly used method in materials science involving the inclusion of atoms or ions of suitable elements in host lattices to create materials with desirable properties and functions. It can also avoid the problem of self-quenching due to their major ensemble stokes shift. The doping in the structure introduces localized states that can trap photo-excited electrons and enhance its PL lifetime. Thus, doping is considered to be the most promising engineering path for the production of highly fluorescent GQDs. The large stokes shift of doped GQDs arises due to their relatively small emission energy gap compared to the absorption band of the undoped system in their atomic-like state of emission.[126]

The elements used for doping can be typically categorized as metal atoms and non-metal atoms (heteroatoms). Of these, non-metal-based doping has shown tremendous potential to improve the optical and electronic properties of GQDs. Metal atom-based doping can also closely modulate the band structure of GQDs; however, toxicity is its major obstacle. In principle, different dopants with particular sizes and valences are investigated and proved feasible for tuning the band gap of GQDs. The effect

of single, double or multiple heteroatom doping on band gap tuning and optical properties has been reported so far.[127, 128]

Among various non-metals, nitrogen is the most widely used dopant due to its comparable atomic size with carbon. By nitrogen doping, nitrogen atom injects electrons into the graphitic lattice of GQDs and alters its internal electronic state which results in band gap tuning.[129] Considering the quantum confinement and edge effects of GQDs, chemical doping with nitrogen atoms, could drastically alter their electronic properties and offer more active sites. Based on hydrothermal treatment with ammonium hydroxide as the doping source for nitrogen, Dai *et al.* reported N-doped graphene quantum dots (N-GQDs).[130] When compared to undoped GQDs (QY 3.5%), N-GQDs showed an enhanced QY of 34.5%. This is because N-doping results in the modification of the electronic structure of N-GQDs induced by the strong electron-withdrawing nature of N atoms, which restores $sp^2$ hybridization and gives delocalized electrons to the $\pi^*$ states, thereby results in a more effective radiative PL emission.

Subsequently, sulphur is also found to be used as dopant to tune the band gap and optical properties of GQDs. Compared to the extent of research to generate N-GQDs, sulphur doped GQDs (S-GQDs) have been rarely reported. S-GQDs have gained considerable attention in recent years because of their enhanced PL properties and they have been synthesized from various precursors like p-toluene sulphonate,[95] 3-mercaptoporpionic acid,[131] sulphuric acid[127] etc. Sulphur doping is distinctive due to the mismatch between the outermost orbitals of S and C, which causes the uniform distribution of spin density, thereby endowing S-doped materials with unique properties and potential for many applications. S atom is larger in size than C atom and the C-S bond length (1.78 Å) is 25% longer than that of the C-C bond. The electronegativity of S (2.58) is close to that of C (2.55), suggesting that S tends to be doped into the graphene framework with similar doping configurations as oxygen. Moreover, the electronegativity difference is too small to provide substantial charge transfer in C-S composites. Li *et al.* synthesized S-GQDs with multiple PL emission colours ranging from blue to red using sulphuric acid as doping source.[127] The introduction of S into GQDs creates additional S-related energy levels between $\pi$ and $\pi^*$ of carbon, which increases the electron transition pathways in both absorption and PL

emission of S-GQDs. Alternate dopants such as silicon (Si)[132], phosphorous (P)[133], boron (B)[134], fluorine (F)[135], chlorine (Cl)[136] or a mixture of different dopants[31] (co-doping) have also been reported to tune and enhance the optical properties.

Xia *et al*. reported a simple solvent-free method to prepare N, S-co-doped GQDs (N, S-GQDs) by using citric acid as carbon source and L-cysteine as a dopant.[137] The intermolecular condensation between the graphene nuclei was shown to generate N, S-GQDs, which exhibited a blue colour PL emission with QY of 74.5 %. The enhanced PL QY was attributed to the co-doping effect of N and S, which had excellent electron-donating power and hence enabled radiative recombination generation. Thus, heteroatom doping could effectively tune the electron density, Fermi level and band gap which in turn could enhance the PL emission and QY.

### 1.5.7. Fluorescence enhancement of GQDs

As discussed in the previous sections, there are various approaches for tuning the band gap and optical properties of GQDs. However, most of the GQDs obtained have low emission efficiency relative to other conventional semiconductor quantum dots even after surface passivation or functionalization. Moreover, for most GQDs, additional passivation is required to obtain sufficient PL, making the synthesis process complex which limits its use in large-scale applications. To improve the fluorescent properties of GQDs are therefore remained a challenge and it is highly desirable to extend their scope for various applications. Recent research is going on to enhance its fluorescent properties in order to meet the application requirements such as increased sensitivity and lower limits of detection (LOD).

To date, various methods for fluorescence enhancement have been explored. Techniques that can more efficiently excite and extract the light emitted by GQDs could therefore lead to fluorescence enhancement and thus lowering the detection limits towards various analytes in sensing applications.[138] Well-ordered assemblies of quantum dots have the potential to be used in various applications where a patterned surface can provide an advantage over flat films of the same material.[139] Because periodical arrays of nanostructures are found to have fluorescence amplification of fluorophores.[140] Melvin *et al.* reported a protein enabled approach to fabricate QD

nanoarrays with a 15-fold increase in surface plasmon-enhanced fluorescence.[141] In another study, Chao *et al.* enhanced the fluorescence signals of polymer-QD composite arrays by hybridizing ultra-thin plasmonic Au walls using single-step patterning and hybridization to the sidewalls of the arrays.[142]

Another approach to enhance the fluorescence emission of QDs is radiative decay engineering with metal nanostructures. Here the fluorescence enhancement is due to the combination of various processes like enhanced fluorophore absorption, changes in the radiative decay pathways and increased fluorescence emission to far-field. Lakowics *et al.* suggested that appropriate localization of fluorophores near metallic surface can result in fluorescence enhancement.[143] Metal enhanced fluorescence (MEF) has also been widely explored for the fluorescence amplification of various fluorophores. Ultimately, the factors that influence the optical properties of plasmonic nanostructure are the size, shape, dielectric property of the material and also the position of the plasmonic structures.[144] Yuan *et al.* reported photoinduced fluorescence enhancement (PFE) in colloidal CdSeTe/ZnS core-shell QDs.[145] They proposed that PFE from single QD is due to the surface passivation induced by photoinduced charge carriers.

Besides all these approaches, fluorescent enhancement of QDs can be achieved by the use of patterned substrates. Fluorescence signal enhancement on colloidal photonic crystals (CPCs) has also emerged as a new method because of its low cost and easy fabrication.[146, 147] CPCs can either inhibit or enhance emission, depending on the position of fluorescence emission maxima and PBG minima.[148] CPCs can therefore provide excellent fluorescence enhancement by tuning their own leaky modes with either fluorophore excitation or emission.[149] To date, various strategies have been explored for further fluorescence enhancement of CPCs. On heterostructure CPCs with dual stop bands, Li *et al.* demonstrated a 162-fold fluorescence enhancement for QDs.[150] Barth *et al.* reported an enhanced fluorescence of lead sulphide QDs that interact with leaky modes of slab structures of silicon photonic crystals.[151] Ehsan *et al*. reported a remarkable fluorescence enhancement using a self-assembled multilayer three-dimensional polystyrene based CPCs.[149]

### 1.5.8. Assembly of GQDs

The geometrically well-defined arrangement of QDs unlocks new openings to control the optical and electronic coupling of individual QD components, thereby covering the advantages of the collective properties of assembled QDs.[152, 153] Li *et al.* demonstrated colloidal GQD assemblies over large area and also their orientation regulation.[154] The orientations of GQDs can be determined as either in-plane ("face-on")or out of-plane ("edge-on") with the substrate. It's chemical functionalization leads to orientation-dependent interactions between GQDs and the surface. Qu *et al.* developed an ordered assembly of GQDs into 1D nanotube (NT) arrays within a nanoporous template by electrophoresis deposition method.[152] The hierarchically porous 1D nanotube arrays formed from 0D GQDs can lead to more effective charge transfer between GQDs and target molecules, resulting in stronger surface-enhanced Raman scattering (SERS) than that on the flat graphene sheet. As a result, this 1D nanotube structure exhibited its great potential as a new metal-free platform for efficient SERS applications.

### 1.5.9. Cytotoxicity

The toxicity of QDs is a matter of concern because of its potential applications in biological field. However, when compared to other conventional semiconductors QDs like CdSe, PbTe, CdTe etc., GQDs reported lower cytotoxicity.[110] Different research groups have studied the cytotoxicity of GQDs. [108, 155] Zhu *et al.* studied the cytotoxicity of GQDs using methyl thiazolyl-tetrazolium bromide (MTT) assay on MG-63 (human osteosarcoma) cells. The results indicated that as-synthesized GQDs possess lower toxicity and hence could be used in bioimaging studies.[155] Zhang *et al*. used three types of stem cells like cardiac progenitor cells (CPCs), neurosphere cells (NSCs) and pancreas progenitor cells (PPCs), for the cell viability study by MTT assay.[156] They obtained average cell viability of around 80 % for NSCs and CPCs and 65% for PPCs after incubating in GQDs for 3 days. All these evidences suggest that GQDs have lower cytotoxicity and hence have great potential for bio applications like *in-vitro* and *in-vivo* imaging studies. Although additional toxicity studies for LD50 (median lethal dose) are needed, some researchers predict that the biocompatibility of such carbon-based

fluorescent materials can replace the existing FDA-approved dyes such as indocyanine green which was used for optical imaging, (LD50 = 60 mg/kg body weight).[157]

## 1.6. Applications of GQDs

GQDs find potential applications in various fields owing to its unique physical and chemical properties such as good solubility, non-toxicity, surface grafting, biocompatibility, stable PL, inertness and superior resistant to photobleaching.[158] Some of these properties are significantly superior to conventional semiconductor quantum dots resulting in various potential applicability in sensing[131], bioimaging[159], theranostics[160], biosensing[23], drug delivery[161], solar cell[162], light-emitting diodes[163], batteries[164], photodetectors[165], catalysis[71] etc.

GQDs are considered particularly suitable for optical applications due to its tunable optical properties, multiple PL emission colour, high quantum efficiency, high extinction coefficient and longer lifetime.[99] Its small size also ensures that electrons do not move as far as larger particles, making it possible for electronic devices to work more quickly. Taking advantage of these electronic properties, GQDs can also be applied in quantum computation, solar cells and transistors.[166] GQDs can significantly improve LED displays with higher peak brightness, better display efficiency, higher colour saturation etc.[167] Because of its high conductivity and larger surface area, electrodes made of GQDs can be applied to batteries and capacitors.[168] Low cytotoxicity, possibility of crossing cell membranes, persistent dispersions in various solvents makes GQD a promising candidate for wide-ranging biomedical applications. GQDs are also promising in catalysis because of their accessibility of active sites and large surface area. Additional excellent properties of GQDs such as high transparency and high surface area have been suggested for energy and display applications.

Therefore, GQDs may become a widespread nanomaterial for advanced technology in the next decade, as it will influence our quality of life and draw significant commercial interest. As shown in **Figure 1.9** GQDs have been exploited in all the above-mentioned fields. It was not until recently that their scientific challenges in the analytical field was not so thoroughly studied. The present thesis addresses a few major applications of GQDs in medical and analytical field *viz,* bioimaging, drug delivery and

sensing, but gives more emphasis on various types of sensors and analytical systems that utilizes GQD as the key component.
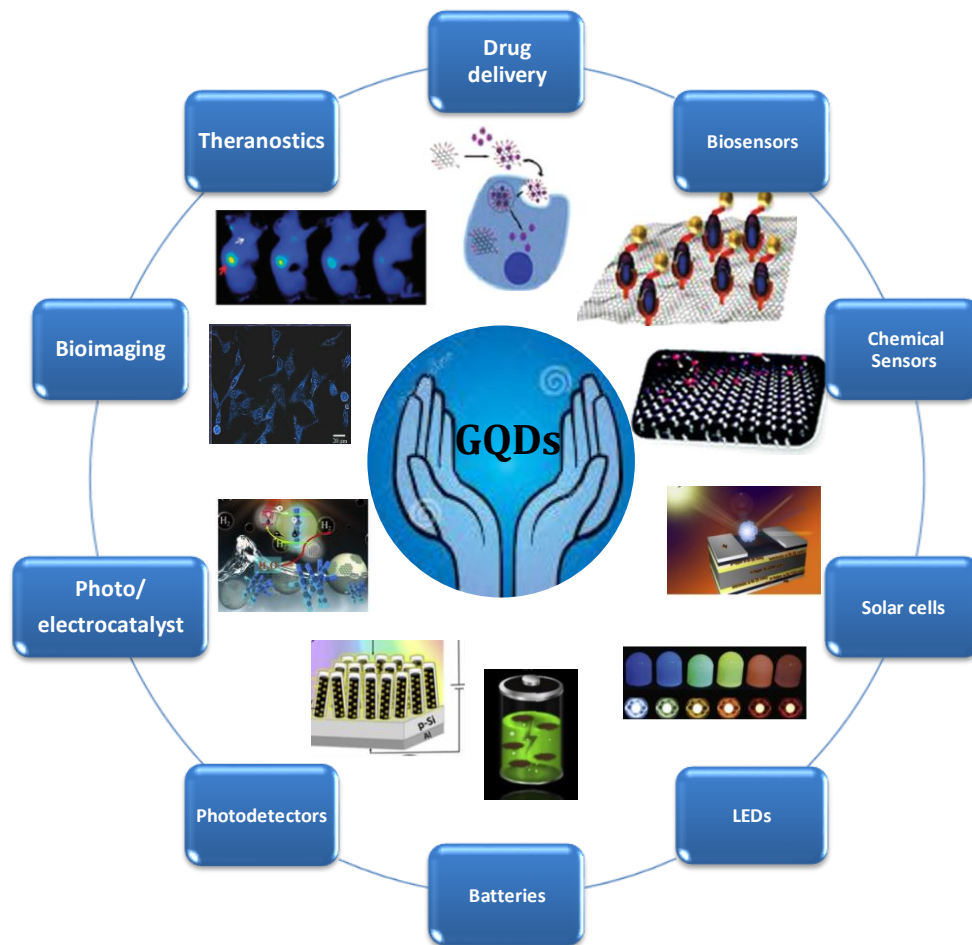


**Figure 1.9.** Applications of GQDs in various fields.

## 1.6.1. Biomedical applications

GQDs have been exploited for biomedical applications due to their non-toxicity and biocompatibility and have shown some excellent performances that could potentially replace some traditional materials in this area.[169] GQDs can easily penetrate across intracellular membrane because of its small size. This unique property makes GQD a promising candidate for bioimaging and drug delivery. Due to the recent promising results in the field, there have been ongoing researches carried out to exploit GQDs for other new medical applications.

### 1.6.1.1. Bioimaging

GQDs were used for medical diagnosis in bioimaging, as they can help to locate cancer cells and assess if drugs were delivered to targeted cells as well as locate the drugs in the cell. The bright and tunable PL, non-toxicity and biocompatibility of GQDs make it possible to use in bioimaging applications. Peng *et al.* used green fluorescence GQDs for bioimaging by incubating it in human breast cancer cell lines T47D.[40] The obtained high contrast fluorescent image of green GQDs around the nucleus indicates that GQDs can be used in high contrast bioimaging. Later, Pu and co-workers demonstrated that $Fe_3O_4$ modified GQDs can be used as efficient fluorescent probes for fluorescent imaging assay. Zhu *et al.* used GQDs synthesized via solvothermal approach for imaging MG63 cells and demonstrated two colour imaging at two different excitation wavelengths.[84] Dong *et al.* incubated human breast cancer cells MCF-7 in green GQDs for 4 h and could image a bright green fluorescence at an excitation wavelength of 488 nm.[45] The above studies used down conversion PL resulted from blue excitation or one photon UV, but the upconversion PL of GQDs had the benefit of harvesting near IR (NIR) region using multiphoton excitation. Zhu *et al.* observed bright green or blue fluorescence inside GQD treated MC3T3 cells under NIR excitation, indicating successful translocation of GQDs across cell membrane.[30] Strong fluorescence, non-toxicity and biocompatibility of GQDs will therefore make it an excellent choice for bioimaging in medical applications.

### 1.6.1.2. Drug delivery

Compact drug delivery nanostructures with multifunctional features are of great interest for cancer therapy due to its therapeutic efficacy and increased dosage tolerance. In addition to the smaller size and different chemical reactivity relative to other carbon materials like GO and CNT, GQDs have many prominent features such as π electron rich $sp^2$ carbons with a variety of functional groups like carboxyl, hydroxyl, epoxy and carbonyl etc. Such features make GQDs an ideal candidate for drug delivery via π-π interaction and the ease of functionalization through oxygen-containing functional groups. Jing *et al.* developed multifunctional core-shell based capsules consisting of porous dual-layer $TiO_2$ shell, olive oil, GQDs and $Fe_3O_4$ for drug delivery application.[170] Here olive oil, GQDs and $Fe_3O_4$ had functioned as the reservoir for oil-

soluble drug, fluorescence agent for imaging and material for magnetic targeting respectively. The results showed that these core-shell based capsules played a significant role in the development of a water-insoluble drug delivery system. Some *et al.* used GQDs as nanovectors to deliver an anticancer drug and carried out its clinical studies.[171] Zhang *et al.* showed that GQDs can also be used in gene delivery.[172] GQD is therefore a promising candidate as a targeting as well as therapeutic agent for theranostic applications.

## 1.6.2. Sensing

GQDs have received increased attention recently in the field of chemical sensing. Due to their intrinsic properties such as bright and stable PL, superior resistance to photobleaching, broad band optical absorption, tunable emission and chemical stability, GQDs have great advantages compared to conventional fluorescence probes such as organic dyes and inorganic semiconductor QDs. In particular, due to these intrinsic properties, GQDs are intended to be excellent alternatives for chemical sensors to detect various analytes. The sensors designed using GQDs so far can generally be classified into photoluminescence sensors, electrochemical sensors, electronic sensors, electrochemiluminescence sensors, electrochemical biosensors, optical biosensors and photoelectrochemical biosensors based on the mode of detection. The features of different sensors using GQDs as sensing probes are summarized in **Table 1.2.**

**Table 1.2.** Summary of GQD based sensors.

| GQD based sensor | Analyte | Transduction mechanism | LOD | Linear range | Ref. |
|---|---|---|---|---|---|
| Lignin sulfonate /GQDs | $Fe^{3+}$ | Fluorescence quenching | 0.5 nM | 0.005-500 µM | [173] |
| Carbon back derived GQDs | $Fe^{3+}$ | Fluorescence quenching | 0.45 µM | 0-60 µM | [174] |
| B-GQD | $Fe^{3+}$ | Fluorescence quenching | 31.2 nM | 50 nM -220 µM | [175] |
| B-GQD | $Al^{3+}$ | Fluorescence enhancement | 3.64 µM | 0-100 µM | [176] |
| N-GQDs | $H_2O_2$ | Electrochemical enhancement | 0.12 µM | 0.25-13327 µM | [177] |
| GQDs/Au | $H_2O_2$ | Electrochemical enhancement | 1 µM | 0.005-4 mM | [178] |
| B-GQD | Cytochrome C | Fluorescence quenching | 5.9 µg/mL | 100-300 µg/mL | [175] |
| GQDs/MoS$_2$ | Cholesterol | Fluorescence enhancement | 35 nM | 0.08-300 µM | [179] |
| GQDs | Concanavalin A | Electrochemiluminescence enhancement | 0.16 pg/mL | 0.0005–1 ng/mL | [180] |
| GQDs | Thrombin | Electrochemical enhancement | 100 nM | 200-500 nM | [181] |
| GQDs-based nanocellulosic hydrogel | Laccase | Fluorescence quenching | 0.048 U/mL | 0.01-10 U/mL | [182] |
| GQDs/Au | Glucose | Electrochemical enhancement | 30 µM | 0.05-100 mM | [178] |
| GQDs/AChE/ CHOx | Methyl paraoxon | Fluorescence recovery | 0.342 µM | 0.40-4.05 µM | [183] |
| GQDs | Ochratoxin A | Fluorescence quenching and recovery | 13 pg/mL | 0-1 ng/mL | [184] |
| N-GQDs | Acid phosphate | Fluorescence recovery | 0.014 mU/mL | 0.04-0.7 mU/mL | [185] |
| GQD/Au | $Pb^{2+}$ | Fluorescence recovery | 16.7 nM | 50 nM-4 µM | [186] |
| GQD/Aptamer/GO | $Pb^{2+}$ | Fluorescence recovery | 0.6 nM | 0.6-400 nM | [187] |
| GQD/Aptamer | Intercellular cytokine | Fluorescence recovery | 2 pg/mL | 71-91 pg/mL | [188] |
| GQD/ Curcumin | APO*e4* DNA | Electrochemical/ Fluorescence dual mode | 0.48 pg/mL | 0-400 pg/mL | [189] |

In view of its PL properties, GQDs have been extensively explored as fluorescent probes to detect various analytes with either signal-off or signal-on processes. Using

GQDs as the sensing probes, metal ions have become the most widely explored analytes to date. In 2012, Wang *et al.* developed the first GQD-based PL sensor for the sensitive and selective detection of $Fe^{3+}$ through charge transfer process.[190] GQD based PL sensors can be used to detect anions as well as cations. Dong *et al.* used strong oxidative free chlorine to destroy the surface passivation layer of GQDs resulting in significant PL quenching and hence developed a facile, selective, sensitive and green sensor for the detection of free chlorine in drinking water.[191] Fan *et al.* reported a simple and effective sensing platform for the ultrasensitive detection of 2,4,6-trinitrotoluene (TNT) by fluorescence resonance energy transfer quenching (FRET) resulting from the π-π stacking between TNT and GQDs.[106] Yang *et al.* employed energy transfer and PL quenching of GQDs arising from π-π stacking or hydrogen bonding interaction between GQDs and pyrocatechol for the sensitive detection of pyrocatechol.[192]

The sensitivity of GQD based sensors towards different analyte molecules could be enhanced by using GQDs with higher quantum yield. Li *et al.* used N and S co-doped QDs with long PL lifetime for the sensitive detection of pesticides.[193] As shown in **Table 1.2**, many of the experiments are conceptually similar in quenching the PL of GQDs by a specific metal of interest. In most cases, innovation comes from the material source or its method of synthesis. Usually, the experiments do not involve any surface modification, so how selectivity is obtained now seems to be an open question. It highlights the need to understand the quenching mechanism and how different preparation methods can make one metal selection over another. Such findings indicate that there is considerable promise to use GQDs for the detection of organic species by photoinduced electron transfer (PET) mechanism. The PET mechanism is observed when the fluorescence of an excited chromophore is quenched by the electron transfer to an acceptor species.

In addition to the above-mentioned signal-off PL sensors, some signal-on PL sensors were also developed. Qu *et al.* reported a signal-on PL sensor based on GQD for the sensitive detection of phosphate ion. The sensing system uses the combination of GQD and $Eu^{3+}$ ions that could interact with the GQD carboxylate group as a bridge to form the aggregates of GQDs.[185] The fluorescence of GQDs was quenched (signal-off) by energy transfer or electron transfer when treated with $Eu^{3+}$ ions. After the introduction

of phosphate ion, the aggregated GQDs could be dissociated due to its high affinity to oxygen donor atoms leading to the redispersion of GQDs which results in the restoration of fluorescence (signal-on). Qian *et al*. reported a GO/GQD hybrid sensor for selective and sensitive detection of $Pb^{2+}$ with a well-controlled fluorescence signal-on process based on PET between GO and GQDs.[187]

Although GQD based fluorescent sensors exhibited high sensitivity towards various analytes, but their selectivity was a matter of concern. Aptasensors are well known for its selectivity towards specific targets because of its remarkable specificity, high affinity, excellent stability, easy modification and target diversity.[194, 195] When compared to other reported recognition elements like antibodies and enzymes, aptamers are more specific, sensitive, easily modifiable and stable.[196, 197] Aptamers are referred to as single stranded small nucleic acid chains, selected in vitro by SELEX (Systematic Evolution of Ligands by Exponential Enrichment) that can fold into specific three-dimensional (3D) structures upon binding with specific targets like proteins, peptides, carbohydrates, toxins, small molecules and even live cells.[198-201] Variety of novel aptasensors coupled with different sensing signals has been designed to detect various targets like pesticides,[202, 203] heavy metals,[186, 204] antibiotics[205] and biotoxins.[206] Recently, Wang *et al.* reported a GQD based aptasensor via inner filter effect (IFE) for ultrasensitive and selective detection of acetamiprid pesticide.[203] However, IFE based sensing approach results in low efficiency and poor sensitivity. A "turn-on" fluorescence sensor based on GQD and gold nanoparticles has also been developed utilizing fluorescence resonance energy transfer (FRET) for $Pb^{2+}$ detection by Niu *et al.[186]* These approaches were very reliable and have high selectivity, but not sensitive enough for the trace level detection.

To address these concerns, a complementary dual mode sensing system can be designed which can provide two types of output signals, making the results more convincing.[153, 207]  In addition, this dual-mode strategy could minimize the risk of false-positive and false negative detection by obtaining results from the dual-channel sensing system, thereby enhancing the accuracy and reliability of the sensing system.[208, 209] Dual-mode detection approaches have recently gained considerable attention and have been shown to be more effective than single-mode detection. Liu *et al*. reported a dual-mode

colorimetric/fluorescence sensor for the detection of ascorbic acid.[210] Wang *et al*. demonstrated a dual-mode SERS and resonance Rayleigh scattering (RRS) sensing platforms based on Ag-doped carbon dots.[211] A dual-mode gold nanoprobe for the detection of telomerase activity was reported based on SERS and colorimetry.[212]

In the near future, GQDs are expected to play a rising role in analytical and bioanalytical science. Meanwhile, research into sensing applications of GQDs will focus on enhancing sensitivity, selectivity and robustness of sensing platforms.

## 1.7. Objectives of the present thesis

The literature search on GQDs, as discussed above, shed light on the unique physical and chemical properties like biocompatibility, superior stability, strong fluorescence, good solubility and surface grafting. Although there are many significant advantages and potential applications of GQDs, in order to meet the application requirements, tremendous effort is required to improve its properties. To challenge the industry requirements, mass production is essential at a relatively low cost. However, the product yield and quantum yield using current preparation methods is considerably low. Hence a simple and rapid synthetic approach for the material with high production yield and relatively higher quantum yield is a real scientific challenge in the present scenario. Therefore, the primary objective of the present thesis is the development of a facile and rapid synthesis route for GQDs with higher production yield and quantum yield.

Compared to other conventional methods, microwave-assisted route offers these requirements under mild conditions and shorter reaction time. Hence, we adopted a new methodology termed as "microwave-assisted sonochemical (MS) synthesis". As the name implies the method involves simultaneous microwave treatment and ultrasonication, focusing on using their combined effect for rapid synthesis of GQDs. Sonochemical synthesis approach offers better control over particle size giving uniform size distribution, improve the dispersibility of precursors in the solvent, which in turn aids in faster penetration of microwaves to the system and helps in rapid synthesis. Therefore, the synergistic action of microwave and ultrasonication can effectively put

the formation of novel architectures with well-defined particle size and narrow size distribution in a shorter reaction time.

GQDs synthesized by most methods have relatively low emission performance, when compared to conventional semiconductor quantum dots, even after surface functionalization or passivation. Therefore, effective means to enhance the fluorescent properties of GQDs is a challenge and it is highly desirable to extend their scope for different applications. Hence, the secondary objective of the present thesis is to tune and enhance the fluorescence properties of the material in order to meet the application requirements such as increased sensitivity and lower limits of detection. GQD-based sensors can achieve high-level performance due to their unique and tunable optical properties. Various sensors can be designed using either turn-off or turn-on processes based on the fluorescence of GQDs.

The main objective of the present research work is to develop a facile and rapid strategy for the synthesis of GQDs using microwave-assisted sonochemical method. The secondary objective is to tune and enhance the optical properties of the system for selective and ultrasensitive detection of a set of environmental pollutants like pesticides and heavy metals. Specific objectives of the thesis are.

1. To develop a facile and rapid strategy for the synthesis of size tunable GQDs with high production yield and quantum yield.
2. To enhance the fluorescence signal of GQDs and thereby enhancing its sensitivity towards various analytes.
3. To tune the optical properties of GQDs by heteroatom doping strategy in order to enhance its quantum yield and quantum efficiency.
4. To design various sensing platforms by surface modifications of GQDs so as to enhance the sensitivity and selectivity of the sensing probe towards various analytes.

## 1.8. Layout of the thesis

The thesis is organized into six chapters, as

**Chapter 1** gives a brief introduction about the synthesis, properties and applications of GQDs. The chapter focuses on various strategies in enhancing the fluorescent properties of GQDs especially emission efficiency which is highly desirable to broaden its widespread application.

**Chapter 2** deals with a facile, rapid and one pot synthesis of size-tunable GQDs by oxidative cutting of GO by the synergistic effect of microwave and ultrasound treatments. Further, the as-synthesized GQDs were demonstrated for bioimaging, detection of physiologically relevant metal ions and fluorescence enhancement studies.

**Chapter 3** focuses on tuning the optical properties of GQDs by heteroatom doping strategy and synthesized sulphur doped GQDs (S-GQDs) by MS method. We also developed S-GQD based fluorescent sensors in aqueous form as well as in flexible (film) form for the sensitive detection of carbamate pesticides with limit of detection at ppb level.

**Chapter 4** demonstrates a simple design for a fluorescent turn-on aptasensor based on S-GQD utilizing specific recognition and binding property of aptamer for the selective detection of omethoate (a common organophosphorus model pesticide). The developed 'switch-on' aptasensor has achieved a limit of detection as low as 1 ppb with high selectivity for omethoate over other control pesticides.

**Chapter 5** deals with the development of a dual-mode SERS/fluorescence sensor based on aptamer modified gold nanoparticles and S-GQD for the ultrasensitive and selective detection of a pesticide, namely omethoate.

**Chapter 6** summarizes the entire thesis work highlighting the advances made in the development and applications of GQD based sensors. We have discussed the scope of future works in this area.

## References

1.      B. C. Brodie, *Philosophical Transactions of the Royal Society of London*, 1859, 249-259.

2.      J. D. Bernal, *Proceedings of the Royal Society of London. Series A, Containing Papers of a Mathematical and Physical Character*, 1924, **106**, 749-773.

3.      P. R. Wallace, *Physical Review*, 1947, **71**, 622.

4.      W. S. Hummers Jr and R. E. Offeman, *Journal of the american chemical society*, 1958, **80**, 1339-1339.

5.      H. Boehm, A. Clauss, G. Fischer and U. Hofmann, *Zeitschrift Für Naturforschung B*, 1962, **17**, 150-153.

6.      D. DiVincenzo and E. Mele, *Physical Review B*, 1984, **29**, 1685.

7.      H. W. Kroto, J. R. Heath, S. C. O'Brien, R. F. Curl and R. E. Smalley, *nature*, 1985, **318**, 162-163.

8.      S. Mouras, A. Hamm, D. Djurado and J. Cousseins, *Revue de chimie minérale*, 1987, **24**, 572.

9.      P. Ajayan and S. Lijima, *Nature*, 1992, **358**, 23-23.

10.     K. S. Novoselov, A. K. Geim, S. V. Morozov, D. Jiang, Y. Zhang, S. V. Dubonos, I. V. Grigorieva and A. A. Firsov, *science*, 2004, **306**, 666-669.

11.     Z. Yin, S. Sun, T. Salim, S. Wu, X. Huang, Q. He, Y. M. Lam and H. Zhang, *ACS Nano*, 2010, **4**, 5263-5268.

12.     Y. Sun, S. Wang, C. Li, P. Luo, L. Tao, Y. Wei and G. Shi, *Physical Chemistry Chemical Physics*, 2013, **15**, 9907-9913.

13.     X. Yan, X. Cui and L.-s. Li, *Journal of the American Chemical Society*, 2010, **132**, 5944-5945.

14.     X. Yan, X. Cui, B. Li and L.-s. Li, *Nano Letters*, 2010, **10**, 1869-1873.

15.     L. Ponomarenko, F. Schedin, M. Katsnelson, R. Yang, E. Hill, K. Novoselov and A. Geim, *Science*, 2008, **320**, 356-358.

16.     X. Xu, R. Ray, Y. Gu, H. J. Ploehn, L. Gearheart, K. Raker and W. A. Scrivens, *Journal of the American Chemical Society*, 2004, **126**, 12736-12737.

17.     D. Pan, J. Zhang, Z. Li and M. Wu, *Advanced Materials*, 2010, **22**, 734-738.

18. X. Zhou, Y. Zhang, C. Wang, X. Wu, Y. Yang, B. Zheng, H. Wu, S. Guo and J. Zhang, *Photo-Fenton Reaction of Graphene Oxide: A New Strategy to Prepare Graphene Quantum Dots for DNA Cleavage*, 2012.

19. Y. Shin, J. Lee, J. Yang, J. Park, K. Lee, S. Kim, Y. Park and H. Lee, *Small*, 2014, **10**, 866-870.

20. S. Wang, Z. Lemon, I. S. Cole and Q. Li, *RSC Advances*, 2015, **5**, 41248-41254.

21. S. Bak, D. Kim and H. Lee, *Current Applied Physics*, 2016, **16**, 1192-1201.

22. C.-T. Chien, S.-S. Li, W.-J. Lai, Y.-C. Yeh, H.-A. Chen, I. S. Chen, L.-C. Chen, K.-H. Chen, T. Nemoto, S. Isoda, M. Chen, T. Fujita, G. Eda, H. Yamaguchi, M. Chhowalla and C.-W. Chen, *Angewandte Chemie International Edition*, 2012, **51**, 6662-6666.

23. Z. Fan, S. Li, F. Yuan and L. Fan, *RSC Advances*, 2015, **5**, 19773-19789.

24. N. Li, X. Wang, J. Chen, L. Sun and P. Chen, *2D Materials*, 2015, **2**, 034018.

25. Y. Dong, *Carbon*, 2012, **v. 50**, pp. 4738-4743-2012 v.4750 no.4712.

26. H. Yue, Z. Yang, L. Gewu, C. Nan, Z. Zhipan, L. Hui, S. Huibo and Q. Liangti, *Nanotechnology*, 2013, **24**, 195401.

27. A. Ananthanarayanan, Y. Wang, P. Routh, M. A. Sk, A. Than, M. Lin, J. Zhang, J. Chen, H. Sun and P. Chen, *Nanoscale*, 2015, **7**, 8159-8165.

28. C. X. Guo, H. B. Yang, Z. M. Sheng, Z. S. Lu, Q. L. Song and C. M. Li, *Angewandte Chemie International Edition*, 2010, **49**, 3014-3017.

29. B. C. M. Martindale, G. A. M. Hutton, C. A. Caputo and E. Reisner, *Journal of the American Chemical Society*, 2015, **137**, 6018-6025.

30. S. Zhu, J. Zhang, S. Tang, C. Qiao, L. Wang, H. Wang, X. Liu, B. Li, Y. Li, W. Yu, X. Wang, H. Sun and B. Yang, *Advanced Functional Materials*, 2012, **22**, 4732-4740.

31. B.-X. Zhang, H. Gao and X.-L. Li, *New Journal of Chemistry*, 2014, **38**, 4615-4621.

32. J. Shen, Y. Zhu, X. Yang and C. Li, *Chemical Communications*, 2012, **48**, 3686-3699.

33. D. Chao, C. Zhu, X. Xia, J. Liu, X. Zhang, J. Wang, P. Liang, J. Lin, H. Zhang and Z. X. Shen, *Nano letters*, 2014, **15**, 565-573.

34. Z. Zhang, J. Zhang, N. Chen and L. Qu, *Energy & Environmental Science*, 2012, **5**, 8869-8890.

35. M. Dutta, S. Sarkar, T. Ghosh and D. Basak, *The Journal of Physical Chemistry C*, 2012, **116**, 20127-20131.

36.    L. Li, G. Wu, G. Yang, J. Peng, J. Zhao and J.-J. Zhu, *Nanoscale*, 2013, **5**, 4015-4039.

37.    Y. Dong, H. Pang, S. Ren, C. Chen, Y. Chi and T. Yu, *Carbon*, 2013, **64**, 245-251.

38.    C. Zhang, Y. Cui, L. Song, X. Liu and Z. Hu, *Talanta*, 2016, **150**, 54-60.

39.    A. El Fatimy, R. L. Myers-Ward, A. K. Boyd, K. M. Daniels, D. K. Gaskill and P. Barbara, *Nature nanotechnology*, 2016, **11**, 335.

40.    J. Peng, W. Gao, B. K. Gupta, Z. Liu, R. Romero-Aburto, L. Ge, L. Song, L. B. Alemany, X. Zhan, G. Gao, S. A. Vithayathil, B. A. Kaipparettu, A. A. Marti, T. Hayashi, J.-J. Zhu and P. M. Ajayan, *Nano Letters*, 2012, **12**, 844-849.

41.    Z. Luo, G. Qi, K. Chen, M. Zou, L. Yuwen, X. Zhang, W. Huang and L. Wang, *Advanced Functional Materials*, 2016, **26**, 2739-2744.

42.    D. B. Shinde and V. K. Pillai, *Chemistry – A European Journal*, 2012, **18**, 12522-12528.

43.    G. Radhakrishnan, P. M. Adams and L. S. Bernstein, *Applied Surface Science*, 2007, **253**, 7651-7655.

44.    S. Kim, S. W. Hwang, M.-K. Kim, D. Y. Shin, D. H. Shin, C. O. Kim, S. B. Yang, J. H. Park, E. Hwang, S.-H. Choi, G. Ko, S. Sim, C. Sone, H. J. Choi, S. Bae and B. H. Hong, *ACS Nano*, 2012, **6**, 8203-8208.

45.    Y. Dong, C. Chen, X. Zheng, L. Gao, Z. Cui, H. Yang, C. Guo, Y. Chi and C. M. Li, *Journal of Materials Chemistry*, 2012, **22**, 8764-8766.

46.    R. Ye, C. Xiang, J. Lin, Z. Peng, K. Huang, Z. Yan, N. P. Cook, E. L. G. Samuel, C.-C. Hwang, G. Ruan, G. Ceriotti, A.-R. O. Raji, A. A. Martí and J. M. Tour, 2013, **4**, 2943.

47.    X. Yan, B. Li, X. Cui, Q. Wei, K. Tajima and L.-s. Li, *The Journal of Physical Chemistry Letters*, 2011, **2**, 1119-1124.

48.    R. Liu, D. Wu, X. Feng and K. Müllen, *Journal of the American Chemical Society*, 2011, **133**, 15221-15223.

49.    K. Habiba, V. I. Makarov, J. Avalos, M. J. F. Guinel, B. R. Weiner and G. Morell, *Carbon*, 2013, **64**, 341-350.

50.    L. Tang, R. Ji, X. Li, G. Bai, C. P. Liu, J. Hao, J. Lin, H. Jiang, K. S. Teng, Z. Yang and S. P. Lau, *ACS Nano*, 2014, **8**, 6312-6320.

51.    J. Lu, P. S. E. Yeo, C. K. Gan, P. Wu and K. P. Loh, *Nature Nanotechnology*, 2011, **6**, 247.

52.    H. X. Zhao, L. Q. Liu, Z. D. Liu, Y. Wang, X. J. Zhao and C. Z. Huang, *Chemical Communications*, 2011, **47**, 2604-2606.

53.    K. P. Loh, Q. Bao, G. Eda and M. Chhowalla, *Nature chemistry*, 2010, **2**, 1015.

54.    L.-L. Li, J. Ji, R. Fei, C.-Z. Wang, Q. Lu, J.-R. Zhang, L.-P. Jiang and J.-J. Zhu, *Advanced Functional Materials*, 2012, **22**, 2971-2979.

55.    D. Pan, L. Guo, J. Zhang, C. Xi, Q. Xue, H. Huang, J. Li, Z. Zhang, W. Yu and Z. Chen, *Journal of Materials Chemistry*, 2012, **22**, 3314-3318.

56.    H. Tetsuka, R. Asahi, A. Nagoya, K. Okamoto, I. Tajima, R. Ohta and A. Okamoto, *Advanced Materials*, 2012, **24**, 5333-5338.

57.    S. Zhu, J. Zhang, X. Liu, B. Li, X. Wang, S. Tang, Q. Meng, Y. Li, C. Shi, R. Hu and B. Yang, *RSC Advances*, 2012, **2**, 2717-2720.

58.    J. Wang, M. Gu, J. Di, Y. Gao, Y. Wu and Y. Tu, *Bioprocess and Biosystems Engineering*, 2007, **30**, 289-296.

59.    L. Zheng, Y. Chi, Y. Dong, J. Lin and B. Wang, *Journal of the American Chemical Society*, 2009, **131**, 4564-4565.

60.    S. L. null, L. D. null and L. F. null, *SCIENCE CHINA Chemistry*, 2015, **58**, 417.

61.    J. Lu, J.-x. Yang, J. Wang, A. Lim, S. Wang and K. P. Loh, *ACS Nano*, 2009, **3**, 2367-2375.

62.    A. Ciesielski, S. Haar, A. Aliprandi, M. El Garah, G. Tregnago, G. F. Cotella, M. El Gemayel, F. Richard, H. Sun, F. Cacialli, F. Bonaccorso and P. Samorì, *ACS Nano*, 2016, **10**, 10768-10777.

63.    J. P. Guin, S. K. Guin, T. Debnath and H. N. Ghosh, *Carbon*, 2016, **109**, 517-528.

64.    D. K. Nguyen and T. Kim, *Applied Surface Science*, 2018, **427**, 1152-1157.

65.    S. Sarkar, D. Gandla, Y. Venkatesh, P. R. Bangal, S. Ghosh, Y. Yang and S. Misra, *Physical Chemistry Chemical Physics*, 2016, **18**, 21278-21287.

66.    J. M. Tour, R. Ye, C. Xiang, J. Lin, Z. Peng and G. Ceriotti, Google Patents, 2018.

67.    Y.-W. Shih, G.-W. Tseng, C.-Y. Hsieh, Y.-Y. Li and A. Sakoda, *Acta Materialia*, 2014, **78**, 314-319.

68.    A. Gedanken, *Ultrasonics sonochemistry*, 2004, **11**, 47-55.

69.    N. S. M. Yusof, B. Babgi, Y. Alghamdi, M. Aksu, J. Madhavan and M. Ashokkumar, *Ultrasonics sonochemistry*, 2016, **29**, 568-576.

70.   H. Li, X. He, Y. Liu, H. Huang, S. Lian, S.-T. Lee and Z. Kang, *Carbon*, 2011, **49**, 605-609.

71.   S. Zhuo, M. Shao and S.-T. Lee, *ACS Nano*, 2012, **6**, 1059-1064.

72.   H. Lais, P. S. Lowe, T.-H. Gan and L. C. Wrobel, *Ultrasonics sonochemistry*, 2018, **45**, 7-16.

73.   Y. Zhu, G. Wang, H. Jiang, L. Chen and X. Zhang, *Chemical Communications*, 2015, **51**, 948-951.

74.   P. Lidström, J. Tierney, B. Watheyb and J. Westmana, *Tetrahedron*, 2001, **57**, 9225-9283.

75.   J.-S. Schanche, *Molecular Diversity*, 2003, **7**, 293-300.

76.   G. Novak Travis, J. Kim, H. Song Sung, H. Jun Gwang, H. Kim, S. Jeong Mun and S. Jeon, *Small*, 2016, **12**, 994-999.

77.   C. D. Simpson, J. D. Brand, A. J. Berresheim, L. Przybilla, H. J. Räder and K. Müllen, *Chemistry–A European Journal*, 2002, **8**, 1424-1429.

78.   J. Wu, W. Pisula and K. Müllen, *Chemical reviews*, 2007, **107**, 718-747.

79.   Z. Guo, B. Cai, Q. Cao, Y. Su, M. Li, J. Hu, Z. Yang and Y. Zhang, *Fullerenes, Nanotubes and Carbon Nanostructures*, 2017, **25**, 704-709.

80.   J. Shen, Y. Zhu, X. Yang, J. Zong, J. Zhang and C. Li, *New Journal of Chemistry*, 2012, **36**, 97-101.

81.   F. Wang, Z. Gu, W. Lei, W. Wang, X. Xia and Q. Hao, *Sensors and Actuators B: Chemical*, 2014, **190**, 516-522.

82.   J. Gu, X. Zhang, A. Pang and J. Yang, *Nanotechnology*, 2016, **27**, 165704.

83.   L. Wang, Y. Wang, T. Xu, H. Liao, C. Yao, Y. Liu, Z. Li, Z. Chen, D. Pan and L. Sun, *Nature communications*, 2014, **5**, 5357.

84.   S. Zhu, J. Zhang, C. Qiao, S. Tang, Y. Li, W. Yuan, B. Li, L. Tian, F. Liu and R. Hu, *Chemical communications*, 2011, **47**, 6858-6860.

85.   Z. Huang, Y. Shen, Y. Li, W. Zheng, Y. Xue, C. Qin, B. Zhang, J. Hao and W. Feng, *Nanoscale*, 2014, **6**, 13043-13052.

86.   S. Maiti, S. Kundu, C. N. Roy, T. K. Das and A. Saha, *Langmuir*, 2017, **33**, 14634-14642.

87.     M. Li, C. Yu, C. Hu, W. Yang, C. Zhao, S. Wang, M. Zhang, J. Zhao, X. Wang and J. Qiu, *Chemical Engineering Journal*, 2017, **320**, 570-575.

88.     A. Ananthanarayanan, X. Wang, P. Routh, B. Sana, S. Lim, D. H. Kim, K. H. Lim, J. Li and P. Chen, *Advanced Functional Materials*, 2014, **24**, 3021-3026.

89.     H. Huang, S. Yang, Q. Li, Y. Yang, G. Wang, X. You, B. Mao, H. Wang, Y. Ma, P. He, Z. Liu, G. Ding and X. Xie, *Langmuir*, 2018, **34**, 250-258.

90.     L. Tang, R. Ji, X. Cao, J. Lin, H. Jiang, X. Li, K. S. Teng, C. M. Luk, S. Zeng, J. Hao and S. P. Lau, *ACS Nano*, 2012, **6**, 5102-5110.

91.     A. Prasannan and T. Imae, *Industrial & Engineering Chemistry Research*, 2013, **52**, 15673-15678.

92.     L. Lin and S. Zhang, *Chemical Communications*, 2012, **48**, 10177-10179.

93.     P. Tian, L. Tang, K. Teng and S. Lau, *Materials today chemistry*, 2018, **10**, 221-258.

94.     C. Zhang, Y. Cui, L. Song, X. Liu and Z. Hu, *Talanta*, 2016, **150**, 54-60.

95.     S. Li, Y. Li, J. Cao, J. Zhu, L. Fan and X. Li, *Analytical Chemistry*, 2014, **86**, 10201-10207.

96.     X. Li, S. Zhu, B. Xu, K. Ma, J. Zhang, B. Yang and W. Tian, *Nanoscale*, 2013, **5**, 7776-7779.

97.     Q. Lu, C. Wu, D. Liu, H. Wang, W. Su, H. Li, Y. Zhang and S. Yao, *Green Chemistry*, 2017, **19**, 900-904.

98.     Z.-A. Qiao, Y. Wang, Y. Gao, H. Li, T. Dai, Y. Liu and Q. Huo, *Chemical Communications*, 2010, **46**, 8812-8814.

99.     A. P. Litvin, I. V. Martynenko, F. Purcell-Milton, A. V. Baranov, A. V. Fedorov and Y. K. Gun'ko, *Journal of Materials Chemistry A*, 2017, **5**, 13252-13275.

100.    A. M. Smith and S. Nie, *Accounts of Chemical Research*, 2010, **43**, 190-200.

101.    W. C. W. Chan and S. Nie, *Chan, W.C.W. & Nie, S.M. Quantum dot bioconjugates for ultrasensitive nonisotopic detection. Science 281, 2016-2018*, 1998.

102.    A. Smith and S. Nie, *Smith, A. M. & Nie, S. M. Semiconductor nanocrystals: structure, properties, and band gap engineering. Acc. Chem. Res. 43, 190-200*, 2009.

103.    R. C. Somers, M. G. Bawendi and D. G. Nocera, *Chemical Society Reviews*, 2007, **36**, 579-591.

104.    R. Freeman and I. Willner, *Chemical Society Reviews*, 2012, **41**, 4067-4085.

105. R. Koole, E. Groeneveld, D. Vanmaekelbergh, A. Meijerink and C. de Mello Donegá, in *Nanoparticles*, Springer, 2014, pp. 13-51.

106. L. Fan, Y. Hu, X. Wang, L. Zhang, F. Li, D. Han, Z. Li, Q. Zhang, Z. Wang and L. Niu, *Talanta*, 2012, **101**, 192-197.

107. D. Pan, J. Zhang, Z. Li, C. Wu, X. Yan and M. Wu, *Chemical Communications*, 2010, **46**, 3681-3683.

108. C. Hu, Y. Liu, Y. Yang, J. Cui, Z. Huang, Y. Wang, L. Yang, H. Wang, Y. Xiao and J. Rong, *Journal of Materials Chemistry B*, 2013, **1**, 39-42.

109. S. Zhu, Y. Song, X. Zhao, J. Shao, J. Zhang and B. Yang, *Nano Research*, 2015, **8**, 355-381.

110. S. Sangam, A. Gupta, A. Shakeel, R. Bhattacharya, A. K. Sharma, D. Suhag, S. Chakrabarti, S. K. Garg, S. Chattopadhyay and B. Basu, *Green Chemistry*, 2018.

111. P. R. Kharangarh, S. Umapathy and G. Singh, *Applied Surface Science*, 2018, **449**, 363-370.

112. T. N. Singh-Rachford and F. N. Castellano, *Coordination Chemistry Reviews*, 2010, **254**, 2560-2573.

113. Q. Liu, W. Feng, T. Yang, T. Yi and F. Li, *Nature Protocols*, 2013, **8**, 2033-2044.

114. M. A. Sk, A. Ananthanarayanan, L. Huang, K. H. Lim and P. Chen, *Journal of Materials Chemistry C*, 2014, **2**, 6954-6960.

115. R. Ye, Z. Peng, A. Metzger, J. Lin, J. A. Mann, K. Huang, C. Xiang, X. Fan, E. L. G. Samuel, L. B. Alemany, A. A. Martí and J. M. Tour, *ACS Applied Materials & Interfaces*, 2015, **7**, 7041-7048.

116. X. Hai, J. Feng, X. Chen and J. Wang, *Journal of Materials Chemistry B*, 2018, **6**, 3219-3234.

117. F. Zhang, F. Liu, C. Wang, X. Xin, J. Liu, S. Guo and J. Zhang, *ACS applied materials & interfaces*, 2016, **8**, 2104-2110.

118. H. Kalita, D. B. Shinde, V. K. Pillai and M. Aslam, *Applied Physics Letters*, 2013, **102**, 143104.

119. Z. Qian, J. Ma, X. Shan, H. Feng, L. Shao and J. Chen, *Chemistry–A European Journal*, 2014, **20**, 2254-2263.

120.    H. Sun, N. Gao, L. Wu, J. Ren, W. Wei and X. Qu, *Chemistry–A European Journal*, 2013, **19**, 13362-13368.

121.    G. Eda, Y.-Y. Lin, C. Mattevi, H. Yamaguchi, H.-A. Chen, I. S. Chen, C.-W. Chen and M. Chhowalla, *Advanced Materials*, 2010, **22**, 505-509.

122.    Y. Li, X. Liu, J. Wang, H. Liu, S. Li, Y. Hou, W. Wan, W. Xue, N. Ma and J. Z. Zhang, *The Journal of Physical Chemistry C*, 2016, **120**, 26004-26011.

123.    Q. Mei, K. Zhang, G. Guan, B. Liu, S. Wang and Z. Zhang, *Chemical Communications*, 2010, **46**, 7319-7321.

124.    M. H. Jang, H. D. Ha, E. S. Lee, F. Liu, Y. H. Kim, T. S. Seo and Y. H. Cho, *Small*, 2015, **11**, 3773-3781.

125.    M. Li, W. Wu, W. Ren, H.-M. Cheng, N. Tang, W. Zhong and Y. Du, *Applied Physics Letters*, 2012, **101**, 103107.

126.    Y. Li, Y. Zhao, H. Cheng, Y. Hu, G. Shi, L. Dai and L. Qu, *Journal of the American Chemical Society*, 2012, **134**, 15-18.

127.    X. Li, S. P. Lau, L. Tang, R. Ji and P. Yang, *Nanoscale*, 2014, **6**, 5323-5328.

128.    D. Qu, M. Zheng, P. Du, Y. Zhou, L. Zhang, D. Li, H. Tan, Z. Zhao, Z. Xie and Z. Sun, *Nanoscale*, 2013, **5**, 12272-12277.

129.    B. Guo, Q. Liu, E. Chen, H. Zhu, L. Fang and J. R. Gong, *Nano letters*, 2010, **10**, 4975-4980.

130.    Y. Dai, H. Long, X. Wang, Y. Wang, Q. Gu, W. Jiang, Y. Wang, C. Li, T. H. Zeng and Y. Sun, *Particle & Particle Systems Characterization*, 2014, **31**, 597-604.

131.    S. Bian, C. Shen, Y. Qian, J. Liu, F. Xi and X. Dong, *Sensors and Actuators B: Chemical*, 2017, **242**, 231-237.

132.    P. Gao, K. Ding, Y. Wang, K. Ruan, S. Diao, Q. Zhang, B. Sun and J. Jie, *The Journal of Physical Chemistry C*, 2014, **118**, 5164-5171.

133.    Y. Li, S. Li, Y. Wang, J. Wang, H. Liu, X. Liu, L. Wang, X. Liu, W. Xue and N. Ma, *Physical Chemistry Chemical Physics*, 2017, **19**, 11631-11638.

134.    L. Zhang, Z.-Y. Zhang, R.-P. Liang, Y.-H. Li and J.-D. Qiu, *Analytical chemistry*, 2014, **86**, 4423-4430.

135.    P. Gong, J. Wang, W. Sun, D. Wu, Z. Wang, Z. Fan, H. Wang, X. Han and S. Yang, *Nanoscale*, 2014, **6**, 3316-3324.

136. J. Zhao, L. Tang, J. Xiang, R. Ji, J. Yuan, J. Zhao, R. Yu, Y. Tai and L. Song, *Applied Physics Letters*, 2014, **105**, 111116.

137. C. Xia, X. Hai, X.-W. Chen and J.-H. Wang, *Talanta*, 2017, **168**, 269-278.

138. N. Ganesh, W. Zhang, P. C. Mathias, E. Chow, J. Soares, V. Malyarchuk, A. D. Smith and B. T. Cunningham, *Nature Nanotechnology*, 2007, **2**, 515.

139. M. Hernandez-Guerrero and M. H. Stenzel, *Polymer Chemistry*, 2012, **3**, 563-577.

140. J.-H. Song, T. Atay, S. Shi, H. Urabe and A. V. Nurmikko, *Nano letters*, 2005, **5**, 1557-1561.

141. M. T. Zin, K. Leong, N.-Y. Wong, H. Ma, M. Sarikaya and A. K. Jen, *Nanotechnology*, 2008, **20**, 015305.

142. S.-Y. Cho, H.-J. Jeon, H.-W. Yoo, K. M. Cho, W.-B. Jung, J.-S. Kim and H.-T. Jung, *Nano letters*, 2015, **15**, 7273-7280.

143. J. R. Lakowicz, Google Patents, 2010.

144. A. V. Kabashin, P. Evans, S. Pastkovsky, W. Hendren, G. A. Wurtz, R. Atkinson, R. Pollard, V. A. Podolskiy and A. V. Zayats, *Nat Mater*, 2009, **8**, 867-871.

145. C. Yuan, W. Chou, D. Chuu, Y. Chen, C. Lin and W. Chang, *Applied Physics Letters*, 2008, **92**, 183108.

146. P. Lodahl, A. F. Van Driel, I. S. Nikolaev, A. Irman, K. Overgaag, D. Vanmaekelbergh and W. L. Vos, *Nature*, 2004, **430**, 654.

147. X. Su, X. Sun, S. Wu and S. Zhang, *Nanoscale*, 2017, **9**, 7666-7673.

148. C. Vion, C. Barthou, P. Bénalloul, C. Schwob, L. Coolen, A. Gruzintev, G. Emel'chenko, V. Masalov, J.-M. Frigerio and A. Maître, *Journal of Applied Physics*, 2009, **105**, 113120.

149. E. Eftekhari, X. Li, T. H. Kim, Z. Gan, I. S. Cole, D. Zhao, D. Kielpinski, M. Gu and Q. Li, *Scientific reports*, 2015, **5**, 14439.

150. H. Li, J. Wang, F. Liu, Y. Song and R. Wang, *Journal of colloid and interface science*, 2011, **356**, 63-68.

151. C. Barth, S. Roder, D. Brodoceanu, T. Kraus, S. Burger, M. Hammerschmidt, F. Schmidt and C. Becker, 2016.

152. J. Gao, C. Xu, Y. Hu, F. Zhao, C. Shao, Y. Zhao, S. Chen and L. Qu, *Chemistry – An Asian Journal*, 2017, **12**, 1272-1276.

153.    Y. Yue, T.-Y. Liu, H.-W. Li, Z. Liu and Y. Wu, *Nanoscale*, 2012, **4**, 2251-2254.

154.    I. P. Hamilton, B. Li, X. Yan and L.-s. Li, *Nano Letters*, 2011, **11**, 1524-1529.

155.    S. Zhu, Q. Meng, L. Wang, J. Zhang, Y. Song, H. Jin, K. Zhang, H. Sun, H. Wang and B. Yang, *Angewandte Chemie International Edition*, 2013, **52**, 3953-3957.

156.    Z. Zhang, Q. Liu, D. Gao, D. Luo, Y. Niu, J. Yang and Y. Li, *Small*, 2015, **11**, 3000-3005.

157.    S.-T. Yang, X. Wang, H. Wang, F. Lu, P. G. Luo, L. Cao, M. J. Meziani, J.-H. Liu, Y. Liu and M. Chen, *The Journal of Physical Chemistry C*, 2009, **113**, 18110-18114.

158.    H. Sun, L. Wu, W. Wei and X. Qu, *Materials today*, 2013, **16**, 433-442.

159.    M. K. Kumawat, M. Thakur, R. B. Gurung and R. Srivastava, *ACS Sustainable Chemistry & Engineering*, 2017, **5**, 1382-1391.

160.    K. L. Schroeder, R. V. Goreham and T. Nann, *Pharmaceutical Research*, 2016, **33**, 2337-2357.

161.    Y.-L. Su, T.-W. Yu, W.-H. Chiang, H.-C. Chiu, C.-H. Chang, C.-S. Chiang and S.-H. Hu, *Advanced Functional Materials*, 2017, **27**, 1700056.

162.    Z. Zhu, J. Ma, Z. Wang, C. Mu, Z. Fan, L. Du, Y. Bai, L. Fan, H. Yan, D. L. Phillips and S. Yang, *Journal of the American Chemical Society*, 2014, **136**, 3760-3763.

163.    W. Dai, Y. Lei, M. Xu, P. Zhao, Z. Zhang and J. Zhou, *Scientific reports*, 2017, **7**, 12872.

164.    J. Park, J. Moon, C. Kim, J. H. Kang, E. Lim, J. Park, K. J. Lee, S.-H. Yu, J.-H. Seo and J. Lee, *NPG Asia Materials*, 2016, **8**, e272.

165.    C. O. Kim, S. W. Hwang, S. Kim, D. H. Shin, S. S. Kang, J. M. Kim, C. W. Jang, J. H. Kim, K. W. Lee and S.-H. Choi, *Scientific reports*, 2014, **4**, 5603.

166.    L.-s. Li and X. Yan, *The Journal of Physical Chemistry Letters*, 2010, **1**, 2572-2576.

167.    C. Luk, L. Tang, W. Zhang, S. Yu, K. Teng and S. Lau, *Journal of Materials Chemistry*, 2012, **22**, 22378-22381.

168.    M. Wang, Z. Fang, K. Zhang, J. Fang, F. Qin, Z. Zhang, J. Li, Y. Liu and Y. Lai, *Nanoscale*, 2016, **8**, 11398-11402.

169.    Y. Du and S. Guo, *Nanoscale*, 2016, **8**, 2532-2543.

170.    Y. Jing, Y. Zhu, X. Yang, J. Shen and C. Li, *Langmuir*, 2010, **27**, 1175-1180.

171. S. Some, A.-R. Gwon, E. Hwang, G.-h. Bahn, Y. Yoon, Y. Kim, S.-H. Kim, S. Bak, J. Yang and D.-G. Jo, *Scientific reports*, 2014, **4**, 6314.

172. D. Zhang, L. Wen, R. Huang, H. Wang, X. Hu and D. Xing, *Biomaterials*, 2018, **153**, 14-26.

173. L. Xu, W. Mao, J. Huang, S. Li, K. Huang, M. Li, J. Xia and Q. Chen, *Sensors and Actuators B: Chemical*, 2016, **230**, 54-60.

174. X. Zhu, Z. Zhang, Z. Xue, C. Huang, Y. Shan, C. Liu, X. Qin, W. Yang, X. Chen and T. Wang, *Analytical chemistry*, 2017, **89**, 12054-12058.

175. S. Ge, J. He, C. Ma, J. Liu, F. Xi and X. Dong, *Talanta*, 2019, **199**, 581-589.

176. Z. Fan, Y. Li, X. Li, L. Fan, S. Zhou, D. Fang and S. Yang, *Carbon*, 2014, **70**, 149-156.

177. J. Xi, C. Xie, Y. Zhang, L. Wang, J. Xiao, X. Duan, J. Ren, F. Xiao and S. Wang, *ACS applied materials & interfaces*, 2016, **8**, 22563-22573.

178. J. Wang, H. Zhu, Y. Xu, W. Yang, A. Liu, F. Shan, M. Cao and J. Liu, *Sensors and Actuators B: Chemical*, 2015, **220**, 1186-1195.

179. J. Hassanzadeh and A. Khataee, *Talanta*, 2018, **178**, 992-1000.

180. F. Zuo, C. Zhang, H. Zhang, X. Tan, S. Chen and R. Yuan, *Electrochimica Acta*, 2019, **294**, 76-83.

181. J. Zhao, G. Chen, L. Zhu and G. Li, *Electrochemistry Communications*, 2011, **13**, 31-33.

182. C. Ruiz-Palomero, S. Benítez-Martínez, M. L. Soriano and M. Valcárcel, *Analytica chimica acta*, 2017, **974**, 93-99.

183. C. Sahub, T. Tuntulani, T. Nhujak and B. Tomapatanaget, *Sensors and Actuators B: Chemical*, 2018, **258**, 88-97.

184. S. Wang, Y. Zhang, G. Pang, Y. Zhang and S. Guo, *Analytical chemistry*, 2017, **89**, 1704-1709.

185. Z. Qu, W. Na, X. Liu, H. Liu and X. Su, *Analytica chimica acta*, 2018, **997**, 52-59.

186. X. Niu, Y. Zhong, R. Chen, F. Wang, Y. Liu and D. Luo, *Sensors and Actuators B: Chemical*, 2018, **255**, 1577-1581.

187. Z. S. Qian, X. Y. Shan, L. J. Chai, J. R. Chen and H. Feng, *Biosensors and Bioelectronics*, 2015, **68**, 225-231.

188. G. Liu, K. Zhang, K. Ma, A. Care, M. R. Hutchinson and E. M. Goldys, *Nanoscale*, 2017, **9**, 4934-4943.

189. A. Mars, M. Hamami, L. Bechnak, D. Patra and N. Raouafi, *Analytica chimica acta*, 2018, **1036**, 141-146.

190. D. Wang, L. Wang, X. Dong, Z. Shi and J. Jin, *Carbon*, 2012, **50**, 2147-2154.

191. Y. Dong, G. Li, N. Zhou, R. Wang, Y. Chi and G. Chen, *Analytical chemistry*, 2012, **84**, 8378-8382.

192. F. Yang, M. Zhao, B. Zheng, D. Xiao, L. Wu and Y. Guo, *Journal of Materials Chemistry*, 2012, **22**, 25471-25479.

193. H. Li, C. Sun, R. Vijayaraghavan, F. Zhou, X. Zhang and D. R. MacFarlane, *Carbon*, 2016, **104**, 33-39.

194. X. Liu, Y. Li, J. Liang, W. Zhu, J. Xu, R. Su, L. Yuan and C. Sun, *Talanta*, 2016, **160**, 99-105.

195. Y. Wang, K. Lee and J. Irudayaraj, *Chemical Communications*, 2010, **46**, 613-615.

196. S. Song, L. Wang, J. Li, C. Fan and J. Zhao, *TrAC Trends in Analytical Chemistry*, 2008, **27**, 108-117.

197. R. Y. Robati, A. Arab, M. Ramezani, F. A. Langroodi, K. Abnous and S. M. Taghdisi, *Biosensors and Bioelectronics*, 2016, **82**, 162-172.

198. Y. Li, J. Xu, L. Wang, Y. Huang, J. Guo, X. Cao, F. Shen, Y. Luo and C. Sun, *Sensors and Actuators B: Chemical*, 2016, **222**, 815-822.

199. A. V. Lakhin, V. Z. Tarantul and L. V. Gening, *Acta Naturae*, 2013, **5**, 34-43.

200. K. L. Hong and L. J. Sooter, *BioMed Research International*, 2015, **2015**, 31.

201. S. Gao, X. Zheng, B. Jiao and L. Wang, *Analytical and bioanalytical chemistry*, 2016, **408**, 4567-4573.

202. N. Cheng, Y. Song, Q. Fu, D. Du, Y. Luo, Y. Wang, W. Xu and Y. Lin, *Biosensors and Bioelectronics*, 2018, **117**, 75-83.

203. J. Wang, Y. Wu, P. Zhou, W. Yang, H. Tao, S. Qiu and C. Feng, *Analyst*, 2018, **143**, 5151-5160.

204. Y. Wu, L. Liu, S. Zhan, F. Wang and P. Zhou, *Analyst*, 2012, **137**, 4171-4178.

205. J. Dapra, L. H. Lauridsen, A. T. Nielsen and N. Rozlosnik, *Biosensors and Bioelectronics*, 2013, **43**, 315-320.

206.	T. Guo, X. Lin, Y. Liu, J. Deng, P. Qian, Y. Lyu, Z. Zhang and S. Wang, *Sensors and Actuators B: Chemical*, 2018, **262**, 619-624.

207.	M. Liu, Z. Wang, L. Pan, Y. Cui and Y. Liu, *Biosensors and Bioelectronics*, 2015, **69**, 142-147.

208.	Z. Guo, Y. Jia, X. Song, J. Lu, X. Lu, B. Liu, J. Han, Y. Huang, J. Zhang and T. Chen, *Analytical chemistry*, 2018, **90**, 6124-6130.

209.	S. Pang and L. He, *Analytical Methods*, 2016, **8**, 1602-1608.

210.	Y. Liu, Z. Wei, W. Duan, C. Ren, J. Wu, D. Liu and H. Chen, *Dyes and Pigments*, 2018, **149**, 491-497.

211.	H. Wang, X. Huang, G. Wen and Z. Jiang, *Scientific reports*, 2019, **9**, 1-10.

212.	S. Zong, Z. Wang, H. Chen, G. Hu, M. Liu, P. Chen and Y. Cui, *Nanoscale*, 2014, **6**, 1808-1816.

# Chapter 2

---

**Rapid, Acid-free Synthesis of Size Tunable Graphene Quantum Dots for Bioimaging, Sensing of Metal Ions and Fluorescence Enhancement**

## Abstract

Graphene quantum dots (GQDs) are zero-dimensional (0D) materials that exhibit characteristics of both graphene and quantum dots. Herein, we report a rapid, green, one-pot synthesis of size-tunable GQDs from graphene oxide (GO) by the sonochemical method with microwave heating at a low temperature of 90 °C. The GQDs were synthesized by oxidative cutting of GO using $KMnO_4$ as an oxidizing agent within a short span of time (30 min) in an acid-free condition. The synthesized GQDs were of high quality and exhibited good quantum yield (23.8 %), high product yield (>75 %) and lower cytotoxicity (tested up to 1000 μg/mL). Furthermore, the as-synthesized GQDs were demonstrated as excellent fluorescent probes for bioimaging and label-free sensing of $Fe^{3+}$ ions with a detection limit as low as 10 μM. In order to further enhance the fluorescence emission of GQDs so as to meet the application requirements such as higher sensitivity and lower limits of detection (LOD), we adopted two methodologies, namely breath figure technique and photonic bandgap effect. The ordered assemblies of GQDs on microporous polystyrene (PS) films fabricated by breath figure method could exhibit a 77-fold enhancement of fluorescence emission which was used as a sensing platform for $Fe^{3+}$ ions with LOD as low as 80 nM. In addition, we achieved over 102-fold enhancement of fluorescent emission of GQDs using well-ordered colloidal photonic crystals (CPC) of polystyrene microspheres. Further, the CPC-based GQD platform was used to detect $Fe^{3+}$ ions which exhibited much lower LOD as 30 nM.
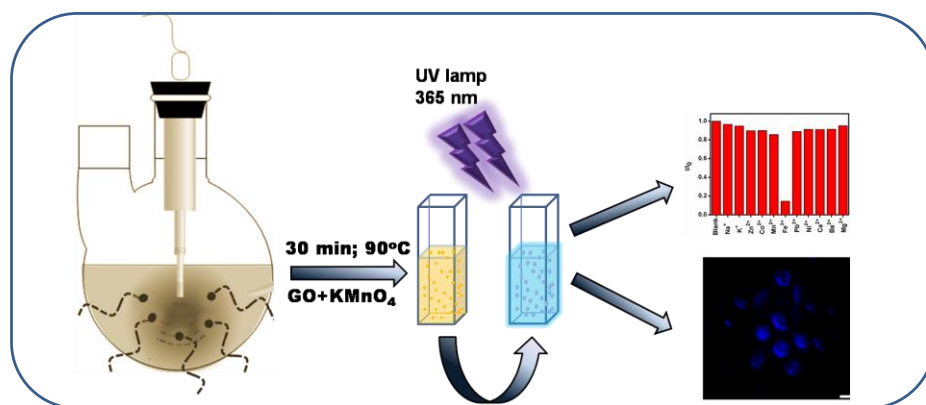
## 2.1. Introduction

Graphene, being a sheet of two-dimensional monolayer of sp[2] bonded carbon atoms, does not show optical photoluminescence due to the absence of bandgap. This, in turn, limits its application in optical sensing, optical imaging, optoelectronics etc. However, by converting this two-dimensional (2D) graphene sheets into zero-dimensional (0D) graphene quantum dots (GQDs), its bandgap can be tuned by quantum confinement and edge effect which unlocked a large window of applications.[1] GQDs consist of an atomic layer of nano-sized graphite which show excellent properties of graphene-like large surface area, high carrier transport, superior mechanical flexibility, and excellent thermal and chemical stability. When compared to widely explored typical semiconductor quantum dots (CdSe, CdTe, PbTe), GQDs show superior properties such as high photostability, aqueous dispersibility, biocompatibility, low cytotoxicity, low cost, etc.[2-5] The unique properties of GQDs find applications in bio-imaging,[6-8] optical sensing,[9-13]    photovoltaics,[14-16]    light-emitting    diodes,[17]    photocatalysis,[18] photodetectors[19] and so forth. Irrespective of the emerging reports on GQDs over the past five years, their wide applicability is limited due to the usage of malicious corrosive chemicals and prolonged reaction time for synthesis.

GQDs have been synthesized from different carbon-based materials like fullerene[20], graphene oxide,[21-25] graphite rods,[26] carbon nanotube,[27] glucose,[1, 28] carbon fibres,[6] coal,[29] etc. Several reports exist describing the synthesis of GQDs using various approaches such as hydrothermal, solvothermal, sonochemical, corrosive chemical oxidation, high-resolution electron beam cutting, etc. Various synthesis methodologies of GQDs are discussed in Chapter 1. Such synthesis approaches involve the use of malevolent harsh chemicals, extreme reaction conditions (high temperature and pressure) and prolonged reaction time. Thus, we adopted an alternative, facile and rapid synthetic approach, which is termed as sonochemical method with microwave heating (MS). Indeed, microwave-assisted synthesis offers several advantages when they are used in combination with other approaches.  The utilization of microwave-assisted method is quite remarkable for rapid, one-step synthesis of nanomaterials that have high energy of activation to achieve high product yield.[30, 31] Similarly, ultrasound-

induced unique morphology formation has been demonstrated for the synthesis of various nanostructures with outstanding properties.[32] Therefore, a synergistic effect of microwave and ultrasonication treatments could be an efficient approach for the synthesis of nanomaterials.

From recent reports, we could see that the major issue of GQDs synthesis is longer reaction time, low quantum yield and production yield, which can be improved by means of various synthesis methods. Zhu *et al*. reported a one-step ultrasonic synthesis of GQDs with a relatively higher quantum yield of 27.8 % however involved a 4h synthesis.[32] Li *et al.* reported microwave-assisted synthesis of greenish-yellow luminescent GQDs that involved use of strong acids and a quantum yield up to 11.7 %.[31] In another report, Wang *et al*. prepared white-light-emitting GQDs by a two-step microwave-assisted hydrothermal method where corrosive acids were used as an oxidizing agent and a reaction time of 14 h.[30] Shin *et al*. obtained GQDs with a relatively poor quantum yield of 9.0 % synthesized from graphite using high power microwave irradiation (600 W) in the presence of sulphuric acid.[33] In another work Lin *et al.* prepared water-soluble GQDs with only 9.9 wt % product yield from graphite flakes using a potassium-intercalation method.[34] Thus, a rapid, environmentally benign method of synthesis with better quantum yield, product yield, aqueous dispersibility and low cytotoxicity is highly required for futuristic applications of GQDs.

In this chapter, a facile, rapid, one-step and acid-free synthetic route using microwave-assisted sonochemical method for the synthesis of high-quality GQDs within a short span of time (30 min) is discussed. Typically, synthesis of GQDs from graphene oxide involves a tedious procedure that uses harsh chemicals (strong acids, organic solvents), elevated temperature and prolonged reaction time. However, our synthetic approach employs $KMnO_4$ for the oxidative cutting of GO in an aqueous medium with the simultaneous treatment of both ultrasound and microwave irradiations **(Scheme 2.1).** The as-synthesized GQDs exhibited good quantum yield, high product yield, lower cytotoxicity and also amicability of GQDs as a fluorescent probe in bioimaging applications were explored. Till date, not many reports exist where green synthesis of GQDs with cell viability was demonstrated for higher concentrations.[35-37] Further, the GQDs were used for the sensitive and label-free detection of metal ions ($Fe^{3+}$ ions) with

a detection limit as low as 20 μM. This study demonstrates the significant potential of the synthesized GQDs in metal ion sensing and bioimaging applications.
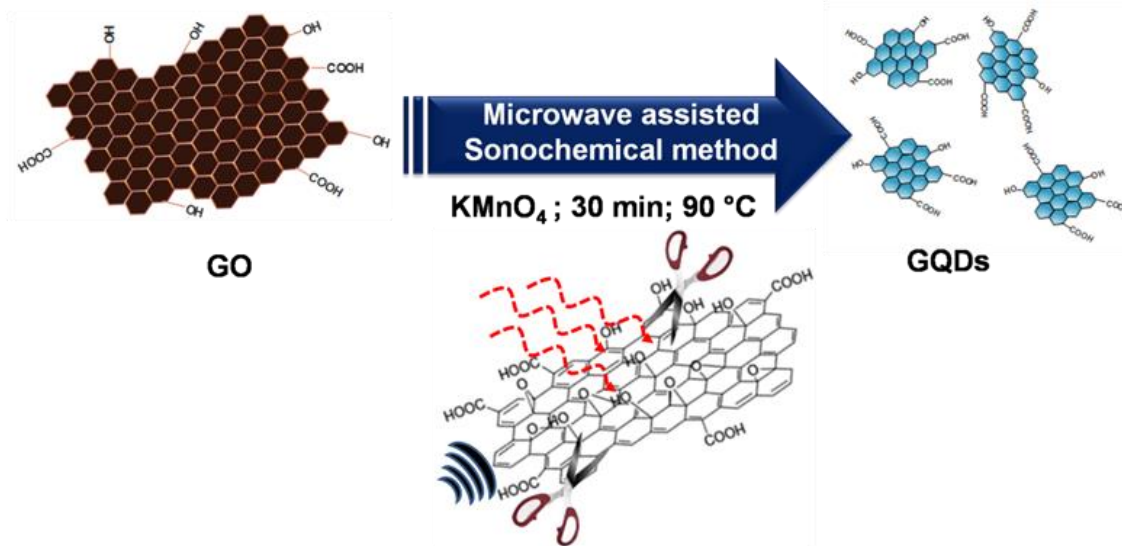


**Scheme 2.1:** Schematic illustration for the synthesis of GQDs by the oxidative cleavage of GO using KMnO$_4$ by microwave assisted sonochemical method.

Even though GQDs have many unique optical properties like broad absorption spectrum, narrow size-tunable emission spectrum and high photostability, some limitations have yet to be addressed.[38] Recent researches are going on to enhance its fluorescent properties in order to meet the application requirements such as increased sensitivity and lower limits of detection (LOD). Techniques that can more efficiently excite and extract the light emitted by GQDs could, therefore, lead to fluorescence enhancement and thus lowering the detection limits towards various analytes in sensing applications.[39] Well-ordered assemblies of quantum dots have the potential to be used in various applications where a patterned surface can provide an advantage over flat films of the same material.[40] Therefore, an attempt has been made to further enhance the fluorescence emission of GQDs by utilizing patterned surfaces fabricated by two methodologies, namely breath figure technique and photonic bandgap effect.

Breath figure (BF) method is a soft templating method used for the fabrication of ordered porous film with a controllable pore size.[41] This type of patterning is an example of a self-assembly process that forms honeycomb-structured films. The films consist of

micropores arranged in honeycomb morphology. The BF method has become a flexible and practical technique for the preparation of micropatterns and porous materials. When compared to other lithographic techniques BF method is inexpensive, rapid and can be easily implemented on a variety of surfaces.[42] Here, the water droplet templating BF method has been employed for GQD assembly. The ordered assemblies of GQDs on microporous polystyrene (PS) films fabricated by BF method could exhibit 77-fold enhancement of fluorescence emission which was used as a sensing platform for $Fe^{3+}$ ions with LOD as low as 80 nM.

Besides this approach, fluorescent signal enhancement on colloidal photonic crystals (CPCs) has also emerged as a new pathway because of its low cost and easy fabrication.[43, 44] Self-assembled CPCs are well-ordered periodic constructions of organic/inorganic monodispersed microspheres and can provide brilliant structural colour due to Bragg diffraction.[45] CPC has a periodic arrangement of colloidal microspheres and air voids[46] that modulates a refractive index in CPCs inhibiting a spectral range of electromagnetic waves, *viz*. a photonic bandgap (PBG) or photonic stopband. Slow photons at the edges of the PBG can control fluorescence by overlapping the PBG with the excitation or emission of fluorophores.[47] CPCs can either inhibit or enhance emission, depending on the fluorescence emission maxima and PBG minima.[48] Thus, CPCs can provide an excellent fluorescence enhancement by tuning their own leaky eigenmodes with either the fluorophore excitation or emission wavelengths.[47] Herein, we demonstrated 102-fold enhancement of fluorescent emission of GQDs on polystyrene-based CPCs. Further, the CPC based enhanced GQD platform was used for the sensitive detection of $Fe^{3+}$ ions with much lower LOD as 30 nM.

## 2.2. Experimental

### 2.2.1. Materials

Graphite (<150 μm), sodium nitrate, hydrogen peroxide, quinine sulphate, sulphuric acid, styrene, chloroform and polystyrene were purchased from Sigma-Aldrich. Potassium permanganate was purchased from SD Fine-Chemicals Limited. Ultrapure deionized water (18.2 MΩ cm, 25 °C, Milli-Q D3, Merck, Germany) was used in all the experiments.

## 2.2.2. Synthesis of graphene oxide

Graphene oxide (GO) was synthesised by Hummers method. 2 g of graphite was added to ice-cold (0 °C) concentrated solutions of $H_2SO_4$ and $NaNO_3$ (4 g) in a 500 ml flask with vigorous stirring by keeping the temperature of the mixture below 10 °C The reaction mixture was stirred at 35 °C for 2 h until it becomes pasty brown and was then diluted with 100 ml deionised water in an ice bath. Again, it is stirred for 30 min and $H_2O_2$ (20 ml, 30 wt %) was added slowly to the mixture to reduce the residual $KMnO_4$ after which the colour of the mixture changes to brilliant yellow. The sample was then filtered and washed with 800 ml 5 % HCl to remove the metal ions followed by the addition of an excess of deionised water to remove the acid. Later, the solution was centrifuged, dried at 60 °C and used for further characterizations.

## 2.2.3. Synthesis of GQDs

GQDs were prepared from GO using $KMnO_4$ as an oxidizing agent in 30 min by microwave-assisted sonochemical method keeping the reaction temperature constant at 90 °C. Briefly 1 mg/ml GO and 1 M $KMnO_4$ were mixed in 1:1 ratio in a RB flask to form a homogeneous mixture. This mixture was treated under microwave-irradiation along with ultrasonication in a microwave reactor (SienoUWave 1000.uv.us) at 90 °C operating at different microwave powers of 100 W, 200 W, 300 W, and 400 W for 30 min. After this treatment, the mixture was centrifuged at 3000 rpm for 10 min to remove the unreacted GO. The supernatant containing GQD was collected after centrifugation. The supernatant solution was then filtered through a 0.45 μm polytetrafluoroethylene membrane and the filtrate was dialysed in 1,000 Da dialysis bag. After purification, the solvent was evaporated to obtain solid GQDs.

## 2.2.4. Characterization

Scanning electron microscope (SEM) micrographs were acquired using EVO 18 special edition scanning electron microscope (Carl Zeiss, Germany) operated at 20 kV acceleration voltage. The size and morphology of GQDs were observed through transmission electron microscope (TEM) operated at an accelerating voltage of 300 kV. High-resolution-TEM (HR-TEM) images were performed on FEI Tecnai 30 G2S-

TWIN transmission electron microscope. The HR-TEM images were further analysed with Gatan Digital Micrograph software. Atomic force microscopy (AFM) imaging was performed in air at ambient temperature (22 ±2 °C) using MultiMode 8 AFM equipped with NanoScope V controller (Bruker, Santa Barbara, CA, USA). Si cantilevers (NSG 01, NT-MDT) with a typical radius of curvature of approximately 10 nm were used. The force constants of AFM probe used was in the range of 2.5-10 N/m and with a resonance frequency in the range of 120-180 kHz. Raw data were processed offline using Bruker's NanoScope Analysis software. The FT-IR spectra were measured with a Perkin Elmer Series Spectrum Two FT-IR spectrometer over the wavenumber range 4000-500 cm$^{-1}$. Wide-angle X-ray scattering measurements were carried out on XEUSS SAXS/WAXS system using the Genisxmicro source from Xenocs operated at 50 kV and 0.6 mA. The Cu K$_\alpha$ radiation ($\lambda$= 1.54 Å) was collimated with FOX2D mirror and two pairs of scattering less slits from Xenocs. The 2D-patterns were recorded on a Mar345 image plate and processed using Fit2D software. The UV-Visible (UV-Vis) absorption spectra of the GQDs were measured using a spectrophotometer (SHIMADZU UV-2401 PC, Shimadzu, Japan) employing a 1 cm path length quartz cell at room temperature. The photoluminescence (PL) spectra of GQDs were recorded on a Spex-Fluorolog FL22 spectrofluorimeter equipped with a double grating 0.22 m Spex 1680 monochromator and a 450 W Xe lamp as the excitation source. Raman spectra were measured using WI-Tec Raman microscope (Witec Inc. Germany, alpha 300R) with a laser beam directed to the sample through 60x water immersion objective and a Peltier cooled CCD detector. Samples were excited with a 632.8 nm excitation wavelength laser and Stokes-shifted Raman spectra were collected in the range of 0 to 3000 cm$^{-1}$ with 1 cm$^{-1}$ resolution. Quantum yield was measured using quinine sulphate in 0.05 M sulphuric acid solution as a standard. Fluorescence lifetime experiments were performed using Delta Flex modular time-correlated single photon counting (TCSPC) spectrometer system employing the 330 nm nanoLED as excitation source and PPD 850 detector. Decay in the fluorescence intensity (I) with time (t) was fitted by three exponential functions. The structural colors of the photonic crystal were recorded using Nikon D4 digital camera. The chemical state and surface composition of the samples was studied using X-ray photoelectron spectroscopy (XPS) (PHI 5000 Versa Probe II ULVAC-PHI Inc., USA) equipped with micro-focused (200

μm, 15 KV) monochromatic Al-Kα X-ray source (hν = 1486.6 eV). Survey scans were recorded with an X-ray source power of 50 W and pass energy of 187.85 eV. Narrow scans (high-resolution spectra) of the major elements were recorded at 46.95 eV pass energy. XPS raw data was analysed using PHI's Multipak software. The binding energy was calibrated with respect to C1s peak at 284.6 eV. The quality of the fits was checked by examining the χ2 value. All experiments were carried out in triplicates.

### 2.2.5. Maintenance of cell lines

The cell line used in the present study is the human cervical cancer cell line, HeLa cells,* obtained from National Centre for Cell Science, Pune, India. For maintenance of cell lines, Dulbeccos Modified Eagle's Medium (DMEM) (Sigma) containing 10 % fetal bovine serum (FBS) (Gibco), antibiotics (100U/mL Penicillin and 100 μg/mL streptomycin) and amphotericin (0.25 μg/mL) (HiMedia) were employed. The cells were maintained in $CO_2$ incubators at 37 °C with 5 % $CO_2$ in air and 99 % humidity. Passaging of cells when confluent was carried out using 0.25 % trypsin and 0.02 % EDTA (HiMedia) in phosphate-buffered saline (PBS). Experiments were carried out after 36 h of seeding the cells at appropriate density in suitable well plates.

### 2.2.6. Assessment of cell viability

Cell viability after incubating HeLa cells with GQDs was determined by MTT [3-(4,5-dimethylthiazol-2-yl)-2,5-diphenyltetrazolium bromide] assay. It is a colorimetric assay based on the ability of live, but not dead cells, to reduce the tetrazolium component of MTT into purple coloured formazan crystals. The cells were spread in 96-well plates at $5 \times 10^3$ cells/well. After 36 h of seeding, the cells were incubated with different concentrations of GQDs (25, 50, 100, 250, 500 and 1000 μg/mL) for 24 h. Subsequently, the cells were exposed to MTT at a concentration of 50 μg/well for 2.5 to 3 h at 37 °C in $CO_2$ incubator. The working solution of MTT was prepared in Hanks balanced salt solution (HBSS). After viewing formazan crystals under the microscope, crystals were solubilised by treating the cells with DMSO: isopropanol solvent mixture at a ratio of 1:1

---

* HeLa is an immortal cell line used in scientific research. It is the oldest and most commonly used human cell line which was derived from cervical cancer cells.

for 20 min at 37 °C. The percentage of cell viability was determined by recording the optical absorbance at 570 nm using a microplate reader (Synergy-4 Multimode reader, Biotek, Winooski, VT) relative to the non-treated cells. Cell viability was calculated using the following equation:

$$\text{Cell viability \%} = \frac{\text{Int}_{\text{GQDs}}}{\text{Int}_{\text{control}}} \times 100 \text{-----------------------(2.1)}$$

where, $\text{Int}_{\text{GQDs}}$ is the OD value of the cells incubated with different concentration of GQDs and $\text{Int}_{\text{control}}$ is the OD value of the cells incubated with the culture medium alone. Cell viability of control cells were kept as 100 %.

## 2.2.7. Cellular uptake of GQDs and in vitro bioimaging

The cellular uptake studies of the GQDs were executed by fluorescence imaging of HeLa cells. The cells were seeded at a density of $5 \times 10^3$ cells/well of 96 well black plates (BD Biosciences, USA) for the purpose. After 36 h of seeding, the cells were incubated with GQDs (25 µg/mL) in HBSS for 4 h. 25µg/mL was chosen for cellular uptake studies as at this concentration maximum cell viability was observed. Subsequently, cells were washed thrice with HBSS to remove the unbound particles. Images of the cells were collected by high-content spinning disk facility (BD Pathway 855; BD Biosciences) using AttoVision 1.5.3 software. The images were taken at 40x magnification, using A360/10 excitation filter and 435 LP emission filter.

## 2.2.8. Sensing of $Fe^{3+}$ ions using GQDs

The sensitive detection of $Fe^{3+}$ ions was done in aqueous medium at room temperature. To study the sensitivity towards $Fe^{3+}$, the fluorescence emission spectrum of GQDs (0.05 mg/mL) was recorded upon the excitation wavelength of 350 nm. Then, a series of concentrations of $Fe^{3+}$ (0-800 µM) was freshly prepared and were added into the aqueous solution containing the same amount of GQDs (0.05 mg/mL) and the corresponding PL spectra were recorded under the same excitation wavelength. The selectivity of $Fe^{3+}$ sensing was evaluated by adding other common metal ions ($Na^+$, $K^+$, $Co^{2+}$, $Mn^{2+}$, $Zn^{2+}$, $Ca^{2+}$, $Ba^{2+}$, $Mg^{2+}$, $Pb^{2+}$, $Ni^{2+}$) of same concentration (100 µM) to GQD solution (0.05 mg/mL) and the PL emission spectra were recorded under identical conditions.

**2.2.9. Fabrication of fluorescent PS-GQD film by BF method**

In BF method **(Figure 2.1)**, 40 μL of polymer solution (3 wt % of PS in chloroform) is casted on to a glass substrate and allowed to evaporate in a humid environment (85 % relative humidity (RH) at 25 °C). After the complete evaporation of solvent and condensed water droplets, microporous PS film with the ordered hexagonal pattern was formed. A short time (15 sec) oxidative plasma treatment of these films was carried out in order to modify the PS surface wettable by water. The obtained film is then vertically dipped in GQD solution (0.05 mg/mL) for 2 h followed by drying under vacuum to obtain PS-GQD film where GQDs are particularly deposited inside this pore structure of PS film.
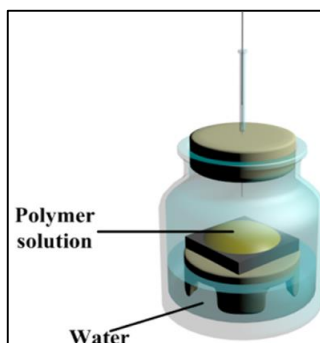


**Figure 2.1.** Experimental set-up for Breath figure method.[42]

**2.2.10. Fluorescence enhancement study and sensing of $Fe^{3+}$ions using PS-GQD films**

For the fluorescence enhancement study, a control sample (PS-GQD control) was prepared by drop-casting PS solution (3 wt % of PS in chloroform) on glass coverslips followed by dipping in GQD solution (0.05 mg/mL). The obtained film was then dried under vacuum and the PL spectra of both PS-GQD and PS-GQD control samples were taken under the excitation wavelength of 350 nm. The sensitive detection of $Fe^{3+}$ using the fabricated PS-GQD film was done at room temperature. To study the sensitivity towards $Fe^{3+}$, PL spectra of PS-GQD films with different concentrations of $Fe^{3+}$ (0-900 nM) was recorded upon the same excitation wavelength.

**2.2.11. Fabrication of fluorescent CPC-GQD films**

The CPCs were prepared via evaporation induced vertical deposition method at

an angle of 45° on glass coverslips.[45] The stopbands of the CPCs were tuned by using different sized polystyrene microspheres as the self-assembly units. As a result, CPCs with different stopbands were obtained, which were labelled as $CPC_C$ (Colourless CPC), $CPC_B$ (Blue CPC) and $CPC_G$ (Green CPC). Equal volumes (20 µL) of 0.05 mg/mL GQD was drop-casted on to each CPC followed by drying under vacuum to prepare different CPC-GQD films viz., $CPC_C$-GQD, $CPC_B$-GQD and $CPC_G$-GQD films. Similarly, control samples were prepared by using CPC films heated at 120 °C for 2 h to obtain planar films on glass substrates. 20 µL of 0.05 mg/mL GQD was drop casted onto the control sample and dried under vacuum in a desiccator.

### 2.2.12. Fluorescence enhancement study and sensing of $Fe^{3+}$ ions using CPC-GQD films

For the fluorescence enhancement study, PL spectra of $CPC_C$-GQD, $CPC_B$-GQD, $CPC_G$-GQD and control films were recorded upon the excitation wavelength of 350 nm. The sensitive detection of $Fe^{3+}$ using the fabricated $CPC_C$-GQD film was carried out by taking the PL spectra of the films with different concentrations of $Fe^{3+}$ (0-390 nM) upon the same excitation wavelength.

## 2.3. Results and Discussion

### 2.3.1. Synthesis and morphological characterizations of GQDs

GQDs were synthesized by oxidative cutting of GO using $KMnO_4$ as oxidizing agent via one-step sonochemical method with microwave heating within 30 min at different microwave powers keeping reaction temperature constant at 90 °C. Samples were synthesized using different microwave powers of 100 W, 200 W, 300 W and 400 W and labelled as GQD 1, GQD 2, GQD 3 and GQD 4, respectively. The product yield of GQD 1-4 were calculated and obtained in the range of 75-81 %. The morphology and nanostructure of GQDs were characterized by TEM and AFM. **Figure 2.2 (a-d)** showed the TEM images of as-synthesized GQDs with relatively uniform shape and size distribution. The corresponding histograms shown in the inset of **Figure 2.2 (a-d)** revealed that GQD 1, GQD 2, GQD 3 and GQD 4 have an average lateral diameter of 5 nm, 4 nm, 3 nm and 2 nm, respectively. The HR-TEM images **[Figure 2.2 (e-h)]** were also

found to be in agreement with the corresponding histograms. The Fast Fourier transform (FFT) patterns of GQD samples were presented as inset figures of corresponding HR-TEM images. From HR-TEM images of single GQD **[Figure 2.2 (i-l)]**, two types of lattice parameters, 0.210 nm and 0.242 nm corresponding to the hexagonal lattice plane spacing of $d_{1100}$ and $d_{1120,}$ respectively were obtained. The AFM image **(Figure 2.3a)** showed the typical topographic morphology of GQDs and **Figure 2.3b** showed the corresponding three-dimensional image. The section profile **(Figure 2.3c)** revealed an average height of 2.5 nm which corresponds to approximately 2-3 layers of graphene.
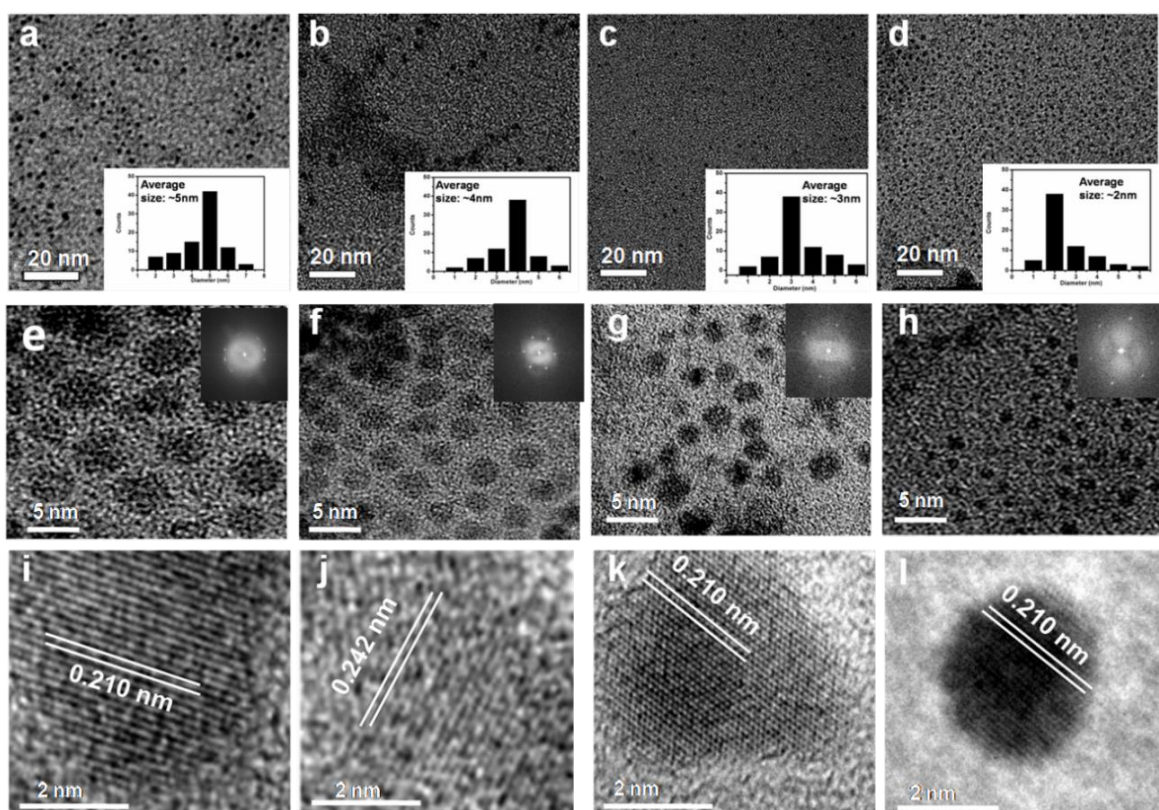


**Figure 2.2.** TEM images of (a) GQD 1, (b) GQD 2, (c) GQD 3 and (d) GQD 4 samples over large area (Scale bar 20 nm) and the inset histograms show size distribution of corresponding GQDs. HR-TEM images of (e) GQD 1, (f) GQD 2, (g) GQD 3 and (h) GQD 4 samples (Scale bar 5 nm) and corresponding FFT patterns of GQDs were showed as inset images. HR-TEM images of single GQD show the lattice fringes of (i) GQD 1, (j) GQD 2, (k) GQD 3 and (l) GQD 4 samples (Scale bar 2 nm).
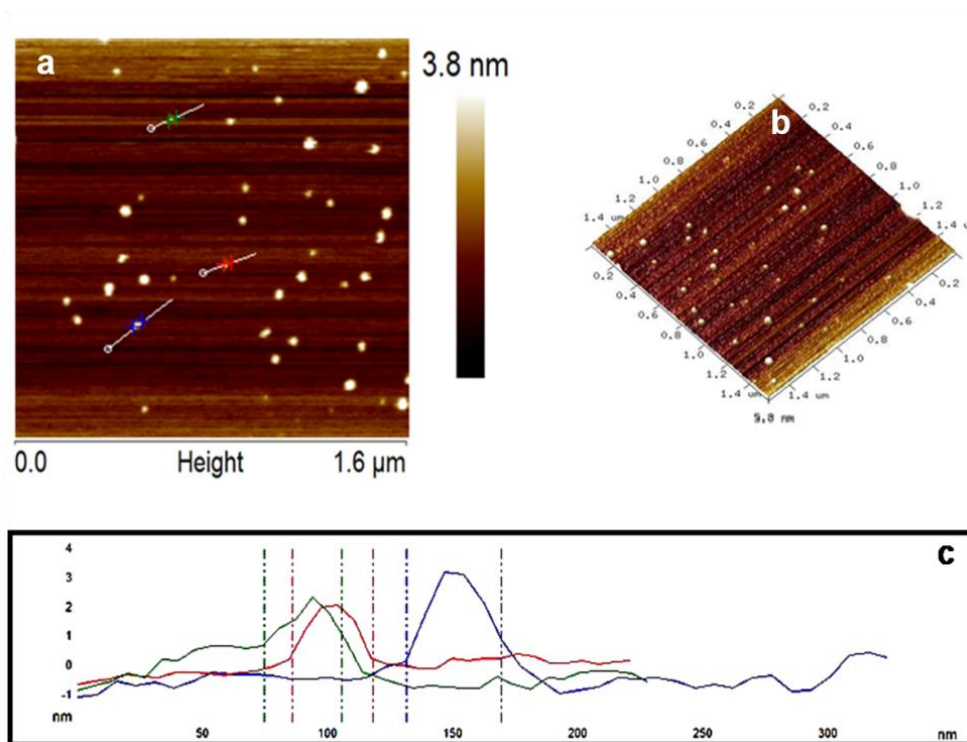
**Figure 2.3.** (a) AFM image of GQDs (b) the corresponding three-dimensional image (c) Height profile of GQDs.

### 2.3.2. FT-IR spectroscopic analysis of GQDs

The surface functionalities of GO and GQDs were studied using FT-IR spectroscopy. From the FT-IR spectra **(Figure 2.4)** it could be inferred that the GQDs exhibited characteristic peak of the carboxyl group at 1386 cm$^{-1}$, carbonyl group at 1700 cm$^{-1}$ and broad absorption peak at 3431 cm$^{-1}$ due to bending vibrations of O-H bonds. Peaks at 2920 cm$^{-1}$and 2850 cm$^{-1}$ are associated with the stretching vibrations of C-H bonds and the peak at 1615 cm$^{-1}$ is due to C=C bonds of benzene ring vibrations. The peaks at 1258 cm$^{-1}$ and 1035 cm$^{-1}$ are attributed to the vibrational absorption bands of C-O-C and C-O stretching vibrations in epoxides respectively. It was observed that the presence of carboxylic, hydroxyl and carbonyl groups render GQDs easy dispersibility in water and high stability.
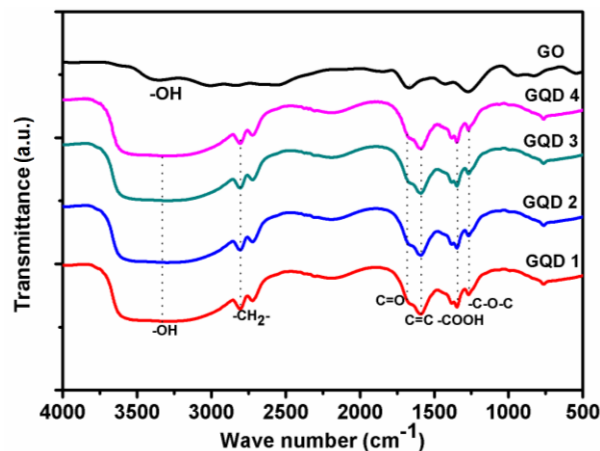
**Figure 2.4** FT-IR spectra of GO and GQD samples.

### 2.3.3. UV-Visible and PL spectroscopic analysis of GQDs

The optical properties of GQDs were studied using UV-Visible and PL spectroscopy. **Figure 2.5a** shows UV-Visible spectra of GQD samples of different sizes synthesized namely, GQD 1, GQD 2, GQD 3 and GQD 4. A distinct broad absorption peak at 350 nm and a strong absorption below 300 nm were observed from the spectra, which are attributed to the n-π* transition and π-π* transition of aromatic sp$^2$ domains, respectively. Additionally, a slight shift towards blue region from 360 to 330 nm was observed as the size of GQDs decreased. This result indicates that the size of GQDs can significantly affect the absorption properties of GQDs. The inset of **Figure 2.5a** shows the photographs of GQDs of different sizes irradiated under 365 nm UV light and GQD 4 sample under daylight. **Figure 2.5b** shows the corresponding PL spectra of the as-synthesized GQDs. The different emission colour may indicate the size-dependent nature of GQDs. The emission maxima of GQD 1, GQD 2, GQD 3 and GQD 4 solutions were at 510 nm, 480 nm, 460 nm and 430 nm, respectively. Excitation dependent emission properties of GQDs were also studied. GQD displayed excitation dependent emission and when the excitation wavelength is varied from 340 to 420 nm, a redshift was observed with a remarkable decrease in PL intensity as shown in **Figure 2.5c.** GQDs usually have quantum confinement effect *i.e.*, it has a size dependent effect on their PL properties. Here the quantum confinement effect was confirmed by the PL spectra **(Figure 2.5b)** and HR-TEM images **(Figure 2.2 e-h)** *i.e.*, smaller sized GQD samples lead to blue shift in the emission.
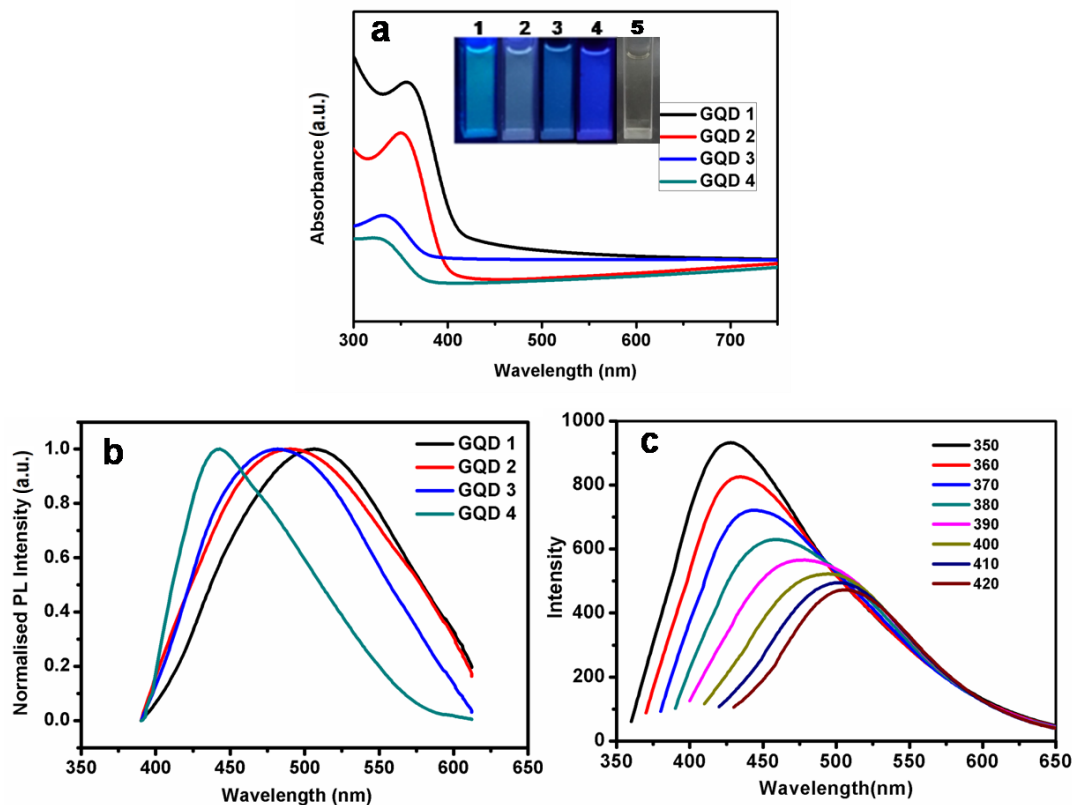
**Figure 2.5.** (a) UV-Vis absorption spectra of GQD 1, GQD 2, GQD 3 and GQD 4 samples. The inset of figure (a) shows photographs of the corresponding GQDs irradiated under 365 nm UV light and GQD 4 under daylight (b) PL spectra of GQD samples excited at 350 nm (c) PL spectra of GQD 4 sample for different excitation wavelengths from 350 nm to 420 nm.

### 2.3.4. Measurement of quantum yield of GQDs

The quantum yield of GQDs was calculated according to the equation number 2.2 [49]:

$$\Phi = \Phi_r \times (I / I_r) \times (A_r / A) \times (n^2 / n_r^2) \text{ ------------------(2.2)}$$

Where $\Phi$ is the quantum yield, A is the optical density, I is the measured integrated emission intensity and n is the refractive index of the solvent (1.33 for water). The subscript "r" refers to the reference molecule with known quantum yield. To minimize reabsorption effects, absorbencies were kept under 0.1 at the excitation wavelength (350 nm). Further, the quantum yield was estimated using quinine sulphate in 0.05 M sulphuric acid solution as the reference **(Table 2.1)**. It could be observed that the maximum quantum yield of 23.8 % was obtained for GQD 4 sample. Among the GQDs

synthesized, GQD 4 was selected for further studies owing to its smaller size and higher quantum yield.

**Table 2.1.** Calculation of quantum yield of GQDs

| Sample | Integrated emission intensity | Abs at 350 nm wavelength | Refractive index of the solvent | Quantum Yield (%) |
|---|---|---|---|---|
| Quinine sulphate | $2.23 \times 10^9$ | 0.1 | 1.33 | 54.6 |
| GQD 1 | $3.74 \times 10^8$ | 0.1 | 1.33 | 9.2 |
| GQD 2 | $4.67 \times 10^8$ | 0.1 | 1.33 | 11.3 |
| GQD 3 | $7.05 \times 10^8$ | 0.1 | 1.33 | 17.2 |
| GQD 4 | $8.95 \times 10^8$ | 0.1 | 1.33 | 23.8 |

### 2.3.5. XPS analysis of GQDs

Among the GQDs synthesized, GQD 4 was selected for further studies owing to its smaller size and higher quantum yield. XPS measurements were carried out to investigate the chemical compositions of GO and GQD 4 samples. The survey spectra **[Figure 2.6(a, b)]** clearly showed C 1s and O 1s peaks at ~284.6 and ~533 eV, respectively indicating carbon and oxygen are major elements present in GO and GQD 4 samples. Further, the quantitative analysis of elemental compositions was estimated from the survey spectra **(Table 2.2)**. A comparison of the high-resolution spectra of C1s revealed an obvious change in the carbon chemical environments from GO to GQD. It is known that GQDs are merited with excellent stability and hydrophilicity due to the presence of abundant hydroxyl and carboxylic groups on their surface and edges.[16] This was evident by C1s spectra, which confirmed that the synthesized GQDs were decorated with hydroxyl, carbonyl and carboxylic acid functionalities **(Figure 2.7b).** Moreover, when compared to the C 1s high-resolution spectrum of GO **(Figure 2.7a)**, the atomic % of -COOH functionality was found to be increased in GQD sample which indicates that strong oxidation has occurred.
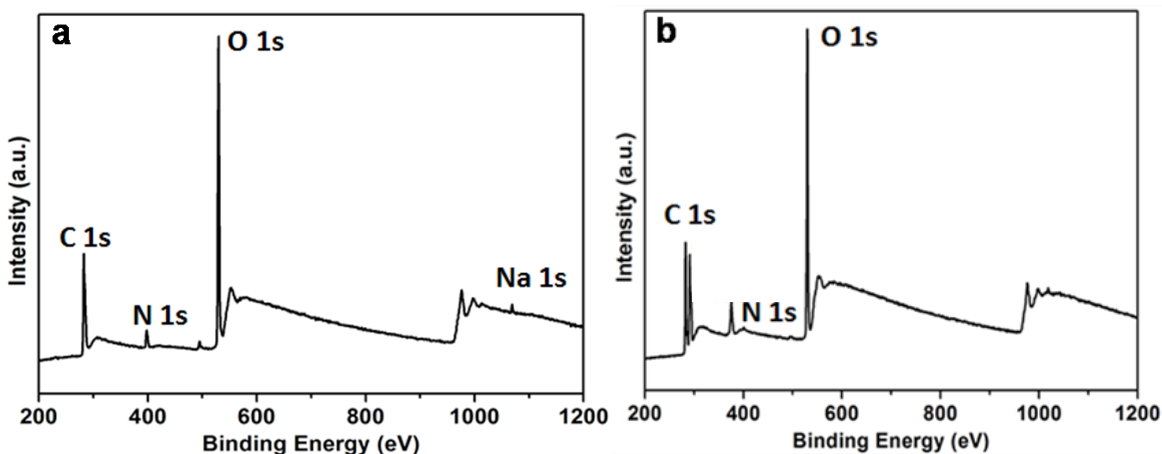
**Figure 2.6**. XPS survey spectra of (a) GO and (b) GQD 4.

**Table 2.2.** Atomic percentage compositions of C and O in GO and GQD 4.

| Elements | C 1s (At.%) | O 1s (At.%) |
|----------|-------------|-------------|
| GO | 68.4 | 30.2 |
| GQDs | 54.8 | 33.5 |
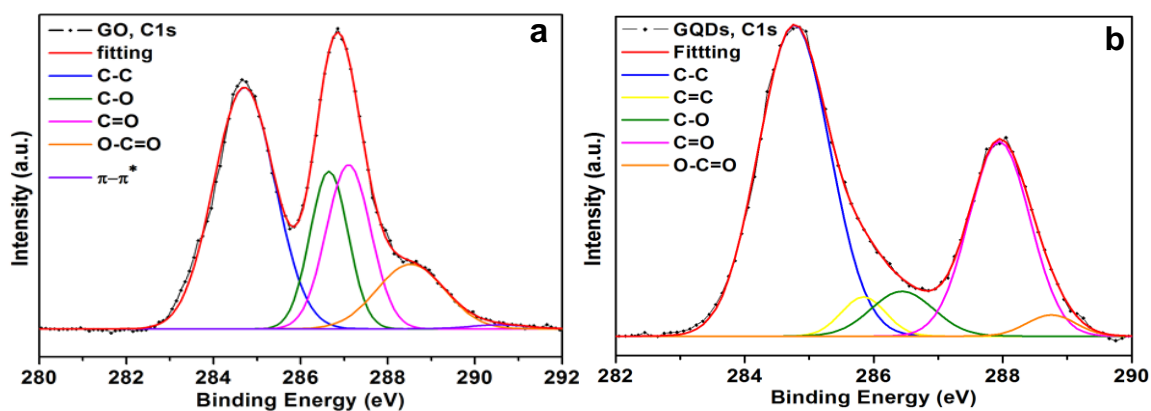
**Figure 2.7**. C1s high resolution XPS spectra of (a) GO and (b) GQD 4.

## 2.3.6. XRD and Raman spectroscopic analysis of GQDs

The crystalline nature of GQDs can be studied by using XRD analysis. The typical XRD patterns of GO sheets and GQD 4 are shown in **Figure 2.8a.** The XRD pattern of GO

showed a strong diffraction peak at 2θ of 10.4° (002) whereas the GQD 4 showed a broader peak centred at 21.4° (002). The formation of smaller sized GQDs with very few graphene layers is responsible for its broadening. Raman spectroscopy was used to investigate the purity, degree of crystallinity and structural disorder in graphene-based materials. **Figure 2.8b** shows the Raman spectra of GO and GQD 4. In the case of GQD 4, the D band (1360 cm$^{-1}$) and G band (1580 cm$^{-1}$) were recorded with the intensity ratio ($I_D/I_G$) of 0.90. As expected, the integrated intensity ratio of the disorder D band to the crystalline G band ($I_D/I_G$) for GO was 0.78 which was increased to 0.90 after the oxidative cutting to form GQDs. The increased disorder may be due to the introduction of defects to the graphene basal planes[†]and the edges. Additionally, GQD 4 sample present 2D band at 2690 cm$^{-1}$ in Raman spectra indicates the formation of high-quality GQDs.[50]
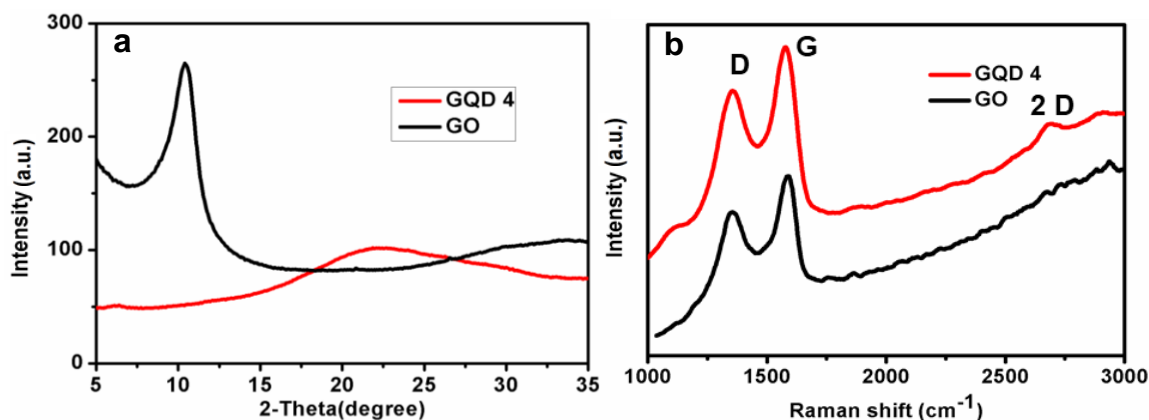


**Figure 2.8.** (a) XRD patterns and (b) Raman spectra of GO and GQD 4.

### 2.3.7. Cytotoxicity assay of GQDs

The biocompatibility of the synthesised GQDs was assessed against human cervical cancer cell line HeLa cells using MTT assay. GQD 4 samples were tested in this study because of its smaller size and high quantum yield. HeLa cells were incubated at six different concentrations of GQD 4 (25, 50, 100, 250, 500 and 1000 µg/mL) for 24 h. The potential toxicity of the nanoparticles is determined by a colorimetric technique based on the ability of live cells to reduce yellow coloured MTT to purple formazan crystals.[51] **Figure 2.9a** shows that GQD sample has low cytotoxicity with a cell viability

---

[†] The basal plane is the plane perpendicular to the principal axis in the crystal systems.

≥ 90 % for concentrations ranging from 25-1000 μg/mL. It is noteworthy that GQDs even at a relatively higher concentration of 1000 μg/mL have not shown cytotoxicity with cell viability of > 92 %. Moreover, the morphology of the cells incubated with GQDs appeared normal as that of the untreated control cells. Thus, MTT assay, as well as visual observation of the cells, ascertained the excellent biocompatibility for GQDs. Thus, GQDs could be used as efficient biocompatible nanoprobe for bioimaging as well as for theranostic applications. Considering the excellent biocompatibility and photostability of the GQDs, they were further utilized as fluorescent nanoprobes for bioimaging applications. The concentration at which the maximum viability was observed was taken as the optimum concentration for bioimaging studies.

### 2.3.8. In-vitro bioimaging studies

One of the major challenges in cellular imaging using semiconductor quantum dots is its intrinsic toxicity which has limited its application. The GQDs synthesized in this work showed several advantages over existing ones in terms of ease of size tunability, green synthetic approach, surface functionality, physiological stability, photostability, size tuned emission, excellent biocompatibility making it suitable for bioimaging applications. The *in-vitro* cellular imaging studies of GQD 4 sample was carried on HeLa cells. Optimum concentration chosen for cellular uptake studies was 25 μg/mL. GQD sample was incubated with HeLa cells for a period of 4 h. This was visualized by the intrinsic fluorescence property of the GQDs when excited using A360/10 excitation filter. The blue fluorescence observed was uniformly distributed throughout the cell. The transmitted light images of the cells and their corresponding fluorescence images have been shown in **Figure2.9 (b-c)**. The bright-field images of the cells incubated with GQDs showed normal morphology of HeLa cells **(Figure 2.9c)** confirming the biocompatibility of GQDs. The cells incubated with GQDs exhibited bright blue fluorescence and it was clearly observed in the fluorescent image when excited at a wavelength of 350 nm **(Figure 2.9b). Figure 2.9(d, e)** showed the fluorescent and bright-field images of the HeLa cells without GQDs. It could be noted that there is no fluorescence in control cells confirming that the emission is from the GQDs in **Figure 2.9b.** The GQDs were found to be cell membrane permeable and found to generate

fluorescence inside the cell. It could be observed that GQDs owing to its size, biocompatibility, and surface functionality can be easily internalized through the cell membrane. It is well documented that carboxylated GQDs exhibit good biocompatibility and exhibits great potential for *in-vitro* as well as *in-vivo* bioimaging applications.[52] Thus these GQDs serve as a suitable nanoprobe that has immense potential in live-cell imaging as well as biomedical applications.
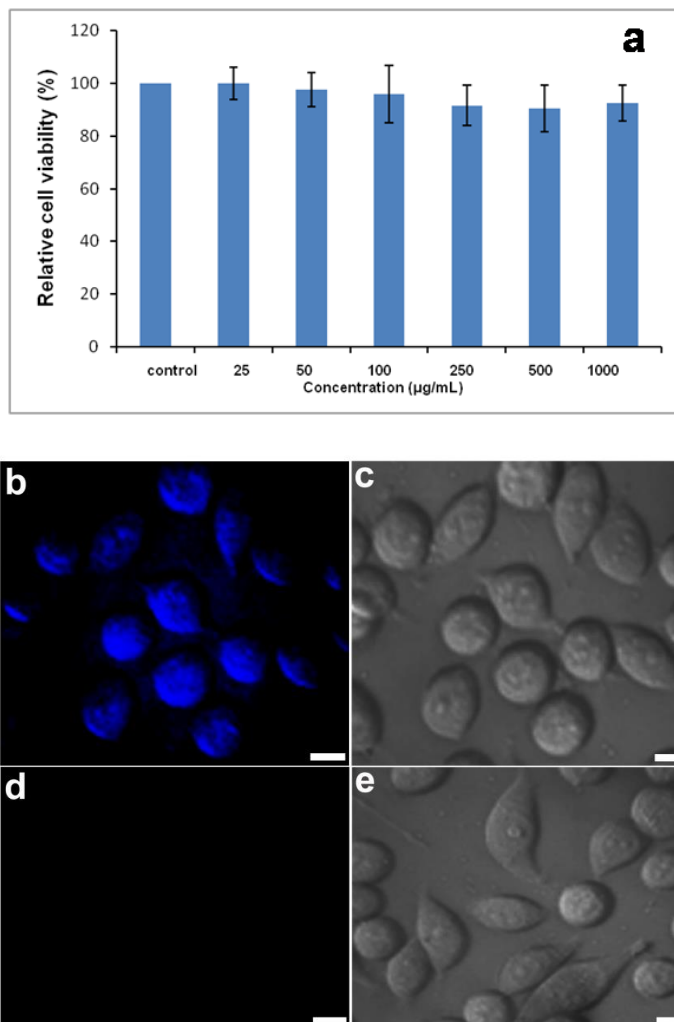


**Figure 2.9.** (a) Cytotoxicity analysis of various concentrations of GQD 4 (25- 1000 μg /mL) on HeLa cells incubated for 24 h MTT assay, Confocal fluorescence images of HeLa cells incubated for 4 h in the presence and absence of GQD 4 with an excitation 350 nm, (b) and (c) showed the fluorescent image and bright field image of the HeLa cells with GQD 4 (25 μg /mL) and (d) and (e) showed the fluorescent and bright-field images of the HeLa cells without GQDs (Scale bar 20 μm).

**2.3.9. Sensing of $Fe^{3+}$ ions using GQD**

GQDs could be promising nanomaterials as fluorescent sensors due to their small size, unique optical properties and high photostability. In the present study, we explored the as-synthesized GQD 4 sample for sensitive, selective and label-free detection of $Fe^{3+}$ metal ions. It is well-known that, $Fe^{3+}$ ions play an important role in biochemical process in living systems by complexation with various regulatory proteins. On the other hand, excess $Fe^{3+}$ ions results in over-production of free radicals and hence induces cytotoxicity. The high $Fe^{3+}$ concentration in neurons is also a key marker for Parkinson's disease.[30] Therefore, it is significant to detect $Fe^{3+}$ ions in biological systems and environmental monitoring. To study the selectivity of synthesised fluorescent probe, the effect of various metal ions ($Fe^{3+}$, $Na^+$, $K^+$, $Co^{2+}$, $Mn^{2+}$, $Zn^{2+}$, $Ca^{2+}$, $Ba^{2+}$, $Mg^{2+}$, $Pb^{2+}$, $Ni^{2+}$ etc) of same concentration (100 µM) on the fluorescent intensity of GQD 4 sample (0.05 mg/mL) was studied by recording its PL spectra at an excitation wavelength of 350 nm. As shown in **Figure 2.10a**, there is an apparent quenching of fluorescence intensity in the presence of $Fe^{3+}$ when compared to other metal ions. From previous reports, it is known that hydroxyl groups showed a good binding affinity towards $Fe^{3+}$ ions. The fluorescence quenching in the case of $Fe^{3+}$ ion may be due to the complexation of $Fe^{3+}$ ions and phenolic hydroxyl groups of GQDs which resulted in the electron transfer to *d*-orbital of $Fe^{3+}$ ions.[53, 54] Thus, fluorescence quenching of GQDs is highly sensitive and selective to $Fe^{3+}$ ions while other metal ions are not able to exert significant quenching and hence GQDs can be used for the selective sensing of $Fe^{3+}$ ions. **Figure 2.10b** shows the photographs of GQDs in the presence of different concentrations of $Fe^{3+}$ ions (0 µM, 20 µM, 600 µM and 800 µM) under 365 nm UV light irradiation. From **Figure 2.10c**, it could be observed that fluorescence quenching of $Fe^{3+}$ ion is concentration-dependent and therefore experiments were carried out at various concentrations of $Fe^{3+}$ ions (0–800 µM). It was observed that, the fluorescence intensity of GQDs gradually decreases upon increasing $Fe^{3+}$ ion concentration. The quenching efficiency showed a good linear relationship with linear regression value, $R^2$ of 0.992 for a concentration range of 10-120 µM of $Fe^{3+}$ ions **(Figure 2.10d)**. Thus, GQDs were used for sensitive and label-free detection of metal ions ($Fe^{3+}$) with a detection limit as low as 20 µM.
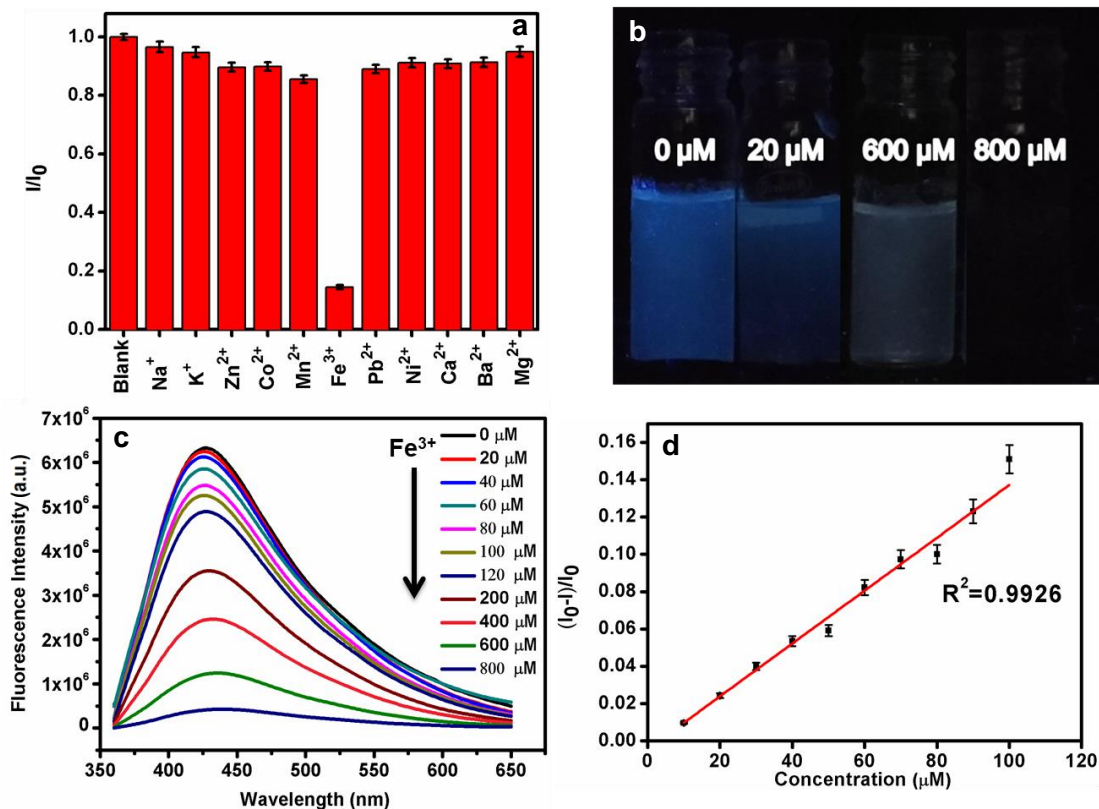
**Figure 2.10.** (a) Effect of different metal ions (concentration: 100 μM) on the fluorescent intensity of GQDs (0.05 mg/mL), (b) Photographs of GQDs with different concentrations of $Fe^{3+}$ ions (0 μM, 20 μM, 600 μM and 800 μM) under 365 nm UV light (c) PL emission spectra of GQDs in the presence of varying concentrations of $Fe^{3+}$ ions (0-800 μM), and (d) Linear regression plot performed in the low concentration range of 10-120 μM .

In order to investigate the fluorescence response between GQDs and $Fe^{3+}$, TEM imaging **(Figure 2.11 a, b)** was done where the aggregation of GQDs due metal ions could be confirmed. It could be observed that the GQDs tend to aggregate in the presence of $Fe^{3+}$ ions which forms a complex with the GQD 4 system **(Figure 2.2d)**. This provides convincing evidence for the aggregation of GQDs in the presence of $Fe^{3+}$. Also, the FT-IR spectrum of GQD-$Fe^{3+}$ complex exhibited redshift and weakened absorption of characteristic peaks when compared to that of GQD **(Figure 2.12a).** This indicates that there is a change in the chemical behaviour of surface functionalities of GQDs due to the strong affinity between $Fe^{3+}$ and phenolic hydroxyl groups of GQDs. In order to confirm aggregation-induced fluorescence quenching, fluorescence lifetime analysis of GQD and

GQD-$Fe^{3+}$ complex was studied using time-correlated single-photon counting (TCSPC) under 330 nm excitation (Table 2.3). The fluorescence lifetime of GQDs is 2.26 ns and has two components: 2.5 ns (ca. 52.08 %) and 3.3 ns (ca.47.92 %). On the addition of $Fe^{3+}$ ions, the average decay time of GQD-$Fe^{3+}$ complex is decreased to 0.037 ns, which confirms the formation of aggregated GQD-$Fe^{3+}$ complex **(Figure 2.12b).** Thus, the changes observed in morphology, FT-IR spectra and fluorescence lifetime confirm the formation of an aggregate complex between GQDs and $Fe^{3+}$ ions, revealing the mechanism behind the fluorescence quenching of GQDs.
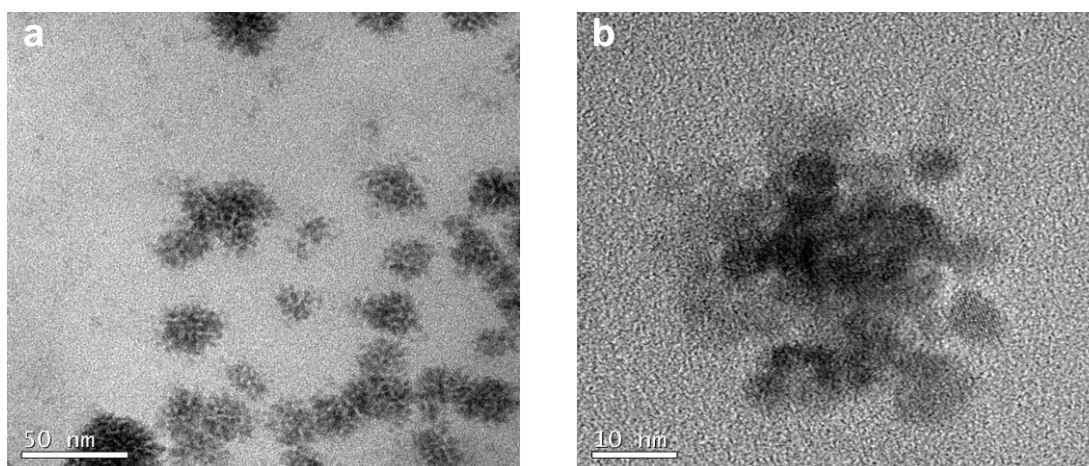


**Figure 2.11.** (a) TEM image of GQD-$Fe^{3+}$ (Scale bar 50 nm) (b) HR-TEM image of GQD-$Fe^{3+}$ (Scale bar 10 nm).
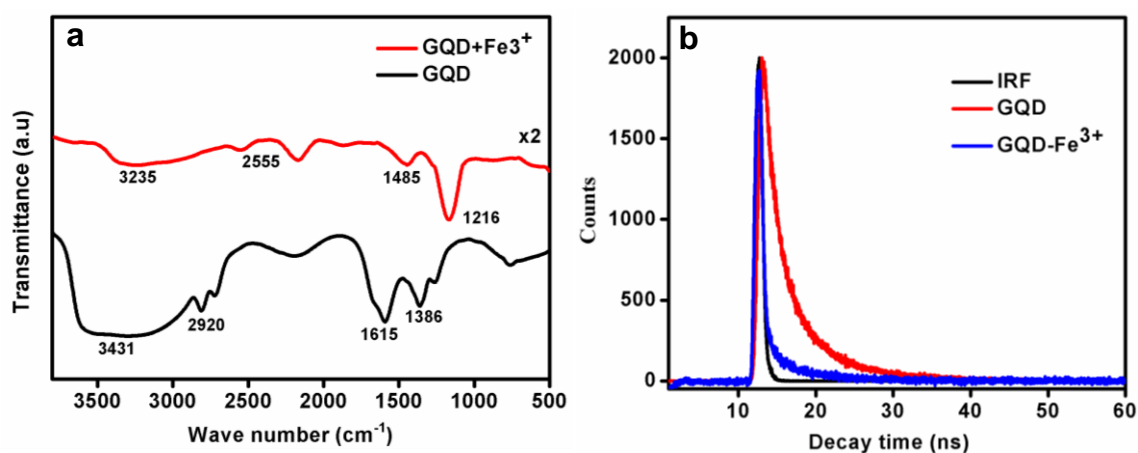


**Figure 2.12.** (a) FT-IR spectra of GQD and GQD-Fe [3+] (b) time-correlated single-photon counting (TCSPC) spectra of GQDs (red) and GQD-$Fe^{3+}$ (blue) (330 nm excitation and delay time at 427 nm emission).

**Table 2.3.** Fluorescence lifetime, relative percentage and the average lifetime of GQD and GQD-$Fe^{3+}$.

| Sample | Lifetime (ns) | Amplitude | Average lifetime (T) |
|--------|---------------|-----------|----------------------|
| GQD | T1=2.513 <br> T2=3.365 | A1=52.08 % <br> A2=47.92 % | 2.26 ns |
| GQD-$Fe^{3+}$ | T1=0.073 <br> T2=0.128 | A1=56.43 % <br> A2=43.57 % | 0.037 ns |

### 2.3.10. Fabrication of microporous PS film by BF method and its mechanism

Further enhancement in the fluorescence of GQD was achieved by the use of patterned substrates in order to meet the application requirements such as enhanced sensitivity and lower LOD. For making patterns of GQDs in a simple and cost-effective we use a microporous polymeric film as a supporting structure for GQD, which was fabricated by BF technique. BF phenomenon accounts for the formation of hexagonal microporous arrays on polymer film.[41] The formation mechanism of BF film is very complicated as the process is controlled by various experimental parameters, such as temperature, humidity, physical properties of the solvents and the solution, physical and chemical properties of the solute (polymer) and the nature of the substrate.[42] The well-accepted mechanism of the entire BF process includes the following steps, as shown in **Figure 2.13.** The steps include- (1) cooling of the solution and moisture nucleation, creating small disordered water droplets on the solution surface; (2) growth and self-assembly of these water droplets produced an ordered closely packed water droplet array which covers the entire solution surface; and (3) complete evaporation of the solvent and condensed water droplets, resulting in the formation of hexagonal porous structure on the dry film.[42]
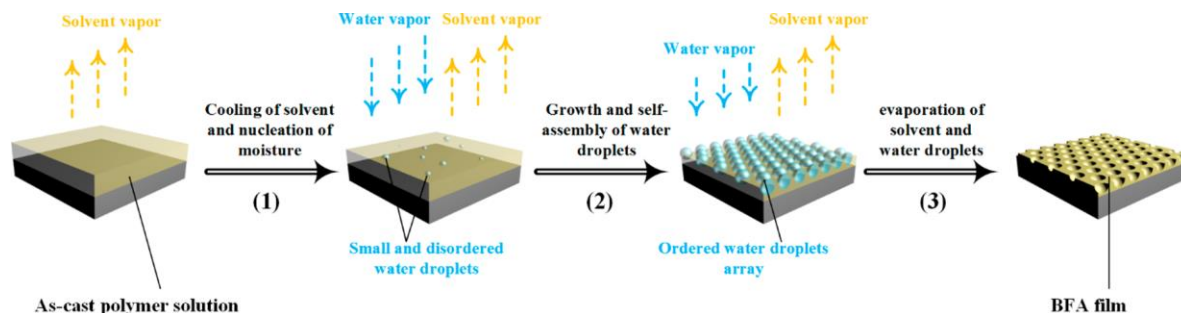
**Figure 2.13.** Formation mechanism of breath figure film.[42]

The patterning of microporous BF film depends upon several key parameters which include the nature of solvents, solute, substrates, humidity, gas flow, and concentration of the polymer solution. The microporous PS films were prepared using different concentrations of polystyrene solution (0.5, 1.0, 2.0, 3.0 wt %) in chloroform. **Figures 2.14 (a-d)** show the corresponding SEM images. For 0.5 wt %, the pores were scattered for **(Figure 2.14a),** because the solvent evaporates quickly and the water droplets aggregate easily. When the concentration reached 3 wt %, the viscosity of the solution was higher, making the film thicker. However, the pore depth was lower because water droplets float on the surface but, the aspect ratio of pores became smaller. In order to get uniform pores and a relatively high aspect ratio, 2 wt % is found to be suitable. The effect of humidity was also studied from 35 % to 95 % RH as shown in **Figures 2.14 (e-h)**. Within this range the average pore size of the film increased from 2 to 5 µm, because the water vapour pressure is more at higher humidity which hinders the increase in solvent's partial pressure, thereby chloroform evaporates more slowly. Longer drying time induces more water droplet to coalesce into the bigger pore. Thus, the porous film prepared under 85 % RH and 2 wt % polymer solution which had a pore size of 3 µm is selected for further studies. The AFM image of the corresponding film is shown in **Figure 2.15.**
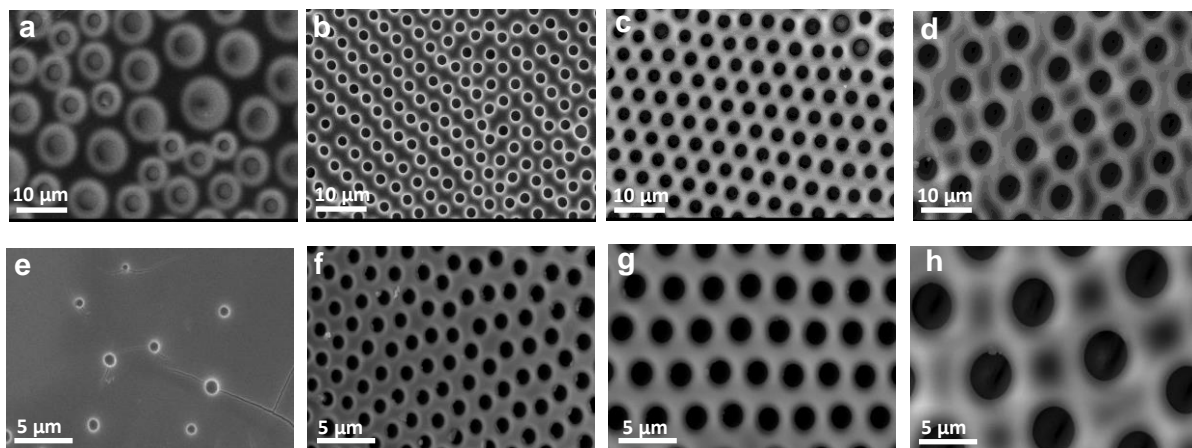
**Figure 2.14.** SEM images of PS porous film prepared by BF method using the concentrations of (a) 0.5, (b) 1.0, (c) 2.0, (d) 3.0 wt % of polystyrene in chloroform and under the RH of (e) 35 % (f) 65 % (g) 85 % and (f) 95 %.
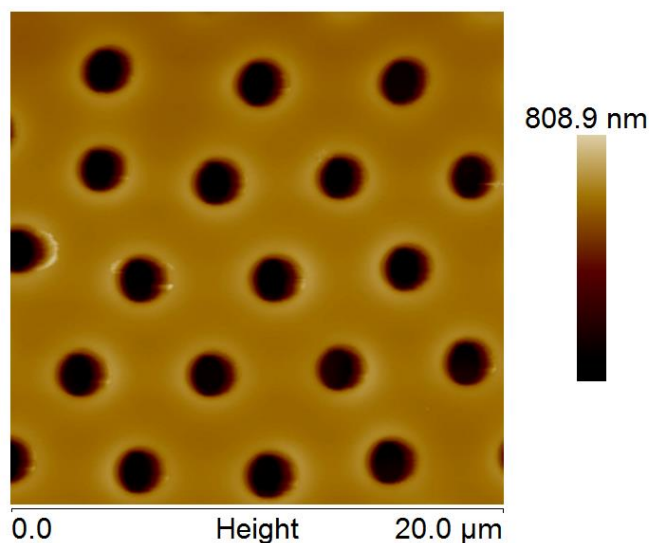


**Figure 2.15.** AFM height image of PS microporous film prepared using 2 wt % of polystyrene in chloroform under the RH of 85 %.

## 2.3.11. Fabrication of fluorescent PS-GQD film and fluorescence enhancement study

The microporous PS films fabricated by BF method were subjected to short time (15 sec) oxidative plasma treatment in order to increase their wettability in water. The obtained PS film is then vertically dipped in GQD solution for 2 h to obtain PS-GQD film where

GQDs are particularly deposited inside this pore structure of PS film. **Figure 2.16a** shows the fluorescence optical microscopic image and **Figure 2.16b** shows the SEM image of the obtained PS-GQD film where we could see the aggregated particles of GQDs inside the pore structure.
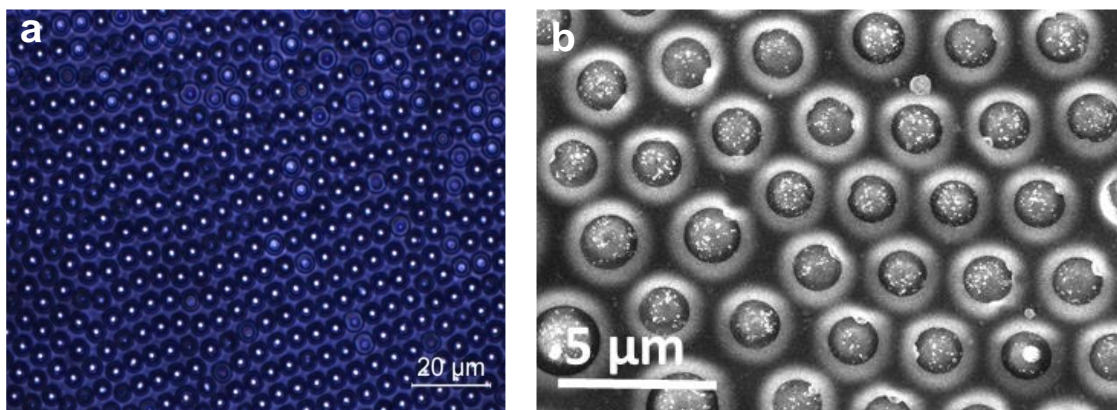


**Figure 2.16**. (a) Fluorescence optical microscopic image and (b) SEM image of PS-GQD film prepared by dipping the microporous PS film in GQD solution for 2 h.

The fluorescence enhancement study was carried out by taking the PL spectra of PS-GQD film and PS-GQD control sample at an excitation of 350 nm. From the spectra **(Figure 2.17a)**, it was observed that PS-GQD film showed around a 77-fold enhancement of fluorescence emission when compared to the control sample. **Figure 2.17b** showed the corresponding normalized PL spectra in which a slight red shift was observed, which could be due to the aggregation of the particles. This is typical evidence for aggregation-induced emission enhancement (AIEE).[55] The movement of surface groups is strictly restricted when GQDs aggregate within the pore structure due to the physical restriction associated with the space limitation. Thus, the non-radiative pathway is largely blocked in PS-GQD film resulting in enhanced PL intensity. On the other hand, if the surface groups will rotate, bend or vibrate dynamically, it will act as non-radiative relaxation routes for the excited state to return to the ground state.[55] Non-radiative relaxation is usually faster than radiative recombination, signifying the non-radiative pathways have a higher priority than radiative recombination and the PL efficiency is very low in this case.
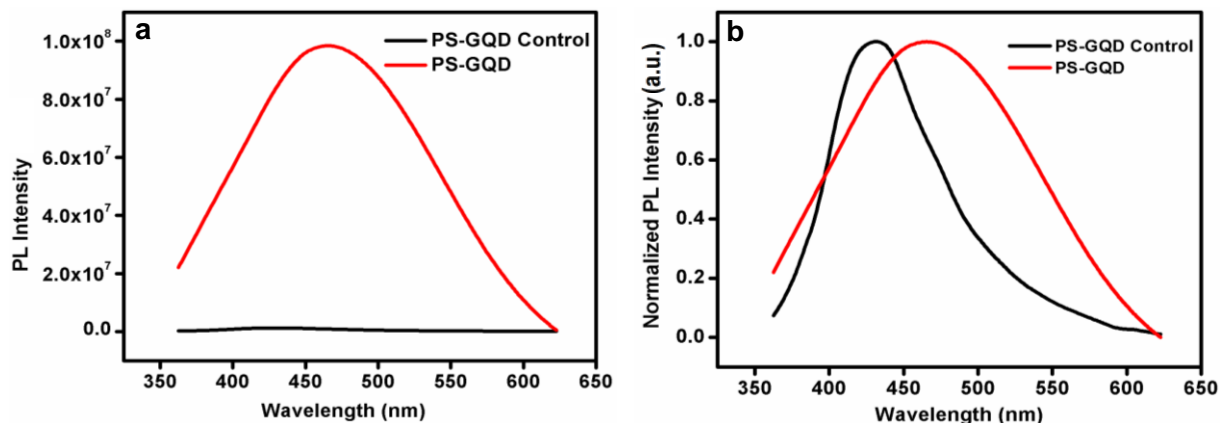
**Figure 2.17.** (a) PL spectra and (b) Normalised PL spectra of PS-GQD control and PS-GQD film.

### 2.3.12. Sensing of $Fe^{3+}$ ions using PS-GQD film

In order to compare the sensitivity results with previous observation, the sensing of $Fe^{3+}$ ions using the fabricated PS-GQD film was carried out at room temperature. To study the sensitivity towards $Fe^{3+}$, PL spectra of PS-GQD films with different concentrations of $Fe^{3+}$ (0-900 nM) was recorded upon the excitation wavelength of 350 nm. From **Figure 2.18a**, it was observed that fluorescence quenching of $Fe^{3+}$ ion is concentration-dependent and the fluorescence intensity of PS-GQD films gradually decreases upon increasing $Fe^{3+}$ ion concentration. The quenching efficiency also showed a good linear relationship with linear regression value, $R^2$ of 0.997 for a concentration range of 0-900 nM of $Fe^{3+}$ ions **(Figure 2.18b)**. Thus, PS-GQD films were also used for sensitive detection of $Fe^{3+}$ ions with LOD as low as 80 nM. Therefore, we could enhance the sensitivity towards $Fe^{3+}$ ions using the PS-GQD films when compared to GQDs in aqueous phase.
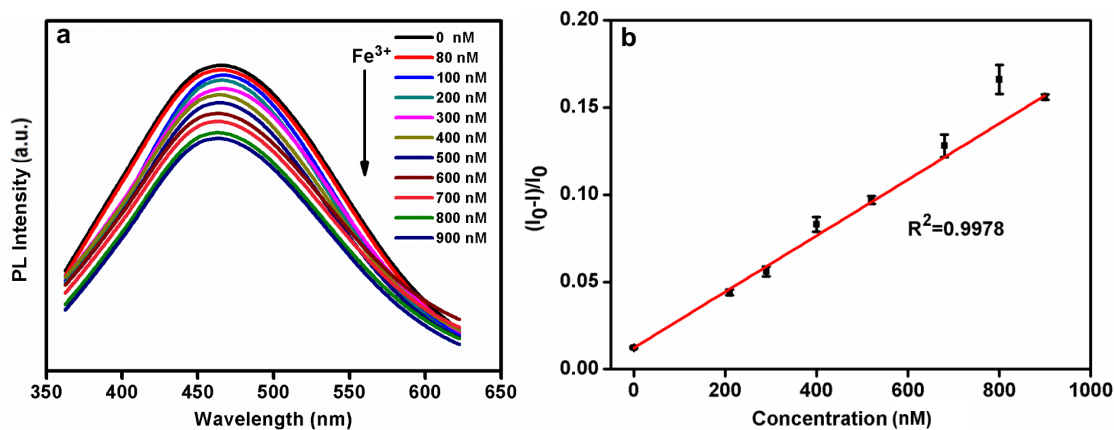
**Figure 2.18.** (a) PL emission spectra of PS-GQD films in the presence of varying concentrations of $Fe^{3+}$ ions (0-900 nM) and (b) Linear regression plot performed in the concentration range of 0-900 nM.

## 2.3.13. Fabrication of CPCs-based on polystyrene microspheres

In another effort to enhance the fluorescence emission of GQDs *via* enhanced excitation or light extraction using photonic crystal, the photonic bandgap edge (PBG) of a CPC should be overlapped with the excitation or emission wavelength of GQD. For the enhancement study, we fabricated CPCs using PS microspheres with different PBGs, which was tuned by varying the diameters of microspheres. PS-based CPCs were fabricated by evaporation induced vertical deposition method on plasma-cleaned hydrophilic glass coverslips.[45] CPCs with different PBG namely, $CPC_C$, $CPC_B$ and $CPC_G$ were prepared from different sized PS microspheres. **Figures 2.19 (a-c)** showed the SEM images of $CPC_C$, $CPC_B$ and $CPC_G$, respectively. From the SEM images, it was observed that CPCs exhibited a well-ordered long-range arrangement of the microspheres, which was responsible for their brilliant colours due to Bragg diffraction.[56] The inset of the **Figures 2.19 (a-c)** showed the digital photographs of the corresponding CPCs, where $CPC_C$ is colourless, $CPC_B$ appeared as blue in colour and $CPC_G$ as green in colour. The PBGs of the CPCs were obtained from their reflectance spectra using UV-Visible modular spectrometer. **Figures 2.19 (d-f)** showed the PBGs of $CPC_C$, $CPC_B$ and $CPC_G$, respectively. $CPC_C$ exhibited photonic stopbands in the UV region with $\lambda_{max}$ at 335 nm, whereas both $CPC_B$ and $CPC_G$ exhibited a photonic stop band in the visible region with $\lambda_{max}$ at 423 nm and 490 nm, respectively, imparting their characteristic colours.
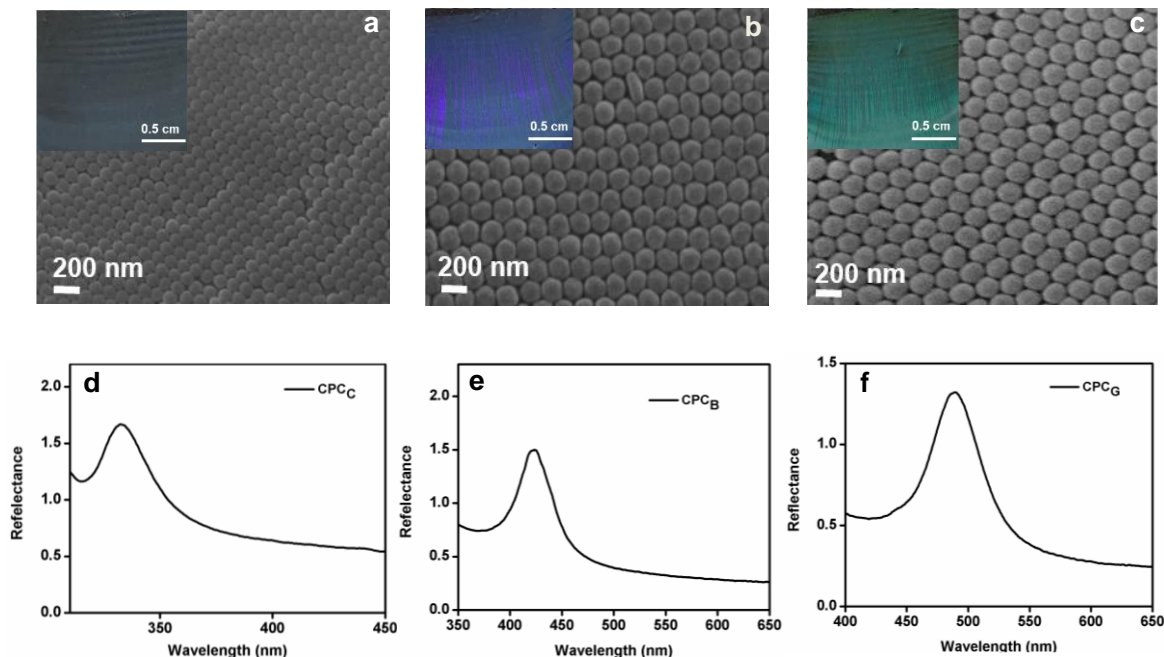
**Figure 2.19.** SEM images, corresponding digital photographs (inset) of (a) CPC$_C$ (b) CPC$_B$, (c) CPC$_G$, (d) reflectance spectra of CPC$_C$, (e) CPC$_B$ and (f) CPC$_G$

### 2.3.14. Fluorescence enhancement of GQDs using PS-based CPCs

To study the effect of PBG on the fluorescence enhancement of GQDs on CPCs, absorption and emission maxima of GQD in aqueous solution was measured. From **Figure 2.20a**, it was observed that GQD exhibited absorption maxima at 350 nm and emission maxima at 428 nm at an excitation wavelength of 350 nm. To further analyse the PBG effects on fluorescence emission using the fabricated CPCs, we prepared different CPC-GQD films viz., CPC$_C$-GQD, CPC$_B$-GQD and CPC$_G$-GQD films by drop-casting equal volume (20 μL) of GQDs on to each CPC followed by drying under vacuum. Also, we prepared a control sample using CPC film heated to 120 °C for 2 h to obtain planar films on glass substrates followed by adding same amount of GQD for the comparison of fluorescence intensities with CPCs. The fluorescence enhancement study was carried out by taking the PL spectra of CPC$_C$-GQD, CPC$_B$-GQD, CPC$_G$-GQD films and control film upon the excitation wavelength of 350 nm **(Figure 2.20b)**. From the spectra it was found that maximum fluorescence emission was obtained for CPC$_C$-GQD film when compared to other CPC-GQD films and control sample and the corresponding enhancement factors

(EF) were also calculated. The fluorescence EF was measured as the ratio of the fluorescence intensities of GQD on CPC-GQD films to that of GQD on the control film at 428 nm. The fluorescence EFs of GQDs were calculated as 102, 25.5 and 14.7 for of $CPC_C$-GQD, $CPC_B$-GQD, $CPC_G$-GQD films respectively. Much greater fluorescence EF in $CPC_C$-GQD is due to the overlapping of the excitation wavelength of GQD (350 nm) with PBG edge of $CPC_C$. It was observed that the PBG edge of $CPC_G$-GQD film is not at the excitation wavelength of GQDs. However, its fluorescence intensity is higher than that of a smooth PS control film due to the large specific surface area of the 3D porous structure of the CPC. When compared to the $CPC_G$-GQD, the fluorescence EF of $CPC_B$-GQD were relatively higher because the PBG edge of $CPC_B$-GQD are near to the excitation wavelength of GQD. Therefore, the fluorescence emission was enhanced due to enhanced excitation which arises from photonic band edge effect. Based on all these observations, we could confirm that maximum fluorescence enhancement was obtained for $CPC_C$-GQD film compared to other CPCs which can be attributed to the PBG effect.
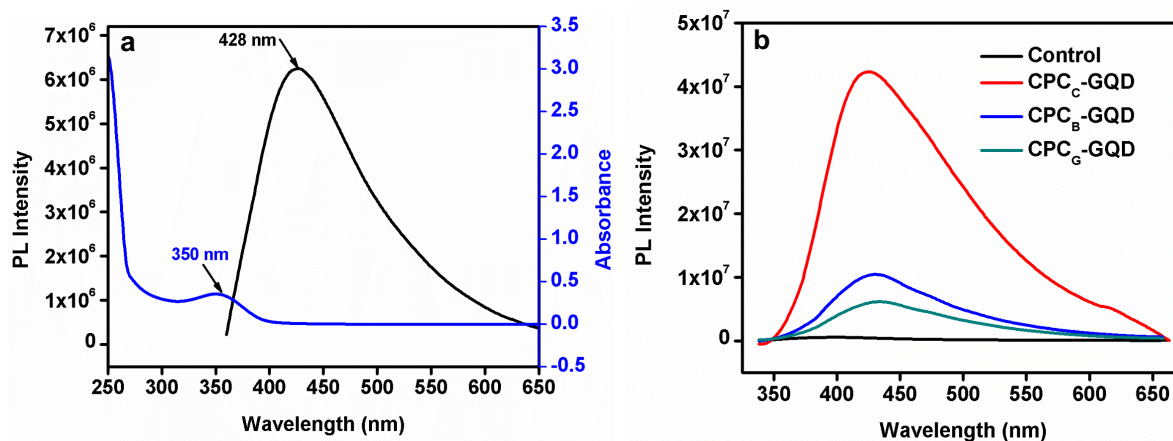


**Figure 2.20.** (a) UV-Visible absorption (blue) and PL spectra (black) of GQD, (b) PL spectra of $CPC_C$-GQD, $CPC_B$-GQD and $CPC_G$-GQD films.

## 2.3.15. Sensing of $Fe^{3+}$ ions using $CPC_C$-GQD film

As the maximum fluorescence enhancement was obtained for $CPC_C$-GQD film, the sensitivity study was carried out at room temperature using the same film. To study the sensitivity towards $Fe^{3+}$, PL spectra of $CPC_C$-GQD films with different concentrations of $Fe^{3+}$ (0-390 nM) were recorded upon the excitation wavelength of 350 nm. It was

observed that fluorescence quenching of $Fe^{3+}$ ion is concentration-dependent and the fluorescence intensity of $CPC_C$-GQD films gradually decreases upon increasing $Fe^{3+}$ ion concentration **(Figure 2.21a)**. The quenching efficiency also showed a good linear relationship with linear regression value, $R^2$ of 0.981 for the concentration range of 0-300 nM of $Fe^{3+}$ ions **(Figure 2.21b)**. Thus, $CPC_C$-GQD films were also used for sensitive detection of $Fe^{3+}$ ions with LOD as low as 30 nM. Thus, we could further enhance the sensitivity towards $Fe^{3+}$ ions using $CPC_C$-GQD films.
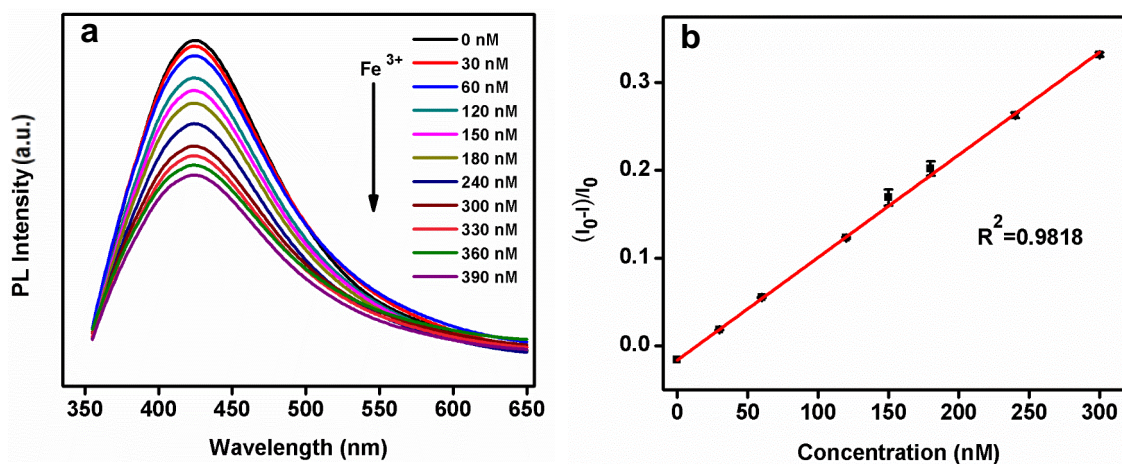


**Figure 2.21.** (a) PL emission spectra of $CPC_C$-GQD films in the presence of varying concentrations of $Fe^{3+}$ ions (0-390 nM) and (b) Linear regression plot performed in the concentration range of 0-300 nM.

## 2.4. Conclusions

In the current chapter, we reported a rapid, acid-free, one-step sonochemical strategy with microwave heating for the synthesis of size-tunable high-quality GQDs by the oxidative cutting of GO using $KMnO_4$ within half an hour. The synthesized GQDs are highly crystalline and have uniform size distribution. These GQDs exhibited good quantum yield up to 23.8 %, high product yield (75-81 %) and stable size-dependent photoluminescence in aqueous solutions. Our studies indicate that the GQDs possess very good biocompatibility, good aqueous dispersibility, low cytotoxicity, high photostability and hence can be applied as excellent fluorescent probes for live-cell imaging. Fluorogenic probes are of particular interest in the area of cancer detection or bioimaging. Our findings on the biocompatibility and fluorogenic property of the GQDs

observed in cancer cells highlight their significance in clinical diagnostic applications. They can further be used as targeting moieties for drug delivery applications as well. The GQDs synthesized were also demonstrated for the detection of physiologically relevant metal ions and particularly for the sensing of $Fe^{3+}$ ions in aqueous media. Also, we have achieved a good enhancement of fluorescence emission of GQDs in order to enhance its sensitivity by two approaches, namely breath figure technique and photonic bandgap effect. By breath figure method, we could exhibit a 77-fold enhancement of fluorescence emission through AIEE and hence the sensitivity towards $Fe^{3+}$ was also enhanced with LOD as low as 80 nM. Further, we could achieve a 102-fold enhancement of fluorescence emission of GQDs on PS based CPCs *via* PBG effect. CPC based GQD platform was further used for the sensitive detection of $Fe^{3+}$ ions with much lower LOD as 30 nM.

# References

1.      J. Gu, M. J. Hu, Q. Q. Guo, Z. F. Ding, X. L. Sun and J. Yang, *RSC Advances*, 2014, **4**, 50141-50144.

2.      F. Liu, Y. Sun, Y. Zheng, N. Tang, M. Li, W. Zhong and Y. Du, *RSC Advances*, 2015, **5**, 103428-103432.

3.      X. T. Zheng, A. Than, A. Ananthanaraya, D.-H. Kim and P. Chen, *ACS Nano*, 2013, **7**, 6278-6286.

4.      Y. Zhang, C. Wu, X. Zhou, X. Wu, Y. Yang, H. Wu, S. Guo and J. Zhang, *Nanoscale*, 2013, **5**, 1816-1819.

5.      S. Zhu, Y. Song, X. Zhao, J. Shao, J. Zhang and B. Yang, *Nano Research*, 2015, **8**, 355-381.

6.      J. Peng, W. Gao, B. K. Gupta, Z. Liu, R. Romero-Aburto, L. Ge, L. Song, L. B. Alemany, X. Zhan, G. Gao, S. A. Vithayathil, B. A. Kaipparettu, A. A. Marti, T. Hayashi, J.-J. Zhu and P. M. Ajayan, *Nano Letters*, 2012, **12**, 844-849.

7.      H. Sun, L. Wu, N. Gao, J. Ren and X. Qu, *ACS Applied Materials & Interfaces*, 2013, **5**, 1174-1179.

8.      S. Zhu, J. Zhang, S. Tang, C. Qiao, L. Wang, H. Wang, X. Liu, B. Li, Y. Li, W. Yu, X.

Wang, H. Sun and B. Yang, *Advanced Functional Materials*, 2012, **22**, 4732-4740.

9.    H. Xu, S. Zhou, L. Xiao, H. Wang, S. Li and Q. Yuan, *Journal of Materials Chemistry C*, 2015, **3**, 291-297.

10.   A. Ananthanarayanan, X. Wang, P. Routh, B. Sana, S. Lim, D.-H. Kim, K.-H. Lim, J. Li and P. Chen, *Advanced Functional Materials*, 2014, **24**, 3021-3026.

11.   S. Li, Y. Li, J. Cao, J. Zhu, L. Fan and X. Li, *Analytical Chemistry*, 2014, **86**, 10201-10207.

12.   J. Ju and W. Chen, *Biosensors and Bioelectronics*, 2014, **58**, 219-225.

13.   C. Zhang, Y. Cui, L. Song, X. Liu and Z. Hu, *Talanta*, 2016, **150**, 54-60.

14.   Y. Li, Y. Hu, Y. Zhao, G. Shi, L. Deng, Y. Hou and L. Qu, *Advanced Materials*, 2011, **23**, 776-780.

15.   V. Gupta, N. Chaudhary, R. Srivastava, G. D. Sharma, R. Bhardwaj and S. Chand, *Journal of the American Chemical Society*, 2011, **133**, 9960-9963.

16.   L. Li, G. Wu, G. Yang, J. Peng, J. Zhao and J.-J. Zhu, *Nanoscale*, 2013, **5**, 4015-4039.

17.   L. Tang, R. Ji, X. Cao, J. Lin, H. Jiang, X. Li, K. S. Teng, C. M. Luk, S. Zeng, J. Hao and S. P. Lau, *ACS Nano*, 2012, **6**, 5102-5110.

18.   J. Liu, Y. Liu, N. Liu, Y. Han, X. Zhang, H. Huang, Y. Lifshitz, S.-T. Lee, J. Zhong and Z. Kang, *Science*, 2015, **347**, 970.

19.   Q. Zhang, J. Jie, S. Diao, Z. Shao, Q. Zhang, L. Wang, W. Deng, W. Hu, H. Xia, X. Yuan and S.-T. Lee, *ACS Nano*, 2015, **9**, 1561-1570.

20.   J. Lu, P. S. E. Yeo, C. K. Gan, P. Wu and K. P. Loh, *Nat Nano*, 2011, **6**, 247-252.

21.   D. Pan, J. Zhang, Z. Li and M. Wu, *Advanced Materials*, 2010, **22**, 734-738.

22.   J. Shen, Y. Zhu, C. Chen, X. Yang and C. Li, *Chemical Communications*, 2011, **47**, 2580-2582.

23.   F. Yang, M. Zhao, B. Zheng, D. Xiao, L. Wu and Y. Guo, *Journal of Materials Chemistry*, 2012, **22**, 25471-25479.

24.   S. Kim, S. W. Hwang, M.-K. Kim, D. Y. Shin, D. H. Shin, C. O. Kim, S. B. Yang, J. H. Park, E. Hwang, S.-H. Choi, G. Ko, S. Sim, C. Sone, H. J. Choi, S. Bae and B. H. Hong, *ACS Nano*, 2012, **6**, 8203-8208.

25.   F. Liu, M.-H. Jang, H. D. Ha, J.-H. Kim, Y.-H. Cho and T. S. Seo, *Advanced Materials*, 2013, **25**, 3657-3662.

26.  Z. Zhang, Q. Liu, D. Gao, D. Luo, Y. Niu, J. Yang and Y. Li, *Small*, 2015, **11**, 3000-3005.

27.  D. B. Shinde and V. K. Pillai, *Chemistry – A European Journal*, 2012, **18**, 12522-12528.

28.  L. Tang, R. Ji, X. Li, K. S. Teng and S. P. Lau, *Particle & Particle Systems Characterization*, 2013, **30**, 523-531.

29.  R. Ye, C. Xiang, J. Lin, Z. Peng, K. Huang, Z. Yan, N. P. Cook, E. L. G. Samuel, C.-C. Hwang, G. Ruan, G. Ceriotti, A.-R. O. Raji, A. A. Martí and J. M. Tour, 2013, **4**, 2943.

30.  Z. Luo, G. Qi, K. Chen, M. Zou, L. Yuwen, X. Zhang, W. Huang and L. Wang, *Advanced Functional Materials*, 2016, **26**, 2739-2744.

31.  L.-L. Li, J. Ji, R. Fei, C.-Z. Wang, Q. Lu, J.-R. Zhang, L.-P. Jiang and J.-J. Zhu, *Advanced Functional Materials*, 2012, **22**, 2971-2979.

32.  Y. Zhu, G. Wang, H. Jiang, L. Chen and X. Zhang, *Chemical Communications*, 2015, **51**, 948-951.

33.  Y. Shin, J. Lee, J. Yang, J. Park, K. Lee, S. Kim, Y. Park and H. Lee, *Small*, 2014, **10**, 866-870.

34.  L. Lin and S. Zhang, *Chemical Communications*, 2012, **48**, 10177-10179.

35.  Y. Sun, S. Wang, C. Li, P. Luo, L. Tao, Y. Wei and G. Shi, *Physical Chemistry Chemical Physics*, 2013, **15**, 9907-9913.

36.  M. K. Kumawat, M. Thakur, R. B. Gurung and R. Srivastava, *ACS Sustainable Chemistry & Engineering*, 2017, **5**, 1382-1391.

37.  H. Jia, X. Gao, Y. Shi, N. Sayyadi, Z. Zhang, Q. Zhao, Q. Meng and R. Zhang, *Spectrochimica Acta Part A: Molecular and Biomolecular Spectroscopy*, 2015, **149**, 674-681.

38.  Y. Du and S. Guo, *Nanoscale*, 2016, **8**, 2532-2543.

39.  N. Ganesh, W. Zhang, P. C. Mathias, E. Chow, J. Soares, V. Malyarchuk, A. D. Smith and B. T. Cunningham, *Nature Nanotechnology*, 2007, **2**, 515.

40.  M. Hernandez-Guerrero and M. H. Stenzel, *Polymer Chemistry*, 2012, **3**, 563-577.

41.  Y. Dou, M. Jin, G. Zhou and L. Shui, *Membranes*, 2015, **5**, 399-424.

42.  A. Zhang, H. Bai and L. Li, *Chemical Reviews*, 2015, **115**, 9801-9868.

43.  P. Lodahl, A. F. Van Driel, I. S. Nikolaev, A. Irman, K. Overgaag, D.

Vanmaekelbergh and W. L. Vos, *Nature*, 2004, **430**, 654.

44.    X. Su, X. Sun, S. Wu and S. Zhang, *Nanoscale*, 2017, **9**, 7666-7673.

45.    V. Vipin, P. R. Chandran, A. M. Ramachandran, A. Mohamed and S. Pillai, *New Journal of Chemistry*, 2019, **43**, 16264-16272.

46.    H. S. Lee, T. S. Shim, H. Hwang, S.-M. Yang and S.-H. Kim, *Chemistry of Materials*, 2013, **25**, 2684-2690.

47.    E. Eftekhari, X. Li, T. H. Kim, Z. Gan, I. S. Cole, D. Zhao, D. Kielpinski, M. Gu and Q. Li, *Scientific reports*, 2015, **5**, 14439.

48.    C. Vion, C. Barthou, P. Bénalloul, C. Schwob, L. Coolen, A. Gruzintev, G. Emel'chenko, V. Masalov, J.-M. Frigerio and A. Maître, *Journal of Applied Physics*, 2009, **105**, 113120.

49.    J. Liang, R. T. K. Kwok, H. Shi, B. Z. Tang and B. Liu, *ACS applied materials & interfaces*, 2013, **5**, 8784-8789.

50.    D. Voiry, J. Yang, J. Kupferberg, R. Fullon, C. Lee, H. Y. Jeong, H. S. Shin and M. Chhowalla, *Science*, 2016.

51.    Y. Liu, D. A. Peterson, H. Kimura and D. Schubert, *Journal of Neurochemistry*, 1997, **69**, 581-593.

52.    M. Nurunnabi, Z. Khatun, K. M. Huh, S. Y. Park, D. Y. Lee, K. J. Cho and Y.-k. Lee, *ACS Nano*, 2013, **7**, 6858-6867.

53.    S. Zhu, Q. Meng, L. Wang, J. Zhang, Y. Song, H. Jin, K. Zhang, H. Sun, H. Wang and B. Yang, *Angewandte Chemie International Edition*, 2013, **52**, 3953-3957.

54.    Y. Song, S. Zhu, S. Xiang, X. Zhao, J. Zhang, H. Zhang, Y. Fu and B. Yang, *Nanoscale*, 2014, **6**, 4676-4682.

55.    R. Guo, T. Li and S. Shi, *Journal of Materials Chemistry C*, 2019, **7**, 5148-5154.

56.    H. Mıguez, C. López, F. Meseguer, A. Blanco, L. Vázquez, R. Mayoral, M. Ocaña, V. Fornés and A. Mifsud, *Applied Physics Letters*, 1997, **71**, 1148-1150.

# Chapter 3

## Sulphur-Doped Graphene Quantum Dots Based Fluorescent Sensors in Aqueous and Flexible Forms for Sensitive Detection of Pesticide

# Abstract

In the present chapter, the optical properties of graphene quantum dots are tuned by heteroatom doping strategy to prepare green fluorescent sulphur-doped graphene quantum dots (S-GQDs) which is used as a fluorescent sensor for sensitive detection of carbamate pesticides. S-GQDs are synthesized from graphene oxide via sonochemical method with microwave heating within 5 min, using $KMnO_4$ as oxidizing agent and $H_2SO_4$ as the doping precursor. S-GQDs exhibits uniform particle size distribution ($\sim$5 nm), high crystallinity, monolayer thickness, high production yield (85 %) and good quantum yield (27.8 %). Sulphur-doping is confirmed from XPS and FT-IR analysis. Sulphur-doping increases the fluorescence intensity, lifetime and quantum yield of GQDs by introducing additional energy levels which effectively creating new electron transition pathways in the band structures. The green fluorescent S-GQDs in aqueous phase exhibits a detection limit of 0.45 ppb for carbofuran and 1.6 ppb for thiram. S-GQDs are then incorporated into poly (vinyl alcohol) [PVA] matrix for the preparation of flexible, solid-state fluorescent sensing platforms. Unlike the solid-state S-GQD, it imparts fluorescent properties to the polymeric matrix based platform, making it a suitable probe for pesticide detection. PVA/S-GQD flexible film exhibits a limit of detection of 60 ppb and 210 ppb for carbofuran and thiram, respectively. Finally, the fluorescent sensor is successfully demonstrated for the detection of carbofuran in a real sample with ppb level sensitivity.
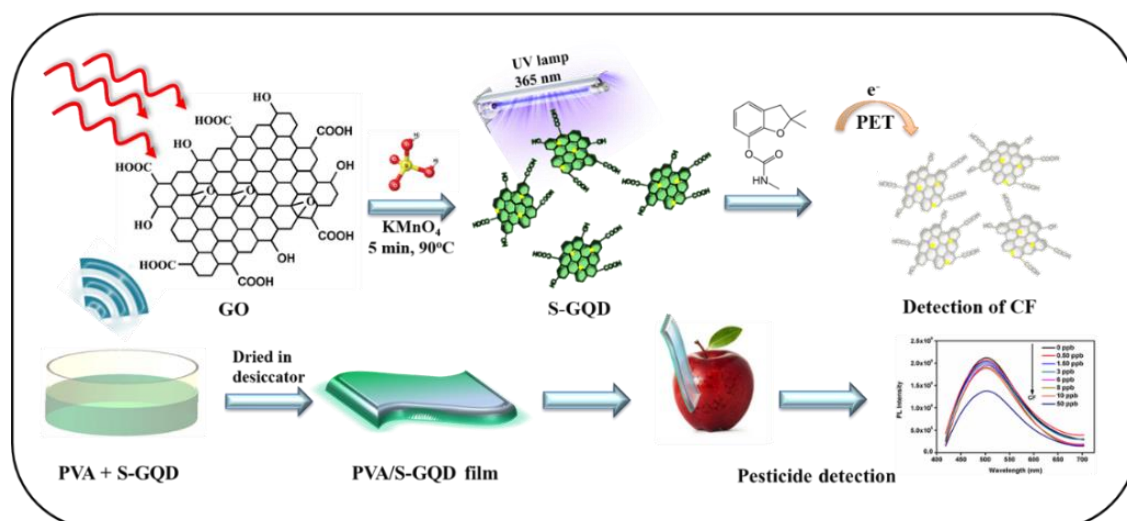
## 3.1. Introduction

Pesticides are largely used to curb the growth of weeds and pests for increasing crop productivity. However, their high dose and persistent use can lead to environmental pollution and have adverse effects on human health that include carcinogenicity, genotoxicity, respiratory and immunological disorders, infertility, irritancy, nerve and bone marrow disorders, endocrine disruptive activity etc.[1-4] Because of the strict policy guidelines enforced by various government regulators, the maximum tolerance level of pesticide residues in food crops are defined for monitoring purpose.[5] The overuse of pesticides in agriculture has generated numerous concerns in food safety and resulted in environmental imbalance.[6, 7] However, it is quite challenging to detect pesticide residues present in crops below the ppm level and their impact on ecosystem.[7, 8] Carbofuran (CF) and Thiram (Tr) are widely used a pesticides in modern agriculture to protect the crops, vegetables and fruits from damages caused by insects in order to boost the crop production.[9, 10] CF is marketed under the trade name, Furadan. Tr is used as a fungicide in the world on a large variety of fruits such as apples, pears, strawberries, tomatoes, grapes, peaches, etc.[10] Typically, these harmful pesticide residues are detected through conventional analytical methods such as liquid chromatography, ion trap mass spectrometry, electrochemical techniques, etc.[11-14] Although these methods exhibit excellent sensitivity, they often involve the usage of sophisticated equipment, laborious sample preparation, residue extraction and require trained labour personnel.[15, 16] Therefore, the development of an alternative facile, rapid and practical approaches for the trace-level detection of pesticide residues is of great importance for application in food safety and environment monitoring.

Among all, optical methods based on photoluminescence of fluorescent probe appears as an ideal approach for the facile and ultra-sensitive detection of pesticide residues.[17, 18] Li *et al.* developed a fluorescent sensor based on N, S co-doped carbon dots for the ultrasensitive detection of pesticides with detection limit of 5 ppb.[18] Paulami *et al* reported a simple fluorescence sensor based on carbon dots for the detection of some common pesticides, such as atrazine, chlorpyrifos, imidacloprid, lindane, and tetradifon.[19] Recently, fluorescent probes like graphene quantum dots have received much attention as optical sensor due to their unique optical properties,

tunable surface functionality and high production yield.[20, 21] When compared to other graphene derived materials, graphene quantum dots (GQDs) show superior properties such as high photostability, aqueous dispersibility, biocompatibility, lower toxicity, good chemical and thermal stabilities.[22, 23] These unique properties of GQDs finds application in the field of bioimaging,[24] photovoltaics,[25] light-emitting diodes,[26] photocatalysis,[27] chemical sensors[28] and biosensors.[29] Moreover, this metal-free GQD exhibits high surface area and rich in carboxylic functional groups on its surface and edges, which help them to form a complex with other functional chemicals.[30] However, GQDs exhibit relatively low emission efficiency when compared to the conventional semiconductor that is toxic in nature.[31] Efficient means to improve its fluorescent properties have therefore remained a challenge and it is highly desirable to extend its potential applications in various fields. Elemental doping can be used to tune the fluorescence properties and is considered as a promising engineering method to generate highly fluorescent GQDs.[32, 33]  The heteroatom doping strategy can further enhance its quantum yield by introducing localized states which change their electron transfer properties, overcome the self-quenching problem and thus potentially enhance their application in various fields such as catalysis, energy storage, sensors etc.[34-37] Non-metal doping at specific sites can introduce more defects and additional energy levels, resulting in the modification of the band gap of GQD and thus improved its fluorescence properties due to quantity confinement and edge effects.[37-39]  Thus, to develop simple and rapid techniques using cost-effective less toxic GQD with enhanced fluorescent properties as a sensing probe will be a promising solution for the ultrasensitive detection of these pesticide residues.

In the present chapter, we synthesized S-GQDs from graphene oxide (GO) using $KMnO_4$ as an oxidizing agent and $H_2SO_4$ as doping source for sulphur by combined sonochemical and microwave heating method keeping the reaction temperature constant at 90 °C in 5 min. Further, as-synthesized S-GQDs were well-characterized for its structural and optical properties. S-GQDs showed a relatively higher quantum yield of 27.8 %, production yield of 85 % and longer lifetime. As-synthesized S-GQDs exhibited high crystallinity, uniform size distribution (~5 nm) and monolayer graphene thickness. The S-GQDs also exhibited a versatile colour shift from blue to green with respect to the undoped GQDs, by creating new electron

transition pathways in the band structures. In the present study, we demonstrated fluorescent sensors based on S-GQDs in aqueous form as well as in flexible film form for the trace-level detection of carbamate pesticides *viz.* CF and Tr **(Scheme 3.1).** In order to prepare a solid-state flexible fluorescent sensing probe, PVA was chosen as the matrix polymer and PVA/S-GQDs composites were prepared by casting from aqueous solutions. Besides serving the role of matrix, the flexible polymer can provide increased mechanical and chemical stabilities.[40, 41] The polymer can limit the agglomeration of GQDs and thereby, maintaining their fluorescent emission.[42] Moreover, due to the solid and flexible nature of sensor probe, the minimum amount of analyte is required and on-site sample collection would be possible. The as-synthesized S-GQDs and S-GQD based fluorescent (PVA/S-GQD) films were used for the ultrasensitive and selective detection of carbamate pesticides with a limit of detection at ppb level. Further, the fluorescent probe was applied for the detection of CF residue in real sample with ppb level sensitivity.
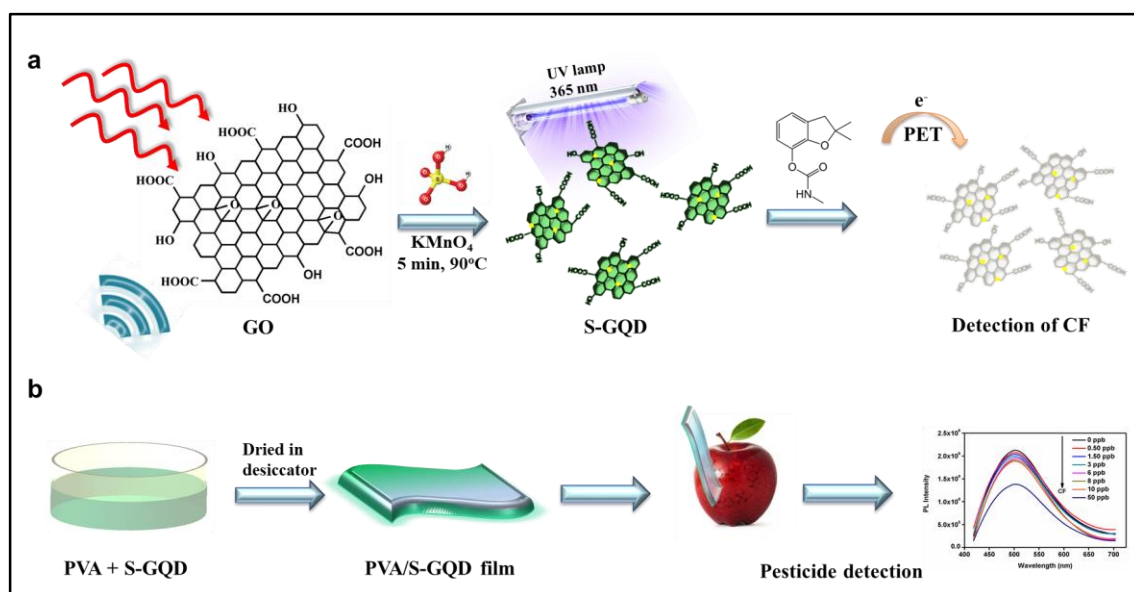


**Scheme 3.1**. Schematic illustration of (a) synthesis of S-GQD by microwave-assisted sonochemical method and (b) the fabrication of S-GQD based fluorescent (PVA/S-GQD) films for the ultrasensitive detection of CF.

## 3.2. Experimental

### 3.2.1. Materials

Graphite (<150 μm), hydrogen peroxide ($H_2O_2$), sodium nitrate ($NaNO_3$), sulphuric acid ($H_2SO_4$), quinine sulphate, Poly(vinyl) alcohol (Mw-31,000-50,000, 98-99 % hydrolysed), carbofuran and thiram were purchased from Sigma-Aldrich (India). Potassium permanganate ($KMnO_4$) was purchased from SD Fine-Chemicals Limited (India). For all experiments ultrapure deionized water with a resistivity of 18.2 MΩ.cm at 25 °C (Milli-Q D3, Merck, Germany) was used.

### 3.2.2. Synthesis of sulphur-doped graphene quantum dots (S-GQDs)

Sulphur-doped graphene quantum dots (S-GQDs) were prepared from GO using $H_2SO_4$ as doping source and $KMnO_4$ as oxidizing agent. Briefly, GO (1 mg/mL) and $KMnO_4$ (1 M) were mixed in 1:1 ratio in 10 ml of $H_2SO_4$ (0.1 M) to form a homogeneous mixture. This mixture was treated under microwave-assisted sonochemical method in a microwave reactor (Sieno UWave 1000.uv.us) for 5 min at a microwave power of 400 W at 90 °C. The mixture was then centrifuged at 3000 rpm for 10 min to remove the unreacted GO. The supernatant solution obtained after centrifugation was then filtered using a 0.45 μm polytetrafluoroethylene membrane and the filtrate was dialyzed using 1,000 Da dialysis bag. Then the solvent was evaporated to obtain pure solid S-GQDs.

### 3.2.3. Fabrication of Poly (vinyl) alcohol/S-doped GQD (PVA/S-GQD) composite film

To fabricate PVA/S-GQD composite films, the PVA pellets and varying amounts of S-GQDs (Table 3.1) were mixed in 20 mL of water by stirring at 70 °C for 4 h. The S-GQDs dispersed almost instantly. Additional bath sonication was done for 10 min to ensure the good dispersion. Subsequently, 5 mL of PVA/S-GQD solution was poured into a glass petri dish and dried under vacuum (12 torr pressure) in a desiccator for 24 h at room temperature. PVA/S-GQD nanocomposites containing different weight percentages of S-GQDs (1 wt %, 5 wt %, 10 wt %, 20 wt % and 30 wt %) were prepared.

**Table 3.1.** Composition of bare PVA and S-GQD for the fabrication of PVA/S-GQD.

| Sl. No: | PVA | S-GQD | Wt% of S-GQD in PVA/S-GQD |
|---------|-------|--------|---------------------------|
| 1 | 99 mg | 1 mg | 1 wt % |
| 2 | 95 mg | 5 mg | 5 wt % |
| 3 | 90 mg | 10 mg | 10 wt % |
| 4 | 80 mg | 20 mg | 20 wt % |
| 5 | 70 mg | 30 mg | 30 wt % |

### 3.2.4. Sensitive detection of pesticides

The sensitive detection of a set of pesticides was done using an aqueous solution of S-GQD and its composite film form (PVA/S-GQD) at room temperature. For the detection, two common carbamate pesticides carbofuran (CF) and thiram (Tr) were selected. To study the sensitivity towards these pesticides, the fluorescence emission spectra of S-GQDs (0.05 mg/mL) as well as PVA/S-GQD composite films in the presence and absence of these pesticides were recorded with an excitation wavelength of 380 nm. For aqueous form detection, a series of concentrations of CF (0 ppb-225 ppb), and Tr (0 ppb-800 ppb) were freshly prepared and mixed with S-GQDs (0.05 mg/mL). For the study using PVA/S-GQD composite film, the films were immersed in pesticide solutions (CF and Tr) at concentrations ranging from 0-1.5 ppm for 30 min and dried at room temperature. The quenching effects of fluorescence of both S-GQD and PVA/S-GQD films with the presence of these pesticides were analysed by recording the PL spectra.

### 3.2.5. Detection in real samples

To demonstrate the applicability of S-GQD-based fluorescent sensors in practical applications, real samples (apple fruit) purchased from local market was tested. The pre-treatment processing of the sample was done as described in the literature.[43] Firstly, the fruit sample was homogenized to a free-flowing puree in a mortar, and then centrifuged for 10 min at 3000 rpm to remove the solid content. The supernatant was then filtered through 0.22 μm membrane filter. Various

concentrations (0-50 ppb) of carbofuran (CF) were spiked to this filtered solution and mixed with GQDs (0.05 mg/mL) for further analysis.

### 3.2.6. Characterizations

The size and morphological characterizations of S-GQDs were carried out using transmission electron microscope (TEM) operated at an accelerating voltage of 300 kV on FEI Tecnai 30 G2S-TWIN transmission electron microscope. The HR-TEM images were further analysed with Gatan Digital Micrograph software. Atomic force microscopy (AFM) analysis was performed at ambient temperature using MultiMode 8 AFM equipped with NanoScope V controller (Bruker, Santa Barbara, CA, USA). Si cantilevers (NSG 01, NT-MDT) with a typical radius of curvature of approximately 10 nm were used. The force constant of AFM probe used was in the range of 2.5-10 N/m with a resonance frequency in the range of 120-180 kHz. The scan rate used was 1 Hz. Raw data were processed using Bruker's NanoScope Analysis software. The FT-IR spectra were measured with a Perkin Elmer Series Spectrum Two FT-IR spectrometer over the wavenumber range 4000-500 $cm^{-1}$. Wide angle X-ray scattering measurements were carried out on XEUSS SAXS/WAXS system using the Genix micro source from Xenocs operated at 50 kV and 0.6 mA. The Cu $K_\alpha$ radiation ($\lambda$= 1.54 Å) was collimated with FOX2D mirror and two pairs of scattering fewer slits from Xenocs.

The UV-Visible (UV-Vis) absorption spectra of the GQDs were measured using a spectrophotometer (SHIMADZU UV-2401 PC, Shimadzu, Japan) using a 1 cm path length quartz cell at room temperature. The photoluminescence (PL) spectra of GQDs were recorded on a Spex-Fluorolog FL22 spectrofluorimeter equipped with a double grating 0.22 m Spex 1680 monochromator and a 450 W Xe lamp as the excitation source. Raman spectra were recorded using WI-Tec Raman microscope (Witec Inc. Germany, alpha 300R) with a laser beam directed to the sample through 60x water immersion objective and a Peltier cooled CCD detector. Samples were excited with a 632.8 nm excitation wavelength laser and Stokes-shifted Raman spectra were collected in the range of 0 to 3000 $cm^{-1}$ with 1 $cm^{-1}$ resolution. X-ray photoelectron spectroscopy (XPS) was carried out using PHI 5000 Versa Probe II (ULVAC-PHI Inc., USA) equipped with micro-focused (200 μm, 15 KV) monochromatic Al-Kα X-Ray source (hν = 1486.6 eV). Survey scans were recorded at pass energy of 187.85 eV and high-resolution spectra of the major elements were recorded at 46.95 eV pass energy.

The deconvolution of peaks was performed by using the Multipak software (PHI). Quantum yield was measured using quinine sulphate in 0.05 M sulphuric acid solution as a standard. Fluorescence lifetime experiments were conducted using a Delta Flex modular time-correlated single photon counting (TCSPC) spectrometer system, employing the 370 nm nano LED as the excitation source and PPD 850 detector. Decay in the fluorescence intensity (I) with time (t) was fitted by two exponential functions. The quality of the fits was checked by examining the $\chi 2$ value.

## 3.3. Results and discussions

### 3.3.1. Morphological analysis of synthesized S-GQDs

S-GQDs were synthesized using $H_2SO_4$ as the doping source within a short span of time. The structural and morphological analysis of S-GQDs were studied using TEM and AFM. **Figures 3.1 (a-b)** showed TEM images of S-GQDs with relatively uniform shape and size distribution (~5 nm). The Fast Fourier Transform (FFT) pattern is presented as the inset of the corresponding TEM image **(Figure 3.1b).** The HR-TEM images of a single S-GQD indicated **(Figures 3.1c & d)**, two types of lattice parameters which correspond to the hexagonal lattice spacing of $d_{1002}$ (0.340 nm) and $d_{1120}$ (0.242 nm) planes. The AFM height image **(Figure 3.2a)** showed the typical topographic morphology of S-GQDs and the section profile **(Figure 3.2b)** revealed an average height of 400 pm–800 pm which indicates highly exfoliated monolayer graphene quantum dots.
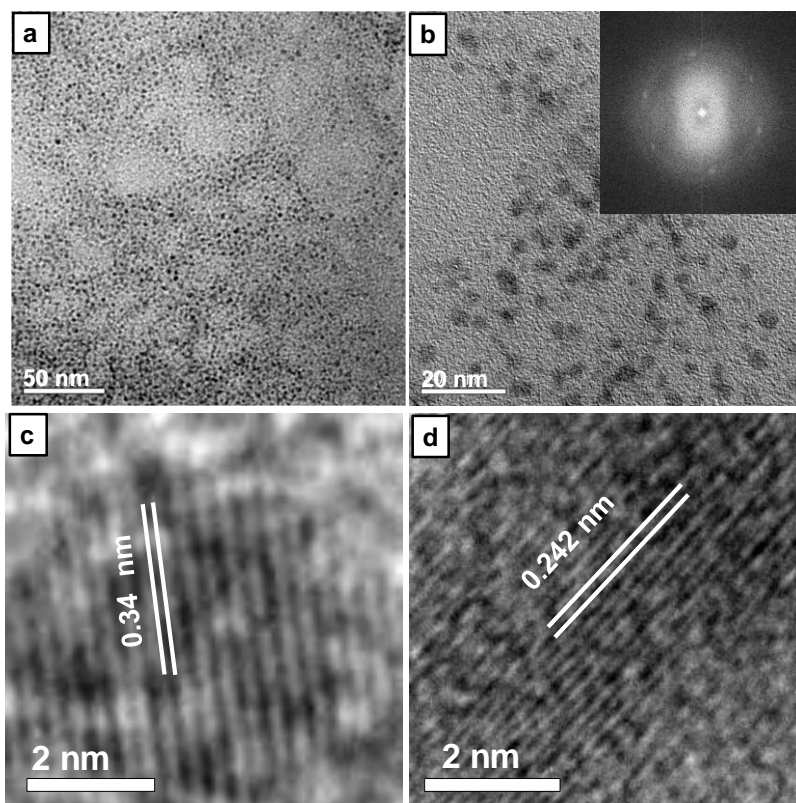
**Figure 3.1**. TEM images of S-GQD at different magnifications (a) Scale bar 50 nm and (b) Scale bar 20 nm. Inset (b) shows the FFT pattern of the corresponding S-GQD. (c) HR-TEM image of a single S-GQD showing the lattice parameters 0.340 nm (d) 0.242 nm.
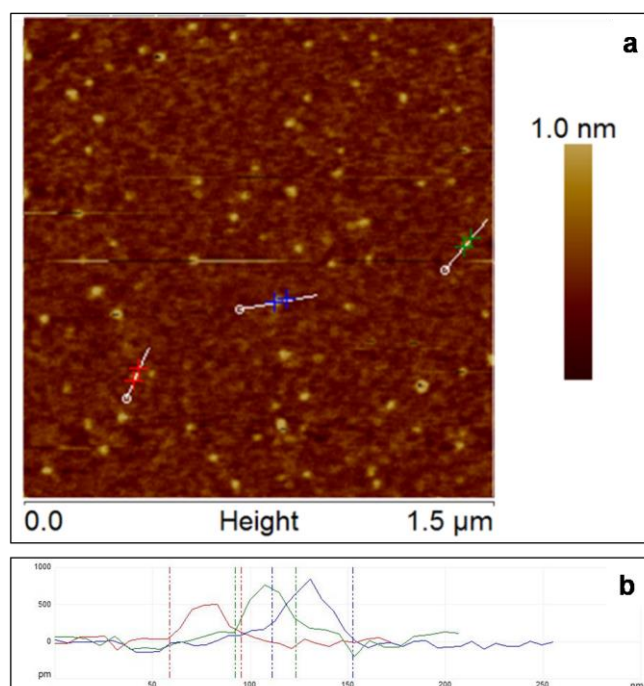


**Figure 3.2**. (a) AFM image of S-GQD and (b) the corresponding height profile.

### 3.3.2. XRD and Raman spectroscopic analysis

The XRD patterns of GO sheets and S-GQD are shown in **Figure 3.3a**. In this case, GO showed a characteristic strong diffraction peak at 2θ of 10.4 ° (002) whereas S-GQD showed a broad and less intense peak of the (002) plane at 2θ of 25.4° indicating that the as-synthesized S-GQDs were of small size consisting of very few layered graphene. Further, Raman spectroscopy was used to investigate the degree of structural disorder in graphene-based materials [44, 45] The Raman spectra of S-GQDs showed two characteristic peaks centred at 1368 and 1647 cm$^{-1}$, attributed to the D-band and G-band respectively **(Figure 3.3b)**. The D-band generally arises due to the defects in the sp$^2$ hybridized carbon and G-band is observed due to the first-order scattering of the stretching vibration mode E$_{2g}$ of sp$^2$ carbon of graphitic domains and the in-plane vibration of sp$^2$ carbon bonded atoms.[46, 47] When compared to undoped graphene quantum dot (GQD), the Raman spectrum of S-GQD showed a slight peak shift to higher wavenumber. The D-band was shifted by 11cm$^{-1}$ and the G-band by 69 cm$^{-1}$. Generally, the intensity ratio of D-band (I$_D$) to G-band (I$_G$), [I$_D$/I$_G$ ] in Raman spectra was calculated for the estimation of disorder in graphene materials.[48] The I$_D$/I$_G$ ratio for the S-GQD was calculated to be 1.38 which is higher than that of undoped GQD.[49] Moreover, similar to other doped graphitic materials, the shift of G-band may be due to the structural distortions in S-GQDs caused by different bond distances of C-C and C-S. Thus, the augmented I$_D$/I$_G$ value and the corresponding shift of the bands of S-GQD indicates the successful doping of sulphur.
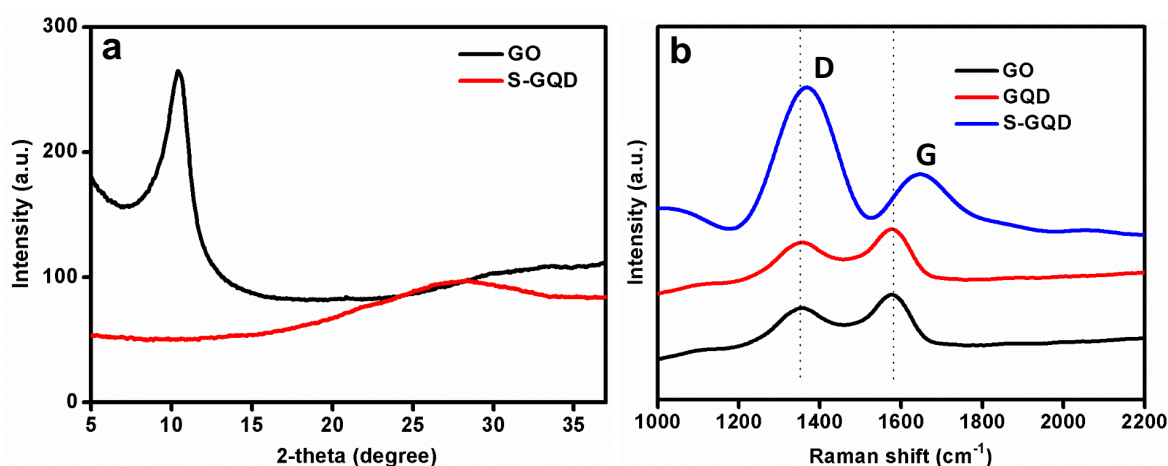


**Figure 3.3**. (a) XRD patterns (b) Raman spectra of GO, GQD and S-GQD

### 3.3.3. FT-IR Spectroscopic Analysis

The surface functionalities of GO and S-GQDs were studied using FT-IR spectroscopy **(Figure 3.4)**. The FT-IR spectra revealed that S-GQD exhibited characteristic peaks of the carboxyl group at 1370 cm$^{-1}$, carbonyl group at 1700 cm$^{-1}$ and the broad absorption peak at 3340 cm$^{-1}$ due to bending vibrations of O-H bonds. The chemical state of S is confirmed based on the peaks of 1096 cm$^{-1}$ (stretching vibrations of S=O) and 635 cm$^{-1}$ (stretching vibrations of C-S). The peak at 1600 cm$^{-1}$ is due to C=C bonds of benzene ring vibrations and that at 1258 cm$^{-1}$ is attributed to the vibrational absorption bands of C-O-C stretching vibrations in epoxides. The remarkable water dispersibility with high stability of S-GQD is ascribed due to the presence of carboxylic, hydroxyl and carbonyl groups in S-GQDs.
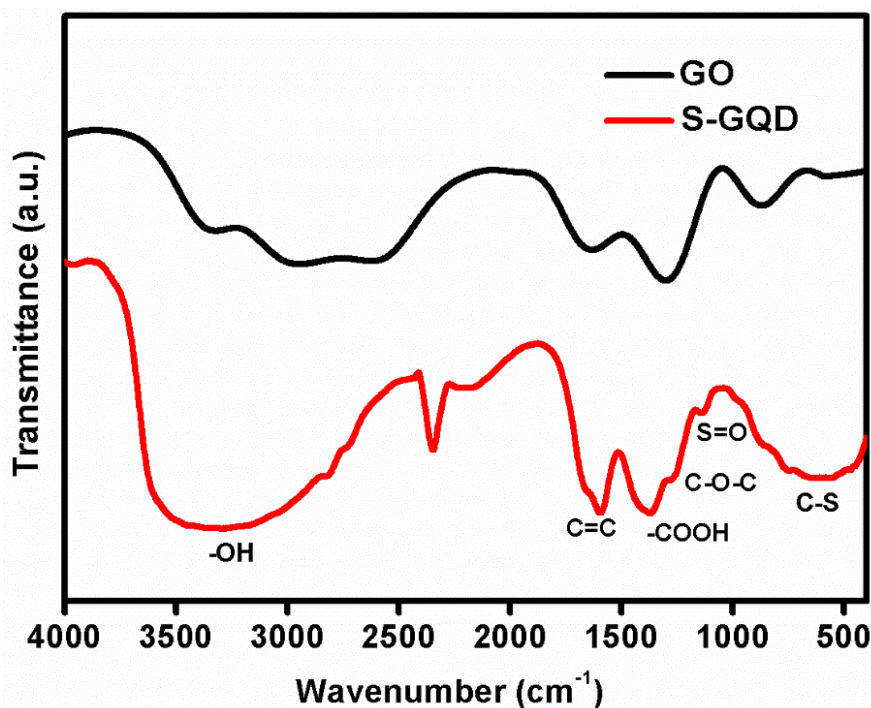


**Figure 3.4**. FT-IR spectra of GO and S-GQD

### 3.3.4. XPS analysis

Furthermore, XPS analysis was carried out to understand the extent of sulphur doping in S-GQDs. The survey spectrum **(Figure 3.5)** of S-GQD clearly showed the presence of C, O and S as major elements with atomic percentages of 58.5 %, 37.3 % and 3.3 %, respectively **(Table 3.2)**. **Figures 3.6 (a-c)** represents the narrow scan of C 1s, O 1s and S 2p in S-GQDs. The deconvoluted C 1s spectrum of S-GQDs **(Figure 3.6a)** revealed the presence of C=C (284.5 eV), C=O (288 eV) and C-S

(286.8 eV) which is in agreement with FT-IR results. Among all, the deconvoluted peak, C=C component shows a higher percentage value, which means that the S-GQDs possess an abundant graphitic structure. The O 1s spectrum **(Figure 3.6b)** of S-GQD was deconvoluted into three peaks at 530.2 eV, 531.5 eV and 529.5 eV that correspond to the presence of -COOH, -OH and C-O, respectively. The S 2p spectrum **(Figure 3.6c)** inferred the existence of C-S bonds in S-GQDs. The peaks located at 167.0 eV and 168.5 eV in the S 2p spectrum of S-GQD confirmed the presence of oxide sulphur and C-S bond in S-GQD.
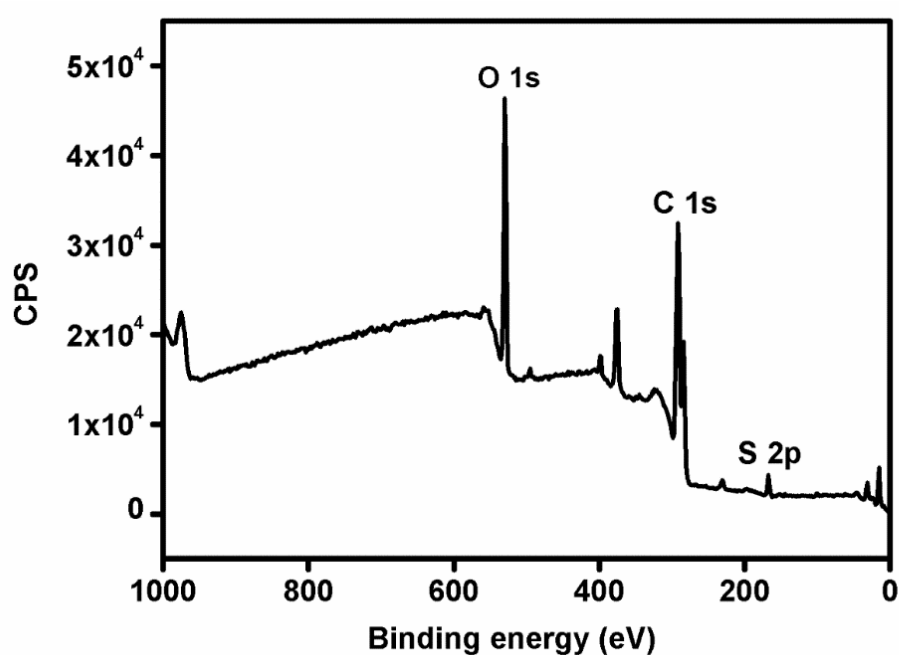


**Figure 3.5.** XPS survey spectrum of S-GQD

**Table 3.2.** Atomic percentage compositions of C, O and S in GO, GQD and S-GQD

| Elements (At %) | C 1s | O 1s | S 2p |
|---|---|---|---|
| GO | 68.4 | 30.3 | - |
| GQD | 54.8 | 33.5 | - |
| S-GQD | 58.5 | 37.3 | 3.3 |
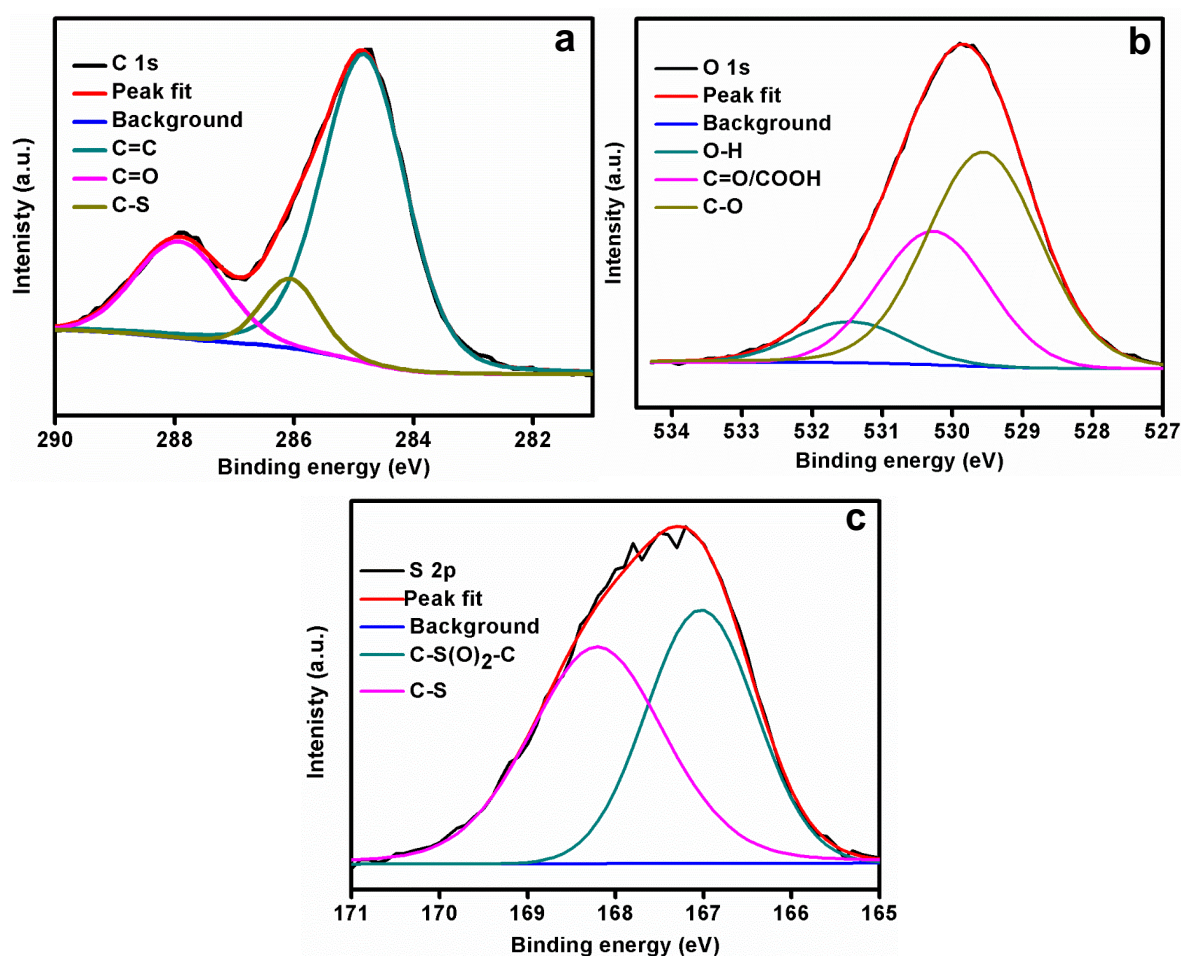
**Figure 3.6**. XPS Narrow scan of, (a) C 1s, (b) O 1s and (c) S 2p of S-GQD.

### 3.3.5. UV-Visible and PL spectroscopic analysis

The optical properties of the fluorescent S-GQDs were studied using UV-Vis and fluorescence spectra. UV-Vis spectra of S-GQD **(Figure 3.7a)** showed distinct broad absorption peak at 380 nm and a strong absorption below 300 nm, which is attributed to the n-π* transition and π-π* transition of aromatic $sp^2$ domains, respectively. Compared to GQD, S-GQD showed a slight red shift from 350 nm to 380 nm. The inset of **Figure 3.7a** shows the digital photographs of GQD and S-GQD irradiated upon 365 nm UV light. The PL spectra of GQD and S-GQD showed the characteristic emission maxima at 430 nm and 500 nm which corresponds to blue and green emissions, respectively **(Figure 3.7b)**. Thus the heteroatom doping strategy results in tuning of optical properties of S-GQD when compared to the undoped GQD.[50] In addition, S-GQD exhibited an excitation-dependent emission and when the excitation wavelength is varied from 400 to 470 nm a red shift was

observed with a remarkable decrease in PL intensity as shown in **Figure 3.7c**. **Figure 3.7d** depicts the respective coordinates in the Commission Internationale de l'Eclairage (CIE) diagram of GQD and S-GQD which confirms the shift in emission spectra.
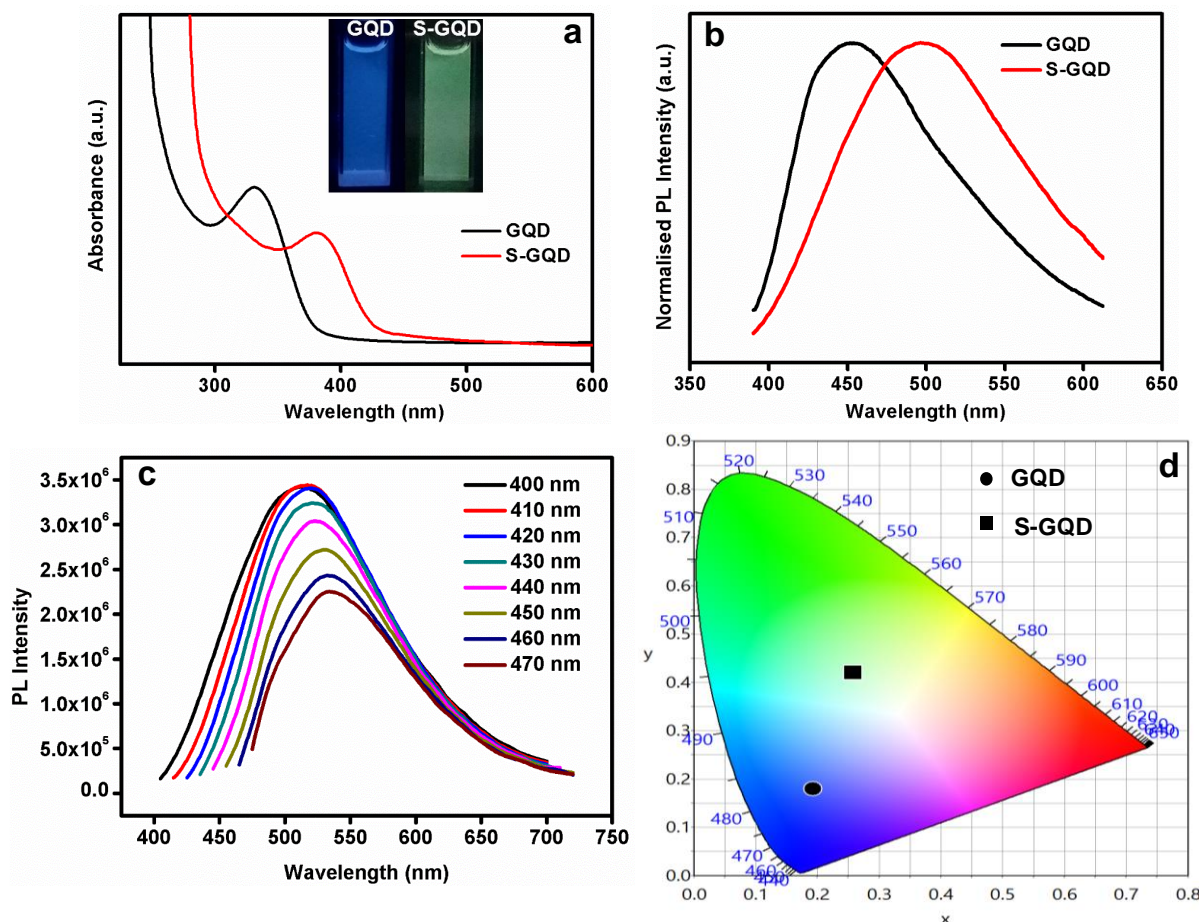


**Figure 3.7** (a) UV-Vis absorption spectra of GQD and S-GQD. The inset shows photographs of GQD and S-GQD irradiated under 365 nm UV light. (b) Normalized PL spectra of GQD and S-GQD excited at 350 nm and 380 nm respectively. (c) PL spectra of S-GQD at different excitation wavelengths from 400 nm to 470 nm. (d) CIE diagram showing the colour coordinates of GQD and S-GQD.

### 3.3.6. Band gap analysis

The optical tuning of S-GQD was further confirmed by band gap calculation using Tauc plot** by plotting h$v$ versus $(\alpha h v)1/2$. The absorption coefficient $\alpha$ is related to

---

**Tauc plot is used to determine the band gap of semiconductors materials, was proposed by Jan Tauc. For a material, its optical absorption depends on the difference between incident light energy and its band gap (Eg), shown as, $(\alpha h v) n\ 1 = A\ (h v - Eg)$, the value of exponent n denotes the direct or indirect band gap materials.

the band gap Eg as, $\alpha h\nu = A\ h\nu - Eg\ \frac{1}{2}$, where hv is the incident photon energy and A is a constant. **Figures 3.8a & b** represent Tauc plots of GQD and S-GQD, respectively. In comparison with the undoped GQD, S-GQD showed a reduction in band gap from 3.05 eV to 2.95 eV which confirms the red shift in PL spectra of S-GQD.[51]
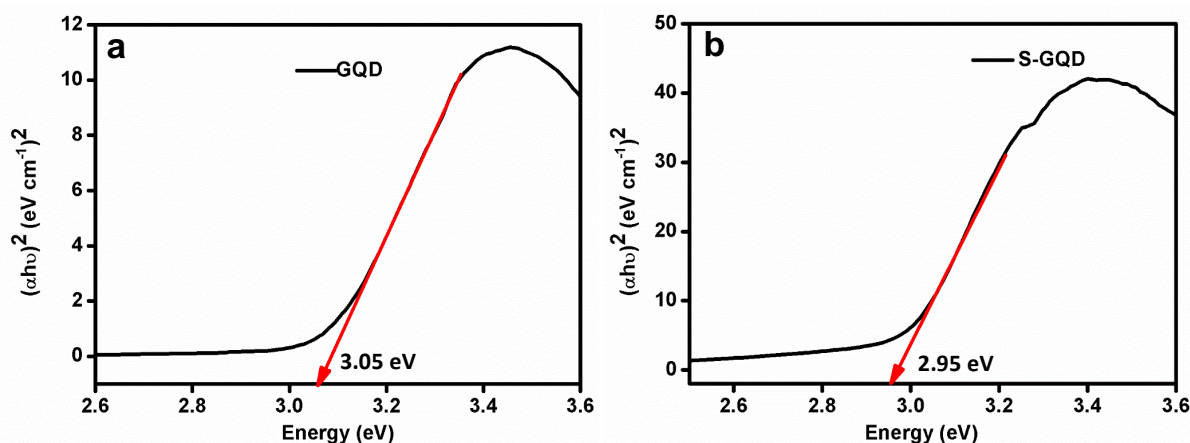


**Figure 3.8.** Tauc plot of (a) GQD showing the band gap of 3.05 eV (b) S-GQD showing the band gap of 2.95 eV.

### 3.3.7. Quantum yield calculation and lifetime analysis

Further, the quantum yield (QY) was estimated using quinine sulphate in 0.05 M sulphuric acid solution as reference. In comparison with GQD which showed QY of 23.7 %,[52] S-GQD showed an improved QY of 27.8 % **(Table 3.3)**. As carbon and sulphur atoms have similar electronegativity, sulphur atoms could replace some of the carbon atoms easily and reduce the aromatic-rich carbon-domains which results in improved fluorescence quantum yield of S-GQDs.[53] The PL lifetime of S-GQD was studied using time-correlated single photon counting (TCSPC) under 378 nm excitation **(Table 3.4)**. The fluorescence lifetime of S-GQDs obtained is 3.3 ns and has two components: 1.82 ns (ca. 38.85 %) and 6.78 ns (ca. 61.15 %) which is longer than undoped GQDs (2.6 ns) **(Figure 3.9).** The doping in the system introduces localized states which can trap photo-excited electrons and hence enhances their PL lifetime.[18] This longer lifetime is beneficial for the application as a fluorescence probe.

**Table 3.3.** Calculation of quantum yield for GQD and S-GQD.

| Sample | Peak Area | Abs at excitation wavelength | Refractive index of the solvent | Quantum Yield (%) |
|---|---|---|---|---|
| Quinine sulphate | $2.23 \times 10^9$ | 0.1 | 1.33 | 0.546 |
| GQD 4 | $8.95 \times 10^8$ | 0.1 | 1.33 | 0.238 |
| S-GQD | $1.17 \times 10^9$ | 0.1 | 1.33 | 0.278 |
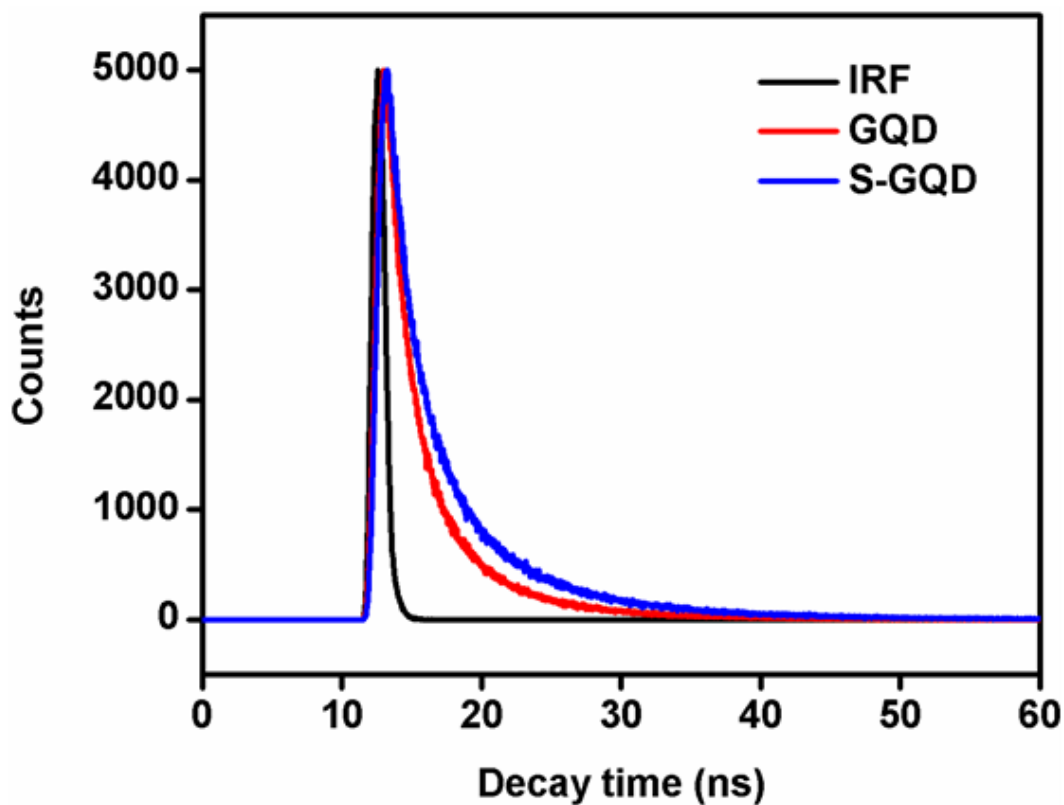


**Figure 3.9.** Time-correlated single photon counting (TCSPC) spectra of GQDs (red) and S-GQD (blue) (378 nm excitation)

**Table 3.4.** Fluorescence lifetime, relative percentage and average lifetime of GQD and S-GQD

| Sample | Life time | Amplitude | Average lifetime (T) |
|--------|-----------|-----------|----------------------|
| GQD | T1=2.513 | A1=52.08 % | 2.26 ns |
|  | T3=3.365 | A3=47.92% |  |
| S-GQD | T1=1.827 | A1=38.85% | 3.30 ns |
|  | T2=6.784 | A2=61.15% |  |

### 3.3.8. Preparation and morphological characterizations of poly (vinyl alcohol)/ S-GQD (PVA/S-GQD) composite film

Poly (vinyl alcohol)/S-GQD composite films containing different weight percentages (1 wt %, 5 wt %, 10 wt %, 20 wt %, and 30 wt %) of S-GQDs were fabricated by mixing corresponding amounts of PVA pellet and S-GQDs in water and stirring at 70 °C for 4 h. Later, 5 mL of PVA/S-GQD dispersion was solution casted and dried at ambient temperature. TEM images show a uniform distribution of S-GQDs in PVA film **(Figures 3.10 a-d)**. **Figure 3.10a** shows TEM image of bare PVA film and **Figures 3.10(b-d)** shows TEM images of different weight percentages of S-GQD (10 wt %, 20 wt %, 30 wt %) loading in PVA matrix. The images with lower loading of S-GQDs demonstrate excellent dispersibility in PVA matrix without any additional surface modifications as it possesses several surface functionalities. This would be a remarkable benefit of S-GQDs over other semiconductor QDs that normally require surface treatments in order to prevent agglomeration.[40] Additionally, the AFM image **(Figure 3.11)** shows well-dispersed S-GQDs in the PVA matrix.
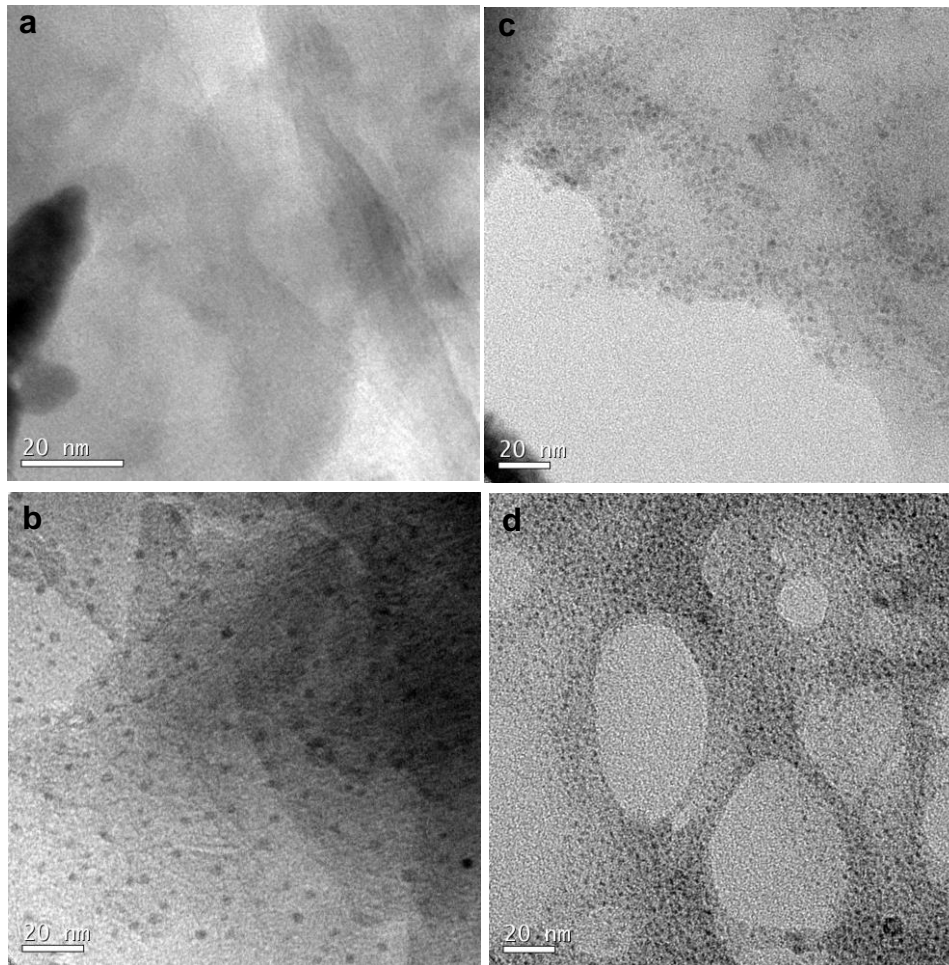
**Figure 3.10**. TEM images of (a) Bare PVA, PVA/S-GQD composite films containing (b) 10 wt %, (c) 20 wt %, and (d) 30 wt % S-GQD loading.
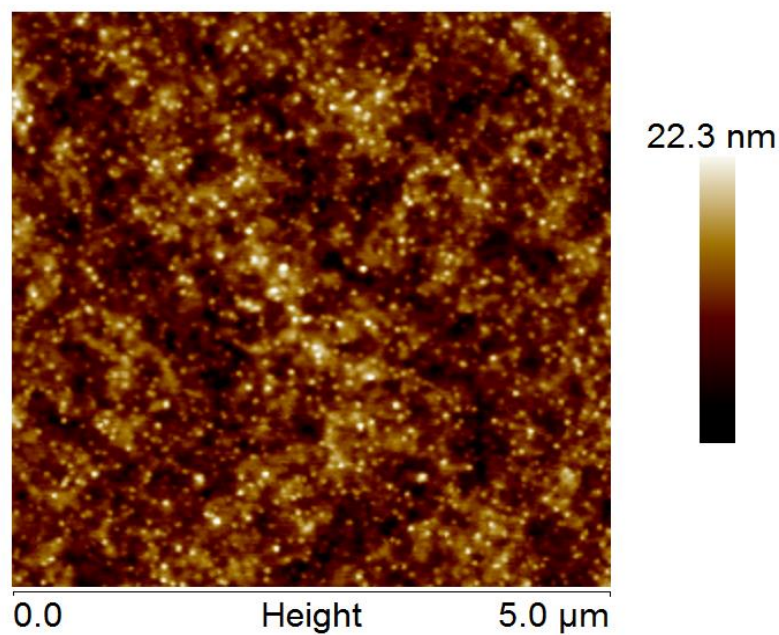


**Figure 3.11**. AFM image of PVA/S-GQD composite containing 20 wt % S-GQD.

### 3.3.9. FT-IR spectroscopic analysis of PVA/S-GQD composite film

To understand the chemical interactions between the PVA matrix and S-GQDs, FT-IR analysis was carried out. The FT-IR spectra of bare PVA and PVA/S-GQD composite films with different S-GQD loadings are shown in **Figure 3.12**. For bare PVA, the broad absorption peak at 3296 cm$^{-1}$ is due to the symmetrical stretching vibration of -OH groups. Generally, the -OH stretching peak is sensitive to the association or disassociation of hydrogen bonding, which will lower the stretching frequencies of O-H bonds.[54] **Figure 3.12** shows that on increasing the amount of S-GQD loading, there is a shift in -OH stretching peak to lower wavenumber in the PVA/S-GQDs composites (from 3296 cm$^{-1}$ of bare PVA to 3261 cm$^{-1}$ of PVA/S-GQD 30 wt %). Thus, the FT-IR studies indicate the formation of hydrogen bonding between S-GQDs and PVA.
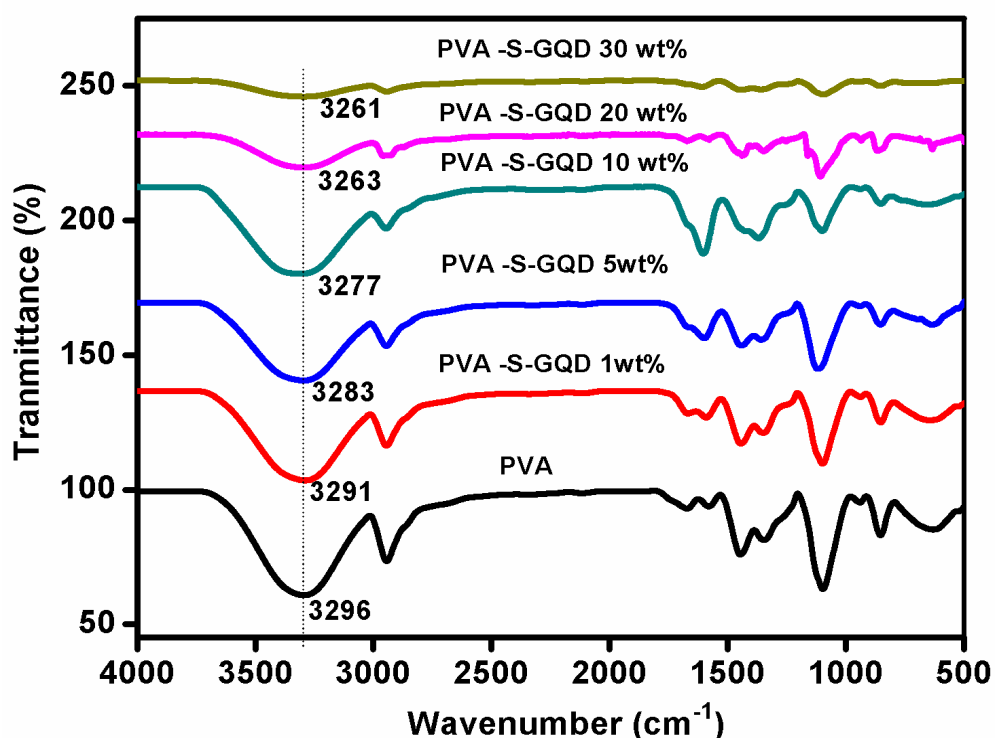


**Figure 3.12.** FT-IR spectra of bare PVA and PVA/S-GQD composites.

### 3.3.10. Optical characterizations of PVA/S-GQD composite films

The optical properties of as-prepared PVA/S-GQD composite films were studied using UV-Visible and PL spectroscopy. **Figure 3.13a** shows UV-Vis spectra of bare PVA and PVA/S-GQD composites containing different weight percentages of S-GQDs (1 wt %, 5 wt %, 10 wt %, 20 wt % and 30 wt %). It is obvious that a distinct

broad absorption peak at 380 nm and a strong absorption below 300 nm were observed from the spectra, which correspond to the n-π* transition and π-π* transition of aromatic sp² domains, respectively. The PL spectra of composite films are quite similar to that of S-GQD excited at 380 nm whereas the PL intensity varies with varying S-GQD loading **(Figure 3.13b)**. The incorporation of S-GQD in PVA matrix imparts luminescence properties to PVA/S-GQD composite films. **Figure 3.13c** presents the respective colour coordinates in the CIE diagram of PVA/S-GQD composite films. As the PVA/S-GQD films exhibit broad photoluminescence emission spectra covering the entire visible region, it opens up the possibility of using these materials as luminophores in white LED.[54] The luminescence behaviour of the composite films was visualized by capturing its photographs under UV light with 365 nm excitation **(Figure 3.13d)**.
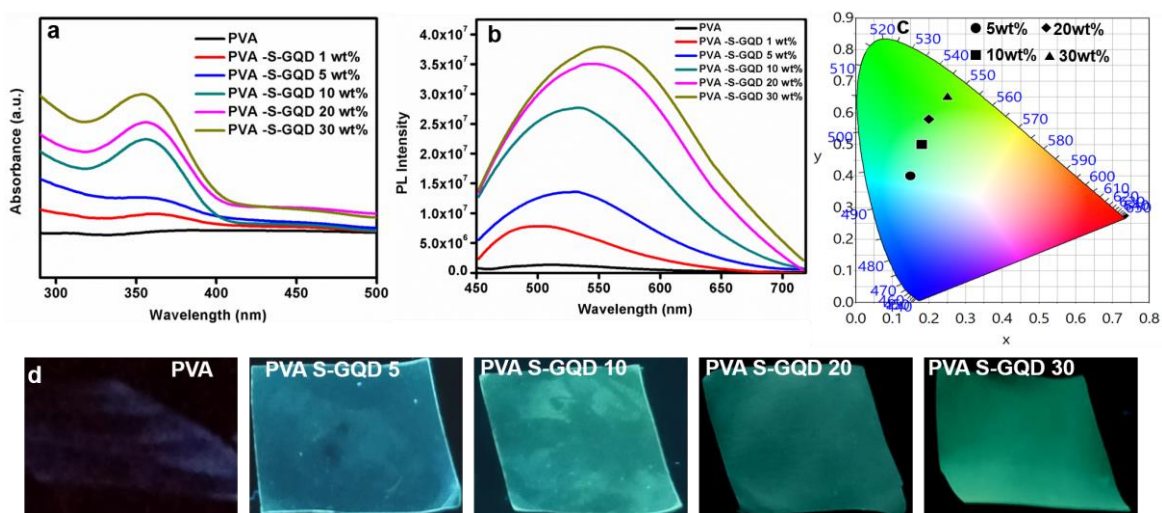


**Figure 3.13.** (a) UV-Vis spectra (b) PL spectra of bare PVA and PVA/S-GQD composites (c) CIE diagram showing the colour coordinates of PVA/S-GQD composites with 5 wt %, 10 wt %, 20 wt % and 30 wt % S-GQD loading. (d) Digital photographs of bare PVA and PVA/S-GQD composites with 5 wt %, 10 wt %, 20 wt %, and 30 wt % S-GQD loading captured under UV light of 365 nm excitation.

### 3.3.11. Sensitive detection of pesticides using aqueous S-GQD and PVA/S-GQD composite films

GQDs have been used as fluorescent sensors due to their unique and tunable optical properties, high photostability and size tunability. In the present study, we employed as-synthesized S-GQDs both in aqueous form and solid-state (PVA/S-GQD composites) for the detection of two carbamate pesticides (CF and Tr) which are extensively used in the agricultural sector to increase crop production. The influence of CF and Tr on the fluorescent intensity of S-GQD in the aqueous phase and composite film were studied by recording its PL spectra in the presence and absence of these pesticides. Experiments were conducted at varying concentrations of CF and Tr, in both solution phase and composite film. It was observed that the fluorescence quenching by these pesticides were concentration dependent. As the concentration of these pesticides increases, the fluorescence intensity of aqueous S-GQD **(Figures 3.14 a-b)** and PVA/S-GQD composites **(Figures 3.15 a-b)** decreases gradually. It is noteworthy that in solution phase, S-GQD shows significant quenching upon increasing the concentration of pesticides with a limit of detection of 0.45 ppb for CF, 1.6 ppb for Tr. **Figures 3.14 (c-d)** show the corresponding linear regression plots of S-GQD with CF and Tr. Further, PVA/S-GQD composite film as solid-state fluorescent sensor was also tested for the detection of these pesticides and it was found that limit of detection was 60 ppb and 210 ppb for CF, and Tr, respectively. **Figures 3.15 (c-d)** shows the corresponding linear regression plots of PVA/S-GQD composite films with CF, and Tr. The mechanism of fluorescent quenching in both aqueous S-GQD and PVA/S-GQD composites by these pesticides is due to the complexation followed by the photo-induced electron transfer mechanism.[†] The oxygen atoms of surface carboxyl groups and sulphur atoms of sulphonic groups of S-GQD, have strong electronegativity and can form complex with carbamate groups of these pesticides through hydrogen bonding. An electron from this complex jumps from ground state to excited state with the absorption of photons and then the electron of the complex goes back to the ground state with the release of heat to the surroundings, and the quenching of S-GQDs occur.[55] Thus, based on the fluorescence quenching responses

---

[†]Photoinduced electron transfer (PET) is an excited state electron transfer process by which an excited electron is transferred from donor to acceptor. Due to PET a charge separation is generated, i.e., redox reaction takes place in excited state.

of S-GQD, both in aqueous solution and solid-state PVA/S-GQD film by these pesticides, a simple fluorescence sensor for the sensitive detection of commonly used toxic carbamate pesticides were demonstrated with fast response and limit of detection in ppb level. We achieved a remarkable limit of detection of pesticides such as carbofuran (0.45 ppb) and thiram (1.6 ppb) in parts per billion (ppb) level.
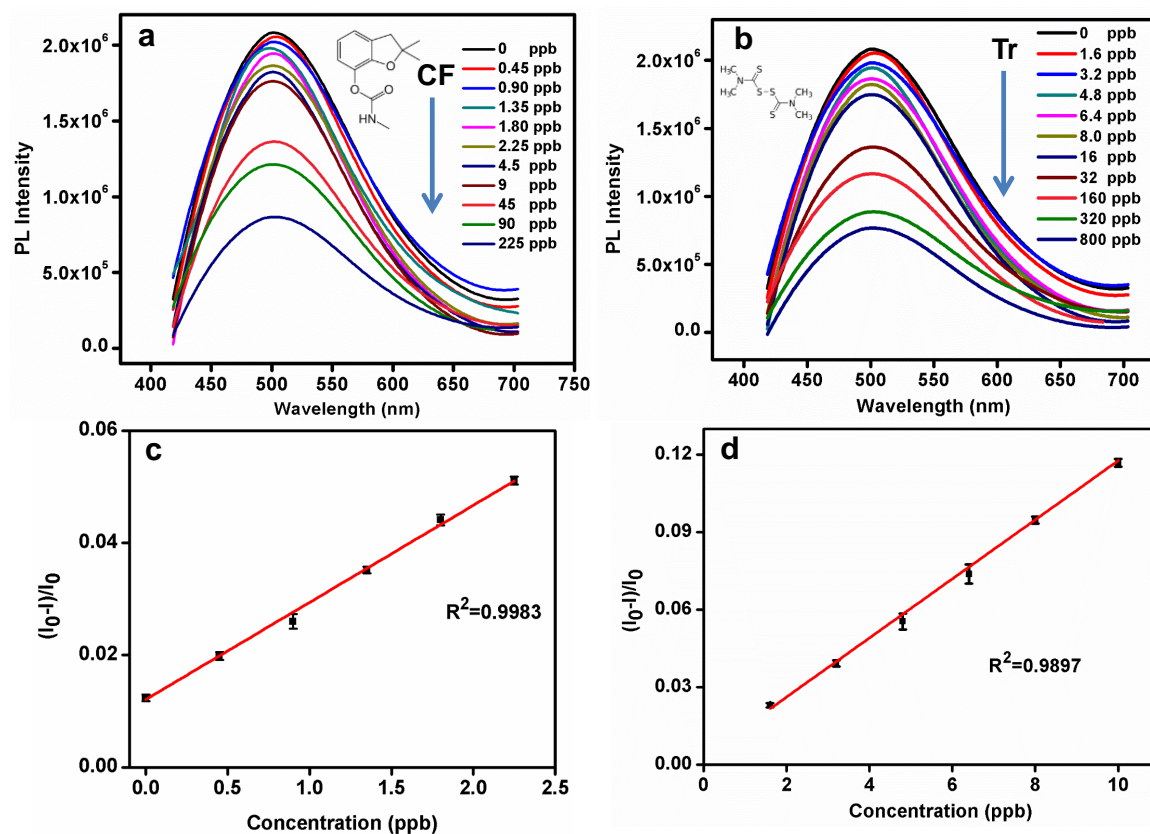


**Figure 3.14.** PL spectra of aqueous S-GQD in the presence of various pesticides namely, (a) Carbofuran and (b) Thiram (c-d) show the corresponding linear regression plots with regression coefficients ($R^2$) values of 0.998 and 0.989, respectively.
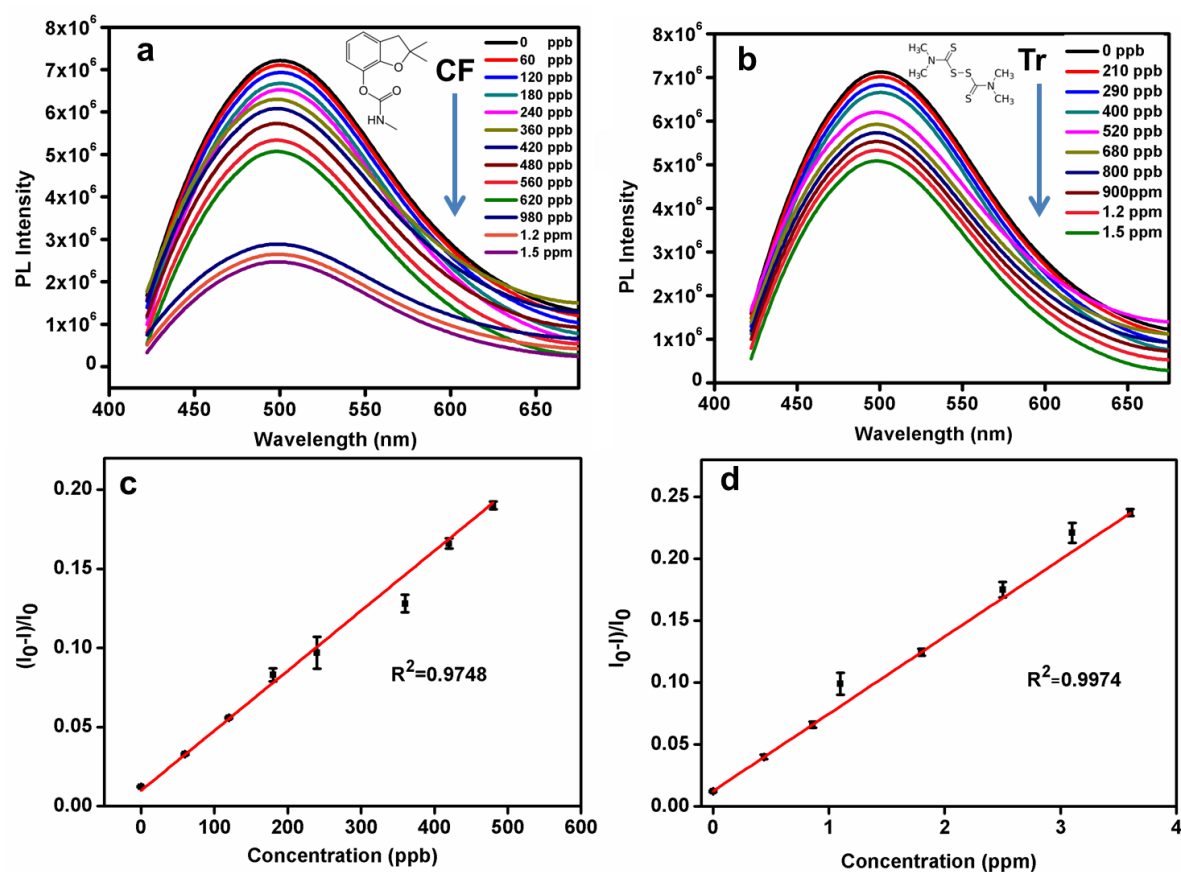
**Figure 3.15.** PL spectra of PVA/S-GQD nanocomposite film in the presence of various pesticides namely, (a) Carbofuran and (b) Thiram (c-d) show the corresponding linear regression plots with regression coefficients ($R^2$) values of 0.974 and 0.997, respectively.

### 3.3.12. Real sample analysis

To validate the practical feasibility of employing S-GQD based fluorescent sensor in real sample analysis, the detection of CF pesticide in apple fruit was studied. The PL spectra of S-GQD with different concentrations of CF spiked apple samples are shown in **Figure 3.16a**. From the figure, it is obvious that S-GQD showed significant quenching upon increasing the concentration of CF with a limit of detection of 0.5 ppb. The fluorescent quenching value (ΔF) showed a linear relationship with the concentration of CF ranging from 0 – 10 ppb **(Figure 3.16b)**.
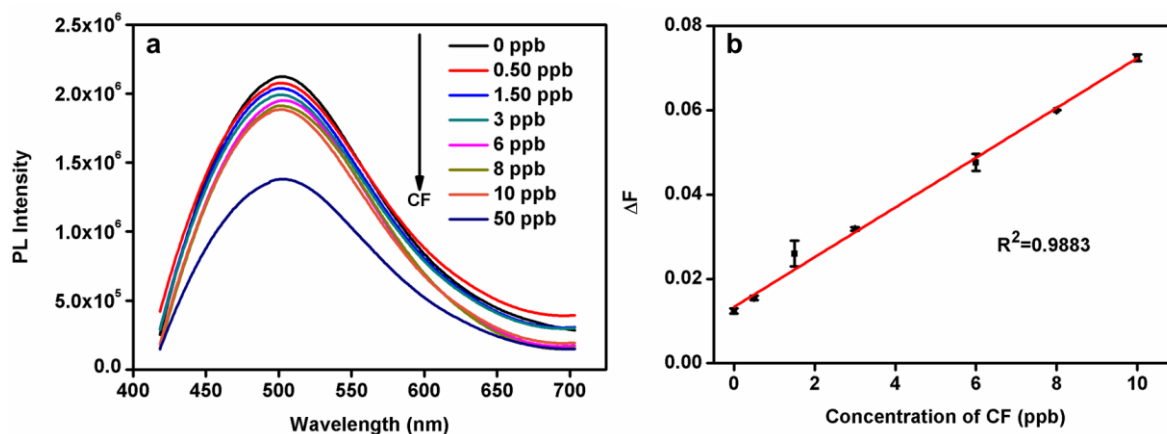
**Figure 3.16.** (a) PL spectra of S-GQD in the presence of different concentrations (0-50 ppb) of CF spiked real samples (b) Linear regression plot of the fluorescent quenching value (ΔF) *vs* concentration of CF ranging from 0 to 50 ppb with regression coefficient ($R^2$) value of 0.988.

## 3.4. Conclusions

In conclusion, a facile S-GQD-based fluorescence sensor was demonstrated for the sensitive detection of commonly used carbamate pesticides. In the present chapter, S-GQDs with stable green fluorescence, relatively higher quantum yield, longer lifetime and high production yield was synthesized from graphene oxide within 5 min. Successful doping of sulphur atom in S-GQD was confirmed with XPS and FT-IR spectroscopy. As part of realization of a simple flexible solid-state fluorescent sensor, PVA/S-GQD composite films were fabricated. Both aqueous S-GQD and PVA/S-GQD flexible films were demonstrated as excellent fluorescent probes for the ultrasensitive detection of pesticides with a remarkable limit of detection at ppb level for CF (0.45 ppb) and Tr (1.6 ppb). Additionally, the S-GQD -based fluorescent sensor was successfully applied for the detection of CF pesticide in real samples with ppb level sensitivity. Thus, our approach would be suitable for the cost-effective synthesis of relatively non-toxic quantum dots with high production yield which can be applied as viable fluorescent sensors for the trace-level detection of pesticide residues for food safety and environment monitoring.

# References

1.      M. A. Beketov, B. J. Kefford, R. B. Schäfer and M. Liess, *Proceedings of the National Academy of Sciences*, 2013, **110**, 11039-11043.

2.      G. Aragay, F. Pino and A. Merkoci, *Chemical reviews*, 2012, **112**, 5317-5338.

3.      N. Duan, S. Wu, S. Dai, H. Gu, L. Hao, H. Ye and Z. Wang, *Analyst*, 2016, **141**, 3942-3961.

4.      S. A. Nsibande and P. B. C. Forbes, *Analytica Chimica Acta*, 2016, **945**, 9-22.

5.      D. Barceló, *Journal of Chromatography A*, 1993, **643**, 117-143.

6.      M. Z. Khan and F. C. Law, *Proceedings of the Pakistan Academy of Sciences*, 2005, **42**, 315-323.

7.      G. Matthews, *Pesticides: health, safety and the environment*, John Wiley & Sons, 2015.

8.      X. Yan, H. Li and X. Su, *TrAC Trends in Analytical Chemistry*, 2018, **103**, 1-20.

9.      G. Begum, *Aquatic toxicology*, 2004, **66**, 83-92.

10.     B. Singh, D. Sharma and A. Gupta, *Journal of hazardous materials*, 2009, **161**, 208-216.

11.     O. Kiguchi, K. Oka, M. Tamada, T. Kobayashi and J. Onodera, *Journal of Chromatography A*, 2014, **1370**, 246-254.

12.     H. Chen, H. Zhang, R. Yuan and S. Chen, *Analytical chemistry*, 2017, **89**, 2823-2829.

13.     D. Liu, W. Chen, J. Wei, X. Li, Z. Wang and X. Jiang, *Analytical chemistry*, 2012, **84**, 4185-4191.

14.     C. K. Zacharis, I. Rotsias, P. G. Zachariadis and A. Zotos, *Food chemistry*, 2012, **134**, 1665-1672.

15.     A. M. Hegazy, R. M. Abdelfatah, H. M. Mahmoud and M. A. Elsayed, *Beni-Suef University Journal of Basic and Applied Sciences*, 2018, **7**, 598-605.

16.     G. Zweig, *Chromatographic Reviews*, 1964, **6**, 110-128.

17.     I. Walton, M. Davis, L. Munro, V. J. Catalano, P. J. Cragg, M. T. Huggins and K. J. Wallace, *Organic letters*, 2012, **14**, 2686-2689.

18.     H. Li, C. Sun, R. Vijayaraghavan, F. Zhou, X. Zhang and D. R. MacFarlane, *Carbon*, 2016, **104**, 33-39.

19.    P. Mandal, D. Sahoo, P. Sarkar, K. Chakraborty and S. Das, *New Journal of Chemistry*, 2019, **43**, 12137-12151.

20.    A. M. Gravagnuolo, E. Morales-Narváez, S. Longobardi, E. T. da Silva, P. Giardina and A. Merkoçi, *Advanced Functional Materials*, 2015, **25**, 2771-2779.

21.    M. Li, W. Wu, W. Ren, H.-M. Cheng, N. Tang, W. Zhong and Y. Du, *Applied Physics Letters*, 2012, **101**, 103107.

22.    R. Ye, Z. Peng, A. Metzger, J. Lin, J. A. Mann, K. Huang, C. Xiang, X. Fan, E. L. Samuel and L. B. Alemany, *ACS applied materials & interfaces*, 2015, **7**, 7041-7048.

23.    D. Pan, J. Zhang, Z. Li and M. Wu, *Advanced Materials*, 2010, **22**, 734-738.

24.    M. Nurunnabi, Z. Khatun, G. R. Reeck, D. Y. Lee and Y.-k. Lee, *ACS applied materials & interfaces*, 2014, **6**, 12413-12421.

25.    J. Shen, Y. Zhu, X. Yang and C. Li, *Chemical Communications*, 2012, **48**, 3686-3699.

26.    Z. Luo, G. Qi, K. Chen, M. Zou, L. Yuwen, X. Zhang, W. Huang and L. Wang, *Advanced Functional Materials*, 2016, **26**, 2739-2744.

27.    S. Zhuo, M. Shao and S.-T. Lee, *ACS Nano*, 2012, **6**, 1059-1064.

28.    J.-J. Liu, X.-L. Zhang, Z.-X. Cong, Z.-T. Chen, H.-H. Yang and G.-N. Chen, *Nanoscale*, 2013, **5**, 1810-1815.

29.    C. Sahub, T. Tuntulani, T. Nhujak and B. Tomapatanaget, *Sensors and Actuators B: Chemical*, 2018, **258**, 88-97.

30.    H. Tetsuka, R. Asahi, A. Nagoya, K. Okamoto, I. Tajima, R. Ohta and A. Okamoto, *Advanced Materials*, 2012, **24**, 5333-5338.

31.    S. Zhu, J. Zhang, X. Liu, B. Li, X. Wang, S. Tang, Q. Meng, Y. Li, C. Shi, R. Hu and B. Yang, *RSC Advances*, 2012, **2**, 2717-2720.

32.    Y. Du and S. Guo, *Nanoscale*, 2016, **8**, 2532-2543.

33.    Q. Xu, T. Kuang, Y. Liu, L. Cai, X. Peng, T. S. Sreeprasad, P. Zhao, Z. Yu and N. Li, *Journal of Materials Chemistry B*, 2016, **4**, 7204-7219.

34.    F. Joucken, Y. Tison, J. Lagoute, J. Dumont, D. Cabosart, B. Zheng, V. Repain, C. Chacon, Y. Girard and A. R. Botello-Méndez, *Physical Review B*, 2012, **85**, 161408.

35.    Y. Dong, H. Pang, H. B. Yang, C. Guo, J. Shao, Y. Chi, C. M. Li and T. Yu, *Angewandte Chemie*, 2013, **125**, 7954-7958.

36.    Q. Xu, P. Pu, J. Zhao, C. Dong, C. Gao, Y. Chen, J. Chen, Y. Liu and H. Zhou, *Journal of Materials Chemistry A*, 2015, **3**, 542-546.

37.    Y. Luo, M. Li, L. Sun, Y. Xu, M. Li, G. Hu, T. Tang, J. Wen, X. Li, J. Zhang and L. Wang, *Journal of Colloid and Interface Science*, 2018, **529**, 205-213.

38.    S. Kadian, G. Manik, A. Kalkal, M. Singh and R. P. Chauhan, *Nanotechnology*, 2019, **30**, 435704.

39.    S. Li, Y. Li, J. Cao, J. Zhu, L. Fan and X. Li, *Analytical Chemistry*, 2014, **86**, 10201-10207.

40.    G. Yang, X. Wan, Y. Liu, R. Li, Y. Su, X. Zeng and J. Tang, *ACS Applied Materials & Interfaces*, 2016, **8**, 34744-34754.

41.    T. Ramanathan, A. Abdala, S. Stankovich, D. Dikin, M. Herrera-Alonso, R. Piner, D. Adamson, H. Schniepp, X. Chen and R. Ruoff, *Nature nanotechnology*, 2008, **3**, 327.

42.    B. Upama and C. Devasish, *Nanotechnology*, 2016, **27**, 145501.

43.    J. Wang, Y. Wu, P. Zhou, W. Yang, H. Tao, S. Qiu and C. Feng, *Analyst*, 2018, **143**, 5151-5160.

44.    K. Ganesan, S. Ghosh, N. G. Krishna, S. Ilango, M. Kamruddin and A. Tyagi, *Physical Chemistry Chemical Physics*, 2016, **18**, 22160-22167.

45.    S. Sangam, A. Gupta, A. Shakeel, R. Bhattacharya, A. K. Sharma, D. Suhag, S. Chakrabarti, S. K. Garg, S. Chattopadhyay and B. Basu, *Green Chemistry*, 2018.

46.    S. Kumar, S. T. Aziz, O. Girshevitz and G. D. Nessim, *The Journal of Physical Chemistry C*, 2018, **122**, 2343-2349.

47.    A. C. Ferrari and J. Robertson, *Physical review B*, 2000, **61**, 14095.

48.    M. Li, S. K. Cushing, X. Zhou, S. Guo and N. Wu, *Journal of Materials Chemistry*, 2012, **22**, 23374-23379.

49.    Y.-C. Lin, C.-Y. Lin and P.-W. Chiu, *Applied Physics Letters*, 2010, **96**, 133110.

50.    X. Hai, J. Feng, X. Chen and J. Wang, *Journal of Materials Chemistry B*, 2018, **6**, 3219-3234.

51.    Noor-Ul-Ain, M. O. Eriksson, S. Schmidt, M. Asghar, P.-C. Lin, P. O. Holtz, M. Syväjärvi and G. R. Yazdi, *Nanomaterials*, 2016, **6**, 198.

52.   R. V. Nair, R. T. Thomas, V. Sankar, H. Muhammad, M. Dong and S. Pillai, *ACS Omega*, 2017, **2**, 8051-8061.

53.   P. R. Kharangarh, S. Umapathy and G. Singh, *Applied Surface Science*, 2018, **449**, 363-370.

54.   A. Kovalchuk, K. Huang, C. Xiang, A. A. Martí and J. M. Tour, *ACS Applied Materials & Interfaces*, 2015, **7**, 26063-26068.

55.   L. Li, G. Wu, G. Yang, J. Peng, J. Zhao and J.-J. Zhu, *Nanoscale*, 2013, **5**, 4015-4039.

# Chapter 4

## Sulphur-Doped Graphene Quantum Dot Based Fluorescent Turn-On Aptasensor for Selective and Ultrasensitive Detection of Omethoate

# Abstract

Development of selective, rapid and facile methods for the detection of harmful substances like pesticides and hazardous chemicals is quite important in environmental monitoring, food safety and safeguarding public health. With an aim of achieving high selectivity towards a particular pesticide, in the current chapter, we design a simple and efficient fluorescent turn-on aptasensor based on sulphur-doped graphene quantum dot (S-GQD) utilizing specific recognition and binding properties of aptamer for the selective and sensitive detection of omethoate, which is a systemic organophosphorus model pesticide. The detection strategy of aptasensor is based on tuning the aggregation-disaggregation mechanism of S-GQD by way of conformational alteration of the recognition probe. Fluorescence turn OFF-ON process includes aggregation-induced quenching of S-GQD with aptamer via S-GQD-aptamer complex formation and its subsequent fluorescence recovery with the addition of omethoate by structural switching of S-GQD-aptamer complex to aptamer-omethoate complex. The sensing strategy does not require any modification of either the signal transmitting nanoparticle or the reporter probe which makes it facile to construct a simple and novel turn-on aptasensor for pesticide detection. The developed 'switch-on' aptasensor has achieved a limit of detection as low as 1 ppb with high selectivity for omethoate over other control pesticides.
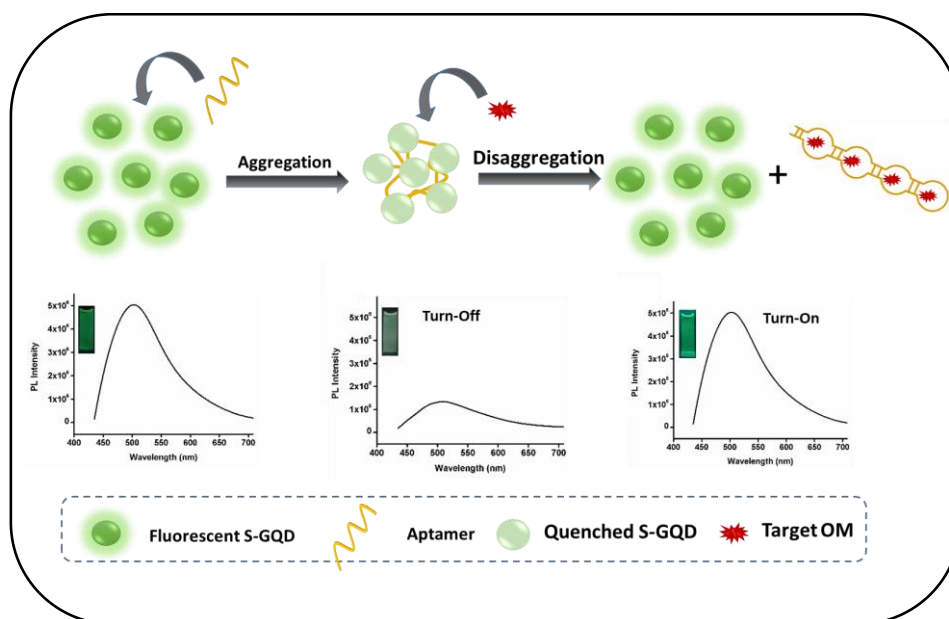
## 4.1. Introduction

In modern commercial and terrace farming agricultural practices, pesticides have become an inevitable component. However, the extensive use of pesticides can cause lethal effects to the environment and living things.[1-3] Hence the simple and rapid detection of pesticides at the levels prescribed by Environmental Protection Agency (EPA) remains as a challenging task for the research community.[4, 5] Current methods for pesticide detection involve spectrophotometric and chromatographic techniques, which are highly sensitive but time-consuming, laborious and require expensive equipment and trained personnel.[6, 7] Therefore, researchers are trying to develop simple and cost-effective sensors for the rapid detection of pesticides.[8, 9] Recent developments for the detection of pesticides rely on the development of biosensors which are highly sensitive, selective and can be miniaturized. A biosensor comprises of a biological recognition element that specifically interacts with a target molecule and a signaling component or transducer that converts the biological interactions into detectable signals.[10, 11] So far, various transducers including optical,[12] colorimetric,[13] acoustic[14] and electrochemical[15] biosensors have been developed.

Though numerous sensors have been reported with different recognition elements, antibodies and enzymes are the most commonly used recognition probes as they have high selectivity and specificity.[16, 17] However, high-temperature sensitiveness and easily denaturing behavior of these recognition probes have limited their applications. Out of the reported recognition elements, aptamers are more specific, sensitive, easily modifiable and stable.[18, 19] Aptamers are referred to as single stranded small nucleic acid chains, selected in vitro by SELEX (Systematic Evolution of Ligands by Exponential Enrichment)* that can fold into specific three-dimensional (3D) structures upon binding with specific targets like proteins, peptides, carbohydrates, toxins, small molecules and even live cells.[20-23] Even though aptamers are termed as chemical antibodies, they are proved to have a number of advantages over antibodies.[24-26] As antibodies are considered, the selection of a

---

*Systematic evolution of ligands by exponential enrichment (SELEX), also referred to as in vitro selection or in vitro evolution, is a combinatorial chemistry technique in molecular biology for producing oligonucleotides of either single-stranded DNA or RNA that specifically bind to a target ligand or ligands.

particular antibody requires a biological system and hence it is very difficult to develop an antibody against non-immunogenic targets and toxins.[27, 28] Therefore, aptamers are proved to be an alternative ligand for the development of new biosensor platforms. In recent times, several aptasensors have been developed adopting different sensing strategies like, electrochemical,[29] optical,[30] fluorescence,[31, 32] Quartz Crystal Microbalance (QCM),[33] etc. Nowadays, quite a lot of fluorescence-based aptasensors have been realized using different fluorophores with the advantage of simplicity, expedient signal transduction, ease in operation and quick response.[32, 34] Widely explored fluorophores are fluorescent dyes,[35] metal quantum dots[36, 37] and graphene quantum dots.[38, 39] Compared with other semiconductor quantum dots (QDs) like CdSe, InAs etc. and organic fluorescent dyes, the advantages of graphene quantum dots (GQD) are low cost, low toxicity and simple synthesis.[40, 41] Mostly the strategy adopted for the development of fluorescence-based aptasensor is the inner filter effect (IFE),[†] which requires a fluorophore as well as an absorber.[42] An aptamer-based fluorescent method has been developed by Li *et al.* for the analysis of bisphenol A based on the IFE of gold nanoparticles on the fluorescence of CdTe quantum dots.[20] But these metallic QDs have higher cytotoxicity and lower biocompatibility, which limits its role in biosensing.[43] Recently, Wang and co-workers have reported an aptasensor based on IFE for ultrasensitive and selective detection of acetamiprid pesticide.[32] However, IFE based sensing approach results in low efficiency and poor sensitivity. A "turn-on" fluorescence sensor based on graphene quantum dots and gold nanoparticles has also been developed utilizing fluorescence resonance energy transfer (FRET)[‡] for $Pb^{2+}$ detection by Niu *et al.*[31] FRET-based sensors have the disadvantage of giving false results, as any external species can cause quenching of the fluorophore. Therefore, current fluorescence-based researches prefer "turn-on" sensors to FRET-based sensors. To the best of our knowledge, there are few reports on the detection of pesticide residues through

---

[†] Inner filter effects results in spectral distortion and in some cases complete loss of signal. It includes reabsorption which happens because another molecule or part of a macromolecule absorbs at the wavelengths at which the fluorophore emits radiation. At that time, some or all of the photons emitted by the fluorophore may be absorbed again.

[‡] Fluorescence resonance energy transfer (FRET) is a physical phenomenon which relies on the distance-dependent transfer of energy from a donor molecule to an acceptor molecule. It is a mechanism describing energy transfer between two light-sensitive molecules. A donor chromophore, initially in its electronic excited state, may transfer energy to an acceptor chromophore through nonradiative dipole–dipole coupling.

"turn-on" principle using non-toxic GQDs.

Omethoate (OM) is a systemic organophosphorus insecticide used in agriculture and horticulture.[44, 45] Even though, it is listed as a human carcinogen and mutagenic, it is still widely used all over the world with the implementation of strict regulations by various monitoring agencies.[46, 47] It is classified as toxicity class Ib of agricultural chemical by the World Health Organization (WHO).[48] In the present chapter, we demonstrated a simple design for a 'turn-on' fluorescence-based aptasensor for the selective detection of the pesticide omethoate. Aptamer strategy based on tuning the aggregation-disaggregation property of sulphur-doped graphene quantum dot (S-GQD) is adopted here for target-specific sensing. Initially, aggregation-induced quenching of S-GQD was mediated by its complex formation with aptamer. Eventually, highly sensitive detection of the pesticide omethoate was achieved by turning on fluorescence signal by structural switching of GQD-aptamer complex to aptamer-omethoate complex. High affinity and specific binding of aptamer to target molecule facilitated in realizing a simple, highly selective and sensitive aptasensor for OM.

## 4.1. Experimental

### 4.2.1. Materials

Graphite (<150 μm), hydrogen peroxide ($H_2O_2$), sodium nitrate ($NaNO_3$), sulphuric acid ($H_2SO_4$), omethoate, carbofuran, methyl parathion, and thiram were purchased from Sigma-Aldrich. Potassium permanganate ($KMnO_4$) was purchased from SD Fine-Chemicals Limited. Ultrapure deionized water (18.2 MΩ cm, 25 °C, Milli-Q D3, Merck, Germany) was used in all the experiments. The oligonucleotides were purchased from Eurofins Genomics. The base sequences are as follows: 5′-AAG CTT GCT TTA TAG CCT GCA GCG ATT CTT GAT CGG AAA AGG CTG AGA GCT ACG C-3′

### 4.2.2. Synthesis of sulphur-doped graphene quantum dots (S-GQDs)

Sulphur-doped graphene quantum dots (S-GQDs) were prepared as said in our Chapter 3. The procedure was described briefly as follows. S-GQDs were prepared from GO using $KMnO_4$ as an oxidising agent and 0.1 M $H_2SO_4$ as a doping source for sulphur by microwave-assisted sonochemical method keeping the reaction temperature constant at 90 °C at a microwave power of 400 W in 5 minutes.

### 4.2.3. Preparation of S-GQD-Apt sensing probe

The as-synthesized S-GQDs were dispersed in water to obtain a concentration of 0.05 mg/mL. The aptamer sequence was selected based on a previous report in which the aptamer sequence, AAG CTT GCT TTA TAG CCT GCA GCG ATT CTT GAT CGG AAA AGG CTG AGA GCT ACG C, have been identified for the selective binding of omethoate by SELEX technique.[49] S-GQD aptamer complex (S-GQD-Apt) was prepared by adding 20 µL of aptamer solution (200 nM) to S-GQD and vortex mixed for 10 min at room temperature. This mixture was centrifuged with a speed of 8000 rpm for 10 min and washed with water to remove excessive aptamer and the obtained S-GQD-Apt complex was used as the sensing probe for the detection of OM.

### 4.2.4. Aptamer based fluorescence detection of OM

The sensitive detection of OM was done using S-GQD-Apt complex in an aqueous medium at room temperature. To study the sensitivity towards OM, fluorescence emission spectra (PL spectra) of S-GQD and S-GQD-Apt complex in the presence and absence of OM was recorded with an excitation wavelength of 380 nm. For the detection, a series of concentrations of OM (0.001 ppm-200 ppm) were freshly prepared and added to S-GQD-Apt complex. The subsequent fluorescence recovery was measured by recording the corresponding PL spectra after 2 h of incubation under the same excitation wavelength. The selectivity towards OM was evaluated by taking the PL emission spectra of S-GQD-Apt complex in the presence of some other pesticides such as carbofuran (CF), methyl parathion (MPr), and Thiram (Tr) of the same concentration (100 ppm) under identical conditions.

### 4.2.5. Recovery of S-GQD (S-GQD-Rec)

100 µL of 300 ppm OM was mixed with the S-GQD-Apt complex and the obtained mixture was vortex mixed for 5 min so that OM and S-GQD-Apt complex can interact with each other efficiently. The S-GQD-Apt-OM mixture was then dialysed in a 12 kDa dialysis bag against ultrapure deionized water for 24 hours. The outer solution containing free S-GQD was replaced with ultrapure water every four hours and stored. The collected outer solution was then concentrated to obtain S-GQD with concentration of 0.039 mg/mL which was about 78 % of initial S-GQD taken. Thus, recovered S-GQD is labelled hereafter as S-GQD-Rec.

### 4.2.6. Characterizations

Transmission electron microscope (TEM) operated at an accelerating voltage of 300 kV on FEI Tecnai 30 G2S-TWIN transmission electron microscope was used for the morphological characterizations. Gatan Digital Micrograph software was used for the analysis of the HR-TEM images. Perkin Elmer Series Spectrum Two FT-IR spectrometer over the wavenumber range 4000-500 cm$^{-1}$ was used for recording FT-IR spectra. The UV-Visible (UV-Vis) absorption spectra were measured using a spectrophotometer (SHIMADZU UV-2401 PC, Shimadzu, Japan) using a 1 cm path length quartz cell at room temperature. Spex-Fluorolog FL22 spectrofluorimeter equipped with a double grating 0.22 m Spex 1680 monochromator and a 450 W Xe lamp as the excitation source was used for recording photoluminescence (PL) spectra. Fluorescence lifetime experiments were conducted using a Delta Flex modular time-correlated single-photon counting (TCSPC) spectrometer system, employing the 330 nm nano LED as the excitation source and PPD 850 detector. Decay in the fluorescence intensity (I) with time (t) was fitted by three exponential functions. The quality of the fits was checked by examining the $\chi 2$ value. X-ray photoelectron spectroscopy (XPS) was performed using PHI 5000 Versa Probe II (ULVAC-PHI Inc., USA) equipped with microfocused (200 μm, 15 KV) monochromatic Al-Kα X-Ray source (hν = 1486.6 eV). Survey scans were recorded with X-ray source power of 23.7 W and pass energy of 187.85 eV. High-resolution spectra of the major elements were recorded at 46.95 eV pass energy. Multipak software (PHI) was used for the deconvolution of peaks.

## 4.3. Results and discussion

### 4.3.1. Design of the sensing probe

Sulphur-doped graphene quantum dots (S-GQDs) with bright green fluorescence were synthesized from graphene oxide (GO) using $H_2SO_4$ as doping source as described in experimental section. We adopted a fluorescence sensing strategy for pesticide detection based on tuning of aggregation-disaggregation of S-GQD. The feasibility of the proposed strategy is validated by treating S-GQDs with an aptamer (Apt) which is a specific recognition molecule for the pesticide, OM. The obtained system, S-GQD-Apt complex which is labelled as S-GQD-Apt is used as the sensing probe for the selective detection of OM.

### 4.3.2. UV-Visible spectroscopic analysis

S-GQD and S-GQD-Apt complex were characterized by UV-Visible spectroscopy. The UV-Visible absorption spectrum of S-GQD-Apt complex indicates the complexation of aptamer with S-GQD **(Figure 4.1)**. Here, in addition to the characteristic absorption peak of S-GQD at 380 nm, an additional peak at 260 nm was observed which corresponds to aptamer, indicating successful complexation of aptamer with S-GQD.
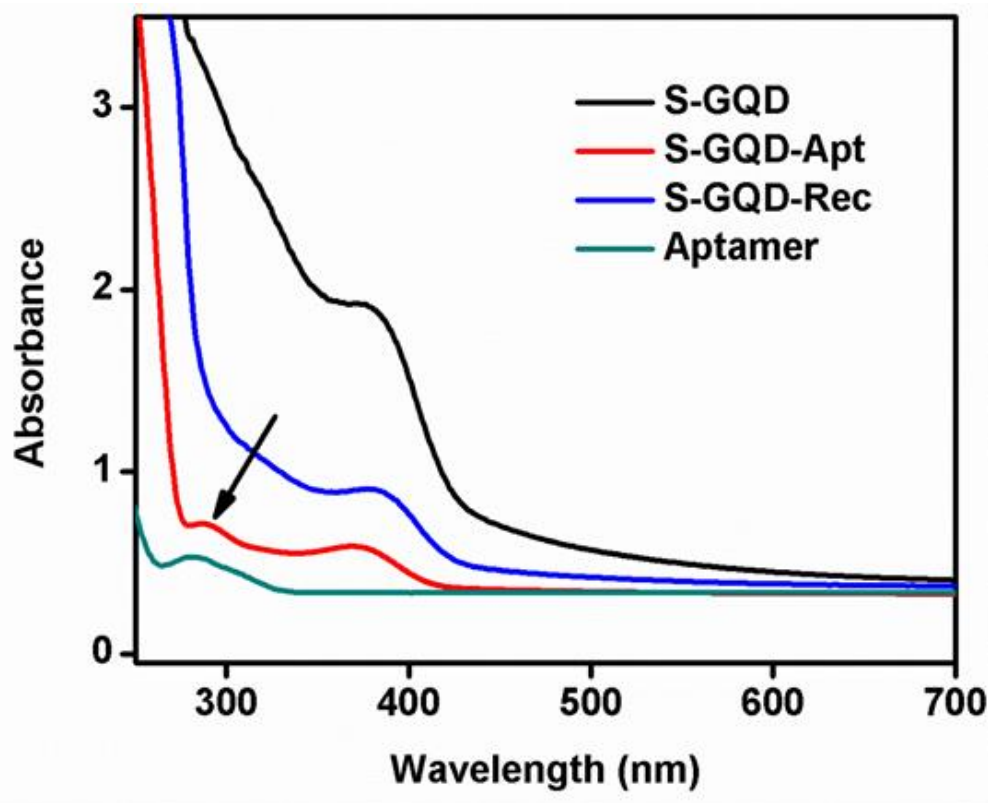


**Figure 4.1.** UV-Visible Spectra of S-GQD, S-GQD-Apt complex and SGQD-Rec**.**

### 4.3.3. FT-IR spectroscopic analysis

From the FT-IR spectra it is observed that both S-GQD and S-GQD-Apt complex showed characteristic peaks including a broad bending vibration of -OH at 3340 cm$^{-1}$, C=O vibration peaks at 1700 cm$^{-1}$, C=C stretching vibration peaks at 1600 cm$^{-1}$, S=O at 1096 cm$^{-1}$ and C-S stretching vibrations at 635 cm$^{-1}$ **(Figure 4.2)**. Besides, a few additional peaks at 1130 cm$^{-1}$, 851 cm$^{-1}$ and 640 cm$^{-1}$ corresponding to symmetric phosphate, P-O and P-C, respectively were obtained in S-GQD-Apt complex which shows the complexation of S-GQD with aptamer (Inset of **Figure 4.2)**.
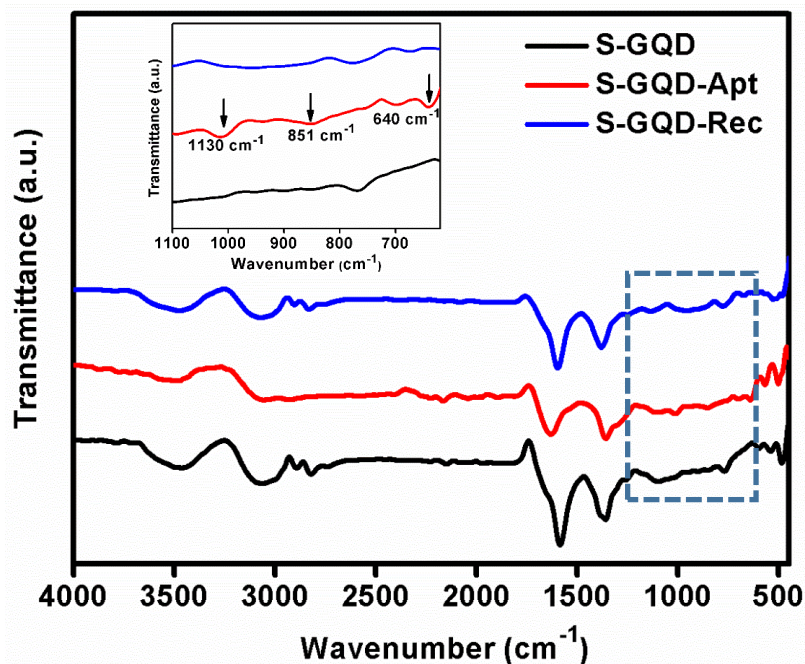
**Figure 4.2.** FT-IR spectra of S-GQD, S-GQD-Apt complex and SGQD-Rec

### 4.3.4. XPS analysis

Further, XPS analysis was carried out to confirm the formation of S-GQD-Apt complex. The survey spectra **(Figure 4.3)** of S-GQD-Apt complex showed C, O and S as major elements. Additionally, it showed peaks at 399.4 eV and 133.2 eV corresponding to N 1s and P 2p, respectively, indicating the formation of S-GQD-Apt complex. The atomic percentage compositions of the characteristic elements in the complex are shown in **Table 4.1**. **Figures 4.4 (a-e)** show the deconvoluted C 1s, O 1s, S 2p, N 1s and P 2p spectra of S-GQD-Apt complex. The C 1s peaks at 288.4 eV (N-C=O), O 1s peaks at 133.7 eV (P=O), N 1s peak at 400.4 eV (HNC=O), P 2p peaks at 132.5 eV (P-O), 133.8 eV (P=O) and 134.3 eV (P-O-C) confirmed the formation of S-GQD-aptamer complex.
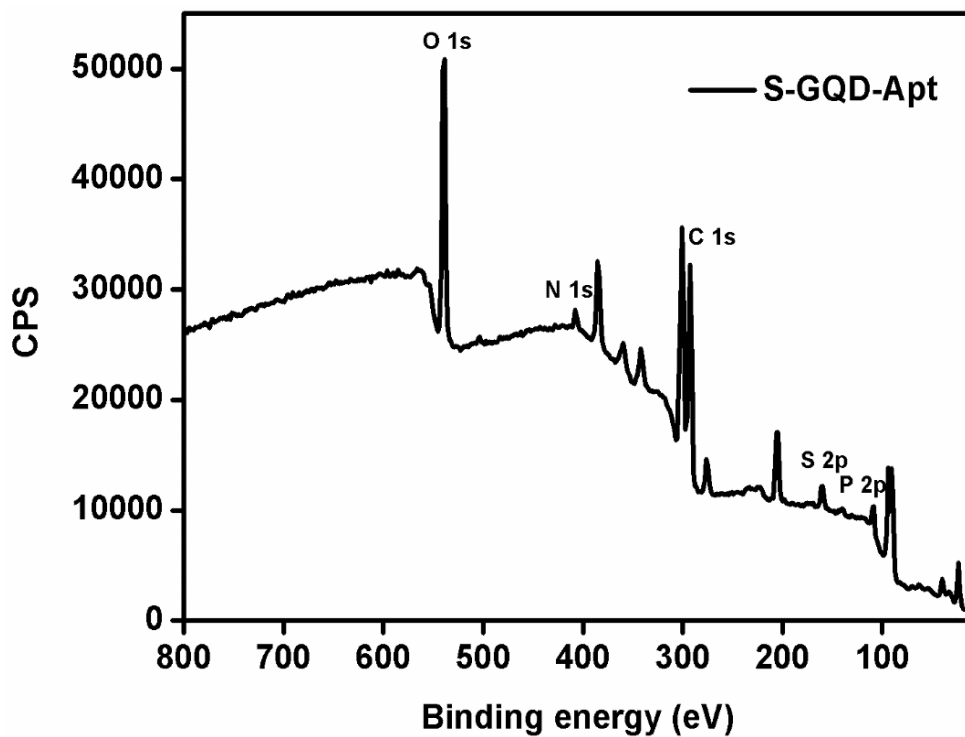
**Figure 4.3.** XPS survey spectra of S-GQD-Apt complex

**Table 4.1.** Atomic percentage compositions of the characteristic elements in S-GQD, S-GQD -Apt complex and S-GQD-Rec

| Elements (At %) | C 1s | O 1s | S 2p | N 1s | P 2p |
|:---:|:---:|:---:|:---:|:---:|:---:|
| S-GQD | 58.5 | 37.3 | 3.3 | - | - |
| S-GQD-Apt | 54.7 | 36.5 | 2.6 | 3.5 | 1.8 |
| S-GQD Rec | 59.2 | 36.8 | 3.1 | - | - |
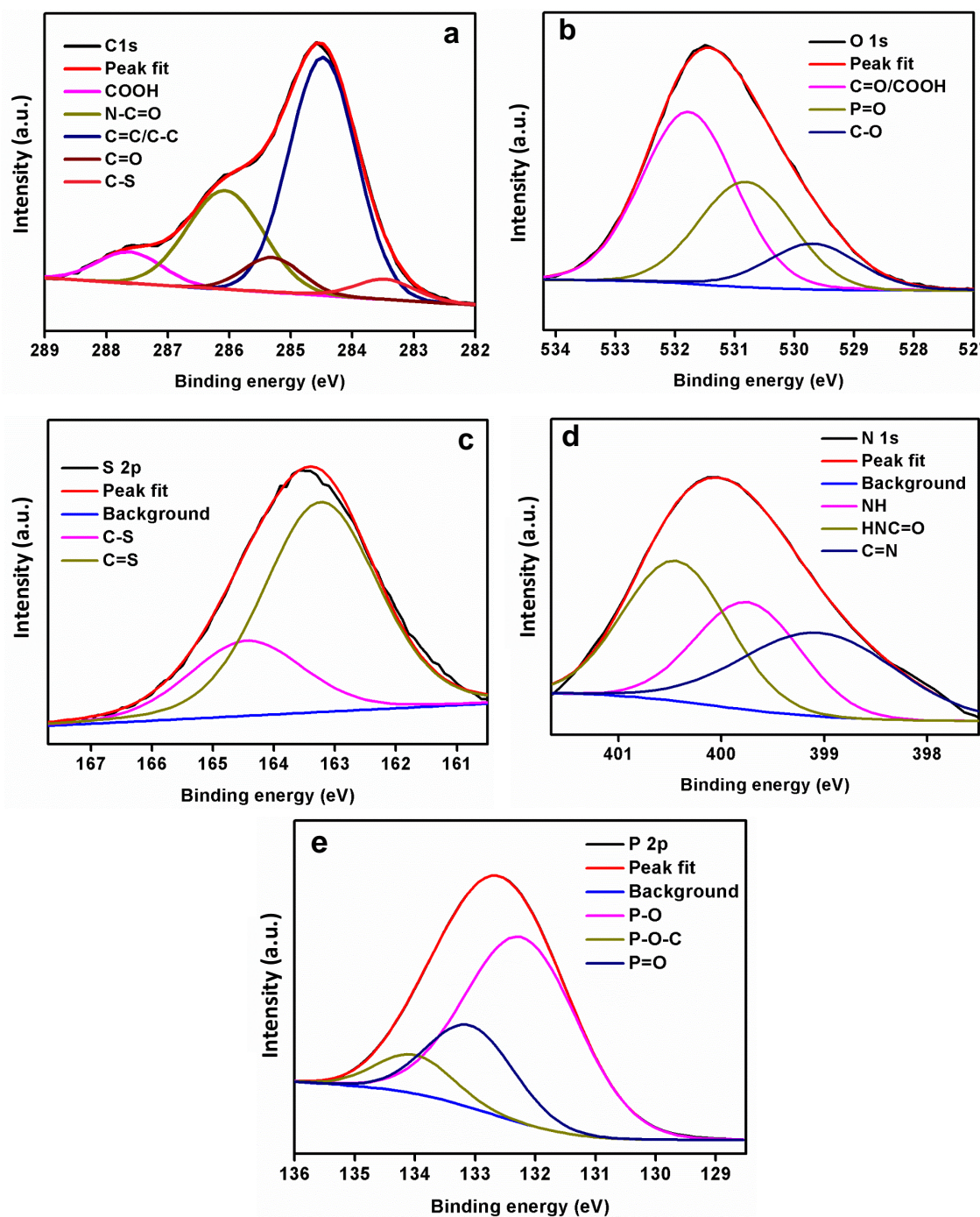
**Figure 4.4.** High resolution XPS spectra (a) C 1s, (b) O 1s, (c) S 2p (d) N 1s and (e) P 2p of S-GQD-Apt complex.

### 4.3.5. PL spectra and lifetime analysis

The photoluminescence (PL) spectra of S-GQD and S-GQD-Apt complex are shown in **Figure 4.5a**. Compared with S-GQD, an apparent fluorescence quenching was observed in the case of S-GQD-Apt complex due to photo-induced electron transfer between S-GQD and aptamer. Therefore, S-GQD-Apt complex is utilized as a

139

sensing probe for the detection of OM, and while adding 300 ppb solution of analyte OM, the fluorescence emission of S-GQD was restored. In the latter case, OM specifically binds to the aptamer of S-GQD/Apt complex to form Apt-OM complex resulting in the recovery of fluorescence of S-GQD. From the PL spectra it was observed that the emission maximum of S-GQD-Rec is almost similar to that of S-GQD confirming the disaggregation of S-GQD. In order to understand the mechanism of the designed sensing strategy which involves aggregation-disaggregation behavior, fluorescence lifetime analysis was carried out using time-correlated single-photon counting (TCSPC). The fluorescence emission lifetime of S-GQD, S-GQD-Apt complex and S-GQD-Rec were measured by monitoring the fluorescence emission intensity decay as a function of time **(Figure 4.5b)**. The fluorescence lifetime of S-GQD was observed as 3.3 ns, which is higher than that of S-GQD-Apt complex (0.9 ns) due to its larger aggregate formation. Compared with S-GQD, reduction in the exciton lifetime of the complex was observed which could be due to the efficient exciton energy transfer from smaller S-GQD to larger aggregates in the complex. As a result, more rapid fluorescence emission decay is observed which leads to fluorescence quenching in S-GQD-Apt complex. Fluorescence recovery of S-GQD after the addition of analyte to S-GQD-Apt complex was again confirmed by the decay analysis. It was found that the fluorescence lifetime of S-GQD-Rec is 2.9 ns which was almost similar to that of initial S-GQD. These fluorescence lifetime results further confirmed the feasibility of 'switch-on' aptasensor for the selective detection of OM.
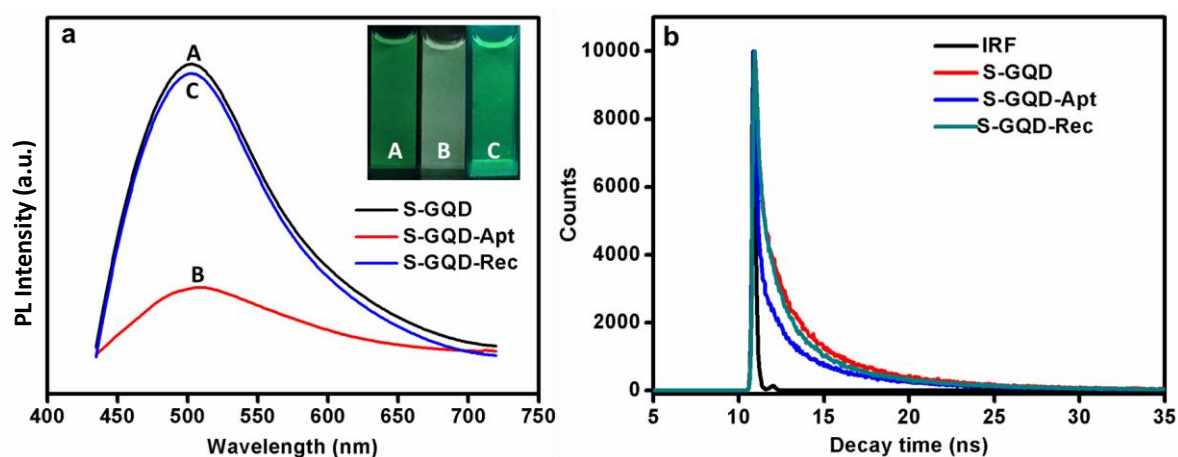


**Figure 4.5.** (a) PL spectra, inset show the photographs of S-GQD, S-GQD-Apt complex and SGQD-Rec (b) Time-correlated single-photon counting (TCSPC) spectra of S-GQD, S-GQD-Apt complex and SGQD-Rec.

**Table 4.2.** Fluorescence lifetime, relative percentage and average lifetime of S-GQD, S-GQD-Apt complex and S-GQD-Rec.

| Sample | Lifetime (ns) | Amplitude | Average life time (T) |
|--------|---------------|-----------|-----------------------|
| S-GQD | T1=1.827 <br> T2=6.784 | A1=38.85% <br> A2=61.15% | 3.302 ns |
| S-GQD- Apt | T1=1.956 <br> T2=8.924 <br> T3=0.460 | A1=20.78% <br> A2=19.37% <br> A3=59.85% | 0.923 ns |
| S-GQD-Rec | T1=1.154 <br> T2=4.056 | A1=48.82% <br> A2=51.18% | 2.910 ns |

### 4.3.6. TEM analysis

Further, the aggregation-disaggregation behaviour of S-GQD in the presence of aptamer and OM was supported by morphological analysis using Transmission Electron Microscopy (TEM). TEM images showed that S-GQDs are evenly dispersed and possess uniform shape and narrow size distribution (~4 nm) **(Figures 4.6a & d).** Meanwhile, for S-GQD-Apt complex, the size of the particles became larger, giving conclusive evidence for the aggregation of S-GQD in the presence of aptamer **(Figure 4.6b & e)**. The addition of OM to S-GQD-Apt complex followed by purification made the larger aggregates to be disappeared and the smaller S-GQDs of 4 nm sizes were again recovered and uniformly distributed **(Figure 4.6c & f)**.
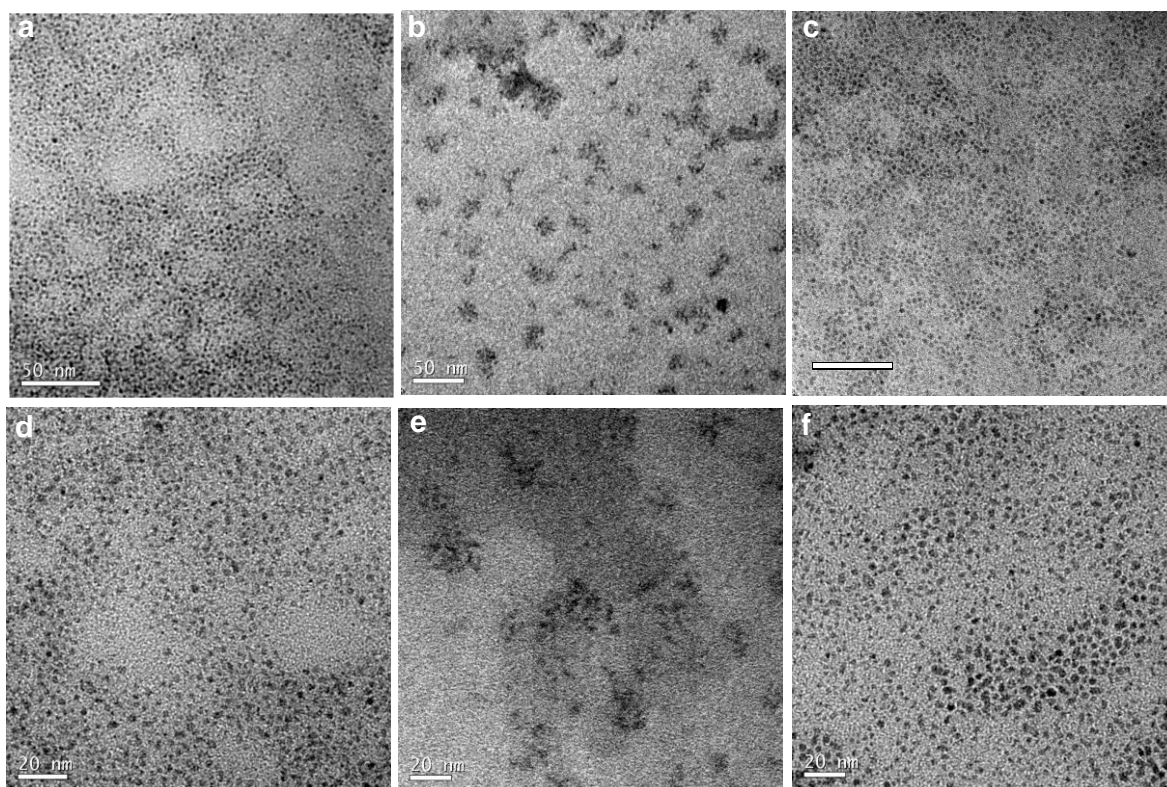
**Figure 4.6**. TEM images of (a) S-GQD, (b) S-GQD-Apt complex, (c) S-GQD-Rec (Scale bar: 50 nm) and (d-f) corresponding magnified images (Scale bar: 20 nm).

### 4.3.7. Circular dichroism spectroscopic analysis

Circular dichroism (CD) spectroscopic analysis was performed to further analyse the sensing process based on the conformational alteration of the aptamer **(Figure 4.7)**. First, we confirmed that there is no CD signal from the target OM. The CD spectrum of aptamer strand exhibited a positive peak at 235 nm and a negative peak at 225 nm which indicates the typical single strand structure of aptamer due to their chiral properties. Upon the addition of OM, the obtained aptamer-OM complex gives a distinct change in CD signal with a positive peak at 230 and a negative band at 220. The spectral difference between aptamer and the obtained complex confirmed the conformational switching of the aptamer strand in our designed strategy, which can thus be used to tune aggregation and disaggregation behaviour of S-GQD for the fluorescence detection.[50]
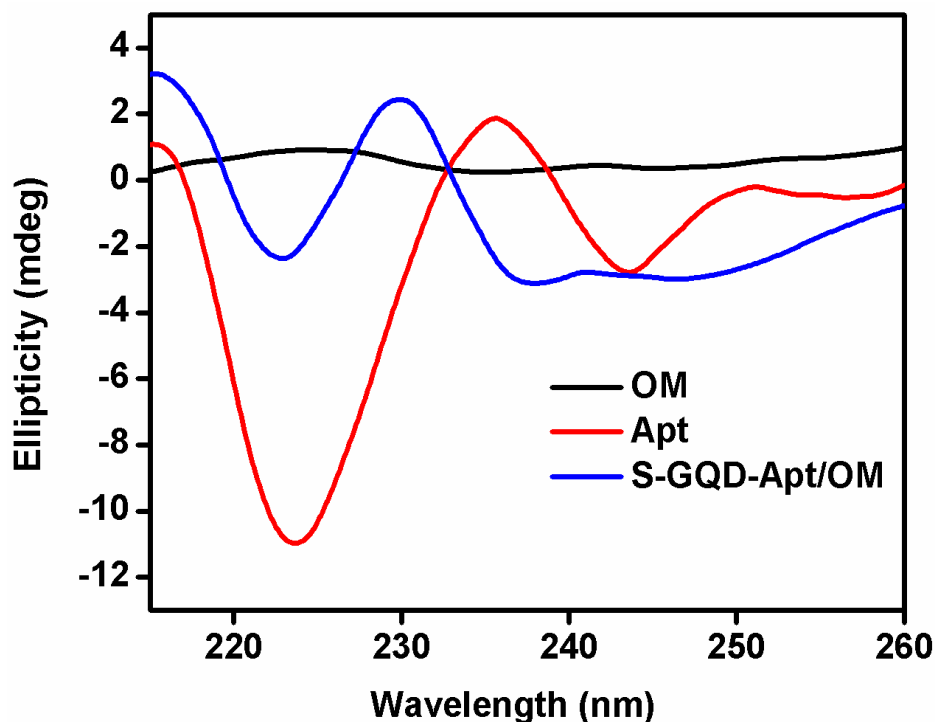
**Figure 4.7**. CD spectra of OM, aptamer and S-GQD-Apt/OM

### 4.3.8. Mechanism of sensing strategy

In the light of above discussions, the mechanism of fluorescence sensing strategy for the detection of OM is illustrated in **Scheme 4.1**. Mixing of aptamer with S-GQD resulted in the quenching of fluorescence owing to the aggregation of S-GQD in the matrix of oligonucleotide. Further, the addition of the analyte OM resulted in high fluorescence recovery, as expected, which in turn can be attributed to the specific binding of Apt and OM. The selective binding to omethoate was achieved by the secondary structure of aptamer where the DNA sequence is subjected to conformational changes resulting in the formation of loops through weak interactions to capture target molecules **(Figure 4.8)**. Wang *et al.* simulated the secondary structure of the aptamer sequence using DNAMAN software and they have estimated the equilibrium dissociation constant for omethoate as 2.5 μM.[49] The recognition and binding with OM persuaded conformational alteration in aptamer and has reversed the binding of S-GQD-Apt complex to Apt-OM complex with the discharge of fluorescent S-GQD. Specific binding induced S-GQD aggregation-disaggregation has led to the idea of developing a 'switch-on' aptasensor for pesticide.

AAGCTTGCTTTATAGCCTGCAGCGATTCTTGATCGGAAAAGGCTGAGAGCTACGC
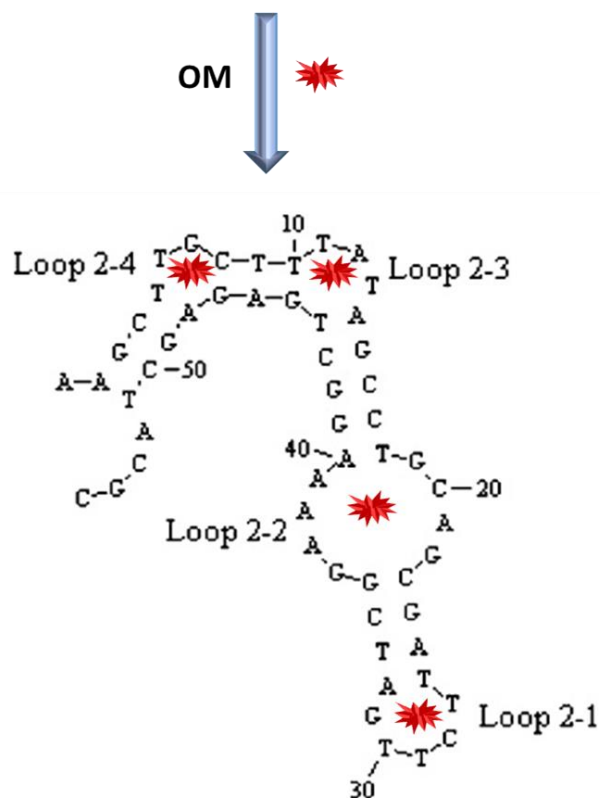


**Figure 4.8**. Conformational change in DNA sequence which results in the formation of loops after capturing the target
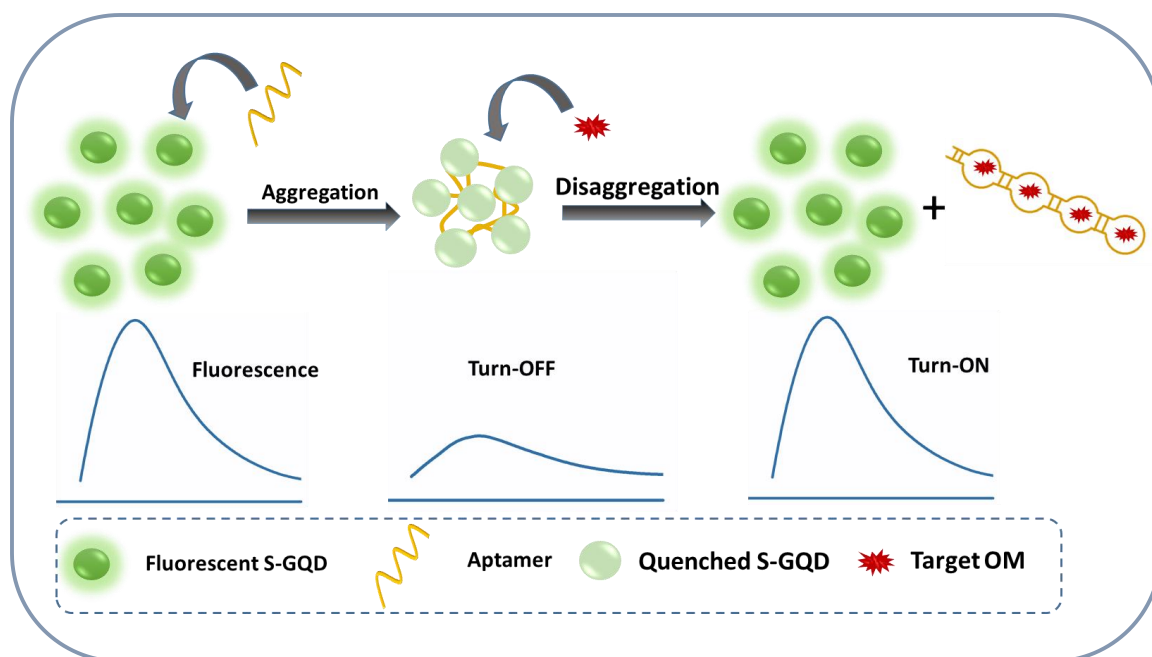


**Scheme 4.1.** Schematic illustration of a fluorescent "switch-on" aptasensor using S-GQD/Aptamer complex for the selective detection of omethoate.

**4.3.9. Role of aptamer in the ultrasensitive detection of OM**

The role of aptamer in the ultrasensitive detection of OM was studied by obtaining PL spectra of S-GQD in the presence and absence of aptamer. The PL spectra of S-GQD in the presence of varying concentrations of two pesticides namely, carbofuran (CF) and OM without aptamer complexation showed aggregation-induced fluorescence quenching. **Figure 4.9a & b** showed PL spectra of S-GQD in the presence of CF and OM, respectively. It is observed that quenching occurred to same extent in both cases. Therefore, it is difficult to achieve selective detection towards a particular pesticide. In order to realize the detection more selective, we designed a 'switch-on' aptasensor by combining OM specific aptamer as a recognition probe with S-GQD to form S-GQD-Apt complex. The PL spectra of S-GQD-Apt complex showed significant fluorescence quenching with respect to S-GQD. To analyse the sensing performance of the designed fluorescent detection probe, OM of varying concentrations (0 ppm-200 ppm) was added to S-GQD-Apt complex and its PL spectra were recorded upon an excitation wavelength of 380 nm. From the PL spectra **(Figure 4.9c)**, it was observed that fluorescence emission intensity enhanced progressively with increase in concentration of OM. This is due to the reversal of S-GQD-Apt complex to very strong and unique Apt-OM complex and discharge of free and fluorescent S-GQD. Thus, OM triggered disaggregation of S-GQD-Apt complex resulted in fluorescence recovery of S-GQD. The fluorescence enhancement showed a good linear relationship with linear regression value, $R^2$ of 0.9926 over the concentration range of 0-200 ppm **(Figure 4.9d)**. The developed 'turn-on' aptasensor has achieved a limit of detection at 0.001 ppm (1 ppb) for OM.
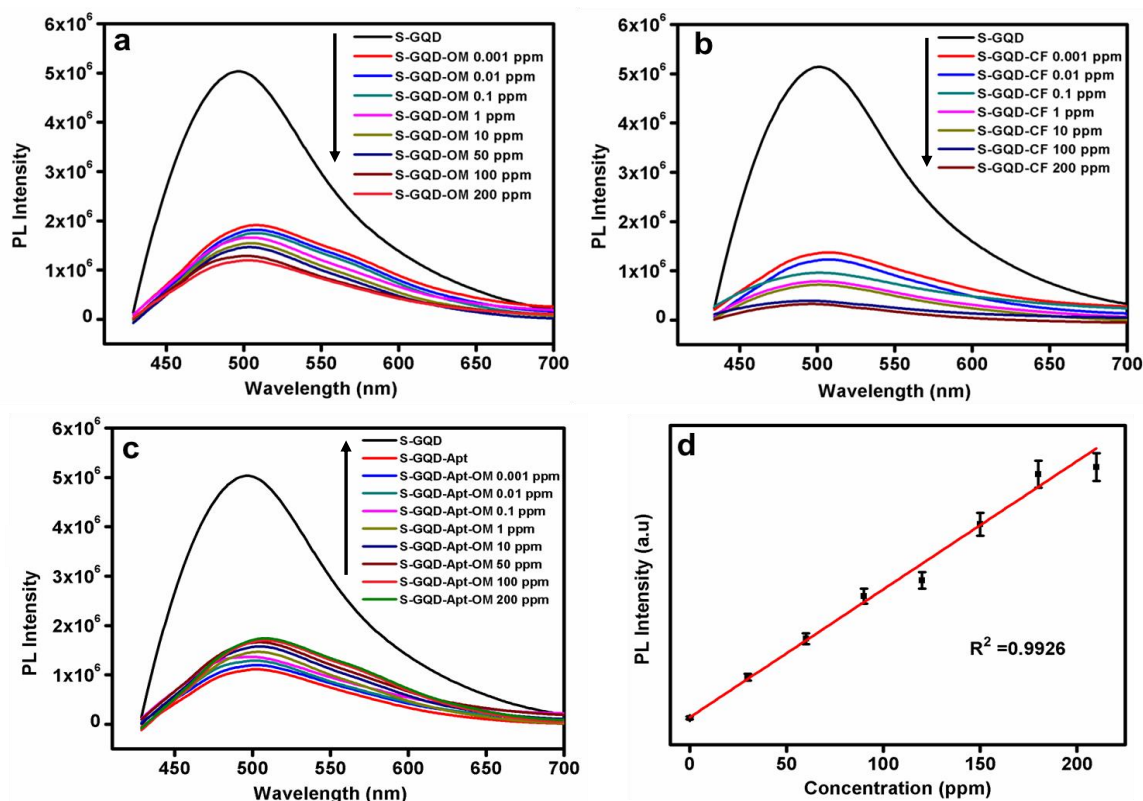
**Figure 4.9**. PL spectra of (a) S-GQD in the presence of OM (0.001 ppm-200 ppm), (b) S-GQD in the presence of CF (0.001 ppm-200 ppm) (c) S-GQD-Apt complex in the presence of OM (0.001 ppm -200 ppm), (d) Linear regression plot with concentration of OM in the range of 0 to 200 ppm.

### 4.3.10. Selectivity study

To demonstrate the specific binding between aptamer and OM, PL spectra of S-GQD-Apt complex in the presence of CF was taken. From the spectra **(Figure 4.10a)**, it was observed that the addition of CF to S-GQD-Apt complex resulted in aggregation-induced fluorescence quenching instead of fluorescent enhancement which suggests that the chosen aptamer sequence has no role in the detection of CF. Linear plot showing the PL intensity of S-GQD with OM and CF in the presence and absence of aptamer, compared fluorescence response of S-GQD with these pesticides and confirmed the role of aptamer in selective detection of OM **(Figure 4.10b)**. From the figure, it is apparent that PL intensity of OM in the presence of S-GQD-Apt complex (S-GQD-Apt-OM) increases, while the others show a sharp decrease in the PL intensity. To further evaluate the selectivity of the designed aptasensor towards OM, fluorescence response of S-GQD-Apt complex towards a set of pesticides such as OM, carbofuran (CF), methyl parathion (MPr) and thiram (Tr) of the same concentration

(100 ppm) was studied. From **Figure 4.10c**, it is clear that only OM exhibited a significant fluorescent recovery, while the others showed a slight decrease in the fluorescent intensity when compared to blank indicating a high selectivity towards OM. These results confirmed that the designed 'switch-on' aptasensor can be used for the selective detection of OM, due to the specific recognition and strong affinity of aptamer towards OM.
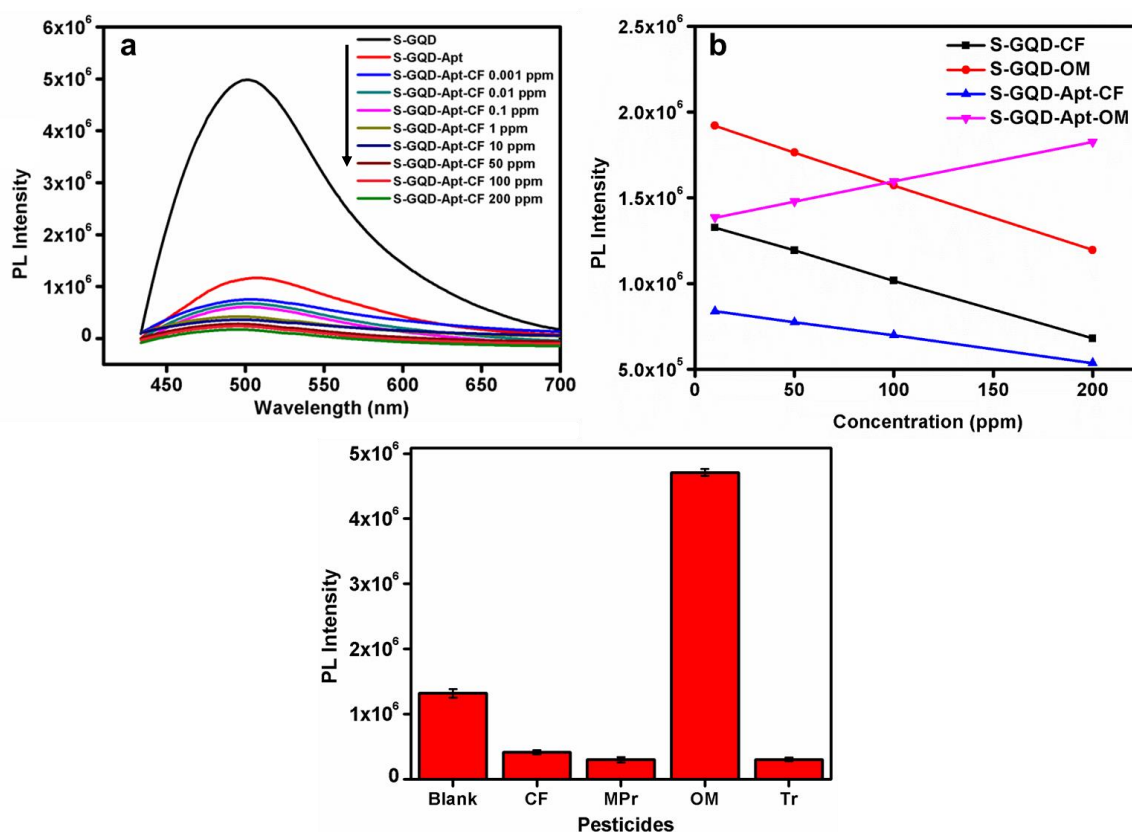


**Figure 4.10.** (a) PL spectra of S-GQD-Apt complex in the presence of CF(0.001 -200 ppm), (b) Linear plot showing PL intensity of S-GQD and S-GQD-Apt complex in the presence of OM and CF (c) Selectivity of the designed aptasensor for OM. (Concentrations of OM and other pesticides were optimised to 100 ppm).

## 4.4. Conclusions

In conclusion, this chapter demonstrated a simple and efficient fluorescent 'turn-on' aptasensor based on specific recognition of aptamer on the fluorescence of sulphur-doped graphene quantum dot for the ultrasensitive and selective detection of omethoate. The aggregation and disaggregation of S-GQDs induced by the structural switching of aptamer lead to fluorescence quenching and fluorescence

recovery, respectively. The developed 'turn-on' aptasensor demonstrates high selectivity for omethoate over other control pesticides. The sensor is highly sensitive and has realised quantitative detection of omethoate with a limit of detection as low as 1 ppb. The proposed turn-on fluorescent aptasensor does not require any modification of signal transmitting nanoparticle or aptamer sequence which makes it facile to construct a simple and novel turn-on aptasensor for omethoate detection. In addition, the sensor is highly selective and ultrasensitive for omethoate detection due to specific binding and high affinity of aptamer to the target molecule. Moreover, the fluorescent signal material used can be recovered for further usage. Considering all the above advantages, we believe that the proposed aptamer strategy can offer alternative approaches for other targets of interest in the field of environmental monitoring and food safety.

## References

1.    B. Eskenazi, A. Bradman and R. Castorina, *Environmental health perspectives*, 1999, **107**, 409-419.

2.    M. Z. Khan and F. C. Law, *Proceedings of the Pakistan Academy of Sciences*, 2005, **42**, 315-323.

3.    G. Matthews, *Pesticides: health, safety and the environment*, John Wiley & Sons, 2015.

4.    D. Barceló, *Journal of Chromatography A*, 1993, **643**, 117-143.

5.    M. A. Beketov, B. J. Kefford, R. B. Schäfer and M. Liess, *Proceedings of the National Academy of Sciences*, 2013, **110**, 11039-11043.

6.    A. M. Hegazy, R. M. Abdelfatah, H. M. Mahmoud and M. A. Elsayed, *Beni-Suef University Journal of Basic and Applied Sciences*, 2018, **7**, 598-605.

7.    G. Zweig, *Chromatographic Reviews*, 1964, **6**, 110-128.

8.    X. Yan, H. Li and X. Su, *TrAC Trends in Analytical Chemistry*, 2018, **103**, 1-20.

9.    H. Li, C. Sun, R. Vijayaraghavan, F. Zhou, X. Zhang and D. R. MacFarlane, *Carbon*, 2016, **104**, 33-39.

10.   N. R. Tanguy, L. K. Fiddes and N. Yan, *ACS Applied Materials & Interfaces*, 2015, **7**, 11939-11947.

11.   C. Sahub, T. Tuntulani, T. Nhujak and B. Tomapatanaget, *Sensors and Actuators B: Chemical*, 2018, **258**, 88-97.

12.    A. Simonian, T. Good, S.-S. Wang and J. Wild, *Analytica chimica acta*, 2005, **534**, 69-77.

13.    M. Liang, K. Fan, Y. Pan, H. Jiang, F. Wang, D. Yang, D. Lu, J. Feng, J. Zhao and L. Yang, *Analytical chemistry*, 2012, **85**, 308-312.

14.    J. Wang, D. Chen, Y. Xu and W. Liu, *Sensors and Actuators B: Chemical*, 2014, **190**, 378-383.

15.    F. Arduini, S. Cinti, V. Caratelli, L. Amendola, G. Palleschi and D. Moscone, *Biosensors and Bioelectronics*, 2019, **126**, 346-354.

16.    J. R. Premkumar, O. Lev, R. S. Marks, B. Polyak, R. Rosen and S. Belkin, *Talanta*, 2001, **55**, 1029-1038.

17.    Y. Liu, B. Lv, A. Liu, G. Liang, L. Yin, Y. Pu, W. Wei, S. Gou and S. Liu, *Sensors and Actuators B: Chemical*, 2018, **265**, 675-681.

18.    S. Song, L. Wang, J. Li, C. Fan and J. Zhao, *TrAC Trends in Analytical Chemistry*, 2008, **27**, 108-117.

19.    R. Y. Robati, A. Arab, M. Ramezani, F. A. Langroodi, K. Abnous and S. M. Taghdisi, *Biosensors and Bioelectronics*, 2016, **82**, 162-172.

20.    Y. Li, J. Xu, L. Wang, Y. Huang, J. Guo, X. Cao, F. Shen, Y. Luo and C. Sun, *Sensors and Actuators B: Chemical*, 2016, **222**, 815-822.

21.    A. V. Lakhin, V. Z. Tarantul and L. V. Gening, *Acta Naturae*, 2013, **5**, 34-43.

22.    K. L. Hong and L. J. Sooter, *BioMed Research International*, 2015, **2015**, 31.

23.    S. Gao, X. Zheng, B. Jiao and L. Wang, *Analytical and bioanalytical chemistry*, 2016, **408**, 4567-4573.

24.    S. D. Jayasena, *Clinical chemistry*, 1999, **45**, 1628-1650.

25.    S. Tombelli, M. Minunni and M. Mascini, *Biosensors and Bioelectronics*, 2005, **20**, 2424-2434.

26.    S. Y. Toh, M. Citartan, S. C. Gopinath and T.-H. Tang, *Biosensors and bioelectronics*, 2015, **64**, 392-403.

27.    M. Blank and M. Blind, *Current opinion in chemical biology*, 2005, **9**, 336-342.

28.    A. Chen and S. Yang, *Biosensors and bioelectronics*, 2015, **71**, 230-242.

29.    S. Wang, L. Zhang, S. Wan, S. Cansiz, C. Cui, Y. Liu, R. Cai, C. Hong, I.-T. Teng and M. Shi, *ACS nano*, 2017, **11**, 3943-3949.

30.    J. S. Lee, M. S. Han and C. A. Mirkin, *Angewandte Chemie International*

*Edition*, 2007, **46**, 4093-4096.

31.    X. Niu, Y. Zhong, R. Chen, F. Wang, Y. Liu and D. Luo, *Sensors and Actuators B: Chemical*, 2018, **255**, 1577-1581.

32.    J. Wang, Y. Wu, P. Zhou, W. Yang, H. Tao, S. Qiu and C. Feng, *Analyst*, 2018, **143**, 5151-5160.

33.    R. Wang and Y. Li, *Biosensors and Bioelectronics*, 2013, **42**, 148-155.

34.    R. Huang, Z. Xi, Y. Deng and N. He, *Scientific reports*, 2016, **6**, 31103.

35.    K. Wang, J. Liao, X. Yang, M. Zhao, M. Chen, W. Yao, W. Tan and X. Lan, *Biosensors and Bioelectronics*, 2015, **63**, 172-177.

36.    E. Sharon, R. Freeman and I. Willner, *Analytical chemistry*, 2010, **82**, 7073-7077.

37.    S. S. Chopra and T. L. Theis, *Environmental Science: Nano*, 2017, **4**, 244-254.

38.    Y. Liu, K. Yan, O. K. Okoth and J. Zhang, *Biosensors and Bioelectronics*, 2015, **74**, 1016-1021.

39.    Z. Fan, S. Li, F. Yuan and L. Fan, *RSC Advances*, 2015, **5**, 19773-19789.

40.    R. V. Nair, R. T. Thomas, V. Sankar, H. Muhammad, M. Dong and S. Pillai, *ACS Omega*, 2017, **2**, 8051-8061.

41.    Z. Zhang, J. Zhang, N. Chen and L. Qu, *Energy & Environmental Science*, 2012, **5**, 8869-8890.

42.    J. Guo, X. Liu, H. Gao, J. Bie, Y. Zhang, B. Liu and C. Sun, *RSC Advances*, 2014, **4**, 27228-27235.

43.    R. C. Somers, M. G. Bawendi and D. G. Nocera, *Chemical Society Reviews*, 2007, **36**, 579-591.

44.    J. Chen, D. Dong and S. Ye, *RSC Advances*, 2018, **8**, 4726-4730.

45.    T. Yaseen, D.-W. Sun, H. Pu and T.-T. Pan, *Food Analytical Methods*, 2018, **11**.

46.    L. Guerrini, S. Sanchez-Cortes, V. L. Cruz, S. Martinez, S. Ristori and A. Feis, *Journal of Raman Spectroscopy*, 2011, **42**, 980-985.

47.    C. Aprea, L. Centi, S. Santini, L. Lunghini, B. Banchi and G. Sciarra, *Archives of environmental contamination and toxicology*, 2005, **49**, 577-588.

48.    Y. Arakawa, *Ind Health*, 2014, **52**, 87-89.

49.    L. Wang, X. Liu, Q. Zhang, C. Zhang, Y. Liu, K. Tu and J. Tu, *Biotechnology letters*, 2012, **34**, 869-874.

50.    M. Yüce and H. Kurt, *RSC Adv.*, 2017, **7**, 49386-49403.

# Chapter 5

## Dual-mode SERS/Fluorescence Sensor Based on Aptamer Modified Gold Nanoparticles and Sulphur-Doped Graphene Quantum Dots for Selective and Ultrasensitive Detection of Omethoate

## Abstract

With the objective of achieving an enhanced sensitivity for the trace level detection of a pesticide, namely, omethoate (OM) in the current chapter, we developed a dual-mode SERS/fluorescence sensor based on aptamer modified gold nanoparticles (Au-Apt) and sulphur-doped graphene quantum dots (S-GQD). The gold nanoparticles are first modified by thiol functionalized aptamer through gold-thiol (Au-SH) affinity interactions. When S-GQD is added to Au-Apt, the fluorescence of S-GQD was effectively quenched by Au-Apt. Upon the addition of OM, due to specific binding between aptamer and OM, S-GQDs were released along with the formation of omethoate-Au-Apt complex (Au-Apt/OM). The released S-GQDs turn-on the fluorescence signal whereas, the component Au-Apt/OM gives the SERS signal. Therefore, S- GQD/Au-Apt system can be used not only as a selective fluorescent turn-on sensor but also as a highly sensitive SERS probe. The sensing based on the fluorescence turn-on shows a linear response for the concentration of OM from 1 ppm to 20 ppm with a limit of detection (LOD) of 1.7 ppm with high selectivity. The new sensing strategy adopted here using Au-Apt/OM SERS probe has enhanced the sensitivity by achieving a LOD of 0.05 ppb and shows a wide range of linear response from 0.05 ppb to 2.5 ppm. Thus, a dual-mode SERS/fluorescence sensor is successfully constructed which provides an efficient way for selective and ultrasensitive detection of OM.
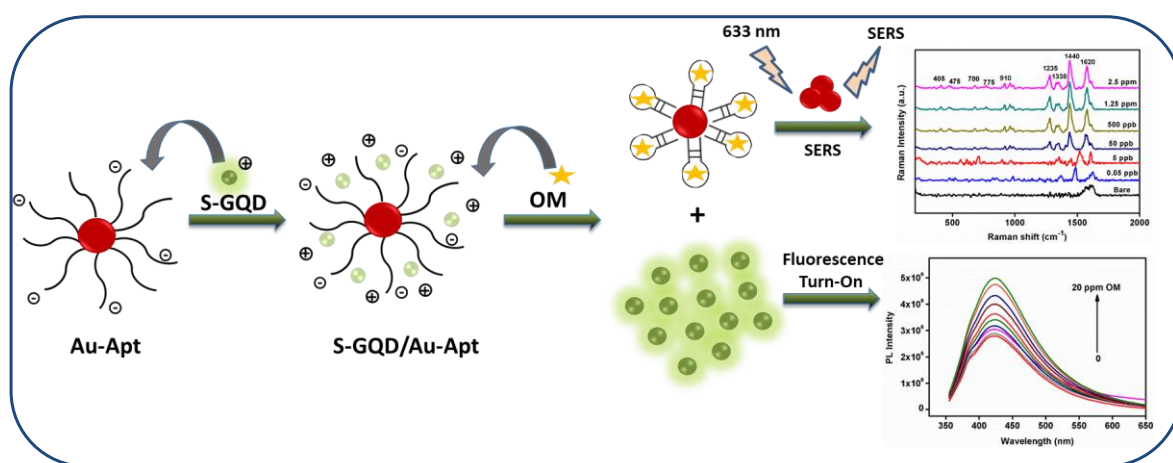
## 5.1. Introduction

Aptasensors are well known for its selectivity towards specific targets because of its remarkable specificity, high affinity, excellent stability, easy modification, and target diversity.[1, 2] Variety of novel aptasensors coupled with different sensing signals were designed for the detection of various targets like pesticides,[3, 4] heavy metals,[5, 6] antibiotics[7] and biotoxins.[8] By these approaches, they achieved good selectivity, but sensitivity in trace level is still a matter of concern. To ensure food safety and human health, it is significant to develop trace level detection methods for these highly toxic chemicals.[9] Sensitive detection of pesticides can be achieved by a number of analytical methods including colorimetry,[10, 11] fluorimetry,[4, 12] chromatography[13, 14] and surface-enhanced Raman spectroscopy (SERS)[15, 16]. Chromatography is the most widely used method due to its accuracy. However, the method requires sophisticated instrumentation, trained personnel, tedious sample preparation and is time-consuming which is unsuitable for onsite detection.[17-19] As a convenient detection method, naked-eye colorimetric assays have drawn much attention because they do not rely on advanced instrumentation and skilled operators.[20] However, colourimetric strategies are susceptible to interference caused by pigments that may exist in the sample and also these are not sensitive enough to meet the toxic levels prescribed by the Environmental Protection Agency (EPA).[14]

SERS is a molecular spectral technique based on the adsorption of certain analytes on the surface of nanoparticles to create localized surface plasmons.[21, 22] It has been proved as a reliable spectroscopic tool used in various fields such as environmental monitoring, biomedicine and food safety.[23-26] There are several reports wherein pesticide residues have been monitored using SERS. For e.g. Fang *et al.* used Ag nanoparticles as an enhancing substrate to detect pesticide resid ues on fruit.[27] Zhai *et al*. detected chlorpyrifos residues on the apple surface using gold nanoparticles as SERS substrate.[28] Zhang *et al*. studied the content of multiple pesticides on fruit surface using SERS technique.[29] Yang *et al*. detected pesticide residues on apple skin using silver nano shells as the SERS substrate.[30] Detection by SERS has many significant characteristics such as rapid detection, enhanced sensitivity, specific recognition, minimal sample preparation, simple operation and

its non-destructive nature.[31-34] However, the reproducibility of SERS assay for the trace level detection was not good. Fluorescence-based methods have also attracted great interest for quantitative detection especially in analytical chemistry because of its selectivity, simplicity and ease of operation.[4, 35, 36] Graphene quantum dots (GQDs) based fluorescent sensors have gained considerable attention due to their excellent fluorescence properties, high aqueous dispersibility, photostability, chemical inertness, low cost, low toxicity and excellent biocompatibility when compared to other semiconductor quantum dots.[6, 37-39] Nan *et al*. designed a GQD based fluorescent sensor for the sensitive detection of a highly toxic organophosphate pesticide, namely, paraxon.[40] Zor *et al*. reported GQD based multifunctional composite materials as photoluminescent sensors for the detection of pesticides.[41] These approaches were stable, but not sensitive enough for the trace level detection.

To address these concerns, a complementary dual-mode sensing system can be designed which can provide two types of output signals, making the results more convincing.[42, 43] Therefore, this dual-mode approach could minimize the risk of false-positive and false detection by obtaining results from the dual-channel sensing system, thereby enhancing the accuracy and reliability of the sensing system..[44, 45] Dual-mode detection methods have recently gained considerable attention and have been shown to be more effective than single-mode detection. A variety of dual-mode assays have been developed, such as electrochemical/fluorescence,[46] magnetic/fluorescence,[47] SERS/colourimetric[48] and SERS/Fluorescence[42] dual-mode sensing systems. Qi *et al*. reported a colourimetric/SERS dual-mode sensing system for Hg (II) based on rhodamine stabilized gold nanobipyramids.[49] Liu *et al*. demonstrated a dual-mode colourimetric/fluorescence sensor for the detection of ascorbic acid.[50] Wang *et al*. demonstrated a dual-mode SERS and resonance Rayleigh scattering (RRS) sensing platforms based on Ag-doped carbon dots.[51] A dual-mode gold nanoprobe for the detection of telomerase activity was reported based on SERS and colourimetry.[52] Qu *et al*. developed SERS/fluorescence dual-mode sensors for the detection of hydroxyl radicals with an LOD of 10 nM/L.[53] To the best of our knowledge, there are no reports about SERS/fluorescence dual-mode sensor based on aptamer modified gold nanoparticles for the selective and ultrasensitive detection of omethoate.

In the present chapter, a dual-mode SERS/fluorescence sensor based on aptamer modified gold nanoparticles (Au-Apt) and sulphur-doped graphene quantum dots (S-GQD) was developed. The gold nanoparticles are first modified by thiol functionalized aptamer through gold-thiol (Au-SH) affinity interactions. By the addition of S-GQD to Au-Apt, the fluorescence of S-GQD was effectively quenched. When OM is added to S-GQD/Au-Apt sensing probe, due to the specific binding between aptamer and OM, S-GQDs were released along with the formation of omethoate-Au-Apt complex (Au-Apt/OM). The released S-GQDs turn on the fluorescence signal and the component Au-Apt/OM gives the SERS signal. Therefore, S- GQD/Au-Apt system can be used not only as a fluorescent turn-on sensor, but also as a highly sensitive SERS probe.

## 5.2. Experimental

### 5.2.1. Materials

Graphite (<150 μm), chloroauric acid ($HAuCl_4$), tri-sodium citrate ($Na_3C_6H_5O_7$), hydrogen peroxide ($H_2O_2$), sodium nitrate ($NaNO_3$), sulphuric acid ($H_2SO_4$), omethoate, carbofuran, imidacloprid, acetamiprid, metalaxyl, methyl parathion, and thiram were purchased from Sigma-Aldrich. Potassium permanganate ($KMnO_4$) was purchased from SD Fine-Chemicals Limited. Ultrapure deionized water (18.2 MΩ cm, 25 °C, Milli-Q D3, Merck, Germany) was used in all the experiments. Thiol modified oligonucleotides were purchased from Eurofins Genomics. The aptamer sequence is as follows: 5′-AAG CTT GCT TTA TAG CCT GCA GCG ATT CTT GAT CGG AAA AGG CTG AGA GCT ACG C-3′/Thiol.

### 5.2.2. Synthesis of S-GQDs

S-GQDs were prepared according to the procedure given in Chapter 3. The procedure is described briefly as follows. S-GQDs were prepared from GO using $KMnO_4$ as an oxidising agent and 0.1 M $H_2SO_4$ as a doping source for sulphur by microwave-assisted sonochemical method keeping the reaction temperature constant at 90 °C at a microwave power of 400 W for 5 min.

### 5.2.3. Synthesis and purification of gold nanoparticles (AuNPs)

Colloidal gold nanoparticle (AuNP) solution was synthesized by a standard method, as described by Turkevich and Frens.[54] The method involves the reduction

of chloroauric acid initiated by the common reducing agent tri-sodium citrate at 100 °C. AuNP of size about 40 nm was synthesized by taking tri sodium citrate and $HAuCl_4$ in the ratio 1:1 at a concentration of 0.25 mM and purified by ultracentrifugation at 15,000 rpm for 30 min.

### 5.2.4 Modification of AuNPs with aptamer

Thiol-terminated aptamer was conjugated to the surface of AuNPs by adopting the following procedure. Thiolated aptamer (200 nM) was vortex mixed with AuNPs at a ratio 1:1 (v/v) for 10 min to facilitate aptamer binding through -SH group. After 30 min incubation at room temperature the excess aptamer was removed by centrifugation at 10,000 rpm for 30 min followed by washing. Finally, the purified aptamer stabilised AuNPs (Au-Apt) were re-dispersed in ultrapure water and used for further studies.

### 5.2.5. Design of the sensing probe

The as-synthesized S-GQDs were taken at a concentration of 0.05 mg/mL in water. The obtained positively charged S-GQDs were vortex mixed with negatively charged Au-Apt at 3:1 ratio (v/v) for 10 min. The solution was incubated for 30 min at room temperature followed by centrifugation to remove excess S-GQDs. The obtained S-GQD/Au-Apt complex was further used as a fluorescent turn-on sensor as well as SERS probe for the detection of OM.

### 5.2.6. Fluorescence detection of OM based on S-GQD/Au-Apt probe

The fluorescence detection of OM was carried out using S-GQD/Au-Apt probe in aqueous medium at room temperature. To study the sensitivity towards OM, fluorescence emission spectra (PL spectra) of S-GQD and S-GQD/Au-Apt complex in the presence and absence of OM was recorded with an excitation wavelength of 380 nm. For the detection, a series of concentrations of OM (1 ppm-20 ppm) were freshly prepared and added to S-GQD-Apt complex. The subsequent fluorescence recovery was measured by recording the corresponding PL spectra after 2 h of incubation under the same excitation wavelength. The selectivity towards OM was evaluated by taking the PL spectra of S-GQD/Au-Apt complex in the presence of different control pesticides such as carbofuran (CF), methyl parathion (MPr), imidacloprid (IM), acetamiprid (AC), metalaxyl (MT), and thiram (Tr) at 100 ppm concentration under

identical conditions.

## 5.2.7. Detection of OM based on S-GQD/Au-Apt probe by SERS

For SERS detection, samples were prepared by mixing different concentrations of OM molecules with S-GQD/Au-Apt probes in the ratio 1:2 (v/v). Then 10 µL of the sample was drop-casted onto the cleaned glass slide (sonicated in toluene and ethanol sequentially followed by UV-ozone treatment for 15 min) and dried at ambient temperature under vacuum. SERS spectra were obtained from at least six different locations for solid samples. All experiments were carried out in triplicates.

## 5.2.8. Recovery of S-GQD (S-GQD-Rec)

200 µL of 300 ppm OM was vortex mixed with S-GQD/Au-Apt complex for 10 min so that OM and S-GQD/Au-Apt complex can interact with each other efficiently. The obtained S-GQD/Au-Apt/OM mixture was then dialysed using dialysis bag (MWCO-12 kDa, Sigma Aldrich) against ultrapure deionized water for 24 h. The dialysing solution containing free S-GQDs was replaced with ultrapure water at 4 h intervals and stored. Collected dialysate was then concentrated to obtain S-GQD with a concentration of 0.042 mg/mL which was about 84 % of initial S-GQD taken. Thus, recovered S-GQD is labelled hereafter as S-GQD-Rec.

## 5.2.9. Characterizations

Transmission electron microscope (TEM) operated at an accelerating voltage of 300 kV on FEI Tecnai 30 G2S-TWIN transmission electron microscope was used for the morphological characterizations. Gatan Digital Micrograph software was used for the analysis of the HR-TEM images. Perkin Elmer Series Spectrum Two Fourier-transform infrared spectroscopy (FT-IR) spectrometer over the wavenumber range 4000-500 cm-1 was used for recording FT-IR spectra. The UV-Visible (UV-Vis) absorption spectra were measured by a spectrophotometer (SHIMADZU UV-2401 PC, Shimadzu, Japan) using a 1 cm path length quartz cell at room temperature. Spex-Fluorolog FL22 spectrofluorimeter equipped with a double grating 0.22 m Spex 1680 monochromator and a 450 W Xe lamp as the excitation source was used for recording photoluminescence (PL) spectra. Fluorescence lifetime experiments were conducted using a Delta Flex modular time-correlated single-photon counting (TCSPC) spectrometer system, employing the 330 nm nano LED as the excitation source and

PPD 850 detector. Decay in the fluorescence intensity (I) with time (t) was fitted by three exponential functions. The quality of the fits was checked by examining the $\chi 2$ value. X-ray photoelectron spectroscopy (XPS) was performed using PHI 5000 Versa Probe II (ULVAC-PHI Inc., USA) equipped with micro-focused (200 μm, 15 KV) monochromatic Al-Kα X-Ray source (hν = 1486.6 eV). Survey scans were recorded with X-ray source power of 23.7 W and pass energy of 187.85 eV. High-resolution spectra of the major elements were recorded at 46.95 eV pass energy. Multipak software (PHI) was used for the deconvolution of peaks. Zeta potential and DLS measurements were done using Nano ZS Malvern instrument. SERS measurements were performed using WI-Tec Raman microscope (WI-Tec, Inc., Germany, alpha 300R) with a laser beam directed to the sample through 20× objective with 600 g/mm grating and a Peltier cooled CCD detector. Samples were excited with a 633 nm wavelength laser and Stokes shifted Raman spectra were collected in the range of 0-3000 cm$^{-1}$ with 1 cm$^{-1}$ resolution and an integration time of 2 s and 10 accumulations. WI-Tec Project plus (v 4.1) software package was used for data interpretation.

## 5.3. Results and discussion

### 5.3.1. Synthesis and characterizations of AuNPs and Au-Apt

The synthesized colloidal solution of AuNPs showed intense and characteristic ruby red color as shown in **Figure 5.1a**, which can be attributed to surface plasmon resonance (SPR). SPR contributes to the plasmon absorption peak at 530 nm **(Figure 5.1b)**. Morphology of AuNPs was studied by TEM and the image shown in **Figure 5.1c** revealed that AuNPs were nearly spherical in shape with a size of about 40 nm. AuNPs were further functionalized with thiolated aptamers (Au-Apt) and were used for the fabrication of S-GQD/Au-Apt sensing probe.
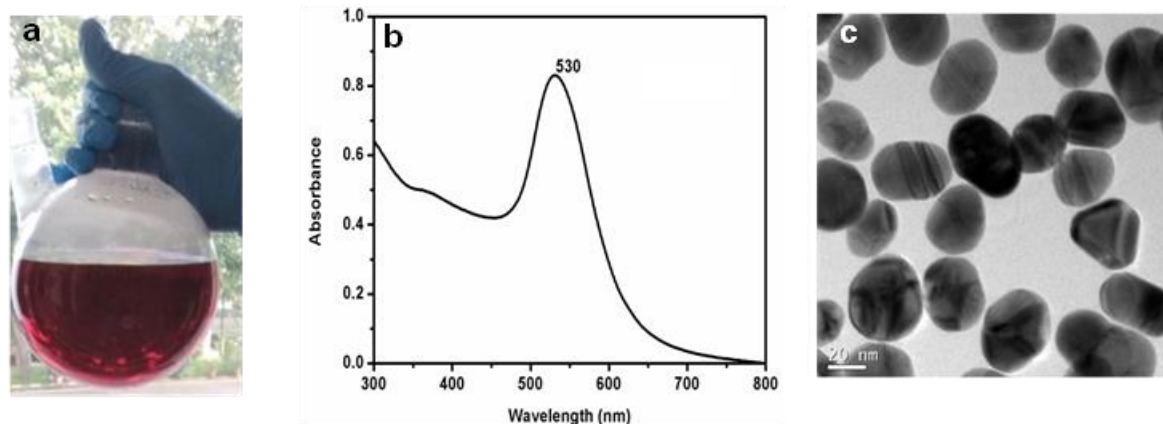
**Figure 5.1.** (a) Photograph (b) UV-Visible absorption spectrum (c) TEM image
(Scale bar: 20 nm) of the synthesized AuNPs.

### 5.3.2. Design and morphological characterizations of the S-GQD/Au-Apt sensing probe

S-GQDs with bright green fluorescence were synthesized from graphene oxide (GO) as described in the experimental section 5.2.2. Upon addition of S-GQDs to Au/Apt, S-GQD/Au-Apt complex is formed and the fluorescence of S-GQDs was effectively quenched by Au-Apt. The morphological characterization of particles in each step of conjugation was carried out by TEM and the **Figures 5.2 (a-c)**, compared the TEM images of AuNPs, Au/Apt and S-GQD/Au-Apt complex, respectively. **Figures 5.2 (d-f)** showed the corresponding HR-TEM images. Images show that AuNPs are dispersed evenly on the substrate, while for Au-Apt, the interparticle spacing is minimal due to the stable Au-SH bond. HR-TEM image **(Figure 5.2f)** of S-GQD/Au-Apt complex showed the aggregated AuNPs surrounded by aptamer layer along with the intense distribution of S-GQDs. Image of S-GQD/Au-Apt complex is more magnified in **Figure 5.3 (a & b)** where S-GQDs can be clearly seen around the aptamer layer. The TEM images suggested/indicated the formation of S-GQD/Au-Apt complex.
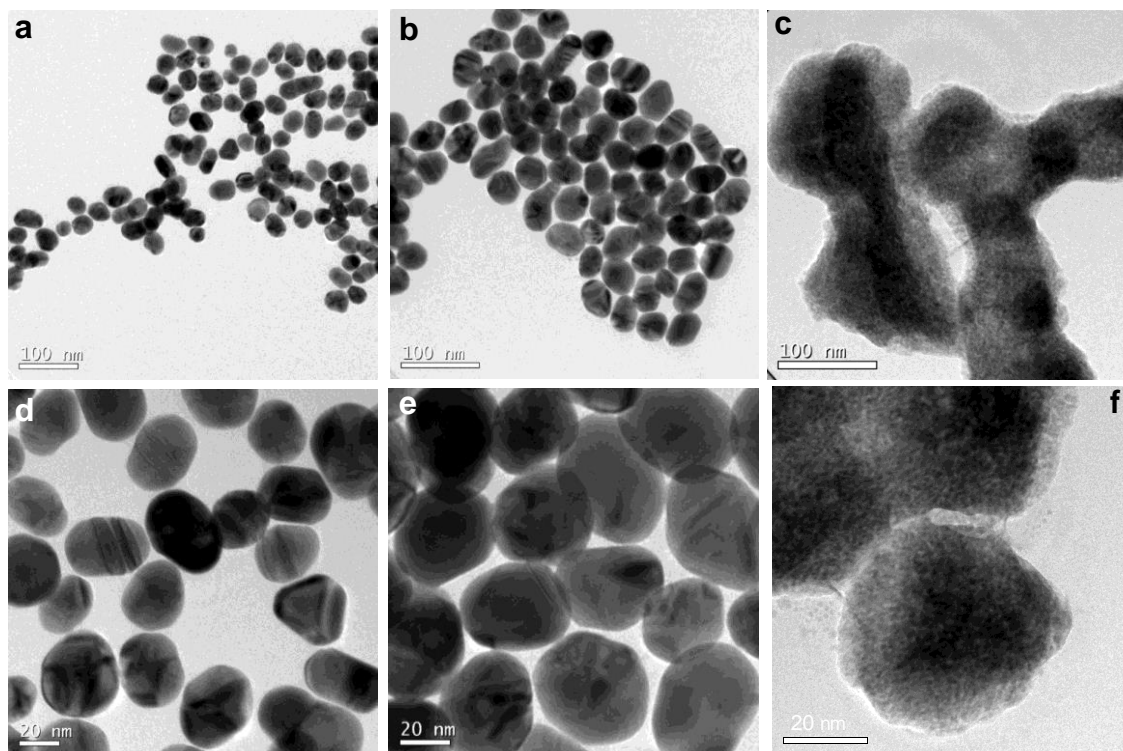
**Figure 5.2.** TEM images of (a) AuNPs (b) Au-Apt (c) S-GQD/Au-Apt complex (Scale bar:100 nm) (d-f) the corresponding HR-TEM images respectively (Scale bar:20 nm)
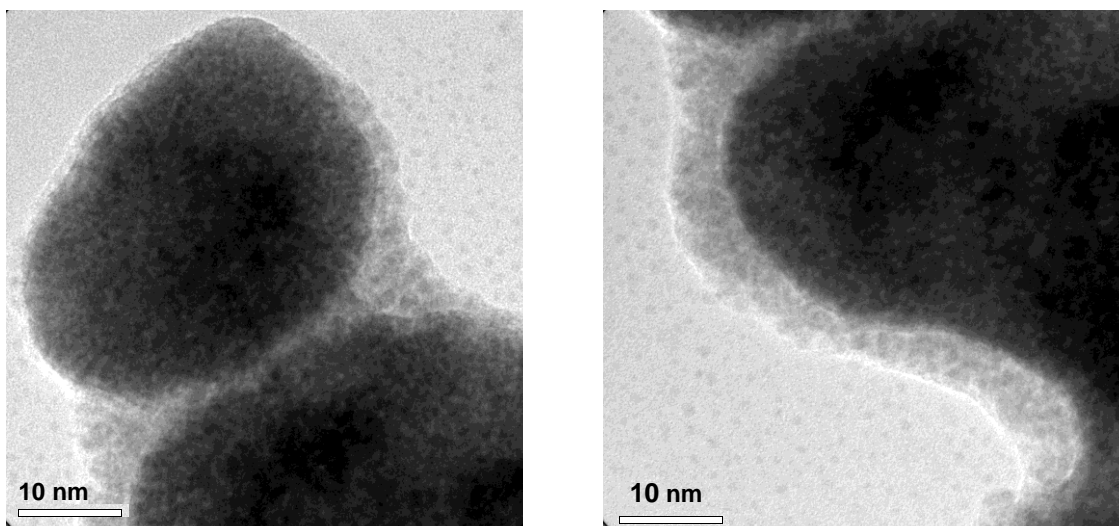


**Figure 5.3.** (a) and (b) High-resolution TEM images of S-GQD/Au-Apt complex (Scale bar:10 nm)

### 5.3.3. Zeta potential measurement

**Table 5.1** shows the zeta potential values and hydrodynamic diameters of AuNP, Au-Apt and S-GQD/Au-Apt complex. Zeta potential of AuNP before conjugation was -25.8 mV, which is attributed to the existence of negatively charged citrate ions on the surface. After modifying with a negatively charged aptamer, the zeta potential value of Au-Apt became more negative -27.3 mV. When S-GQDs were introduced to the Au-Apt system, the zeta potential value was further changed to -4.5 mV. From **Table 5.1**, we could clearly observe that there is a dramatic change of zeta potential from -27.3 mV to -4.5 mV which confirms the incorporation of positively charged S-GQDs onto Au-Apt system.

**Table 5.1.** Zeta potential values and hydrodynamic diameters of AuNP, Au-Apt and S-GQD/Au-Apt

| Sl No: | Sample | Zeta Potential (mV) | Hydrodynamic Diameter (nm) |
|---|---|---|---|
| 1 | AuNP | -25.8 | 59.6 |
| 2 | Au-Apt | -27.3 | 85.3 |
| 3 | S-GQD/Au-Apt | -4.5 | 98.4 |

### 5.3.4. UV-Visible spectroscopic analysis

The formation of S-GQD/Au-Apt sensing probe was monitored by studying the absorption characteristics of AuNPs, Au-Apt and S-GQD/Au-Apt with UV-Visible spectroscopy **(Figure 5.4)**. When compared to the surface plasmon resonance band of the monodispersed AuNPs at 530 nm, Au-Apt showed a slight red shift with decreased absorbance at 536 nm. Moreover, the spectrum of Au-Apt had an additional peak at 260 nm, which corresponds to the characteristic peak of aptamer. With the addition of S-GQD to Au-Apt, the peak was red shifted to 545 nm due to the formation of larger aggregates as indicated in TEM images.
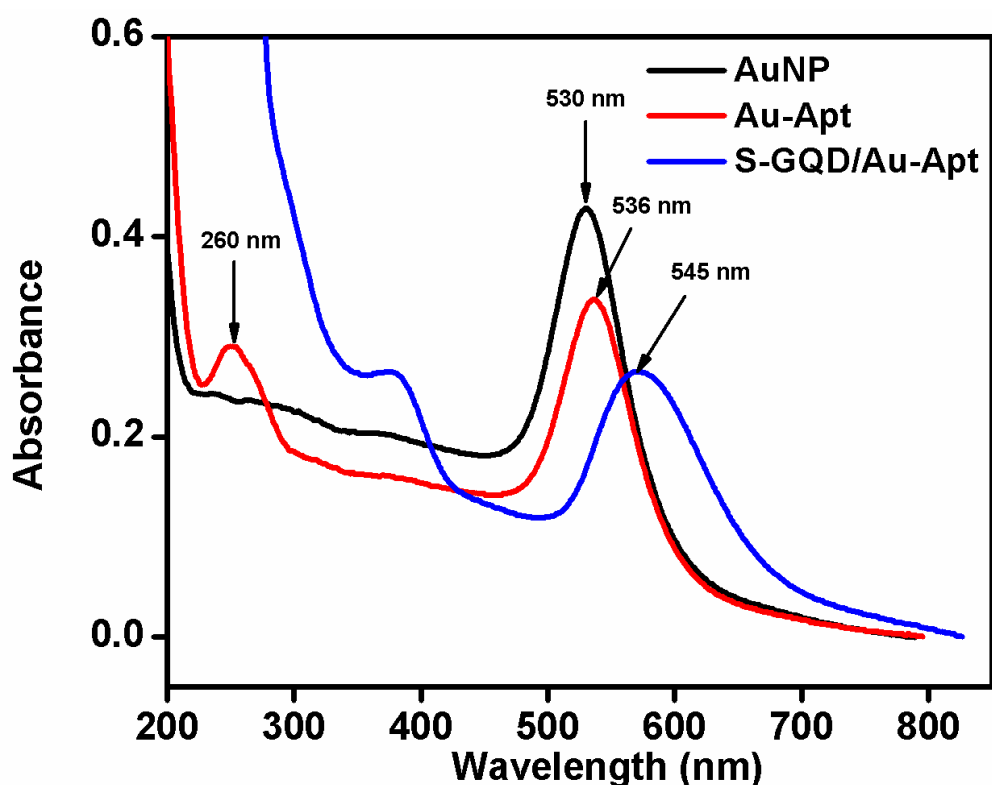
**Figure 5.4.** UV-Visible absorption spectra of Au, Au-Apt and S-GQD/Au-Apt

### 5.3.5. FT-IR spectroscopic analysis

To establish the bonding in S-GQD/Au-Apt complex FT-IR spectra were measured. From the FT-IR spectra it is observed that both S-GQD and S-GQD/Au-Apt complex showed the characteristic peaks including a broad bending vibration of -OH at 3340 cm$^{-1}$, C=O vibration peaks at 1700 cm$^{-1}$, C=C stretching vibration peaks at 1600 cm$^{-1}$, S=O at 1096 cm$^{-1}$ and C-S stretching vibrations at 635 cm$^{-1}$ **(Figure 5.5)**. In addition, a few additional peaks at 1130 cm$^{-1}$, and 851 cm$^{-1}$ corresponding to symmetric phosphate and P-O respectively were obtained in S-GQD-Apt complex which shows the complexation of S-GQD with aptamer **(Inset of Figure 5.5).**
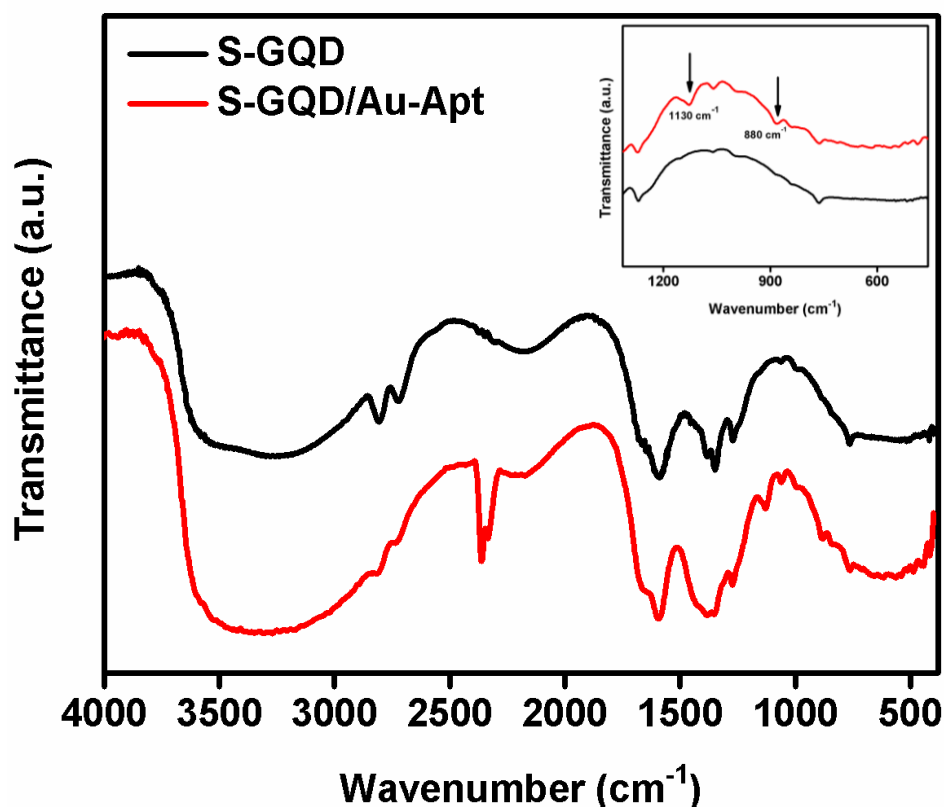
**Figure 5.5.** FT-IR spectra of S-GQD and S-GQD/Au-Apt complex.

### 5.3.6. XPS analysis

Further, XPS analysis was carried out to confirm the formation of S-GQD/Au-Apt complex. The survey spectra **(Figure 5.6)** of S-GQD/Au-Apt complex showed C, O and S as major elements. Additionally, it showed peaks at 399.4 eV, 133.2 eV and 82 eV corresponding to N 1s, P 2p and Au 4f, respectively, indicating the formation of S-GQD/Au-Apt complex. The corresponding atomic percentages are shown in **Table 5.2. Figures 5.7 (a-f)** show the deconvoluted C 1s, O 1s, S 2p, N 1s, P 2p and Au 4f spectra of S-GQD-Apt complex. The C 1s peaks at 288.4 eV (N-C=O), O 1s peaks at 133.7 eV (P=O), N 1s peak at 400.4 eV (HNC=O), P 2p peaks at 132.5 eV (P-O), 133.8 eV (P=O) and 134.3 eV (P-O-C) confirmed the formation of S-GQD/Au-Apt complex.
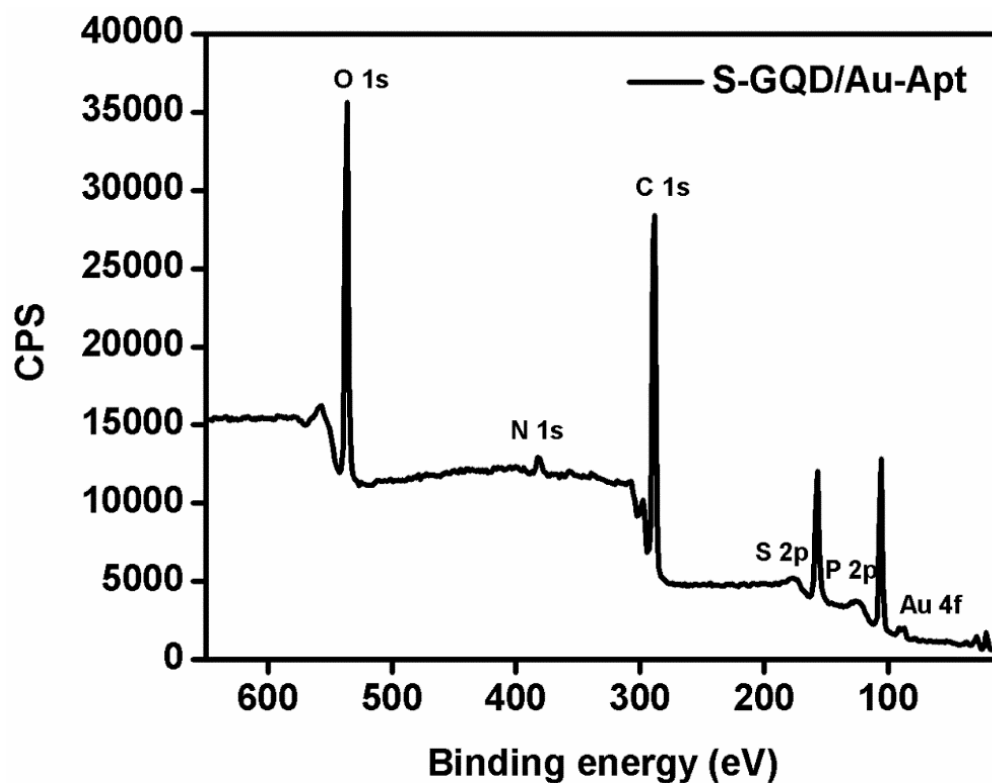
**Figure 5.6.** (a) XPS survey spectrum of S-GQD/Au-Apt complex.

**Table 5.2.** Atomic percentage compositions of the characteristic elements in S-GQD and S-GQD/Au-Apt complex

| Elements (At %) | C 1s | O 1s | S 2p | N 1s | P 2p | Au 4 f |
|---|---|---|---|---|---|---|
| S-GQD | 58.5 | 37.3 | 3.3 | - | - | - |
| S-GQD/Au-Apt | 52.7 | 34.3 | 1.81 | 3.3 | 2.2 | 0.8 |
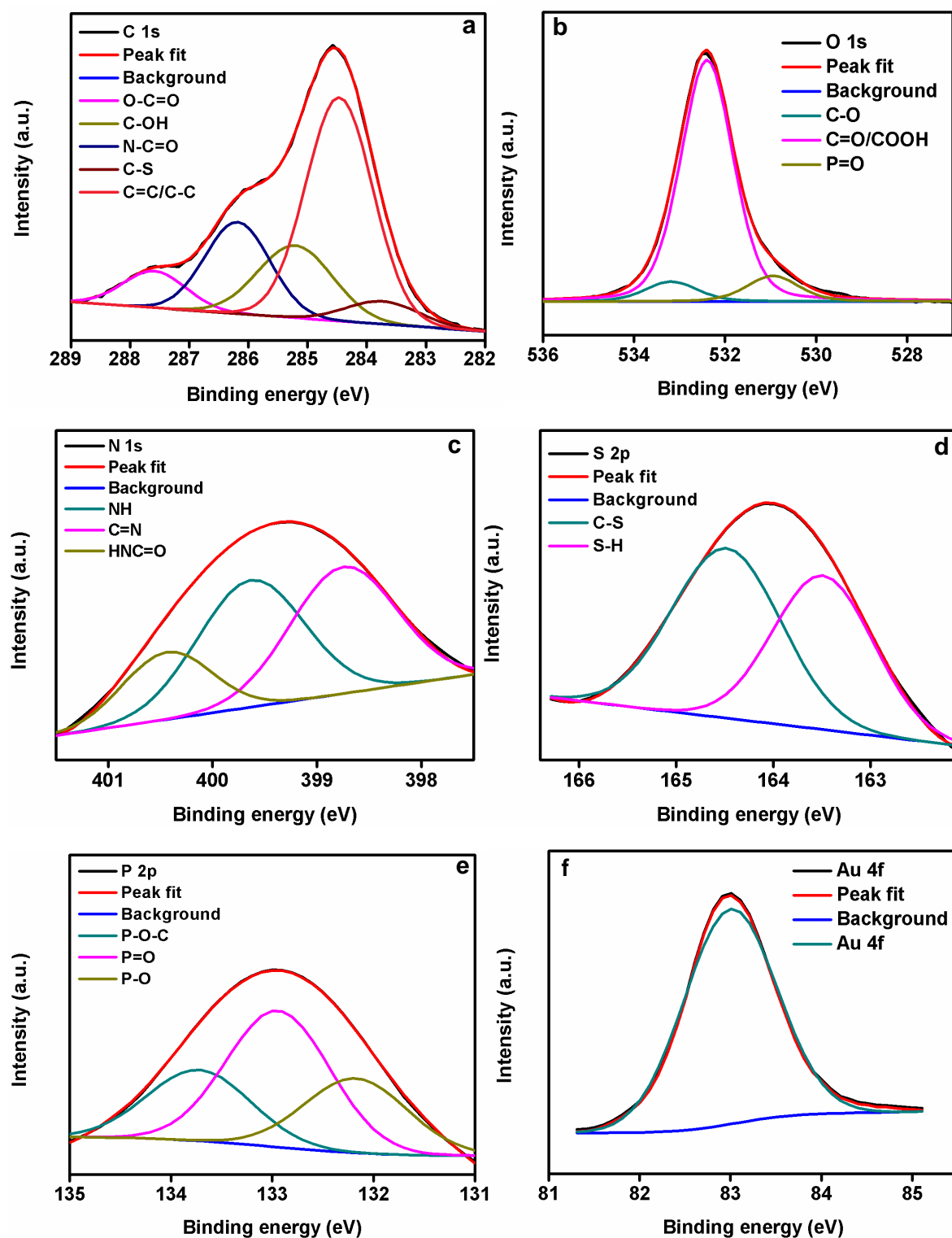
**Figure 5.7.** High resolution XPS spectra (a) C 1s, (b) O 1s, (c) N 1s (d) S 2p (e) P 2p and (f) Au 4f of S-GQD/Au-Apt complex

## 5.3.7. Recovery of S-GQDs (S-GQD-Rec) and its characterizations

One of the advantages of the present system is that the fluorescent molecule, S-GQD can be recovered and reused. Once the sensing of OM has been carried out,

167

due to specific binding of OM with the aptamer present on the surface of Au-Apt, the S-GQDs will be released in the system which results in its fluorescence turn-on behaviour. The released S-GQDs were further purified as described in the experimental section and labelled as S-GQD-Rec. TEM image of S-GQD-Rec **(Figure 5.8a)** showed that S-GQDs are evenly dispersed and possess uniform shape and size distribution (∼4 nm) as that of S-GQD **(Figure 5.8b)** taken initially. Additionally, UV-Visible spectrum **(Figure 5.8c)** of S-GQD-Rec showed the characteristic peak of S-GQD at 380 nm with the nearly same intensity as that of initial S-GQD taken. From **Table 5.3** it is observed that the atomic percentage of the characteristic elements of both S-GQD and S-GQD-Rec obtained from XPS are also comparable. Based on all these observations, it is confirmed that the S-GQDs are absolutely set free upon the addition of the analyte, OM and can be recovered.
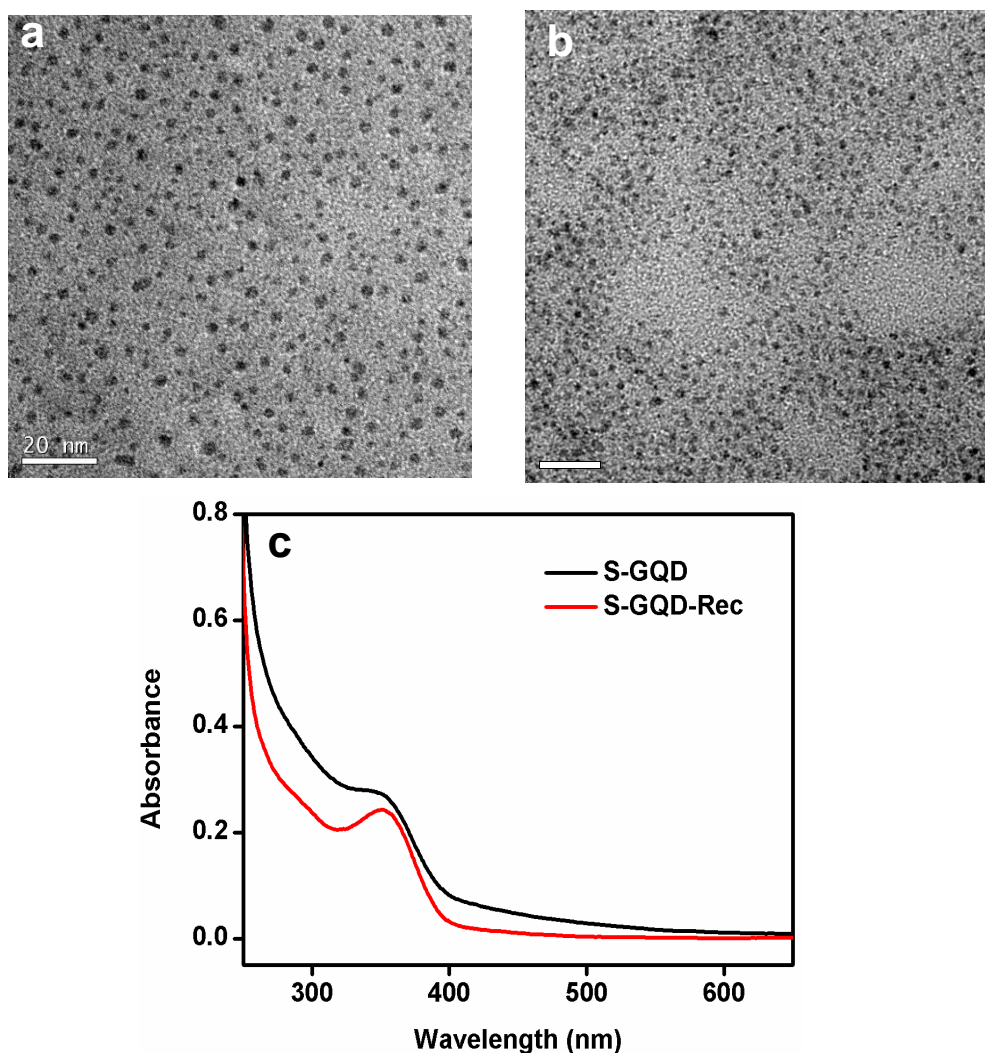


**Figure 5.8.** TEM images of (a) S-GQD-Rec, (b) S-GQD, (c) UV-Visible absorption spectra of S-GQD and S-GQD-Rec

**Table 5.3.** Atomic percentage compositions of the characteristic elements in S-GQD
and S-GQD-Rec

| Elements (At %) | C 1s | O 1s | S 2p |
|---|---|---|---|
| S-GQD | 58.5 | 37.3 | 3.3 |
| S-GQD Rec | 61.8 | 35.3 | 2.85 |

### 5.3.8. PL spectra and lifetime analysis

The sensing efficiency of the developed probe was evaluated by taking PL spectra of S-GQD and S-GQD/Au-Apt complex as shown in **Figure 5.9a**. Compared with S-GQD, an apparent fluorescence quenching was observed in the case of S-GQD/Au-Apt complex due to the scattering effect of Au/Apt. Therefore, S-GQD/Au-Apt complex can be utilized as a fluorescence sensing probe for the detection of OM, and while adding 300 ppb solution of analyte OM, the fluorescence emission of S-GQD was restored. In the latter case, OM specifically binds to the aptamer portion of S-GQD/Au-Apt complex to form Apt-OM complex resulting in the recovery of fluorescence of S-GQD. In the PL spectra shown in **Figure 5.9a**, curve 'C' showing that of S-GQD-Rec confirms the release of S-GQD, where the emission maximum is almost similar to that of S-GQD (curve 'A'). In order to demonstrate the fluorescence turn-off-on behavior, fluorescence lifetime analysis was carried out using time-correlated single-photon counting (TCSPC). The fluorescence emission lifetime of S-GQD, S-GQD/Au-Apt complex and S-GQD-Rec were measured by monitoring the fluorescence emission intensity decay as a function of time **(Figure 5.9b)**. The average fluorescence lifetime of S-GQD/Au-Apt complex was observed as 0.048 ns, which is much lower than that of S-GQD (3.3 ns) due to the significant quenching of S-GQD in the presence of larger aggregates of Au-Apt. Compared with S-GQD, reduction in the exciton lifetime of the complex was observed which could be due to the efficient exciton energy transfer from smaller S-GQD to larger aggregates in the complex.[55] As a result, more rapid fluorescence emission decay is observed which leads to fluorescence quenching in S-GQD/Au-Apt complex. Fluorescence recovery of S-GQD after the addition of analyte to S-GQD/Au-Apt complex was again confirmed by the decay analysis. It was found that the fluorescence lifetime of S-GQD-Rec is 2.8

ns which was almost similar to that of initial S-GQD. These fluorescence lifetime results tabulated in **Table 5.4** further established that the fluorescence of S-GQD is turned off with Au-Apt addition and turned on with the addition of OM, which is more evident in the photographs shown in the inset of **Figure 5.9a.**
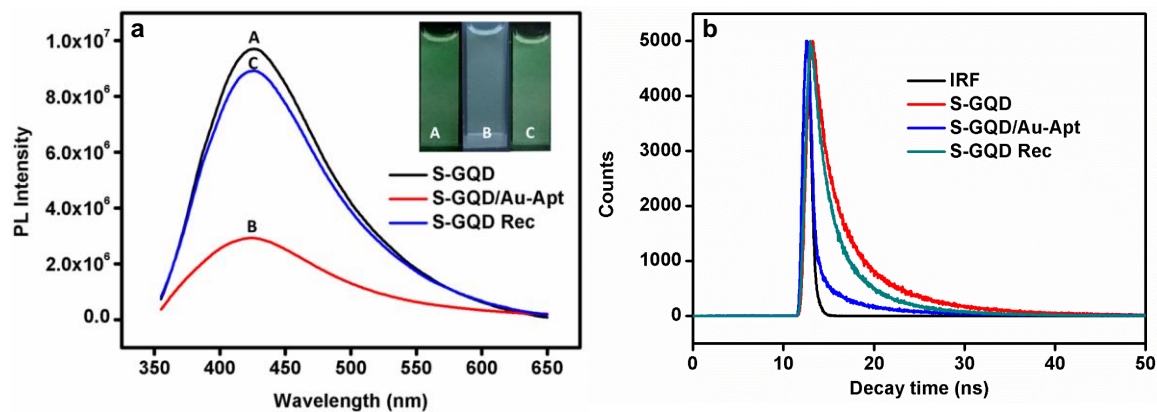


**Figure 5.9.** (a) PL spectra, inset show the photographs of S-GQD, S-GQD/Au-Apt complex and S-GQD-Rec (b) Time-correlated single-photon counting (TCSPC) spectra of S-GQD, S-GQD/Au-Apt complex and SGQD-Rec.

**Table 5.4.** Fluorescence lifetime, relative percentage and the average lifetime of S-GQD, S-GQD/Au-Apt complex and S-GQD-Rec

| Sample | Lifetime | Amplitude | Average lifetime (T) |
|---|---|---|---|
| S-GQD | T1=1.827<br>T2=6.784 | A1=38.85%<br>A2=61.15% | 3.302 ns |
| S-GQD /Au-Apt | T1=2136.67<br>T2=7873.8<br>T3=31.458 | A1=13.78%<br>A2=21.37%<br>A3=64.85% | 0.0485 ns |
| S-GQD-Rec | T1=1.402<br>T2=5.056 | A1=44.13%<br>A2=55.87% | 2.852 ns |

### 5.3.9. Mechanism of sensing strategy

In the light of above discussions, the mechanism of dual mode SERS/fluorescence sensing strategy based on Au-Apt and S-GQD for the ultrasensitive and selective detection of OM is illustrated in **Scheme 5.1**. The AuNPs were first modified by thiolated aptamer through strong gold-thiol (Au-SH) affinity interactions. When S-GQD was added to Au-Apt, S-GQD/Au-Apt complex was formed, resulting in the effective quenching of the fluorescence of S-GQD. Upon the addition of analyte, the OM specific aptamer will recognize the target molecule and will undergo conformational alteration to enclose OM molecules as discussed in Chapter 4. This, in turn, resulted in the reversal of S-GQD/Au-Apt complex to Au-Apt/OM complex and the release of S-GQD. The released S-GQDs turn on the fluorescence signal and Au-Apt/OM complex gives the SERS signal. Therefore, S-GQD/Au-Apt system can be used for dual sensing by way of fluorescence turn-on detection and highly sensitive SERS mode of detection for the selective and ultrasensitive detection of OM.
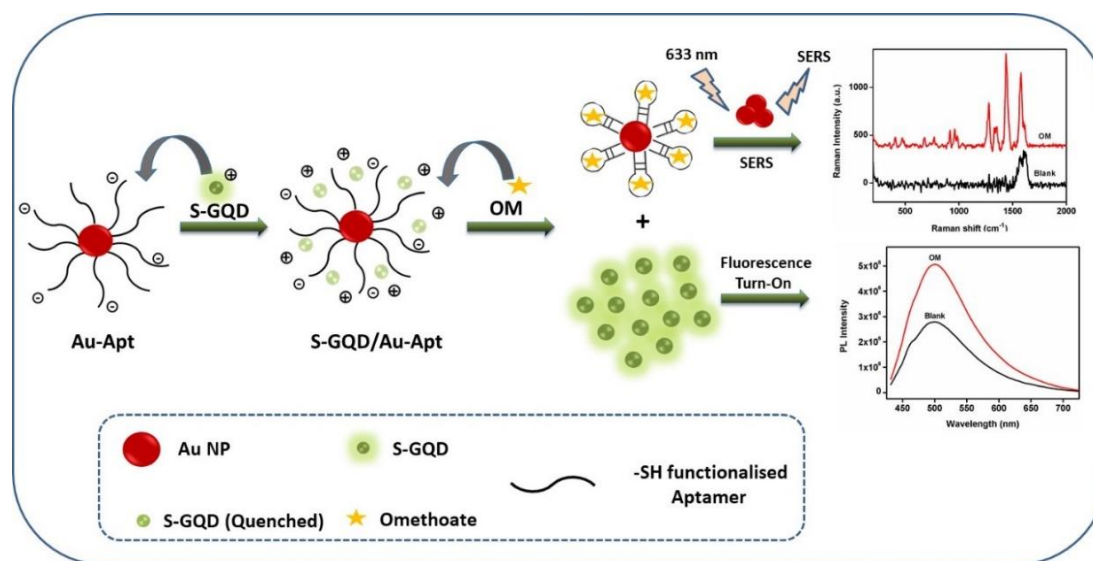


**Scheme 5.1.** Schematic illustration of a dual-mode SERS/fluorescence sensor using S-GQD/Au-Apt complex for the selective and ultrasensitive detection of omethoate.

### 5.3.10. Fluorescence detection of OM based on S-GQD/Au-Apt probe

The fluorescence detection of OM was carried out using S-GQD/Au-Apt probe in aqueous medium at room temperature. To study the sensitivity towards OM, PL spectra of S-GQD and S-GQD/Au-Apt complex in the absence and presence of varying concentrations of OM was recorded at excitation wavelength of 380 nm. From **Figure**

**5.10a** it is observed that the PL spectra of S-GQD/Au-Apt complex showed significant fluorescence quenching with respect to S-GQD due to the quenching effect of Au/Apt. To analyse the sensing performance of the designed fluorescent detection probe, OM of varying concentrations (0 ppm-20 ppm) were added to S-GQD/Au-Apt complex and its PL spectra were recorded at the same excitation wavelength. From **Figure 5.10b,** it was observed that fluorescence emission intensity enhanced progressively with increase in the concentration of OM. This is due to the reversal binding of S-GQD/Au-Apt complex to very strong and unique Au-Apt/OM complex along with the release of free S-GQDs. Thus, OM triggered the release of S-GQDs result in the fluorescence recovery of S-GQD. The fluorescence enhancement showed a good linear relationship with regression value, $R^2$ of 0.992 over the concentration range of 1-17 ppm with LOD 1.7 ppm **(Figure 5.10c)**.
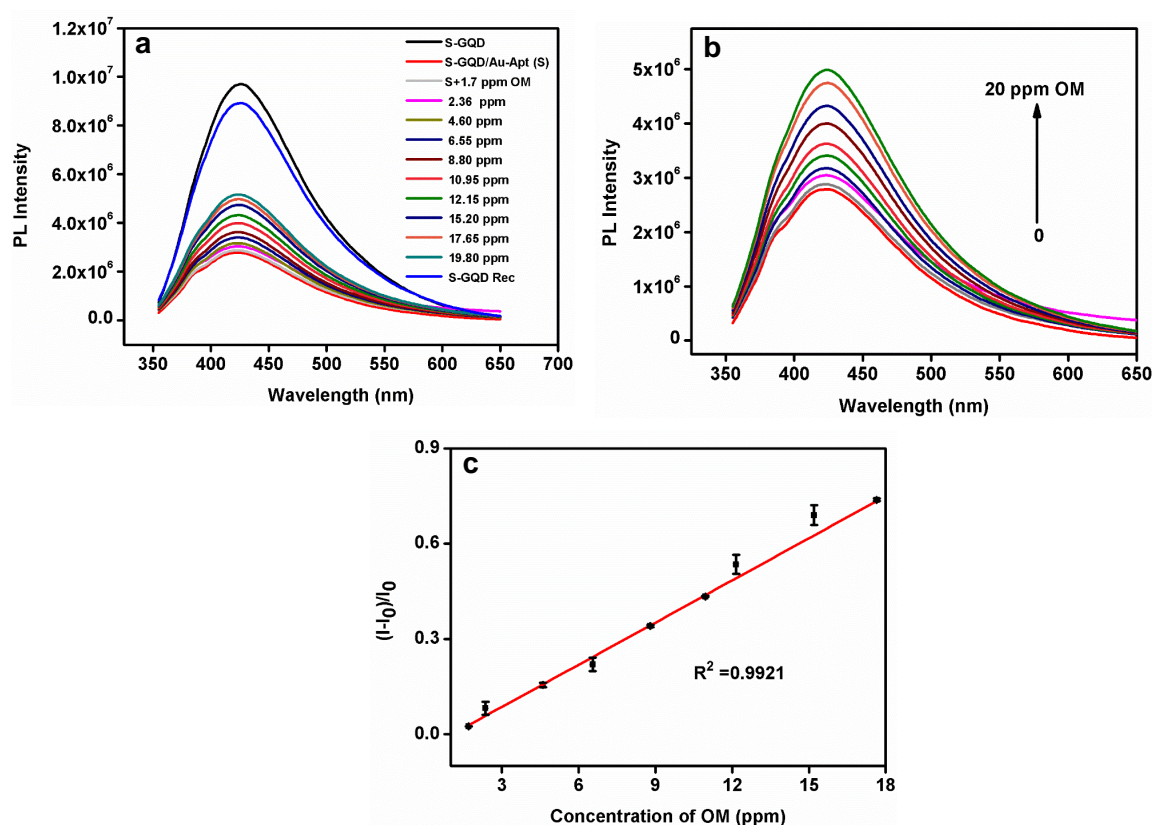


**Figure 5.10**. PL spectra of (a) S-GQD, S-GQD/Au-Apt complex in the presence of varying concentrations of OM (1.7 ppm-20 ppm) and S-GQD-Rec (b) S-GQD/Au-Apt complex with increasing concentrations of OM from 0 to 20 ppm (c) Linear regression plot with concentration of OM in the range of 1 to 17 ppm.

### 5.3.11. Selectivity Study

To further evaluate the selectivity of the designed sensor towards OM, fluorescence response of S-GQD/Au-Apt complex in the presence of different control pesticides such as carbofuran (CF), methyl parathion (MPr), imidacloprid (IM), acetamiprid (AC), metalaxyl (MT), and Thiram (Tr) at same concentration (100 ppm) was studied under identical conditions. From **Figure 5.11**, it is clear that only OM exhibited a significant fluorescent recovery, while the others showed a slight decrease in the fluorescence intensity when compared to blank indicating a high selectivity towards OM. These results confirmed that the designed fluorescence turn-on sensor can be used for the selective detection of OM, due to the specific recognition and strong affinity of aptamer towards OM.
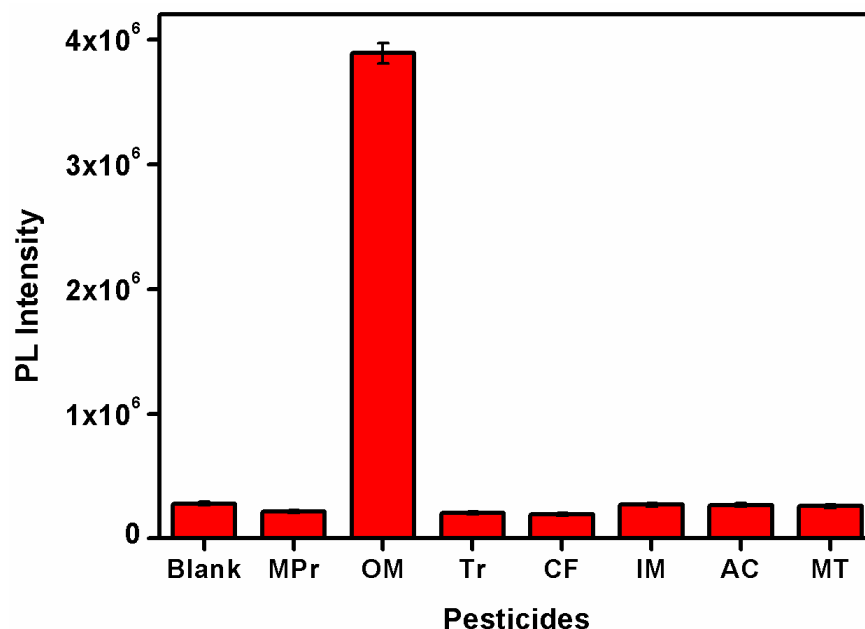


**Figure 5.11.** Bar diagram showing the selectivity of the designed dual-mode sensor for OM. (Concentrations of OM and other pesticides were optimised to 100 ppm).

### 5.3.12. Detection of OM based on S-GQD/Au-Apt probe by SERS

As seen from TEM image **(Figure 5.2 f)**, we successfully obtained aggregated AuNPs in the matrix of aptamer surrounded by S-GQDs as our sensing probe. SERS analysis of OM was carried out using S-GQD/Au-Apt nano probe in order to detect it at further lower dilutions compared to fluorescence study. Raman spectra give the fingerprint region of molecules and SERS can give rise to sensitive and trace level detection at ppb level. Fig 5.12.a. shows the SERS spectra of OM at different

concentrations ranging from 2.5 ppm to 0.05 ppb. The characteristic Raman bands of OM obtained were 405 cm$^{-1}$ corresponds to δs (COPOC), 700 cm$^{-1}$ attributed to ν(C–S)/δ(CNC)/δ(NCO), 775 cm$^{-1}$ corresponds to stretching and symmetric vibrations of ν(P–S)/ν(PO$_2$), 910 cm$^{-1}$ ρ(CH$_3$)/ν(C–C), 1235 cm$^{-1}$ ν(P=O), 1338 cm$^{-1}$ ω(CH$_2$)/δ(NH)/ν(CN) 1440 cm$^{-1}$ (CH$_2$) and 1620 cm$^{-1}$ ν(C=O). It was observed that Raman spectra obtained from bare solution of OM with concentration 1 ppm (Bare) showed weak spectra where no molecular signals were evident even at that concentration. Fig 5.12.b shows a plot of SERS intensity at 1437 cm$^{-1}$ vs concentration of OM. The standard deviations and average values were calculated from more than three independent SERS spectra at varying OM concentrations. It could be observed that the introduction of Au NPs enhanced the detection limit to 0.05 ppb with SERS mode when compared to the fluorescence method. The peaks corresponding to OM were resolved up to ppb level. Further the concentration of OM vs SERS intensity at 1437 cm$^{-1}$ was plotted. The linear regression plot with the regression coefficient, $R^2$ = 0.99 was obtained. The error bars were calculated for spectra taken from 3 random spots in S-GQD/Au-Apt probe.
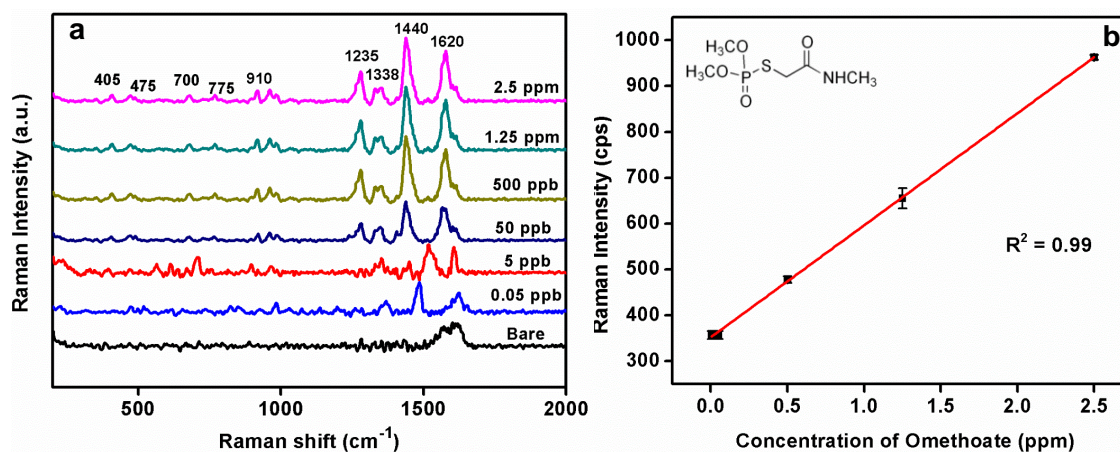


**Figure 5.12**. (a) SERS spectra of OM at different concentration (0.05 ppb-2.5 ppm) (b) The linear regression plot of concentration of OM *vs* SERS intensity at 1437 cm$^{-1}$ with a regression coefficient, $R^2$ = 0.99.

### 5.3.13. Comparison with other fluorescence or SERS methods

Performance comparison of this method with other reported fluorescence or SERS method for the detection of OM has been tabulated in **Table 5.5.** From literature, it could be observed that compared with most of the fluorescence or SERS

method, our dual-mode sensor has a very low LOD of 0.05 ppb. Although some methods show better LOD, all of them are single-mode sensors for OM. However, our designed sensor is a dual-mode sensing platform and can therefore be used to detect OM at higher concentrations simultaneously as a fluorescence turn-on assay ($\geq 7.9 \times 10^{-6}$ M) and a SERS assay at very low concentration of 0.05 ppb ($2.4 \times 10^{-10}$ M). To the best of our knowledge, a dual-mode SERS/fluorescence aptasensor for omethoate was reported for the first time.

**Table 5.5.** Performance comparison of different SERS or fluorescence methods for the detection of omethoate

| Probe | Detection method | LOD | Detection Linear Range | Ref. |
|---|---|---|---|---|
| Gold nanoparticles | SERS | $4.9 \times 10^{-4}$ M | $2.4 \times 10^{-4}$ M – $1.2 \times 10^{-3}$ M | [21] |
| Silver nanoparticles | SERS | $5 \times 10^{-7}$ M | $5 \times 10^{-7} - 1 \times 10^{-5}$ M | [56] |
| Caesium lead halide perovskite QD | Fluorescence | $8.8 \times 10^{-8}$ M | $2.3 \times 10^{-7}$ M- $1.8 \times 10^{-6}$ M | [57] |
| Silver nanoparticles | SERS | $4.69 \times 10^{-9}$ M | $4.69 \times 10^{-9}$ M - $4.69 \times 10^{-3}$ M | [58] |
| Molecular Beacon (MB) | Fluorescence polarization | $23.4 \times 10^{-3}$ M | - | [59] |
| Gold-based nanobeacon | Fluorescence | $2.35 \times 10^{-6}$ M | - | [60] |
| Silver nanoparticles | SERS | $1 \times 10^{-4}$ M | - | [22] |
| Sulphur-doped graphene quantum dots (S-GQDs) | Fluorescence | $4.7 \times 10^{-9}$ M | $4.7 \times 10^{-6}$ M – $4.7 \times 10^{-4}$ M | Chapter-4 |
| Aptamer modified gold nanoparticle and S-GQDS | SERS/ Fluorescence | $2.4 \times 10^{-10}$ M [0.05 ppb (SERS)] $7.9 \times 10^{-6}$ M [1.7 ppm (Fluorescence)] | $2.4 \times 10^{-10}$ M - $1.2 \times 10^{-5}$ M (SERS) $4.7 \times 10^{-6}$ M – $9.4 \times 10^{-5}$ M (Fluorescence) | This work |

## 5.4. Conclusions

In this chapter, we have developed an efficient dual-mode SERS/fluorescence sensor based on aptamer modified gold nanoparticles and S-GQDs for the ultrasensitive and selective detection of omethoate residues in trace levels. The addition of OM to the designed S-GQD/Au-Apt sensing probe induces structural switching of aptamer with the formation of Au-Apt/OM with the simultaneous release of S-GQDs from the complex. The released S-GQDs tun-on the fluorescence signal and the component, Au-Apt/OM gives the SERS signal. This facilitated a dual-mode SERS/fluorescence sensor for OM which improves the reliability and accuracy of the sensor. The sensing based on the fluorescence turn-on has a linear response towards different concentrations of OM (1 ppm to 20 ppm range) with a limit of detection (LOD) of 1.7 ppm with high selectivity. The sensing based on the formation of Au-Apt/OM SERS probe shows enhanced sensitivity with LOD 0.05 ppb and a wide range of linear response from 0.05 ppb to 2.5 ppm. Thus, a dual mode SERS/fluorescence sensor is successfully constructed with broad response range, rapid screening and very high sensitivity which provides an efficient way for selective and ultrasensitive detection of OM. The developed dual-mode sensor also demonstrates high selectivity for omethoate over other control pesticides. Therefore, this dual-mode method could minimize the risk of false-positive and false-negative detection by obtaining results from the dual-channel sensing system, which increases the accuracy and reliability of the sensing system.This strategy offers a new method for designing dual-mode aptasensors combined with different specific aptamers for other targets which can be applied in the field of food analysis and environmental monitoring.

## References

1. X. Liu, Y. Li, J. Liang, W. Zhu, J. Xu, R. Su, L. Yuan and C. Sun, *Talanta*, 2016, **160**, 99-105.
2. Y. Wang, K. Lee and J. Irudayaraj, *Chemical Communications*, 2010, **46**, 613-615.
3. N. Cheng, Y. Song, Q. Fu, D. Du, Y. Luo, Y. Wang, W. Xu and Y. Lin, *Biosensors and Bioelectronics*, 2018, **117**, 75-83.
4. J. Wang, Y. Wu, P. Zhou, W. Yang, H. Tao, S. Qiu and C. Feng, *Analyst*, 2018, **143**,

5151-5160.

5.  Y. Wu, L. Liu, S. Zhan, F. Wang and P. Zhou, *Analyst*, 2012, **137**, 4171-4178.

6.  X. Niu, Y. Zhong, R. Chen, F. Wang, Y. Liu and D. Luo, *Sensors and Actuators B: Chemical*, 2018, **255**, 1577-1581.

7.  J. Dapra, L. H. Lauridsen, A. T. Nielsen and N. Rozlosnik, *Biosensors and Bioelectronics*, 2013, **43**, 315-320.

8.  T. Guo, X. Lin, Y. Liu, J. Deng, P. Qian, Y. Lyu, Z. Zhang and S. Wang, *Sensors and Actuators B: Chemical*, 2018, **262**, 619-624.

9.  M. A. Beketov, B. J. Kefford, R. B. Schäfer and M. Liess, *Proceedings of the National Academy of Sciences*, 2013, **110**, 11039-11043.

10. M. Liang, K. Fan, Y. Pan, H. Jiang, F. Wang, D. Yang, D. Lu, J. Feng, J. Zhao and L. Yang, *Analytical chemistry*, 2012, **85**, 308-312.

11. X. Yan, H. Li and X. Su, *TrAC Trends in Analytical Chemistry*, 2018, **103**, 1-20.

12. S. A. Nsibande and P. B. C. Forbes, *Analytica Chimica Acta*, 2016, **945**, 9-22.

13. G. Zweig, *Chromatographic Reviews*, 1964, **6**, 110-128.

14. D. Barceló, *Journal of Chromatography A*, 1993, **643**, 117-143.

15. L. Tognaccini, M. Ricci, C. Gellini, A. Feis, G. Smulevich and M. Becucci, *Molecules*, 2019, **24**, 292.

16. L. Guerrini, S. Sanchez-Cortes, V. L. Cruz, S. Martinez, S. Ristori and A. Feis, *Journal of Raman Spectroscopy*, 2011, **42**, 980-985.

17. A. M. Hegazy, R. M. Abdelfatah, H. M. Mahmoud and M. A. Elsayed, *Beni-Suef University Journal of Basic and Applied Sciences*, 2018, **7**, 598-605.

18. X. Zhao, W. Kong, J. Wei and M. Yang, *Food chemistry*, 2014, **162**, 270-276.

19. O. Kiguchi, K. Oka, M. Tamada, T. Kobayashi and J. Onodera, *Journal of Chromatography A*, 2014, **1370**, 246-254.

20. Y. Liu, B. Lv, A. Liu, G. Liang, L. Yin, Y. Pu, W. Wei, S. Gou and S. Liu, *Sensors and Actuators B: Chemical*, 2018, **265**, 675-681.

21. J. Chen, D. Dong and S. Ye, *RSC Advances*, 2018, **8**, 4726-4730.

22. H. J. Kim, C. J. Lee, M. R. Karim, M. S. Kim and M. S. Lee, *Spectrochimica Acta Part A: Molecular and Biomolecular Spectroscopy*, 2011, **78**, 179-184.

23. A. P. Craig, A. S. Franca and J. Irudayaraj, *Annual review of food science and technology*, 2013, **4**, 369-380.

24. X. Xie, H. Pu and D.-W. Sun, *Critical reviews in food science and nutrition*, 2018, **58**,

2800-2813.

25. H. Wei, S. M. H. Abtahi and P. J. Vikesland, *Environmental Science: Nano*, 2015, **2**, 120-135.

26. W. Q. Lim and Z. Gao, *Nano Today*, 2016, **11**, 168-188.

27. H. Fang, X. Zhang, S. J. Zhang, L. Liu, Y. M. Zhao and H. J. Xu, *Sensors and Actuators B: Chemical*, 2015, **213**, 452-456.

28. Z. Chen, L. Yongyu, P. Yankun and X. Tianfeng, *International Journal of Agricultural and Biological Engineering*, 2015, **8**, 113-120.

29. Y. Zhang, Z. Wang, L. Wu, Y. Pei, P. Chen and Y. Cui, *Analyst*, 2014, **139**, 5148-5154.

30. J.-K. Yang, H. Kang, H. Lee, A. Jo, S. Jeong, S.-J. Jeon, H.-I. Kim, H.-Y. Lee, D. H. Jeong and J.-H. Kim, *ACS applied materials & interfaces*, 2014, **6**, 12541-12549.

31. G. McNay, D. Eustace, W. E. Smith, K. Faulds and D. Graham, *Applied spectroscopy*, 2011, **65**, 825-837.

32. Y. Yang, Z.-Y. Li, K. Yamaguchi, M. Tanemura, Z. Huang, D. Jiang, Y. Chen, F. Zhou and M. Nogami, *Nanoscale*, 2012, **4**, 2663-2669.

33. C. Zhai, Y. Peng, Y. Li and T. Xu, *Acta Chimica Sinica*, 2015, 6.

34. L. Bi, J. Dong, W. Xie, W. Lu, W. Tong, L. Tao and W. Qian, *Analytica chimica acta*, 2013, **805**, 95-100.

35. Y. Li, J. Xu, L. Wang, Y. Huang, J. Guo, X. Cao, F. Shen, Y. Luo and C. Sun, *Aptamer-based fluorescent detection of bisphenol A using nonconjugated gold nanoparticles and CdTe quantum dots*, 2015.

36. X. Sun, Y. Wang and Y. Lei, *Chemical Society Reviews*, 2015, **44**, 8019-8061.

37. X. Zhao, J. Gao, X. He, L. Cong, H. Zhao, X. Li and F. Tan, *RSC Advances*, 2015, **5**, 39587-39591.

38. R. V. Nair, R. T. Thomas, V. Sankar, H. Muhammad, M. Dong and S. Pillai, *ACS Omega*, 2017, **2**, 8051-8061.

39. A. Ananthanarayanan, Y. Wang, P. Routh, M. A. Sk, A. Than, M. Lin, J. Zhang, J. Chen, H. Sun and P. Chen, *Nanoscale*, 2015, **7**, 8159-8165.

40. N. Li, X. Wang, J. Chen, L. Sun and P. Chen, *2D Materials*, 2015, **2**, 034018.

41. E. Zor, E. Morales-Narváez, A. Zamora-Gálvez, H. Bingol, M. Ersoz and A. Merkoçi, *ACS Applied Materials & Interfaces*, 2015, **7**, 20272-20279.

42. M. Liu, Z. Wang, L. Pan, Y. Cui and Y. Liu, *Biosensors and Bioelectronics*, 2015, **69**,

142-147.

43.    Y. Yue, T.-Y. Liu, H.-W. Li, Z. Liu and Y. Wu, *Nanoscale*, 2012, **4**, 2251-2254.

44.    Z. Guo, Y. Jia, X. Song, J. Lu, X. Lu, B. Liu, J. Han, Y. Huang, J. Zhang and T. Chen, *Analytical chemistry*, 2018, **90**, 6124-6130.

45.    S. Pang and L. He, *Analytical Methods*, 2016, **8**, 1602-1608.

46.    Y. Liu, Z. Wei, W. Duan, C. Ren, J. Wu, D. Liu and H. Chen, *Dyes and Pigments*, 2018, **149**, 491-497.

47.    A. Mars, M. Hamami, L. Bechnak, D. Patra and N. Raouafi, *Analytica chimica acta*, 2018, **1036**, 141-146.

48.    J. Liu, J. Bu, W. Bu, S. Zhang, L. Pan, W. Fan, F. Chen, L. Zhou, W. Peng and K. Zhao, *Angewandte Chemie International Edition*, 2014, **53**, 4551-4555.

49.    Z. Xu, J. Jiang, X. Wang, K. Han, A. Ameen, I. Khan, T.-W. Chang and G. L. Liu, *Nanoscale*, 2016, **8**, 6162-6172.

50.    Y. Qi, J. Zhao, G.-j. Weng, J.-j. Li, X. Li, J. Zhu and J.-w. Zhao, *Journal of Materials Chemistry C*, 2018, **6**, 12283-12293.

51.    H. Wang, X. Huang, G. Wen and Z. Jiang, *Scientific reports*, 2019, **9**, 1-10.

52.    S. Zong, Z. Wang, H. Chen, G. Hu, M. Liu, P. Chen and Y. Cui, *Nanoscale*, 2014, **6**, 1808-1816.

53.    L.-L. Qu, S.-H. He, J.-J. Wang, Z.-C. Lin, D. Barry, G.-H. Yang, P. Wang, P. Zhang and H.-T. Li, *Sensors and Actuators B: Chemical*, 2017, **251**, 934-941.

54.    J. Kimling, M. Maier, B. Okenve, V. Kotaidis, H. Ballot and A. Plech, *The Journal of Physical Chemistry B*, 2006, **110**, 15700-15707.

55.    B. Aswathy and G. Sony, *Microchemical Journal*, 2014, **116**, 151-156.

56.    L. Guerrini, S. Sanchez-Cortes, V. L. Cruz, S. Martinez, S. Ristori and A. Feis, *Journal of Raman Spectroscopy*, 2011, **42**, 980-985.

57.    S. Huang, M. Guo, J. Tan, Y. Geng, J. Wu, Y. Tang, C. Su, C. C. Lin and Y. Liang, *ACS applied materials & interfaces*, 2018, **10**, 39056-39063.

58.    T. Yaseen, D.-W. Sun, H. Pu and T.-T. Pan, *Food Analytical Methods*, 2018, **11**.

59.    C. Zhang, B. Lin, Y. Cao, M. Guo and Y. Yu, *Journal of agricultural and food chemistry*, 2017, **65**, 3065-3073.

60.    X. Dou, X. Chu, W. Kong, J. Luo and M. Yang, *Analytica chimica acta*, 2015, **891**, 291-297.

# Chapter 6

## Summary and Future Perspectives

The present dissertation is focused on the development of a rapid, facile synthetic strategy for the production of size-tunable GQDs with high product yield and improved quantum yield. Relative to other heat treatment methods, microwave-assisted sonochemical method can effectively facilitate the formation of novel architectures with well-defined particle size and narrow size distribution in short reaction time. Various strategies have been explored to improve the fluorescent properties of GQDs such as surface functionalization, chemical doping, tuning the degree of oxidation and controlling the intrinsic properties. Doping of carbon nanomaterials with heteroatoms induce electronic and structural distortion, which provides an efficient way to tune their intrinsic properties, including surface chemistry, chemical composition, electronic properties, and band gap.

In the first part of the thesis, a rapid microwave-assisted sonochemical (MS) synthesis of GQDs was demonstrated. This synthesis strategy facilitated faster reaction rates resulting in the formation of finer particles of GQDs. The GQDs were synthesized within a short span of time (30 min) by oxidative cutting of GO using $KMnO_4$ as an oxidizing agent in an acid-free condition. Indeed, we could tune the particle size by tuning the microwave reaction power. The synthesized GQDs are highly crystalline and have uniform size distribution. These GQDs exhibited relatively higher quantum yield up to 23.8 %, high product yield (75-81 %) and stable size-dependent photoluminescence in aqueous solutions. Our studies indicate that the GQDs possess very good biocompatibility, good aqueous dispersibility, low cytotoxicity, high photostability and hence can be applied as excellent fluorescent probes for cancer cell imaging. Our findings on the biocompatibility and fluorogenic property of the GQDs observed in cancer cells highlight their significance in clinical diagnostic applications. It can further be employed as targeting moieties for drug delivery applications as well. The GQDs synthesized were also demonstrated for the detection of physiologically relevant metal ions and particularly for the sensing of $Fe^{3+}$ ions in aqueous media.

Further, an enhancement in the fluorescence of GQD was achieved using patterned substrates (surface geometry effects) in order to meet the application requirements such as enhanced sensitivity and lower LOD. For the study, we have adopted two methodologies, namely breath figure technique and photonic bandgap effect. Both the methodologies can more efficiently excite and extract the light

emitted by GQDs which leads to fluorescence enhancement and thus lowering the detection limits towards various analytes in sensing applications. By adopting breath figure method, we could achieve a 77-fold enhancement of fluorescence emission through aggregation-induced emission enhancement (AIEE) and hence the sensitivity towards $Fe^{3+}$ was enhanced with LOD as low as 80 nM. In addition, we achieved a 102-fold enhancement of fluorescent emission of GQDs using colloidal photonic crystals (CPCs) having micro and nano-topographies due to closed-pack arrangement of polystyrene microspheres. CPC-based GQD platform was further used for the sensitive detection of $Fe^{3+}$ ions with much lower LOD as 30 nM.

Next, we tuned the optical properties of GQDs by a heteroatom doping strategy to prepare green fluorescent sulphur-doped graphene quantum dots (S-GQDs). S-GQDs were synthesized from graphene oxide via MS method within 5 min, using $KMnO_4$ as an oxidizing agent and $H_2SO_4$ as the doping precursor. S-GQDs exhibited uniform particle size distribution (~5 nm), high crystallinity, monolayer thickness, high production yield (85 %) and improved quantum yield (27.8 %). As part of the realization of a simple flexible solid-state fluorescent sensor, PVA/S-GQD composite films were fabricated. Both aqueous S-GQD and PVA/S-GQD flexible films were demonstrated as excellent fluorescent probes for the ultrasensitive detection of pesticides with a remarkable limit of detection at ppb level for Carbofuran (0.45 ppb) and Thiram (1.6 ppb). Additionally, the S-GQD-based fluorescent sensor was successfully applied for the detection of CF pesticide in real samples with ppb level sensitivity.

Although S-GQD based sensors exhibited high sensitivity towards various pesticides, their selective detection of a particular analyte is challenging. With an aim of achieving high selectivity towards a particular pesticide, we designed a simple and efficient fluorescent turn-on aptasensor based on S-GQD utilizing specific recognition and binding properties of an aptamer selective and sensitive detection of omethoate (OM), which is a systemic organophosphorus model pesticide. The detection strategy of aptasensor is based on tuning the aggregation-disaggregation mechanism of S-GQD by way of conformational alteration of the recognition probes. Fluorescence turn OFF-ON process includes aggregation-induced quenching of S-GQD with aptamer via S-GQD-aptamer complex formation and its subsequent fluorescence recovery with the addition of OM by structural switching of S-GQD-aptamer complex

to aptamer-omethoate complex.   The sensing strategy does not require any modification of either the signal transmitting nanoparticle or the reporter probe which makes it facile to construct a simple and novel turn-on aptasensor for pesticide detection. The developed 'switch-on' aptasensor achieved a limit of detection as low as 1 ppb with high selectivity for OM over other control pesticides. Moreover, the fluorescent signal material used could be recovered for further usage. The proposed aptamer strategy offers a new method for designing various aptasensors combined with different specific aptamers for other molecules of interest.

In order to further enhance the sensitivity and reliability of the signals, a complementary dual-mode sensing system was designed with the aim to provide two output signals, covering a wider detection range and making the sensor more accurate and efficient. In addition, this dual-mode approach, could minimize the risk of false-positive and false negative detection of analytes, by obtaining results from dual-channel sensing system, which improves the accuracy and reliability of the sensing system. With the objective of achieving an enhanced sensitivity for the trace level detection of OM, we designed a dual-mode SERS/fluorescence sensor based on aptamer modified gold nanoparticles (Au-Apt) and S-GQD. The addition of OM to the designed S-GQD/Au-Apt sensing probe induces structural switching of aptamer with the formation of Au-Apt/OM with the simultaneous release of S-GQDs from the complex. The released S-GQDs tun-on the fluorescence signal and the component Au-Apt/OM gives the SERS signal. This facilitated a dual-mode SERS/fluorescence sensor for OM which improves the reliability and accuracy of the sensor. The sensing based on the fluorescence turn-on has a linear response for the concentration of OM from 1 ppm to 20 ppm with a limit of detection (LOD) of 1.7 ppm with high selectivity. The sensing based on the formation of Au-Apt/OM SERS probe shows enhanced sensitivity with LOD 0.05 ppb and a wide range of linear response from 0.05 ppb to 2.5 ppm. Thus, a dual-mode SERS/fluorescence sensor is successfully constructed with broad response range, rapid screening and very high sensitivity which provides an efficient way for selective and ultrasensitive detection of OM. The developed dual-mode sensor also demonstrates high selectivity for OM over other control pesticides. Considering all the above advantages, we believe that the designed dual-mode aptasensor strategy can offer alternative approaches for other targets of interest in the field of environmental monitoring and food safety.

**Future projections**

The results obtained in the present study provide excellent scope for further research as discussed below.

- Tune the bandgap using various non-metals/even multiple elements (co-doping) to obtain NIR emission so that it can be used for several strategic applications like anti-counterfeiting and multi-colour imaging.

- GQDs can be used as targeting and delivery moieties in biomedical and theranostic applications.

- In the present work, we have demonstrated sensors-based on conventional PL of GQDs. The upconversion PL also promote the use of GQDs as a component in various types of sensing and biomedical applications including deep tissue and *in-vivo* sensing.

- Development of well-ordered assembly of zero-dimensional (0 D) GQDs into 1 D nanotube arrays can be used for SERS applications as a metal-free platform. Thus, by using low-cost carbon materials instead of noble metal substrates, the advent of GQD nanotubes will reduce the significant cost of SERS sensors.

- The aptasensor based detection strategy can be extended for different targets of interest.

# THESIS OUTPUT

## List of Publications (From Thesis)

1. **Raji V. Nair,** Reny Thankam Thomas, Vandana Sankar, Hanif Muhammad, Mingdong Dong, Saju Pillai; Rapid, One-Step Acid-Free Synthesis of High-Quality Graphene Quantum Dots for Aggregation Induced Sensing of Metal Ions and Bioimaging, *ACS Omega,* 2017, 2, 8051-8061 [https://doi.org/10.1021/acsomega.7b01262]

2. **Raji V. Nair**, Reny Thankam Thomas, A.P. Mohammad, Saju Pillai; Fluorescent Turn-Off Sensor Based on Sulphur-Doped Graphene Quantum Dots in Colloidal and Film Forms for the Ultrasensitive Detection of Carbamate Pesticides, *Microchemical Journal*, 2020, 157, 104971 [https://doi.org/10.1016/j.microc.2020.104971]

3. **Raji V. Nair**, Parvathy R Chandran, A.P. Mohammad, Saju Pillai; Aptamer Based Sulphur- Doped Graphene Quantum Dot Fluorescent Turn-On Sensor for Selective and Sensitive Detection of Omethoate [*Under review*]

4. **Raji V. Nair**, Parvathy R Chandran, Reny Thankam Thomas, Saju Pillai; Dual mode SERS/Fluorescence Aptasensor for Ultrasensitive and Selective Detection of Omethoate [*Under review*]

5. **Raji V. Nair**, Reny Thankam Thomas, Parvathy R Chandran, Saju Pillai; Enhancement of Fluorescence Emission of Graphene Quantum Dots Guided by Breath Figure Templates and Photonic Band Gap Effect for Rapid and Trace Level Detection of Environmental Pollutants [*Under review*]

## Out of Thesis

6. Kallayi Nabeela, Reny Thankam Thomas, **Raji V. Nair**, Sumina Namboorimadathil Backer, Kiran Mohan, Parvathy R Chandran, Saju Pillai; Direct Visualization of Crystalline Domains in Carboxylated Nanocellulose Fibers, *ACS Omega,* 2020 [https://doi.org/10.1021/acsomega.0c00410]

## Conference Papers and Posters

1. Presented a paper entitled "Fabrication of well-ordered patterns of polymeric porous films by Breath figure technique" in National Conference on Materials Science and Technology **(NCMST 2016)** held at IIST, Trivandrum. (Poster presentation)

2. Presented a paper entitled "Polymer supported large area silver nanostructures as an efficient SERS platform" in International Conference on Polymer Science and Technology **(MACRO 2017)** held at Trivandrum. (Poster presentation)

3. Presented a paper entitled "Polymer supported large area silver nanostructures as an efficient SERS platform" in **Indo-Japan joint symposium**, held at Trivandrum. (Poster presentation)

4. Presented a paper entitled "One pot synthesis of Graphene quantum dots as excellent fluorescent probe for bio-imaging and label free detection of metal ions" in 8th East Asia Symposium on Functional Dyes and Advanced Materials **(EAS8-2017)**, held at CSIR- NIIST, Trivandrum. (Poster presentation)

5. Presented a paper entitled "Rapid, Acid Free Synthesis of Graphene Oxide Quantum Dots as Excellent Fluorescent Probe for Bio-imaging and Environmental Monitoring" in International Conference on Recent Trends in Materials Science & Technology, **(ICMST 2018)** held at VSSC, Trivandrum. (Oral presentation)

6. Presented a paper entitled "Luminescent Poly (Vinyl Alcohol) Composites Containing Sulphur-doped Graphene Quantum Dots for Ultrasensitive Detection of Environmental Pollutants" in 31st **Kerala Science Congress** held at Fatima Mata National College, Kollam. (Oral presentation)

7. Presented a paper entitled "Luminescent Polymeric Films Containing Sulphur-Doped Graphene Quantum Dots for Ultrasensitive Detection of Environmental Pollutants" in **Research Scholars Symposium on Materials Science and Technology,** held at CSIR- NIIST, Trivandrum. (Oral presentation)